Observational characteristics of early star formation

Alison Karen Young

Submitted by Alison Karen Young to the University of Exeter as a thesis for the degree of Doctor of Philosophy in Physics, May, 2019.

I certify that all material in this thesis which is not my own work has been identified and that no material has previously been submitted and approved for the award of a degree by this or any other University.

Signed: .....

Alison Karen Young

Date: .....

Abstract

The formation of low mass stars has been modelled in detail for several decades and in the last 30 years infrared and submillimetre telescopes have observed protostellar sources and discovered faint, embedded protostars, outflows, jets and discs. The first hydrostatic core (FHSC), the first stable pressure–supported object to form during the star formation process, was first predicted in 1969 but has not been definitively observed. Specific criteria are required to distinguish it from other faint pre– and protostellar objects observationally. In this thesis, we develop synthetic observations of the early stages of star formation to help determine how to identify the FHSC in nature.

We present synthetic spectral energy distributions (SEDs) from 3-D radiation hydrodynamical simulations of collapsing pre–stellar cores for a variety of initial conditions. Variations in the initial rotation rate, radius and mass lead to differences in the location of the SED peak and far–infrared flux. We then attempt to fit the SEDs of 15 candidate FHSCs with model SEDs. This showed that the SED can provide an insight into the nature of these sources and enable sources that are probably more evolved to be ruled out.

Next, we produced spectral line observations for CO, HCO^+, CS and SO, calculated from radiation (magneto)hydrodynamical models, chemical modelling and Monte Carlo radiative transfer. Many common molecules are strongly depleted except for in the inner few 10s of AU , after the formation of the FHSC. HCO^+ $(1-0)$ and SO (8_7-7_6) spectra show variations which may allow a candidate FHSC to be distinguished from a more evolved object. It may also be possible to detect the rotation of the outflow in CO $(4-3)$ and $(3-2)$ lines for nearby ($\sim$ 150 pc) sources.

Lastly, we applied the chemical model to a large–scale simulation of cluster formation. This showed, again, that the abundances of most species are depleted with respect to abundances in the interstellar medium and are only released into the gas phase in small scale regions where protostars are forming. This work also highlighted the importance of considering the initial conditions carefully because the physical history has a substantial effect on the calculated abundances in the outer, low density regions.

Declaration of Authorship

Portions of this thesis have been published in peer–reviewed papers. The content of Chapter 3 except for Sections 3.4.5 and 3.4.6 is derived from the paper 'What can the SEDs of first hydrostatic core candidates reveal about their nature?' which was published in the Monthly Notices of the Royal Astronomical Society in 2018 (Volume 474:800-823). The results described in Section 3.4 and the related paragraphs of the Discussion (Section 3.5) differ slightly from the paper as we changed the criterion for selecting model SEDs. Chapter 4 except for Sections 4.3.2 and 4.5.5 is derived from the paper 'Synthetic molecular line observations of the first hydrostatic core from chemical calculations' which was published in the Monthly Notices of the Royal Astronomical Society in 2019 (Volume 487:2853-2873). All of this published content was written by the author of this thesis.

Contents

List of Figures

List of Tables

Acknowledgements

Firstly, I would like to thank my supervisor Prof. Matthew Bate for his guidance and encouragement over the last few years. I am very grateful to the many members of the Exeter Astrophysics Group who have offered assistance and advice for the work presented in this thesis, in particular Prof. Tim Harries, Dr. Jenny Hatchell, Dr. Dave Acreman, Prof. Stefan Kraus, Dr. Pablo Loren-Aguilar, Dr. James Wurster, Dr. Ben Lewis, Dr. Tom Douglas, Prof. Tim Naylor and Dr. Nathan Mayne. Thank you to Sam, Jayesh, Claire, Felix, Ed, Jess and the rest of the 'Not Staff' crew for your friendship and support. Thank you to David Young and Dr. John Allsup for the occasional (mostly Python–related) computing discussions.

I was fortunate to be encouraged by several members of the Norman Lockyer Observatory in my love of astronomy as a teenager. Thanks to Alan Green for my first look through a telescope; to Kathleen Dollery for teaching me about sidereal time and setting circles; and to John Bardsley for showing me how to use Lockyer's own telescope. The view of Mars we had at opposition was unforgettable.

My parents, Karen and Martin, have always been unwaveringly supportive and for this I thank them. My mother maintains that she made sure I saw Comet Hale-Bopp "chugging" across the sky and has endured many meteor showers and lunar eclipses since then. Finally, to Dr. Tim Gray who I married last year: thank you for persuading me to take the leap and apply for a PhD; I've had the best time.

A. Young

Exeter, U.K.

30^{th} May 2019

Can you bind the chains of the Pleiades
or loosen the cords of Orion?
Can you bring out the constellations in their season?
Can you guide the bear with her cubs?
Do you know the laws of the heavens?
Can you regulate their authority over the earth?

— Job 38:31-33 (ISV)

Chapter 1

Introduction

1.1 Introduction to the thesis

One of the most awesome achievements of modern science is to be able to observe the processes associated with the birth of stars and planets. We can now appreciate that we live in a dynamic universe of turbulent gas clouds, sleek protostellar jets and dusty accretion discs sculpted by many interacting physical processes. And yet, as vast as the universe – or even just our Galaxy – is, it is mostly empty space. Molecular clouds are generally little denser than the best laboratory vacuums here on Earth (Zitzwitz and Neff 1995) and these must somehow produce stars that are dense enough to fuse hydrogen.

The majority of stars in our galaxy are classed as "low mass", that is they are no more than a few solar masses. The theory of how these stars form is reasonably well established and technological advances over the last few decades have enabled us to glimpse very young protostars inside their natal clouds and to observe protoplanetary discs where new solar systems are forming. At the same time, developments in computing technology are continually allowing ever more complex simulations and it has been possible to explore the roles played by various physical processes in forming stars.

A dual approach of theory and observation is essential in astrophysics. The science can only be as good as the observations. While models are brought in to explain observed phenomena, theory must also be verified by observing nature, otherwise it remains no

more than a hypothesis. In order to verify theory, we first need to develop predictions and determine what observations are required to test them. This is the sticking point of an early stage of star formation known as the first hydrostatic core (FHSC). So far it has been unclear what the distinctive characteristics of this object might be, therefore it has been very difficult for observers to know what exactly to look for. We aim to develop a better understanding of the observational characteristics of this early phase of star formation to assist with the search for the FHSC in nature.

1.2 An overview of star formation

Star formation occurs in molecular clouds, vast cool regions of dusty gas where hydrogen is primarily in molecular form. Molecular clouds range in size from ~ 0.1 pc to ~ 100 pc and their density is anywhere between $\sim 10^{-24}\,\mathrm{g\,cm^{-3}}$ (~ 1 atom $\mathrm{cm^{-3}}$) to $\sim 10^{-18}\,\mathrm{g\,cm^{-3}}$ ($\sim 10^{6}\ \mathrm{cm^{-3}}$) in the densest regions (Ward-Thompson and Whitworth 2011). They are composed of approximately 70 per cent by mass molecular hydrogen and 28 per cent helium. All other elements, the "metals", make up the remainder, and dust comprises ~ 1 per cent of the mass. The dust grains are sub–micron in size and are composed of silicates and carbon. The small fraction of the cloud composed of metals is nevertheless significant. The density is sufficiently high that simple gas–phase chemical reactions can occur, as can chemical reactions which take place on the surface of dust grains such as the formation of H_2 and CO. In more diffuse regions of the interstellar medium (ISM), molecules are destroyed by UV photons via photodissociation reactions but within dense clouds the gas is well shielded from UV radiation and molecules, often including complex molecules, survive.

These molecules and the dust grains may only make up a few per cent of the cloud mass but they provide the dominant mechanisms responsible for the temperature of the gas. Key cooling processes include thermal emission by dust grains and line emission from CO molecules. Similarly, molecular clouds are heated by ionisation caused by cosmic rays and UV photons as well as thermal heating of dust grains by the interstellar radiation field (ISRF). Starless denser regions are cooler because the optical depth is greater and they are shielded from the ISRF. In cooler regions the thermal pressure is lower and therefore

the mass that can be supported against gravitational collapse decreases. The cooler and denser parts of a cloud may then become unstable to collapse and fragmentation. And so the process of forming a star begins.

Molecular clouds may fragment and form dense cores if the mass within a region exceeds the upper limit that can be pressure supported. For a region of uniform density ρ_0 to be stable against gravitational collapse its diameter must be greater than the *Jeans length*, $\lambda_{\rm J}$ (Jeans 1928):

$$\lambda_{\rm J} = \sqrt{\frac{\pi v_{\rm s}^2}{G\rho_0}}, \tag{1.1}$$

where $v_{\rm s}$ is the sound speed and G is the gravitational constant. This can also be written as limit on the maximum mass that can be thermally supported and this is known as the *Jeans mass*, $M_{\rm J}$:

$$M_{\rm J} = 2.92\frac{v_{\rm s}^2}{G^{3/2}\rho_0^{1/2}}. \tag{1.2}$$

The sound speed in an ideal gas is

$$v_{\rm s} = \frac{\gamma \mathcal{R} T}{\mu}, \tag{1.3}$$

where γ is the adiabatic index, $\mathcal{R}$ is the gas constant and T is the gas temperature. The cloud mass that is stable against collapse ($M_{\rm J}$) therefore strongly depends upon the temperature and is inversely proportional to the average density of the gas. The outcome of this is that as an unstable cloud collapses, it may also fragment further as the Jeans mass decreases with the increasing density. This process is thought to produce the sub–parsec scale cold, dense cores with temperatures ~ 10 K and densities of $\sim 10^{-19}\,{\rm g\,cm^{-3}}$ ($\sim 3 \times 10^4\,{\rm cm^{-3}}$, Ward-Thompson and Whitworth 2011).

It is these dense cores which collapse to form individual (or perhaps binary or multiple) stars, a process first outlined in detail by Larson (1969), following his 1-D numerical calculations of a collapsing uniform density sphere. The first stage of this collapse, the "first collapse", occurs isothermally and the gas is approximately in free–fall. The density is $\lesssim 10^{-13}\,{\rm g\,cm^{-3}}$, therefore the opacity is low and the thermal energy generated by the collapse can be freely radiated away. The density increases at the centre of the core, rising from $\sim 10^{-19}\,{\rm g\,cm^{-3}}$ to $\sim 10^{-13}\,{\rm g\,cm^{-3}}$ over the course of a few 10^4 years. The free–fall

time $t_{\rm ff} \propto 1/\sqrt{\rho}$ which means that the collapse quickens as the density increases and the density becomes increasingly sharply peaked at the centre of the core.

When the central density exceeds $\sim 10^{-13}\,{\rm g\,cm^{-3}}$ the gas becomes optically thick to infrared radiation and the collapse becomes approximately adiabatic. The temperature and pressure rapidly increase with the increasing density and a small core reaches hydrostatic equilibrium in the very centre where the pressure is high enough to stop further gravitational collapse. This object is known as the first hydrostatic core (FHSC) and has a mass of $\approx 0.01\ {\rm M}_\odot$ and is a few AU in radius. Due to the sharp peak in the density distribution, the rest of the dense core outside of this inner adiabatic region is still collapsing in isothermal free–fall after the FHSC has formed. A shock front forms at the edge of the FHSC where the infalling gas reaches the stable FHSC.

The FHSC proceeds to grow in mass as it accretes this infalling material. As the density increases, the pressure and temperature continue to rise. When the temperature reaches $\sim$2000 K molecular hydrogen begins to dissociate. This is an endothermic process, which causes the adiabatic index to drop and so the pressure support is reduced. The centre of the FHSC becomes unstable to gravitational collapse once again and undergoes a "second collapse" until most of the molecular hydrogen has dissociated. The second collapse is far quicker than the first collapse, lasting just a few years, because the density is so much higher. The pressure of the now atomic hydrogen gas increases quickly with the density, giving rise to a stable hydrostatic object, the "second core" or "stellar core". This object is much more compact than the FHSC, with a radius of $\approx 2\ {\rm R}_\odot$ and central density of $10^{-2}\,{\rm g\,cm^{-3}}$ (Larson 1969). The second collapse occurs only in the very centre of the FHSC where the density is highest. The free–fall time is therefore much shorter in that central region than in the rest of the former FHSC and in the few years over which the second collapse takes place, the majority of the FHSC changes little. After stellar core formation, the remnants of the FHSC are gradually accreted as well as the remainder of the infalling envelope. Rotation will slow this accretion and lead to the formation of a disc (Bate 1998; Saigo et al. 2008).

This stellar core is the newly–formed protostar. With a central temperature of $\sim 10^4$ K it is far too cool for nuclear fusion to begin and it must undergo much further

accretion and gravitational contraction in the protostellar phase before it becomes a main sequence hydrogen–burning star. To start with the protostar is still deeply embedded within the cloud core which is still too optically thick for the new protostar to be seen directly but, as it continues accreting and the protostellar outflow clears a cavity, the protostar will gradually become exposed.

1.3 Observing early star formation

Observing pre– and protostellar sources presents a significant challenge since these are intrinsically very faint and cool so they do not emit at visible wavelengths. We also need to relate the theoretically predicted stages to what is observed. In this section I will summarise the key observational methods employed in the detection of protostellar sources including candidate FHSCs.

Within molecular clouds there are particularly dense regions which are categorised somewhat unoriginally as "dense cores". These are observed as dark clouds, or "Bok Globules" (Bok and Reilly 1947), in optical in silhouette due to their high optical depths and the extinction of background stars or nebulosity. Dense cores can also be observed in submillimetre or radio emission produced by the cold dust and embedded young protostars are only observable at far-infrared wavelengths. NH_3 (ammonia) emission is often used to trace these high density regions (e.g. Benson and Myers 1989). Many dense cores do contain infrared sources (e.g. Yun and Clemens 1990), which indicates the presence of a protostar, but others are "starless". It is possible to estimate the evolutionary stage of starless cores in further detail by measuring the deuterium fractionation and N_2H^+ and N_2D^+ column densities, for example (Crapsi et al. 2005). Starless cores that are thought to be gravitationally bound are called "pre–stellar cores" and these correspond to the dense cores which collapse to form a protostar in the theoretical models, although observed starless cores have, naturally, more complex morphology. Pre–stellar cores in the Ophiuchus molecular cloud, for example, are observed to have masses of 0.5 - 10 $\mathrm{M}_\odot$ and to be 2000 - 4000 AU across (Ward-Thompson and Whitworth 2011). Optically thin tracers such as $C^{18}O$ $(2-1)$ or $H^{13}CO^+$ $(1-0)$ are useful but suffer from significant depletion of the source chemical species at high densities so species like NH_3 and N_2H^+ tend to be used

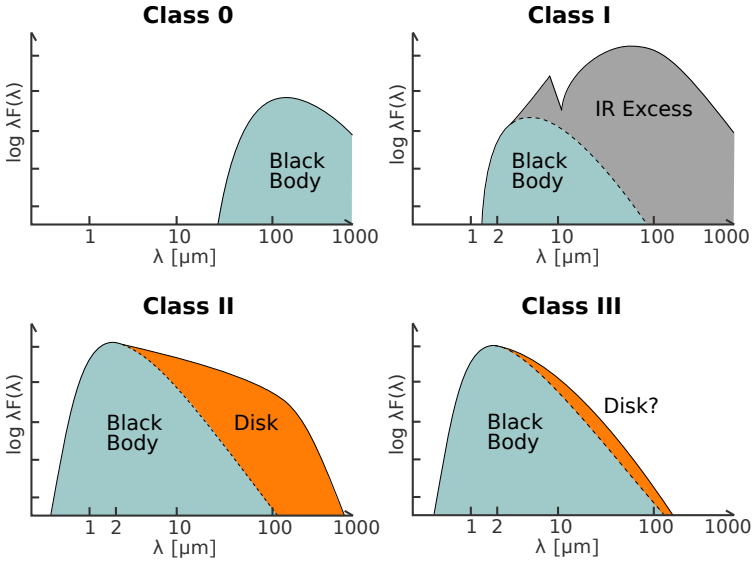

Figure 1.1: Characteristic SEDs of the YSO classes. For class 0 the protostar is obscured by the dense envelope and the SED is similar to that of a cool blackbody. For classes I - III the SED is a combination of the warm blackbody emission of the protostar and cool dust emission from the envelope and disc. The contribution of the dust emission decreases for higher classes, which is assumed to be due to the dispersal of the envelope. Figure: Persson (2014)

as well for observing pre-stellar cores (di Francesco et al. 2007).

From an observational perspective, the stage after the contracting starless pre-stellar core is the class 0 young stellar object (YSO, or class 0 protostar). A class 0 YSO is a protostar which is embedded in a thick infalling envelope and is usually observed to drive an outflow. The significant increase in infrared sensitivity that came with the *Spitzer* Space Telescope led to detections of faint protostars in what were previously starless cores (e.g. Young et al. 2004; Kauffmann et al. 2005). These may be classed as Very Low Luminosity Objects (VeLLOs), which are sources with internal luminosity $L_{\rm int} < 0.1$ $L_{\odot}$, and are thought be low mass class 0 protostars. Class I protostars are still embedded within an envelope but the envelope is typically much less massive than for class 0 sources and there is often a large circumstellar disc through which most of the accretion proceeds. The disc remains for class II, or T Tauri, protostars after most of the envelope has essentially disappeared (White et al. 2007).

Spectral energy distributions (SEDs) are commonly used to distinguish protostars of different evolutionary stages. The SED is constructed by measuring the brightness of a source at several different frequencies, a technique known as photometry. A blackbody spectrum can be fitted to the SED to provide an insight into the characteristic temperature

of the source. The SED deviates from a blackbody curve when the source has two or more components at different temperatures. An example of this is a protostar with a dusty disc. There will be a component of the SED that peaks in the near infrared caused by the protostar itself and another component from the dust emission from the cooler disc which peaks in the far infrared. The protostellar and dust contributions to the SED are shown clearly in Fig. 1.1. Differences in the dust properties can also affect the shape of the SED and may give an indication of dust grain sizes.

The morphologies of YSO SEDs are used to sort them into classes thought to correspond to evolutionary stages, as originally described by Lada and Wilking (1984) and Lada (1987) for classes I – III. Class 0 was added later by Andre et al. (1993) following the discovery of even fainter sources that appeared to be less evolved than class I. The characteristic SEDs of the four classes of protostars are shown in Fig. 1.1 and we now describe their classification. The characteristic SED of class 0 protostars is featureless and can be fitted with a greybody (modified blackbody) spectrum which peaks at $\lambda > 100\ \mu\mathrm{m}$ (Andre et al. 1993). The SEDs of class I protostars peak at slightly shorter wavelengths and most of the emission is still from the dusty envelope but there is an additional "bump" at shorter wavelengths of emission from the protostar itself. At class II the component of the SED caused by the protostar is brightest and peaks around $2\,\mu\mathrm{m}$ and there is significant emission at far infrared wavelengths from the dusty disc and envelope. After this stage the protostar emission dominates the SED and class III protostars do not have significant disc emission.

The sequence of YSO observational classes is primarily due to the gradual brightening of the protostar as it evolves and to the clearing of the envelope. However, this classification is also affected by the viewing inclination if the protostar has a thick circumstellar disc. To address this issue, large sets of synthetic protostar SEDs have been constructed from analytical models with various combinations of protostar, disc and envelope masses and viewing inclinations which can be fitted to protostar observations to aid identification (Robitaille et al. 2006; Robitaille et al. 2007; Robitaille 2017). Observationally, the FHSC is expected to have characteristics between the starless core and class 0 protostar stages and a very low intrinsic luminosity.

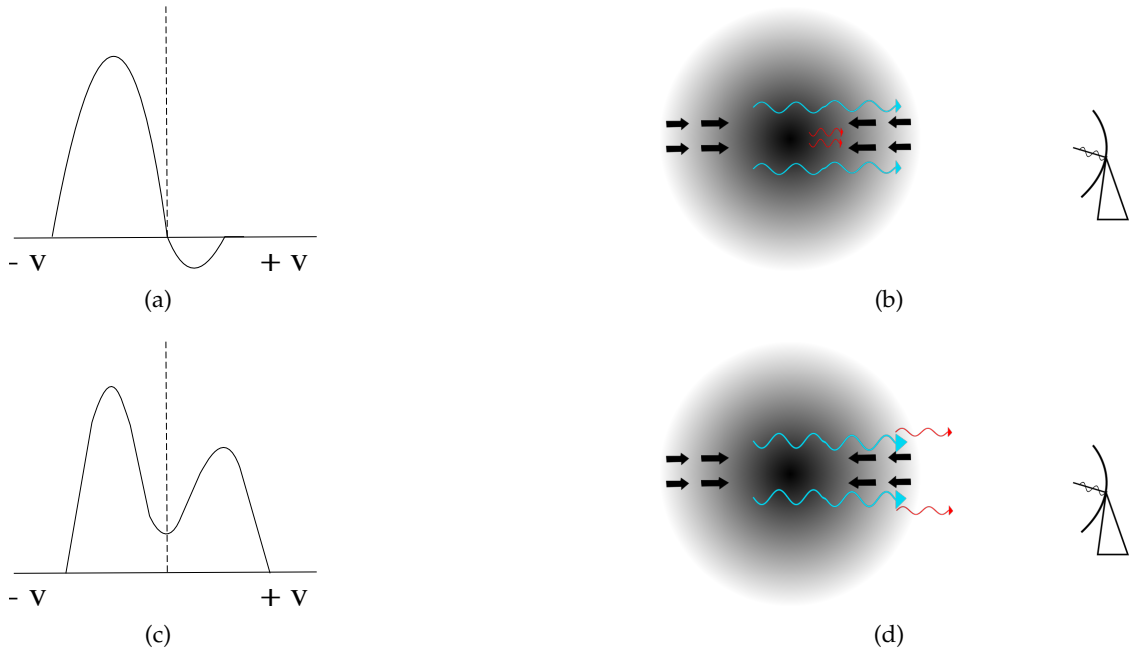

Figure 1.2: (a) The inverse P Cygni line profile taken to be indicative of infalling motions observed in an optically thick transition. (b) Schematic of the formation of this line profile. The infalling gas absorbs frequencies redshifted with respect to the rest frequency. (c) An example of a line profile showing blue asymmetry. The central dip is due to self–absorption. (d) Schematic showing the origin of blue asymmetry. The infalling envelope on the observer's near side is more optically thick at redshifted frequencies. Blueshifted emission originates from the deeper, warmer region so is brighter than the redshifted emission.

Observing the kinematics of a protostellar source provides additional information that can help elucidate its nature. To determine whether a dense core is forming a protostar we can look for evidence of infall. The detection of an "inverse P Cygni" profile is normally taken as evidence of an infalling envelope. A schematic of the line morphology is shown in Fig. 1.2 (a) and its characteristics are a blueshifted emission peak and a redshifted absorption dip. These features may be observed in optically thick transitions where the emission from the far side of the envelope is blueshifted as it falls towards the observer and emission from the near side of the envelope is redshifted as it falls away from the observer. The nearside infalling gas is seen in front of the warmer central core, which means it is likely to be seen as absorption against the continuum emission from the warmer central regions (see Fig. 1.2 (b)). Additionally, because the line is optically thick it suffers from self–absorption and the observed blueshifted emission originates closer to the centre where the temperature is higher and the observed redshifted emission originates further out in the envelope where the temperature is lower. The blueshifted emission is thus brighter than the redshifted emission resulting in the "blue asymmetry" or "blue

bulge", as shown in in Figs. 1.2 (c) and (d). For an optically thin line, the line profile would be symmetrical because absorption effects are far less significant.

Of course, infall is never the only motion within the star–forming cloud core. All such cores rotate, which also affects the spectral line morphology. A rotating object will also produce a double–peaked spectral line when viewed at a nonzero inclination relative to the rotation axis, because this also gives positive and negative line of sight velocities. It is useful to map the line properties spatially, for example by constructing a centroid velocity map, in order to distinguish the different motions (e.g. Adelson and Leung 1988). The "blue bulge" (Walker et al. 1994; Narayanan et al. 1998; Narayanan and Walker 1998) is taken to be a reliable signature of infall even for a rotating core. If the motion is purely rotational, the red– and blueshifted emission will be separated by the rotation axis. In the case of infall, the blueshifted emission will extend across the rotation axis forming a "blue bulge". In the first moment map (intensity–weighted mean velocity) a central blue spot may also indicate infall (Mayen-Gijon et al. 2014; Estalella et al. 2019). Spectral lines are also subject to thermal broadening of a few hundred $\mathrm{m\,s^{-1}}$ due to the thermal motions of the gas particles and turbulent broadening of 0.1–$0.2\ \mathrm{km\,s^{-1}}$ due to turbulent motions within the cloud.

Continuum imaging allows us to see the structure of the source, however at the wavelengths of these sources the angular resolution tends to be low due to the Rayleigh criterion, which states that the minimum resolvable angular separation, θ, is related to the wavelength, λ, and the aperture, D:

$$\theta = 1.22 \left(\frac{\lambda}{D} \right). \tag{1.4}$$

The aperture required to resolve sources expected to be pre– or protostellar, which are often fractions of an arcsecond in size, is larger than most existing telescopes so these sources are usually unresolved. For this reason it is necessary to employ interferometry to gain an acceptable angular resolution at submillimetre wavelengths. Interferometry involves combining the signal from an array of individual dishes separated by finite distances or *baselines*. An interference pattern is produced due to the small differences in path length

for each dish. The contrast between interferences fringes or *visibilities* for a set of baselines can be reconstructed into an image. The combined signal from each pair of dishes provides information on the brightness on a particular scale with larger baselines providing information on smaller scale structures. To ensure the image is reconstructed accurately, observations should be collected for the full range of baselines up to the largest required otherwise there will be information missing on some spatial scales. This means single–dish observations are often combined with the interferometric data to include emission from scales larger than that recoverable by the smallest baseline the array can offer.

A crucial step forward in observing star formation has been the completion of the *Atacama Large Millimeter/submillimeter Array* (ALMA). Astronomers are now exploiting the unprecedented submillimetre sensitivity and resolution, for example to detect fragmentation in starless cores (e.g. Dunham et al. 2016), to image disc structures (e.g. Dipierro et al. 2018), to probe the inner regions of outflows (e.g. Lee et al. 2018) and to detect the chemical differentiation of structures associated with protostars (e.g. Oya et al. 2018).

1.4 The development of the theory of low mass star formation

The calculations of Larson (1969) established the key stages in the collapse of a dense cloud core and predicted the existence of the first and second hydrostatic cores for the first time. These were 1-D spherically–symmetric models with simple assumptions for the initial conditions and boundary conditions. The FHSC formed with radius 4 AU and 0.01 $\mathrm{M}_{\odot}$ and lasted a few hundred years. The stellar core initially had $r \sim 1.3\,\mathrm{R}_{\odot}$, $M \sim 1.5 \times 10^{-3}\ \mathrm{M}_{\odot}$, central density $\rho_{\mathrm{cen}} \sim 0.02\ \ \mathrm{g\,cm^{-3}}$ and temperature $T \approx 2000$ K. Since the process by which a protostar is formed was first described, much work has been undertaken to hone the details of the nature of these objects and how the process might vary under different conditions. Computer models have been extended to two and three spatial dimensions and are capable of increasingly high resolution. More physical processes such as radiative transfer and magnetism can now be included to investigate their effects. The properties of the FHSC were first determined from (comparatively) simple 1-D calculations. Since then some of these properties have been shown to vary greatly with the initial conditions and/or the physics considered. In this section we will review the properties of the FHSC

and associated structures predicted by theoretical modelling with reference to the relevant developments in the models.

1-D hydrodynamical calculations are useful for exploring how the collapse varies under a wide range of initial conditions and for ascertaining the effect of various approximations. Vaytet et al. (2012) performed 1-D multigroup radiation hydrodynamical calculations where the frequencies are binned into five and twelve groups. This allowed them to perform frequency–dependent radiative transfer calculations which could be compared to the results of grey radiative transfer treatments for the collapse of 1 $\mathrm{M}_{\odot}$ cloud cores. The overall properties of the FHSC produced were very similar to the grey simulation but the radius, temperature and mass of the FHSC were slightly lower in the grey simulation. The authors also compared the FHSC formed from 0.1 $\mathrm{M}_{\odot}$ and 10 $\mathrm{M}_{\odot}$ cloud cores and found no significant differences in the FHSC properties. The FHSC had radius $r = 7$ AU and mass 0.02 $\mathrm{M}_{\odot}$.

Bhandare et al. (2018) performed 1-D hydrodynamical simulations to investigate how the collapse and FHSC formation process varies with initial cloud mass by repeating calculations for initial masses of 0.1 - 100 $\mathrm{M}_{\odot}$. Unlike the results of Vaytet et al. (2012), the FHSC properties did vary with the cloud mass. The radius and mass of the FHSC were found to increase with initial cloud mass for initial masses up to 8-10 $\mathrm{M}_{\odot}$, beyond which point the FHSC mass and radius actually decreased with increasing initial cloud mass. The lifetime of the FHSC decreased with initial cloud mass. The FHSC lifetime exceeded 100 years only for initial cloud mass < 10 $\mathrm{M}_{\odot}$ and for the higher mass clouds ($\gtrapprox 20$ $\mathrm{M}_{\odot}$) the lifetime was of the order of years and the authors predict that the FHSC stage does not occur for collapsing higher mass cores because the ram pressure of infalling material exceeds the thermal pressure.

The first 3-D calculations were performed by Bate (1998) using a barotropic equation of state. This work exploited the smoothed particle hydrodynamics (SPH) method and revealed that, if the initial cloud core is rotating moderately quickly, the FHSC takes the form of a rotationally supported disc. This disc structure may be susceptible to non-axisymmetric instabilities and develops spiral arms which transport angular momentum outwards. This eventually allows the second collapse to occur in the very centre. In this

calculation, the FHSC formed with $r \approx 7$ AU and 0.01 $\mathrm{M}_{\odot}$.

Saigo et al. (2008) further investigated the effect of rotation rate with 3-D grid–based calculations, also using a barotropic equation of state. Their work showed that there are three distinct types of FHSC evolution: spherical–type, disc–type and fragment–type. The spherical–type evolution occurs for the slowest rotating cloud cores with a rotation rate given by $\Omega_{C0} t_{\mathrm{ff}} < 0.01$, where Ω_{C0} is the initial angular velocity. In these cases, a spherical FHSC of $r \approx 1$ AU is produced that lasts a few hundred years. A moderately rotating core of $0.01 < \Omega_{C0} t_{\mathrm{ff}} < 0.05$ gives rise to a centrifugally supported FHSC of $r \approx 10$ AU and has a lifetime of > 1000 years. This is similar to what was seen in the results of Bate (1998). At the highest rotation rates ($\Omega_{C0} t_{\mathrm{ff}} > 0.05$) the FHSC has a radius $\gtrsim 15$ AU which fragments into self–gravitating components.

Bate (2010) implemented a realistic equation of state and radiative transfer to perform 3-D calculations that followed the collapse to after the formation of the stellar core. Whereas with a barotropic equation of state the temperature is set by the density of the gas, here there was substantial heating of the disc by the energy released as the stellar core formed. Despite not including magnetic fields, this produced a thermally–driven bipolar outflow which extended to 50 AU in 50 years and which may assist the formation of the magnetically–launched outflow. The effect of different initial rotation rates was studied next (Bate 2011). The evolution of the FHSC was found to be similar to using a barotropic equation of state but the lifetime was a factor of 1.5 - 3 longer. For example, the lifetime of the FHSC produced in a core with initial $\beta = 0.01$, where β is the ratio of rotational energy to gravitational potential energy, was around 3000 years. The faster rotating cores formed discs, as seen by Saigo et al. (2008), of up to 100 AU in radius. These developed spiral arms and, with $\beta = 0.09$, fragmented.

While increased rotation rate appears to increase the lifetime of the FHSC from a few hundred to a few thousand years, Tomida et al. (2010a) showed that very low mass cloud cores of 0.1 $\mathrm{M}_{\odot}$ form FHSCs that last $> 10^4$ years. In these cases, the accretion rate is very low which causes the evolution of the FHSC to proceed more slowly. This result is consistent with the later results of Bhandare et al. (2018), discussed above, which explored the effects of a larger range of initial cloud core masses.

A major step in the development of our understanding of early star formation was the application of magnetohydrodynamics (MHD) to the problem. Outflows are formed due to a combination of rotation and magnetic fields therefore at least two spatial dimensions are required to model this effect and it is much more computationally demanding than earlier simulations.

Axisymmetric MHD calculations were presented by Tomisaka (2002) with a magnetic field initially parallel to the rotation axis of the cloud. This showed that a magnetically–supported pseudo–disc forms, within which the FHSC forms and second collapse occurs, and a bipolar outflow is launched from the FHSC. In 3-D MHD calculations, Banerjee and Pudritz (2006) showed that the outflow reaches 600 AU from the disc during the lifetime of the FHSC and is launched by magnetic pressure. A faster jet is launched from the second core due to the magnetocentrifugal force. The same effect was reported by Machida et al. (2008). The FHSC outflow and second core jet have very distinct velocities of $5\,\mathrm{km\,s^{-1}}$ and $30\,\mathrm{km\,s^{-1}}$ respectively.

The RMHD simulations of Tomida et al. (2010b) implemented MHD alongside realistic thermal evolution. As shown for RHD only simulations, the FHSC had a larger radius and longer lifetime than the pure MHD case with a barotropic equation of state. The outflow reached $\sim$ 100 AU and had a temperature of $\sim$ 30 K. Other RMHD simulations also produced pseudo–discs and outflows of 100 AU (Commerçon et al. 2010)

The implementation of MHD in SPH codes is more difficult than in grid codes. The first (barotropic) SPMHD models of the cloud collapse presented in Price et al. (2012) produced collimated jets from the FHSC with speeds of up to $\sim 7\,\mathrm{km\,s^{-1}}$. Bate et al. (2014) extended this work by including radiative transfer. The resulting outflows were 1 - 2.5 $\mathrm{km\,s^{-1}}$ and were broader with decreasing magnetic field. The authors point out that the outflow rotates and its tangential velocity is similar to the vertical velocity, which has implications for its observational detection.

Lewis and Bate (2017) experimented with changing the relative inclinations of the magnetic field and rotation axis and changing the magnetic field strength. Differences in inclination gave rise to a warped pseudo–disc and outflow velocities were between 2 and

$8\ \mathrm{km\,s^{-1}}$. A relative inclination between the magnetic field and rotation axis somewhat disrupted the outflow. With $\theta < 45^{\circ}$ between the two, a collimated jet formed as well as the broad outflow but at higher inclinations just a very weak broad outflow developed. For the weaker magnetic field, $\mu = 20$, no outflow formed. This work illustrates that the FHSC will not necessarily be accompanied by an outflow.

The MHD models discussed so far are restricted to ideal MHD. In the ideal MHD limit, matter is essentially fixed to magnetic field lines and the magnetic torques are highly effective at removing angular momentum from the collapsing core. A problem arose that in MHD models disc formation was highly suppressed, which is at odds with observations in which discs are seen to be ubiquitous. This became known as the "magnetic braking catastrophe" (Allen et al. 2003; Mellon and Li 2008; Hennebelle and Fromang 2008). The effect is reduced if the magnetic field and rotation axis are misaligned (Hennebelle and Ciardi 2009) however the formation of symmetrical discs and bipolar outflows, which are observed in nature, is also affected by the misalignment so misalignment alone does not solve this problem.

In reality, the gas is not completely tied to magnetic field lines because nonideal processes come into play. The molecular gas is weakly ionised and is therefore composed of both neutral molecules and charged particles (ions and electrons) which may interact via collisions. The charged particles (the plasma) are tied to the magnetic field lines, which provide support against gravitational collapse. Ambipolar diffusion arises because the neutral particles are decoupled from the charged particles. Neutral particles move unhindered by the magnetic field resulting in an ion–neutral drift. Ion–electron drift causes Ohmic resistivity or dissipation, which weakens the magnetic field. Ambipolar diffusion and Ohmic dissipation work to reduce the magnetic field strength in the centre of the core which reduces the efficiency of angular momentum transport. The Hall effect, caused by ion–electron drift, also transports angular momentum but is not dissipative.

Tomida et al. (2013) performed RMHD simulations with Ohmic dissipation and found that where previously no disc formed, with Ohmic dissipation included a small disc with $r < 0.35$ AU formed around the stellar core. When Ohmic dissipation and ambipolar diffusion are included together a ~ 5 AU rotationally supported disc formed

before the stellar core (Tomida et al. 2015; Tsukamoto et al. 2015), partially resolving the magnetic braking catastrophe. With all three nonideal MHD processes, the Hall effect has been found to suppress or enhance disc formation depending on the relative orientation of the magnetic field and rotation vector (Wardle and Koenigl 1993). For example, even in a strong magnetic field, a disc of 13 AU formed when the magnetic field and rotation vectors were anti–aligned (Wurster et al. 2016) and a two–component outflow is produced. At lower ionisation rates a slow ($\sim 4\,\mathrm{km\,s^{-1}}$) conical outflow forms rather than the faster ($14\,\mathrm{km\,s^{-1}}$) bipolar outflow (Wurster et al. 2018).

The initial properties of the second (stellar) core predicted by Larson (1969) are: $M = 1.3 \times 10^{-3}\,\mathrm{M_\odot}$, $r = 1.3\ \mathrm{R_\odot}$, $T = 2000$ K and $\rho = 0.02\,\mathrm{g\,cm^{-3}}$. The calculations of Vaytet et al. (2013) of 0.1 $\mathrm{M_\odot}$, 1 $\mathrm{M_\odot}$ and 10 $\mathrm{M_\odot}$ cores with frequency–dependent and grey radiative transfer supported the idea that the properties of the stellar core are universal. The structure of the stellar core was also found to be unaffected by the initial magnetic field strength following the 3-D MHD calculations of Bate et al. (2014).

In summary, the mass of the FHSC is expected to be 0.01 $\mathrm{M_\odot}$ initially, but this increases as it evolves, and its radius may be a few AU or it may take the form of a disc with radius 10-100 AU depending on the rotation and magnetic field. The lifetime is anywhere between a few hundred to a few thousand years, depending on the mass of the cloud core, the rotation rate and magnetic field strength and orientation. The FHSC may drive a slow, broad outflow of a few $\mathrm{km\,s^{-1}}$ which is very different to the faster protostellar jets.

1.5 Chemical modelling of star–forming cores

Calculating the chemical reactions that take place as a core evolves is computationally demanding. To make such studies feasible, the approach usually involves reducing the number of spatial dimensions, calculating the chemistry by post–processing hydrodynamical simulations or empirical approximations of the physical conditions. It is possible to include "live" chemistry within hydrodynamical models but this can only currently be achieved with a reduced chemical network, which in turn relies on the results obtained from large network calculations to determine which reactions need to be included. This

approach is more useful for assessing the effect of feedback from the chemistry rather than calculating the chemical abundances. Here we review prior work on modelling the chemical evolution of a collapsing cloud core and during the FHSC stage, focussing on the calculation of abundances rather than the thermal feedback.

Aikawa et al. (2008) took a 1-D RHD physical model of a collapsing core and calculated the chemical abundances taking account of gas phase, gas–grain and grain surface reactions. Initially, most species were depleted in the cold, dense core. CO sublimation was found to begin a few hundred years before the formation of the FHSC and the sublimation radius extended to ~ 100 AU during the FHSC phase. Large organic molecules formed on the surface of dust grains at 20-40 K and were released into the gas phase. Comparing the abundances in an isolated core exposed to the full UV radiation of the ISRF and an embedded core, the CO_2 abundance was enhanced in the isolated core and CH_4 and H_2CO abundances were higher in the embedded core.

Extending the chemistry calculations to two spatial dimensions allowed van Weeren et al. (2009) to compare the abundances in the disc and envelope. This model calculated the chemical abundances at 700 locations from a 2-D model using gas–grain and grain surface reactions. This showed a region of sublimation in the centre, as seen by Aikawa et al. (2008), and freeze–out in the disc. In the envelope, the density decreased with time and so the freeze–out rate decreased which resulted in higher gas phase abundances of species with low binding energy. Grain surface reactions were found to be important for CH_3OH, CO_2, H_2O and H_2CO and CO abundances may be overestimated if these are not included.

With chemical abundances calculated for tracer particles taken from 3-D RHD models, Furuya et al. (2012) showed that gas phase abundances in the inner envelope and outer layers of the FHSC where $T \lesssim 500$ K are mainly determined by sublimation. Where $T > 500$ K abundant molecules such as H_2CO are destroyed and simple molecules are reformed. Large organic molecules were found to be associated with the FHSC at $r < 10$ AU .

Modelling only gas–phase and gas–grain reactions and excluding grain surface greatly simplifies the calculation and is less computationally expensive so van Weeren et

al. (2009) tested the effects of removing the grain surface reactions to determine whether it is necessary to include them when modelling the collapse of a pre–stellar core. The abundances of CO, CS, SO, HCN and HNC better matched observations without grain surface reactions but N_2H^+, H_2CO and CH_3OH matched observations well from the model with grain surface reactions. The abundances of HCO^+ calculated with and without grain surface reactions were similar, indicating that HCO^+ is not strongly affected by grain surface chemistry.

Another study of the chemical evolution in 3-D looked specifically at which components of the core were traced by different species and used a full gas–grain network. The results of Hincelin et al. (2016) include that CN, HCO^+, N_2H^+ and H_2CN trace the envelope and that NH_3, N_2H^+ and HCO^+ may help distinguish the pseudo-disc and disc. The abundances were generally higher in the outflows of more highly magnetised cores which may allow some distinction between models with different magnetic field strengths.

Dzyurkevich et al. (2016) used a reduced network of mainly H-C-O gas–grain chemistry to calculate abundances of 56 species at the same time as calculating the dynamical evolution of the collapse of a dense core, experimenting with different dust grain size distributions. Thus showed that the chemistry should be calculated dynamically to obtain gas and ice phase abundances of CO, rather than post–processing a single snapshot because the latter resulted in CO abundances an order or magnitude lower. For mean grain sizes $> 1\,\mu\mathrm{m}$ the gas–dust interaction timescales increased which strongly affects the relative gas and ice phase abundances.

Priestley et al. (2018) developed empirical models of the evolution of the collapse of a core from various numerical calculations, which enabled them to compare the chemical evolution in different hydrodynamical models. Overall, models with higher gas densities led to abundances that were more depleted because the freeze–out rates were higher. The model that included ambipolar diffusion collapsed more slowly and had higher densities at larger radii. The CO and HCN abundances were less sharply depleted towards the centre than for the ideal MHD and non–magnetised models.

1.6 Observations of candidate first hydrostatic cores

This key stage of star formation is still yet to be observed definitively. The observational search for the FHSC has, however, produced several "candidate FHSCs". A low luminosity source ($\lesssim 0.1$ L$_\odot$) is usually designated a candidate FHSC if it is faint or undetected at wavelengths $\lambda < 70\,\mu\mathrm{m}$ and no outflow faster than 10 km s^{-1} is observed. Here we briefly summarise the nature of eight candidate FHSC reported in the literature that will be discussed further and compared with the theoretical results in this thesis.

1.6.1 B1-bN and B1-bS

B1-bN and B1-bS are two FHSC candidates in the Perseus molecular cloud thought to comprise a wide binary system that were first identified via their SEDs (Pezzuto et al. 2012). Further observations revealed two central compact objects on the scale of 100 AU, significant CO depletion and CO outflows of a few $\mathrm{km\,s^{-1}}$ associated with both sources (Hirano and Liu 2014). Interferometric observations with the *IRAM Plateau de Bure* interferometer of methanol showed that the outflows were up to 1300 AU for B1-bN and 3300 AU for B1-bS and allowed the masses of the sources to be estimated at ~ 0.36M$_\odot$ within 250 AU each (Hirano and Liu 2014). B1-bN/bS shows evidence of chemical segregation in combined *NOrthern Extended Millimeter Array* (NOEMA) and IRAM 30 m telescope observations: a rotating pseudo–disc was detected in NH_2D, the infalling envelope was detected in CO isotopologues and the outflows were detected in H_2CO (formaldehyde) and CH_3OH (methanol) (Fuente et al. 2017).

1.6.2 CB17 MMS1

Within the CB17 Bok globule, the source CB17-MMS was discovered (Chen et al. 2012). This has faint dust continuum emission and was not detected in *Spitzer* images at $\lambda < 70\,\mu\mathrm{m}$. There is tentative evidence of an outflow of $\sim 2.5\,\mathrm{km\,s^{-1}}$ and this source is thought to be ~ 0.035 M$_\odot$ and ≤ 0.04 L$_\odot$.

1.6.3 Per-Bolo 58

Per-Bolo 58 was identified in the Perseus molecular cloud (Hatchell et al. 2005; Enoch et al. 2006; Enoch et al. 2010; Schnee et al. 2010). Unusually for a FHSC candidate, there is a detection at $24\,\mu\mathrm{m}$. Despite this, Enoch et al. (2010) were able to fit model SEDs of FHSCs to the data. The observed SED was also fitted by a protostar with a high inclination but the authors qualify this by adding that "if Per-Bolo 58 is a true protostar then it is one of the lowest luminosity embedded protostars known". Outflows extending for several thousand AU and a with maximum velocity of $\sim 7\,\mathrm{km\,s^{-1}}$ have been detected in SMA observations at the source (Dunham et al. 2011). *Combined Array for Research in Millimeter–wave Astronomy* (CARMA) observations of N_2H^+, $C^{18}O$ and others have lead to the conclusion that Per-Bolo 58 is undergoing a turbulent and magnetised collapse and that it lies close to larger scale filamentary structures whose accretion flows may contribute to the spectra (Maureira et al. 2017b).

1.6.4 Chamaeleon-MMS1

Cha-MMS1, located in the Chamaeleon I cloud (Reipurth et al. 1996), is another well–studied candidate FHSC [1]. There are faint detections of Cha-MMS1 at $24\,\mu\mathrm{m}$ and $70\,\mu\mathrm{m}$ and it is thought to have formed a compact central object, no older than the very beginning of the FHSC stage (Belloche et al. 2006). From *Atacama Pathfinder Experiment* (APEX) and *Mopra Radio Telescope* observations Tsitali et al. (2013) find an infall velocity profile that is consistent with theoretical predictions of the FHSC phase and, like Belloche et al. (2006), do not detect an outflow although there could be an unresolved compact outflow. *Australia Telescope Compact Array* (ATCA) observations with a resolution of ~ 1000 AU still did not reveal an outflow, which is surprising considering Cha-MMS1 was also measured to be rotating much faster than the average for such cores (rotational to gravitational potential energy ratio of $\beta = 0.07$ (Väisälä et al. 2014) compared to the typical value of $\beta = 0.02$ (Goodman et al. 1993)) and the region has been found to be significantly magnetised (Whittet et al. 1994; Haikala et al. 2005).

1. Cha-MMS1 is listed as CHAI-04 in Dunham et al. (2016)

1.6.5 L1451-mm

A compact object was found in CARMA and SMA CO $(2-1)$ observations of the dense core L1451-mm (Pineda et al. 2011). The CO $(2-1)$ emission takes the form of red– and blueshifted lobes of around 1100 AU in extent. The authors interpret this as an outflow, albeit "the weakest outflow found so far", but the inclination of the system is not known. The direction of this outflow is perpendicular to the velocity gradient measured in NH_3, N_2H^+ and NH_2D lines, which is consistent with a rotating central object and outflow. With a higher resolution of $\sim$ 210 AU , Tobin et al. (2015b) confirmed the detection of the compact CO outflow. Infall signatures, including an inverse P Cygni profile in HCN $(1-0)$ and a double–peaked profile with blue asymmetry in N_2H^+, were reported by Maureira et al. (2017a) who also note they find no evidence of a more extended outflow on larger scales.

1.6.6 Ophiuchus A N6 and SM1

Two sources in the nearby Ophiuchus star forming region have recently been identified as possible FHSCs: N6 and SM1N (Friesen et al. 2018). A compact continuum source of $\sim$ 100 AU was detected at N6 in *Atacama Large Millimeter/Submillimeter Array* (ALMA) observations with a mass of 0.025 $\mathrm{M}_\odot$ estimated from the total continuum flux. The mass of SM1N was estimated to be 0.03 $\mathrm{M}_\odot$ but the authors were not able to determine its structure. Both sources appear to have CO $(2-1)$ emission of a few $\mathrm{km\,s^{-1}}$ and spanning a few hundred AU associated with them but there is no clear outflow structure.

1.6.7 PACS Bright Red Sources

Among the sources observed in the *Herschel* Orion Protostars Survey (HOPS) were a number or sources that were very faint at $24\ \mu\mathrm{m}$ with the flux ratio $70\,\mu\mathrm{m}$ to $24\,\mu\mathrm{m} > 1.65$ (Stutz et al. 2013). These are known as PACS Bright Red Sources (for the PACS instrument on the *Herschel* telescope). Of these sources, no outflow was detected in the CO $(1-0)$ observations of Tobin et al. (2016b) for HOPS 398, 401, 402 and 404. These sources could, however, contain outflows of less than $2\,\mathrm{km\,s^{-1}}$ which is below the sensitivity of the observations. These sources differ from most Class 0 objects because they were undetected at wavelengths shorter than $70\,\mu\mathrm{m}$ and had no detectable outflows.

Visibility amplitude profiles of these sources at 2.9 mm are presented in Tobin et al. (2015a). HOPS 401, 402 and 404 were found to have flat visibility amplitudes which were reproduced by models with either an unresolved compact central source or an envelope with a very steep density profile. Both scenarios require large amounts of mass within a few thousand AU and this is consistent with the FHSC structures (discs of less than few hundred AU within a dense envelope).

1.7 Synthetic observations

The creation of synthetic observations is essential to compare theoretical models with observations effectively. For example, the measured values of some properties such as the velocity of the outflow may be different to the absolute values predicted by the model because emission from the fastest part of the outflow might not be observable. As discussed above, to identify an FHSC in nature we need to know how to distinguish it from more evolved but faint, young protostars. There have been various attempts to solve this problem by simulating observations to predict the observational properties of the FHSC.

Saigo and Tomisaka (2011) produced synthetic SEDs at various stages throughout the first core phase. Their results show that the SED peak shifts to shorter wavelengths as the FHSC evolves, from $\lambda \simeq 200\,\mu\mathrm{m}$ early on to $\lambda \simeq 80\,\mu\mathrm{m}$ late in the first core phase. They plotted their SEDs along with that of a VeLLO and found that the FHSC has a lower luminosity and is much dimmer at $\lambda \lesssim 100\,\mu\mathrm{m}$.

Commerçon et al. (2012a) produced synthetic SEDs for the evolution of a rotating FHSC from a radiation magnetohydrodynamical model. The SED peaks did not change after FHSC formation and they were not able to distinguish the FHSC from the stellar core from the SEDs. Like Saigo and Tomisaka (2011), they found the SED peak to be at $\lambda \simeq 200\,\mu\mathrm{m}$ early in the FHSC phase. Commerçon et al. (2012a) also found that SEDs cannot be used to distinguish between magnetised and non-magnetised cases but the mid– to far–infra red flux can distinguish between a starless core and a FHSC. They also suggest that chemical analysis may be useful for differentiating between the FHSC and stellar core because at the higher temperatures near the stellar core dust grains have evaporated so

species such as C and Si enter the gas phase. Commerçon et al. (2012b) subsequently calculated synthetic ALMA dust emission maps which showed that ALMA would be able to resolve a fragmenting FHSC but could not reveal any difference between an FHSC and a stellar core. The authors also report that there were distinctive morphological differences between magnetised and non-magnetised models which were observable in the continuum in only $\sim$18 min integration time and in bands 3 and 4 (centred on 100 GHz and 144 GHz respectively).

Tomisaka and Tomida (2011) simulated CS line emission before and after FHSC formation using a fixed CS abundance and found the blue asymmetry characteristic of infall, signatures of a rotating outflow and that the linewidth increases after FHSC formation. The uniform CS abundance is not realistic because the cold, dense nature of the dense core in all but the central few tens of AU leads to significant depletion of gas–phase species (see Chapter 4). The line brightness and morphology is likely to change if depletion is taken into account.

Harsono et al. (2015) produced synthetic observations for snapshots from the collapse of a molecular cloud with the aim of identifying observables to distinguish a rotationally supported disc from a rotating infalling envelope with a pseudo-disc. They found that the disc and pseudo–disc can be distinguished in continuum emission albeit with a spatial resolution of $\sim$14 AU and for systems at low inclination. At high inclination the disc and pseudo-disc show similar shapes in the continuum images. In contrast to Commerçon et al. 2012b, they suggest that features are most easily seen at 450 µm ($\sim$660 GHz).

As well as continuum images, Harsono et al. (2015) simulated rotational lines of CO isotopologues. A depleted CO abundance was used where $T_{\rm dust} < 25\,{\rm K}$. The disc displays a velocity gradient in the same direction as the disc structure visible in the continuum images caused by the rotational motion whereas the pseudo-disc has a velocity gradient perpendicular to the disc structure, due to infalling gas. At high inclinations, however, the velocity gradient in the pseudo-disc case changes to be aligned with the disc structure as the line emissions are affected by the rotational motion of the pseudo-disc when observed at these angles. Position–velocity (PV) diagrams were constructed in the direction of the velocity gradients. The PV map is symmetric for infall dominated systems

but the emission peaks are offset when there is rotation and these showed this rotation signature even in the case of the pseudo-disc. With regard to CO isotopologues, $C^{18}O$ was best for distinguishing the disc and pseudo disc but $C^{17}O$ better showed rotation. The shape of the $C^{17}O$ PV maps could also be mistakenly interpreted as rotational motion when cut perpendicular to the orientation of the pseudo-disc. This indicates that to identify a rotationally supported disc, spatially and spectrally resolved observations of both $C^{17}O$ and $C^{18}O$ lines are required in combination with continuum emission maps to confirm the orientation of the disc structure.

As early as 2001, Rawlings and Yates (2001) performed hydrodynamical, chemical and frequency–dependent radiative transfer simulations to model the line profiles of star–forming cores, focussing on tracers of infall kinematics. They conclude that the models need to be source–specific because the line profiles are very sensitive to differences in depletion, for example. The authors recommend the following strategy for interpreting infall line profiles: the density and temperature profile should be estimated from continuum observations first, then the infall motions can be semi–empirically determined, next chemical abundances can be calculated and lastly, radiative transfer modelling can be performed to predict line profiles.

Lee et al. (2004) also predicted line profiles for an infalling pre–stellar core using a 1-D model, with no grain surface reactions. They suggest that HCN could distinguish FHSCs and Class 0 sources because its abundance increases rapidly during the transition between the two stages. As was discussed in Section 1.5, when calculating abundances in a star–forming core the chemical evolution that takes place during its collapse should be taken into account. Nevertheless, Lee et al. (2004) conclude that CO and HCO^+ can be approximated satisfactorily with a simple drop function.

1.8 Objectives and outline

As we have seen, the FHSC is an important stage in the formation of low mass stars. While the initial properties of the stellar core may not depend on FHSC properties, the properties of the FHSC determine the properties of the outflow and disc and/or pseudo–disc, which

may then affect the envelope structure and accretion rates. The outer regions of the FHSC may form the early protoplanetary disc and this sets the initial physical and chemical conditions of the disc, which may have implications for planet formation.

There are still not enough constraints on the observational properties of the FHSC to be able to distinguish it from other faint protostellar sources. We aim to develop further predictions for the observational characteristics of the early stages of low mass star formation to assist the identification of the FHSC in nature for the first time.

We describe the methods and codes used in this thesis in Chapter 2. In Chapter 3 we calculate a set of SEDs for various FHSC properties and examine the results of fitting these to the observed SEDs of candidate FHSCs. In Chapter 4 we post–process hydrodynamical simulations with an open–source chemical solver to perform a pseudo–time–dependent chemical calculation. The chemical abundances are then used to simulate molecular line observations. In Chapter 5, we apply the chemical solver to a model of star cluster formation and in Chapter 6 we provide a summary of the main conclusions.

Chapter 2

Method

2.1 Introduction

The simulation of observations necessitates the use of several different codes to model the various physical and chemical processes. We begin with radiation (magneto) hydrodynamical modelling of the collapse of a molecular cloud core and the method used to perform these calculations is presented in Section 2.2. The radiative transfer implemented in the former method is frequency–independent and so we employ a Monte Carlo radiative transfer technique to simulate the continuum and molecular line emission, which is detailed in Section 2.3. We quantitatively compare the synthetic spectral energy distributions with observations and describe the method used in Section 2.4. Chemical calculations were performed to obtain abundances from which to model the molecular line spectra. In Section 2.5 we detail the method for calculating chemical abundances.

2.2 Hydrodynamical modelling

2.2.1 Smoothed particle hydrodynamics

To perform the hydrodynamical modelling we use SPHNG (Bate et al. 1995; Bate 1995) which employs the smoothed particle hydrodynamics (SPH) method. The SPH approach involves modelling a fluid as a set of particles without requiring a grid. Particles represent elements of fluid with equal masses and so there are more particles in regions of higher

density, which naturally results in higher spatial resolution in regions of higher density. This property makes SPH an ideal technique for modelling star formation since length scales vary by up to 10 orders of magnitude and the density varies by up to 20 orders of magnitude.

The Lagrangian equations of radiation hydrodynamics with gravity are

$$\frac{D\rho}{Dt} = -\rho\nabla\cdot\mathbf{v}, \tag{2.1}$$

$$\frac{D\mathbf{v}}{Dt} = -\frac{1}{\rho}\nabla p - \nabla\Phi + \frac{\chi\rho}{c}\mathbf{F}, \tag{2.2}$$

$$\rho\frac{D}{Dt}\left(\frac{E}{\rho}\right) = -\nabla\cdot\mathbf{F} - \nabla v : \mathbf{P} + 4\pi\kappa_p\rho B - c\kappa_E\rho E, \tag{2.3}$$

$$\rho\frac{Du}{Dt} = -p\nabla\cdot\mathbf{v} - 4\pi\kappa\rho B + c\kappa\rho E, \tag{2.4}$$

$$\nabla^2\Phi = 4\pi G\rho, \tag{2.5}$$

where $D/Dt \equiv \partial/\partial t + \mathbf{v}\cdot\nabla$ is the convective derivative, ρ is the density, v is the velocity, p is the gas pressure, Φ is the gravitational potential, χ is the opacity, $\mathbf{F}$ is the radiative flux which is discussed in Section 2.2.3, E, is the radiation energy density, $\mathbf{P}$ is the radiation pressure tensor, κ is the opacity, B is the Planck function $B = (\sigma_{\rm B}/\pi)T_{\rm g}^4$, c is the speed of light, u is the specific energy of the gas and G is the gravitational constant.

The values of properties such as density at the position of each particle are found by interpolating values from neighbouring particles combined with a weighting, or kernel, function. A quantity known as the smoothing length, h, determines which particles contribute to the evaluation of the function at a given point. The spatial resolution depends upon the number of SPH particles in a given region, and hence the density. The smoothing length should then change with the density to ensure that a similar number of neighbour-

ing particles contribute to calculations in all regions. Since the density also depends upon the smoothing length the two equations must be solved iteratively, as follows.

The density at a point or particle, a, is calculated through summation of the masses of neighbouring particles, b, weighted with the kernel function, W:

$$\rho(\mathbf{r}_a) = \sum_b m_b W(\mathbf{r}_a - \mathbf{r}_b, h_a), \tag{2.6}$$

where $\mathbf{r}_a - \mathbf{r}_b$ is the separation between particles a and b. The smoothing length of particle a is

$$h_a = \eta \left(\frac{m_a}{\rho_a} \right)^{\frac{1}{n}}. \tag{2.7}$$

Here η is a dimensionless, constant scaling parameter and n is the number of dimensions. For our three–dimensional calculations $\eta = 1.2$ and $n = 3$.

Early SPH codes used a Gaussian kernel, however this has the disadvantage that all particles contribute to the values at every point, even if with a very small weighting. Spline functions are normally used since these can be chosen to have a value of zero beyond a particular radius and have continuous first and second derivatives as required. The kernel function employed is the cubic spline, or M4 kernel, (Price 2012):

$$W(r,h) = \frac{1}{\pi h^3} \begin{cases} 1 - \frac{3}{2}q^2 + \frac{3}{4}q^3, & 0 \leq q < 1; \\ \frac{1}{4}(2-q)^3, & 1 \leq q < 2; \\ 0. & q \geq 2; \end{cases} \tag{2.8}$$

for $q = |\mathbf{r}_a - \mathbf{r}_b|/h$.

In order to simulate shocks, artificial viscosity, Π_{ab}, is required to ensure that the bulk motion is converted to thermal energy after gas passes though a shock front and is given by Equation 2.9:

$$\Pi_{ab} = \begin{cases} \frac{-\alpha \bar{c}_{ab} \mu_{ab} + \beta \mu_{ab}^2}{\bar{\rho}_{ab}} & \mathbf{v}_{ab} \cdot \mathbf{r}_{ab} < 0; \\ 0 & \mathbf{v}_{ab} \cdot \mathbf{r}_{ab} > 0; \end{cases} \quad \text{where } \mu_{ab} = \frac{h \mathbf{v}_{ab} \cdot \mathbf{r}_{ab}}{\mathbf{r}_{ab}^2 + \eta^2}. \tag{2.9}$$

The artificial viscosity is controlled via two parameters, α and β, and the parameter η^2

is selected to prevent singularities while being small enough to stop the viscous term in high density regions being smoothed too much (Monaghan 1992). For the cloud collapse simulations we use the variable artificial viscosity of Morris and Monaghan (1997) where α_v ranges from 0.1 and 1.0 and $\beta_v = 2\alpha_v$. $\overline{c}_{ab}$ is the average sound speed at a and b and $\overline{\rho}_{ab}$ is the average of the two densities.

The hydrodynamical equations are written using derivatives of the kernel, ∇W (Monaghan 1992; Price 2012). For example, the momentum equation for particle a (c.f. Equation 2.2) with constant smoothing length (ignoring gravity and radiation pressure) is written as

$$\frac{d\mathbf{v}_a}{dt} = -\sum_b m_b \left(\frac{p_b}{\rho_b^2} + \frac{p_a}{\rho_a^2} + \Pi_{ab} \right) \nabla_a W_{ab}, \tag{2.10}$$

where p is the pressure, determined from the equation of state which is described later.

The equations are integrated for each particle via a second order Runge–Kutta-Fehlberg integrator (Fehlberg 1969) and the particles are moved accordingly. Individual timesteps are used and are calculated for each particle for each step (Bate et al. 1995). The timestep depends upon the sound speed (and hence the density and coordinates), viscosity and force terms (Monaghan 1992). Alternatively, the timestep can be set via a tolerance on the change in the particle's velocity, acceleration, internal energy and smoothing length if this timestep is smaller than the former.

Two different models for radiation hydrodynamics are used in this thesis. First in 2.2.3 we outline the flux–limited diffusion method which is incorporated into SPHNG as described in Whitehouse et al. (2005) and Whitehouse and Bate (2006) and in 2.2.4, the inclusion of various physical processes of the interstellar medium as presented in Bate and Keto (2015).

2.2.2 Magnetohydrodynamics

Ideal MHD is incorporated into SPHNG using the formalism of Price and Monaghan (2005). Magnetism is modelled by evolving the induction equation

$$\frac{D}{Dt}\left(\frac{\mathbf{B}}{\rho}\right) = \left(\frac{\mathbf{B}}{\rho} \cdot \nabla\right) \mathbf{v}, \tag{2.11}$$

where B is the magnetic field, and adding the corresponding magnetic terms to Equation 2.2:

$$\frac{Dv}{Dt} = \frac{1}{\rho}\nabla\left(P + \frac{1}{2}\frac{B^2}{\mu_0} - \frac{\mathbf{BB}}{\mu_0}\right) - \nabla\phi + \frac{\kappa\mathbf{F}}{c}. \tag{2.12}$$

Divergence cleaning is implemented to ensure $\nabla \cdot \mathbf{B} = 0$ (Tricco and Price 2012) and the artificial resistivity of Tricco and Price (2013) is used.

2.2.3 Radiation hydrodynamics: Flux limited diffusion

The transfer of energy by radiation is included in the hydrodynamical model by evolving the radiation energy density (Equation 2.3) and including terms for radiative feedback to the momentum and energy equations (Equations 2.2 and 2.4). The flux–limited diffusion (FLD) approximation allows radiative transfer to be calculated efficiently at the same time as the hydrodynamics. FLD assumes that the radiation field is isotropic and that the flux is proportional to the gradient of the radiation energy. A "flux–limiter" is implemented to avoid the problem of the flux tending to infinity in optically thin regions (e.g. Whitehouse et al. 2005).

In the FLD approximation, the Planck function is integrated over all frequencies so the flux is written as

$$\mathbf{F} = -\frac{c}{3\kappa_{\mathrm{R}}\rho}\nabla E, \tag{2.13}$$

with a frequency–independent grey opacity, κ_{R} the Rosseland mean opacity and $E = aT_r^4$. Here, c is light speed, $a = 4\sigma_{\mathrm{B}}/c$, σ_{B} is the Stefan–Boltzmann constant and T_r is the radiation temperature. This gives the correct flux in regions that are highly optically thick but in optically thin regions $\kappa_{\mathrm{R}}\rho \to 0$ and the flux becomes unphysically large. Equation 2.13 can be written in the form of a diffusion equation (Levermore and Pomraning 1981) with a dimensionless function known as the flux limiter which is adjusted to prevent the flux becoming infinite. The flux becomes

$$\mathbf{F} = -D\nabla E, \tag{2.14}$$

where the diffusion constant is

$$D = \frac{c\lambda}{\kappa_{\mathrm{R}}\rho}. \tag{2.15}$$

The flux limiter of Levermore and Pomraning (1981) is used and is given by

$$\lambda(R) = \frac{2+R}{6+3R+R^2}, \tag{2.16}$$

where $R = |\nabla E|/(\kappa_{\rm R}\rho E)$.

2.2.4 Radiation hydrodynamics: ISM heating and cooling processes

Dust and gas temperatures are only well coupled at higher densities ($> 10^5$ cm^{-3}) (Burke and Hollenbach 1983; Goldsmith 2001; Glover and Clark 2012b). The FLD method outlined in 2.2.3 works well for the high density ISM where the dominant cooling mechanism is dust emission and the dust and gas temperatures are well–coupled by collisions. In the diffuse ISM, however, gas and dust temperatures may differ and other heating and cooling mechanisms become important.

The second method of radiation hydrodynamics employed here is that of Bate and Keto (2015), which was specifically designed for modelling the radiation hydrodynamics of the low density ISM. Extra terms are added to the thermal energy and radiation energy equations for cosmic ray heating, heating due to the photoelectric effect, dust grain heating, the thermal interaction of gas and dust via collisions, cooling due to atomic and molecular line emission and electron recombination emission. Gas, dust and radiation temperatures are evolved separately and separate dust and gas mean opacities are used. Dust grains cool more effectively than gas but are also subject to heating by the interstellar radiation field (ISRF).

In the cold neutral medium, atomic fine structure emission from oxygen and carbon are the major coolants. At higher densities ($n_{\rm H} \gtrsim 10^3$ cm^{-3}) cooling by CO emission becomes more important than by C^+. A simple chemical model is used to calculate abundances of C^+, C and CO so that fine structure cooling of C^+ and CO line cooling can be calculated. The chemical model requires the calculation of the visual extinction of the ISRF which is found from the column density, as follows. The mean visual extinction is

$$\langle \exp(-A_v) \rangle = \frac{1}{4\pi} \int \exp(-A_v) d\Omega, \tag{2.17}$$

where $A_v = \Sigma Q_v(V)$. Σ is the column density in $\mathrm{g\,cm^{-2}}$ and $Q_v(V)$ is the absorption efficiency, calculated for light with a wavelength of $550\,\mathrm{nm}$. We make use of the calculated mean visual extinction later in the chemical calculations as well.

The electron abundance is estimated through a simple parameterization for the calculation of electron recombination cooling.

2.2.5 Equation of State

The pressure is determined through the ideal gas equation of state:

$$p = \frac{T_g \mathcal{R} \rho}{\mu_g}. \tag{2.18}$$

T_g is the gas temperature, $\mathcal{R}$ is the gas constant and the mean molecular mass of the gas $\mu_g = 2.38$ for the molecular gas. The gas temperature is related to the specific internal energy, u, and the specific heat capacity, c_v, via $T_g = u/c_v$. The heat capacity of Black and Bodenheimer (1975) includes the dissociation of molecular hydrogen, the ionisation of hydrogen and helium and the variation in the mean molecular mass with temperature. The ionisation fractions of hydrogen and helium are calculated using the Saha equation.

2.3 Frequency–dependent radiative transfer modelling

The emission and transport of radiation must also be modelled in order to investigate observational properties of objects generated in the hydrodynamical simulations. Firstly, thermal emission can be simulated to calculate the luminosity and to generate continuum images and spectral energy distributions (SEDs). Secondly, spectral line emission from various molecular species can be modelled, taking into account the motion of the emitting gas and the opacity of the surrounding material at those particular wavelengths. These calculations are not performed in the SPH code because the radiative transfer method used there is frequency–independent. Instead we use TORUS , a grid–based radiative transfer code which uses a Monte Carlo method to generate photons in a simulated astrophysical object and model their transport to an "observer" (Harries 2000).

2.3.1 Monte Carlo radiative transfer

The transport of radiation is described by the following equations, which must be integrated to the edge of the grid to determine the radiation reaching an observer:

$$\frac{dI_\nu}{d\tau_\nu} = -I_\nu + S_\nu, \tag{2.19}$$

$$d\tau_\nu = \kappa_\nu ds. \tag{2.20}$$

I_ν is the specific intensity, τ_ν is the optical depth for a specific frequency ν, κ_ν is the absorption coefficient, ds is the path length element and the source function,

$$S_\nu = j_\nu/\kappa_\nu, \tag{2.21}$$

is the ratio of the emission coefficient to the absorption coefficient. The Monte Carlo method involves calculating the probabilities of photon absorption, emission and scattering events and sampling the radiation with a large number of photon packets and following their random walks through the grid. TORUS can calculate temperatures via a radiative equilibrium calculation but this is not necessary here because the gas and dust temperatures are obtained from the SPH models and there are no point sources of radiation (i.e. stars). A detailed description of the features and operation of TORUS is given in Harries et al. (2019).

The Monte Carlo approach employed by TORUS to calculate the transfer of radiation has the following steps for each photon packet:

1. The grid cell locations for a photon packet of dust continuum emission are found by sampling the probability density function of dust emissivities and then a random direction is assigned to the photon packet.

2. The frequency of the photon packet is determined by sampling randomly from the emission spectrum. For dust continuum emisson, this is the Planck function for the temperature of the grid cell.

3. The photon packet is propagated for a random optical depth. The distance travelled

therefore depends on the opacity.

4. A random number is compared with the albedo to determine whether the photon packet is absorbed or scattered after this distance.

5. If the photon is absorbed, another photon is emitted at that same location with a new random direction and a frequency obtained from sampling the emissivity at that location. If the photon is scattered, the frequency remains unchanged and the new direction is found from a Mie scattering phase matrix.

6. The photon packet is propagated for another random optical depth and so on, until it leaves the grid.

The observer is placed at some distance outside of the grid. Photon packets arriving at this observer from a predefined direction are collected to construct an image or other observation.

2.3.2 SPH particle mapping and the grid

An adaptive mesh refinement (AMR) method is used in TORUS so that regions with densities spanning several orders of magnitude can all be adequately modelled. The AMR grid is created starting with a parent cell. If the mass contained within the cell, range of densities or range of velocities exceeds some predefined criteria the cell is divided. Each cell is divided recursively until the criteria are met. Here, SPH simulations are used so it is necessary to map the quantities stored as SPH particles onto the grid. The method for this is described in Rundle et al. (2010) and Harries et al. (2019), and tests of the accuracy of the method were presented in Acreman et al. (2010b) and Acreman et al. (2010a). As discussed in Section 2.2, SPH particles are assigned a smoothing length, h, which is used to determine the distance over which the particles contributes to calculations of, for example, density and acceleration. When the particles are translated onto a grid, this means that particles outside a grid cell may contribute to the value of a quantity within it so it becomes necessary to use a smoothing kernel function to calculate the contribution of each particle to a point in a grid cell. The smoothing length of this function must be chosen to include particles within a sufficiently large region while retaining computational effi-

ciency. This is achieved by searching first of all within a defined maximum h then only searching for more distant particles when no particles are found within the region defined by the first value of h.

2.3.3 Dust continuum and SEDs

To calculate dust opacities we need to specify the dust grain properties. The distribution of grain sizes is set via the ISM power law size distribution function (Mathis et al. 1977)

$$n(a) \propto a^{-q}, \tag{2.22}$$

with $n(a)$ the number of particles of size a. Mathis et al. (1977) find q to be in the range $3.3 < q < 3.6$ for various substances including graphite and silicates and so we take the accepted ISM value of $q = 3.5$. The range of dust grain sizes for the distribution was $a_{\rm min} = 0.001\,\mu{\rm m}$ to $a_{\rm max} = 1.0\,\mu{\rm m}$, unless otherwise stated. The albedo and scattering properties are also determined by the grain type, for which we use the silicate grain type of Draine and Lee (1984).

SEDs are calculated following the method outlined in Section 2.3.1 except that each time a photon packet is absorbed or scattered the probability of its reaching the observer is calculated. The flux, weighted by this probability, is added to the observed SED. This approach is far more efficient than recording only photon packets that are scattered or emitted in the direction of the observer.

2.3.4 Molecular spectra

For calculating molecular line spectra the molecular abundances must first be known. There are three ways to set the abundance in TORUS. Firstly, the abundance relative to H_2 can be set to a uniform value across the whole grid. Secondly, a "drop model" can be used to set normal and depleted abundance values which are selected for each grid cell depending on its temperature and density. This is a simple way to approximate the effect of freeze–out of species such as CO. Thirdly, chemical abundances can be read in from the SPH particles if the hydrodynamical model has been post–processed with a chemistry model as described later in Section 2.5.

The relative fractional level populations of the species are calculated via a statistical equilibrium calculation, using the rate coefficients of collision and Einstein coefficients taken from the LAMDA database of Schöier et al. (2005). We assume LTE because the density in the simulated collapsing cloud is higher than the critical density for the species and transitions considered. Next, the line emissivities and opacities can be found, which enables TORUS to calculate the optical depths through the object for that particular transition.

The synthetic molecular line observations are produced by ray tracing rather than the Monte Carlo method used for SEDs and continuum images. The ray trace begins at the location of the observer and progresses through the grid until the far side is reached. At each point the intensity I_ν is updated (Harries et al. 2019):

$$I_\nu^{\rm new} = I_\nu^{\rm old} + S_\nu \left(1 - e^{-d\tau_\nu}\right) e^{-d\tau_{\rm total}}, \tag{2.23}$$

where $d\tau_\nu$ is given by Equation 2.20. The source function is calculated from Equation 2.21 but the emission and absorption coefficients are multiplied by a line profile function ϕ_ν centred on the rest frequency, ν_0. The line profile is given by

$$\phi_\nu = \frac{c}{v_{\rm turb}\nu_0\sqrt{\pi}} \exp\left(-\frac{\Delta v^2}{v_{\rm turb}^2}\right), \tag{2.24}$$

where $v_{\rm turb}^2$ is found calculated from the thermal and non–thermal turbulent components of the gas velocity and Δv is the equivalent velocity needed to Doppler shift ν_0 to ν (Rundle et al. 2010). The final intensity values in each direction are assembled for each frequency bin to create a data cube.

2.4 SED photometry and fitting

After producing synthetic SEDs with TORUS as outlined above, we need to compare the model SEDs quantitatively with those of observed FHSC candidates. It is necessary to simulate photometry from the model SEDs in order to properly compare them with observations, which record the flux received in a particular bandpass of finite width. The sensitivity of the instrument is not constant over the frequency range of the bandpass and

this must also be accounted for. The method for performing the synthetic photometry will first be described, followed by the fitting method.

2.4.1 Simulated Photometry

We calculated the monochromatic fluxes for each instrument by folding the model SEDs with the instrument response functions[1] and redistributing the flux over the assumed SED shape following the method of Robitaille et al. (2007) which we now describe. Information on the assumed SED for each instrument were taken from Mayne et al. (2012) and the Spanish Virtual Observatory (2019).

For an instrument such as *Spitzer* IRAC which assumes a flat SED ($\nu F_\nu \propto \mathrm{constant}$) and measures the electron "count" in photon units ($e^-\mathrm{photon}^{-1}$):

$$F_{\nu_0}[\mathrm{quoted}] = \frac{\int F_\nu[\mathrm{model}](\nu_0/\nu)R(\nu)d\nu}{\int(\nu_0/\nu)^2 R(\nu)d\nu}. \tag{2.25}$$

Here $F_\nu[\mathrm{model}]$ refers to the raw model flux, $R(\nu)$ is the spectral response function of the instrument and ν_0 is calculated from the central wavelength of the filter ($\nu_0 = c/\lambda_0$). For other instruments such as *Spitzer* MIPS which measure the electron "count" in units of energy ($e^-/\mathrm{unit\ energy}$) and assume a $10\,000\,\mathrm{K}$ blackbody spectrum:

$$F_{\nu_0}[\mathrm{quoted}] = \frac{\int F_\nu[\mathrm{model}]R(\nu)d\nu}{\int(\nu/\nu_0)^2 R(\nu)d\nu}. \tag{2.26}$$

To implement Equations 2.25 and 2.26 we first need to extract the model values within the instrument bandpass. Sometimes the nearest model point to the edge of the band, as defined by the shortest or longest wavelength given in the spectral response function, is just outside of the band. If only model values within the band were used, we would not be integrating over the whole band and this leads to differences of ~ 1 per cent in the quoted flux. To resolve this, we interpolate the model flux values at the edges of the band to ensure the flux is integrated over the full width of the band. This is achieved by lin-

1. Response functions were taken from the Spanish Virtual Observatory's Filter Profile Service `http://svo2.cab.inta-csic.es/theory/fps3/`(2012; 2013), `http://www.adamgginsburg.com/filters/bolocam_passband.txt`, `http://www.eaobservatory.org/jcmt/instrumentation/continuum/scuba-2/filters/` and `https://astro.uni-bonn.de/~bertoldi/projects/mambo/manuals.html`.

ear interpolation of the model values either side of these wavelengths. The value of the response function at each of the model wavelengths is found by linear interpolation and the integration is then performed using the trapezoidal rule. The trapezoidal rule is still valid when used with the unequally spaced wavelength points in the model SEDs, unlike alternative methods such as Simpson's Rule. This integration was tested with half the total number of model points and the difference in the calculated flux was found to be < 1 per cent for $\lambda \geq 70\,\mu\mathrm{m}$ and < 5 per cent for $\lambda = 24\,\mu\mathrm{m}$. The similarity shows that the trapezoidal rule is sufficiently accurate for this integration. There is a larger difference at $24\,\mu\mathrm{m}$ because there are fewer data points within the filter bandpass and the model SEDs are affected by Monte Carlo noise at these shorter wavelengths (because there are fewer shorter wavelength photon packets). An additional advantage of integrating the flux over a bandpass is that the Monte Carlo noise that is present at the shorter wavelengths is averaged out.

This method is used for each model SED, however not all model SEDs have values for $\lambda < 20\,\mu\mathrm{m}$ because the fluxes become very small ($\lesssim 1 \times 10^{-6}\,\mathrm{Jy}$) at short wavelengths for some models. For instrument bandpasses for which there is no data in the model SED, a value of zero is set for the flux. This is only the case for observations at $\lambda < 20\,\mu\mathrm{m}$. In cases where the model only covers part of an instrument bandpass we perform the integration over the range of wavelengths available. The missing fluxes are mostly orders of magnitude smaller and would therefore make only a negligible contribution to the total flux. Nevertheless, we note which photometry values have been calculated from an incomplete set of wavelengths.

Results from this photometry procedure were compared with those obtained from the photometry routine of the SED fitting tool of Mayne et al. (2012). Photometry for nine instruments was performed for a model SED with both codes and the resulting fluxes differed by < 3.5 per cent. These percentage differences were all smaller than the typical observational uncertainties and so we consider this method of synthetic photometry to be reliable.

2.4.2 χ^2 fitting

Observed SEDs were compared to the complete set of model SEDs following a similar method to that of Robitaille et al. (2007). We selected the models with the smallest χ^2 - per-point for the observed SED, where

$$\chi^2 = \frac{1}{N}\sum_{i=1}^{N}\left(\frac{F_{\mathrm{obs,i}} - F_{\mathrm{mod,i}}}{\sigma_i}\right)^2. \tag{2.27}$$

$F_{\mathrm{obs,i}}$ and $F_{\mathrm{mod,i}}$ are the observed and model fluxes respectively for each wavelength, σ is the uncertainty in the observed flux and N is the number of observed wavelengths. Where possible, all observed SED points are included in the χ^2 calculation. In the cases where there is a detection at a shorter wavelength than available in a given model SED the model SED is discarded because the model flux would be many orders of magnitude lower than required to provide a good fit to the observation. This only affects observations at $\lambda < 24\,\mu\mathrm{m}$.

For observations where there are upper limits (U_{i}), models with $F_{\mathrm{mod,i}} < U_{\mathrm{i}}$ are assigned a χ^2 contribution of zero. For models with $F_{\mathrm{mod,i}} > U_{\mathrm{i}}$, the χ^2 contribution is

$$\chi^2 = -2\log\left(1 - \mathrm{confidence}\right), \tag{2.28}$$

where the confidence is found from the stated observational uncertainty (Robitaille et al. 2007). Where this is not reported we assume a 2σ upper limit and hence a confidence of 0.9545. This treatment of the upper limits is not strictly statistically accurate but a better method would require more complete data. Non–detections are reported in the literature as an upper limit with an uncertainty, whereas it would be more helpful in this case to use the actual measured flux and uncertainty, as argued by Mayne et al. (2012). Literature reports of upper limits provide no information on where the flux lies between zero and the detection limit so we cannot make any assumptions and must take the probability distribution of the "true" flux value to be constant below the quoted upper limit. The upper limit itself has an associated uncertainty, which means that there is a finite probability that the "true" flux value may lie above the quoted upper limit. A 5σ upper limit is a "harder" upper limit than a 2σ upper limit: the "true" flux is less likely to be greater than

the quoted upper limit. Equation 2.28 accounts for this by giving a higher χ^2 weighting to models exceeding the upper limit when the confidence in the upper limit is greater. However, this still does not distinguish between a model value which exceeds the upper limit only slightly and a value which is much greater than the upper limit.

The model SEDs must be scaled to allow for differences in the masses and distances of the sources and so each model SED is multiplied by constant values to minimise its χ^2. It is then these final χ^2 values that are compared to determine the best fitting models. The scaling is discussed in detail in Chapter 3.4.2. We do not consider reddening because this effect is negligible at the wavelengths of the cold dust emission of pre-stellar cores. It is also unnecessary to take into account background emission because this is effectively removed when the background subtraction is performed as part of the photometry procedure when processing the observations.

2.5 Chemical modelling

2.5.1 Overview

Chemical abundances were calculated by post–processing the hydrodynamical simulations. In the ISM and pre–stellar cores, the densities and temperatures are very low which means that reaction timescales are long and equilibrium chemistry is not applicable. Chemical equilibrium is reached when the Gibbs free energy is minimised and this requires that all forward and back reactions are able to occur, which is only possible when the temperature is high enough for activation barriers to be overcome (usually $T > 1000$ K, Hincelin et al. 2016). Modelling chemical reactions in this regime therefore requires a chemical kinetics approach.

The kinetics approach involves calculating the rates of all of the chemical reactions. These equations may be functions of temperature, visual extinction, or cosmic ray ionisation rate, depending on the type of reaction, and the details of how the rates are calculated can be found in Section 2.5.2. The reaction rates are multiplied by the abundances of the reactants to give the rate of change of the chemical abundances. For each chemical species, the rate of change of abundance is calculated by adding together the rates of production

and destruction of that species from every reaction in which it is involved. This gives a set of ordinary differential equations which must be solved for a prescribed timestep to calculate new abundances.

In this section, we describe the chemical solver used here (Section 2.5.3), the chemical network (Section 2.5.2) and the implementation of the chemistry from the SPH model.

2.5.2 Chemical network

Different types of chemical reactions become relevant in different environments. For example, in regions where there is a high UV flux, such as near a protostar, photodissociation reactions will be dominant. Therefore, an appropriate chemical network should be found for the conditions to be modelled.

In this work, the KIDA 2011 network of gas–phase and grain charge transfer reactions is used (Wakelam et al. 2012). This network is designed for calculating ISM chemistry and contains reactions for the temperature range 10 - 800 K, although it has only been tested up to $300\,\mathrm{K}$. The temperature in the hydrodynamical models only exceeds $300\,\mathrm{K}$ within the FHSC itself at $r \lesssim 3$ AU at the time of stellar core formation and only exceeds $800\,\mathrm{K}$ within 1 AU. These scales are unobservable due to the high densities (see Chapter 3) and so this network is appropriate to use here.

We combine the gas–phase KIDA 2011 network (Wakelam et al. 2012), including grain charge transfer reactions, with gas–grain reactions from the network of Reboussin et al. (2014) which was based on that of Garrod et al. (2007). This includes adsorption reactions and both thermal desorption reactions and desorption induced by cosmic rays. The KIDA 2011 network was chosen over the 2014 network because it better matches the observed abundances of a greater number of species that we wished to model (with the exception of SO) (Wakelam et al. 2015). This gives a gas–grain network of 7009 reactions and 651 chemical species, where species frozen out onto the grain surface are counted separately. We neglect grain surface reactions, and therefore also desorption via exothermic surface reactions, to simplify the calculations and because they are much less significant for the simpler molecules considered here. The exception is the formation of H_2, for which

Table 2.1: Formulae for calcualting gas–phase reaction rate coefficients. α, β and γ are coefficients taken from a chemical network. ζ is the cosmic ray ionisation rate (unit s^{-1}), A_v (in magnitudes) is the visual extinction and T (K) is the gas temperature.

Reaction Type	Formula	ID number in network
Cosmic ray ionisation	$k = \alpha\zeta$	1
Photodissociation	$k = \alpha e^{\gamma A_v}$	2
Modified Arrhenius	$k(T) = \alpha(T/300)^{\beta} e^{-\gamma/T}$	3
Ion polar 1	$k(T) = \alpha\beta(0.62 + 0.4767\gamma(300/T)^{0.5})$	4
Ion polar 2	$k(T) = \alpha\beta(1 + 0.0967\gamma(300/T)^{0.5} + \frac{\gamma^2}{10.526}\frac{300}{T})$	5

we use the parameterization of the KIDA 2011 network. In Appendix A we compare abundances calculated with the KIDA 2014 network and find no significant differences that would affect the modelling in this thesis.

2.5.2.1 Reaction equations

The formulae for calculating rates of the gas–phase reactions from the coefficients provided by the chemical network are summarised in Table 2.1. It is also possible to formulate gas–grain and grain surface reactions such that they can be implemented in a similar manner to the gas–phase reactions (Hasegawa et al. 1992). For this, the adsorbed species are treated as separate species with their own abundances and we detail the method for including gas–grain reactions in the following two sections.

Ionisation by cosmic rays and cosmic ray induced far ultra-violet (FUV) photons is calculated via Equation 1 in Table 2.1. This assumes a cosmic ray ionisation rate of $\zeta_{\rm CR} = 1.3 \times 10^{-17}\,{\rm s}^{-1}$.

Photodissociation reactions occur on the absorption of a photon. The rate is found using equation 2 in table 2.1. The coefficient α in the network used here is calculated for the Draine (1978) ISRF. The visual extinction takes into account the attenuation of the ISRF by dust continuum absorption and is obtained from the SPH output from calculating the column density to the edge of the cloud.

2.5.2.2 Adsorption onto grain surface

Adsorption reactions result in the "freeze-out" of species onto the surface of dust grains. The rate of adsorption of a species onto the grain surface is

$$k_{\rm ads}(i) = \sigma_{\rm d} \langle v(i) \rangle n_{\rm d}, \tag{2.29}$$

where $\sigma_{\rm d}$ is the cross–section of the dust grain and $n_{\rm d}$ is the dust grain number density (e.g. Hasegawa et al. 1992). We assume a grain radius of $a = 0.1\,\mu{\rm m}$ and a dust-to-gas mass ratio of 1:100. $\langle v(i) \rangle$ is the mean thermal velocity of the species:

$$\langle v(i) \rangle = \sqrt{\frac{8 k_{\rm B} T}{\pi \mu(i) m_{\rm p}}}, \tag{2.30}$$

where $k_{\rm B}$ is the Boltzmann constant, T is the gas temperature, $\mu(i)$ is the reduced mass of species i and $m_{\rm p}$ is the proton mass. Here we approximate $\mu(i) m_{\rm p}$ to the molecular mass. We implement the rate equation with KROME using the formalism of Hasegawa et al. (1992), multiplying by the species number density at runtime.

2.5.2.3 Thermal desorption

Ices are deposited on the surface of dust grains with a layered onion–like structure. Thermal desorption does not therefore occur at a single temperature because, in addition to the simple solid phase, molecules such as CO may be adsorbed onto the H_2O ice surface, trapped in pores in the H_2O ice or adsorbed onto other ices Collings et al. (2004) and Collings and McCoustra (2012). Some desorption may occur as molecular species with lower desorption temperatures are released into the gas phase (e.g. Muñoz Caro et al. 2010). "Volcano desorption" occurs as the crystal structure of H_2O ice changes and molecules trapped in pores in the ice are released (Smith et al. 1997). After the desorption temperature of the pure solid phase molecule has been reached, molecules may remain bound to H_2O ice and are released at a higher temperature when the H_2O ice sublimates (Collings and McCoustra 2012).

For this work, we do not treat grain surface structures or chemistry and so we assume that thermal desorption occurs at a single temperature. The rate of thermal desorp-

tion of a species (i) from the grain surface back to the gas–phase is given by

$$k_{\rm des}(i) = \nu_0(i) \exp\left(-\frac{E_{\rm D}(i)}{T_{\rm g}}\right), \tag{2.31}$$

where $E_{\rm D}(i)$ is the desorption energy of species i (in Kelvin[2]) and $T_{\rm g}$ is the temperature of the dust grain. The values of desorption energy for an H_2O ice grain surface were taken from the Kinetic Database for Astronomy (KIDA)[3] (Wakelam et al. 2012; Wakelam et al. 2015). The characteristic vibration frequency for the adsorbed species i is

$$\nu_0(i) = \sqrt{\frac{2 n_{\rm s} E_{\rm D}(i)}{\pi^2 m(i)}}, \tag{2.32}$$

where $n_{\rm s}$ is the surface density of binding sites (we use $1.5 \times 10^{15}\,{\rm cm}^{-2}$ following Reboussin et al. 2014) and $m(i)$ is the mass of species i in grams.

2.5.2.4 Cosmic ray desorption

The temperature of a dust grain is raised after it is hit by a cosmic ray and this can also lead to desorption of grain surface species. A cosmic ray is assumed to transfer 0.4 MeV to a dust grain, which heats the $0.1\ \mu{\rm m}$ grain to a peak temperature of 70 K (Leger et al. 1985). The rate of cosmic ray desorption is given by the desorption rate for a grain temperature of 70 K scaled by the fraction of time the grain spends at 70 K, $f(70\ {\rm K})$ (Hasegawa and Herbst 1993):

$$k_{\rm CR}(i) = f(70\ {\rm K}) k_{\rm des}(i, 70\ {\rm K}). \tag{2.33}$$

$f(70\ {\rm K})$ is found from the ratio of the timescale for the cooling by evaporation of volatiles to the time between cosmic ray hits causing the heating to 70 K. For a cosmic ray ionisation rate of $\zeta = 1.3 \times 10^{-17}\,{\rm s}^{-1}$, $f(70\ {\rm K}) \approx 10^{-5}\ {\rm s}/10^6\ {\rm yr} \approx 3.16 \times 10^{-19}$ (Reboussin et al. 2014).

2.5.2.5 H_2 formation

The formation of molecular hydrogen takes place on the surface of dust grains. The approximation of the KIDA 2011 network is used which considers H_2 formation to be a two–

2. Strictly speaking this value is $E_{\rm D}/k_{\rm B}$
3. `http://kida.obs.u-bordeaux1.fr/`

stage process. First, atomic hydrogen is adsorbed with the following rate:

$$k_{\rm H,acc} = \pi a^2 \sqrt{\frac{8 k_B T}{\pi m_{\rm H}}} n_d. \tag{2.34}$$

With the grain radius $a = 0.1$ μm, Equation 2.34 becomes

$$k_{\rm H,acc} = 7.92 \times 10^{-5} \sqrt{\frac{T_{\rm gas}}{300.0}} n_d. \tag{2.35}$$

The number density of dust grains, n_d, is set from the dust–to–gas ratio and the total gas density, which is provided in the call to KROME. This avoids any issues caused by the number density of dust grains in the calculation varying during the iteration.

The second step considers the reaction of hydrogen atoms on the dust grain to produce H_2. The molecular hydrogen is then assumed to be immediately released into the gas phase. The rate equation for this process is

$$k_{\rm H_2,form} = \frac{\nu_0 \exp\left(-E_b/k_B T\right)}{N_s n_d}, \tag{2.36}$$

where ν_0 is defined in Equation 2.32 with $E_D/k_B = 450$ K, E_b is the surface binding energy and N_s is the number of binding sites per grain. Taking $E_b/k_B = 225$ K and $N_s = 10^6$ Equation 2.36 becomes

$$k_{\rm H_2,form} = \frac{8.64 \times 10^6}{n_d} \exp\left(-225.0/T_{gas}\right). \tag{2.37}$$

2.5.3 The chemical solver and implementation from SPH models

The chemical calculations were performed using KROME (Grassi et al. 2014), which is a publicly available code for solving the kinetic equations of non–equilibrium gas–phase chemistry and is based on the DLSODES solver (Hindmarsh 1983). KROME uses a *Python* script to generate the *Fortran* routines for a given network file that contains the list of reactions and their rates or equations for calculating the rate. This script produces an equation for the rate of change of each chemical species using the reaction rate coefficients from the network and the number densities from the initial abundances or the previous iteration.

This provides the set of ordinary differential equations to be passed to the solver when KROME is run.

These rate equations for first–order reactions such as photo-dissociation for chemical species i take the form

$$R_i = k_i n_i, \tag{2.38}$$

and for second–order reactions the reaction rate R_{ij} is

$$R_{ij} = k_{ij} n_i n_j. \tag{2.39}$$

Here, k_i and k_{ij} are the rate coefficients, calculated according to the type of reaction as described in Section 2.5.2.1, and n_i and n_j are the number densities of species i and j respectively.

There are a number of types of reaction already provided with KROME but we input the equations in Section 2.5.2.1 separately as "user" equations to be certain that they are correct for the network. The KIDA network is formatted differently to that required by KROME. The main difference is that the KIDA network contains a set of coefficients for each reaction and a number specifying the formula that should be used for calculating the rate whereas the KROME network requires the rates, or the formulae for calculating them. Before running KROME to generate the *Fortran* subroutines we must first reformat the network and pre–calculate the rates as far as possible. KROME is compiled as a library so that the solver and other chemistry related functions can be easily be called from a simple 0-D code to evolve initial abundances or from a code handling SPH files.

Several quantities must be passed to KROME to evolve the chemical abundances. Firstly, the initial number density (or mass fraction) of each species. The gas density is also required if mass fractions are used. The gas temperature, visual extinction and cosmic ray ionisation rate must also be set when KROME is called. The UV flux is accounted for in the rate coefficients given by the chemical network as will be discussion in Section 2.5.2.

In the SPHNG output, each particle has a certain density, temperature and visual extinction among other values so it is straightforward to call KROME for each particle. The

visual extinction, A_v, and dust temperature, $T_{\rm dust}$, are set in KROME for each particle so that they are available for use in the rate equations. The loop over all particles for calling the chemical solver was parallelised using OPENMP and MPI, for which the particles were simply distributed over several compute nodes.

We calculate pseudo–time–dependent chemistry as a post–process by running KROME for all SPH particles in subsequent dump files and using the chemical abundances calculated for the previous dump as the initial abundances for the next. First initial abundances are assigned to every particle. These may be elemental abundances or pre–calculated abundances. Next, the new values of ρ, $T_{\rm gas}$, $T_{\rm dust}$ and A_v are obtained from the next timestep from the hydrodynamical model and the new chemical abundances are calculated for the time between current and previous timesteps.

It is not always necessary to calculate the chemical abundances for every hydrodynamical timestep when there are only small changes in temperature and density. For this reason, we can set a minimum chemistry timestep. For the cloud collapse models the minimum chemistry timestep is set relative to the local free–fall time

$$\delta t = \frac{1}{3} t_{\rm ff}, \tag{2.40}$$

where the free–fall time is defined as

$$t_{\rm ff} = \sqrt{\frac{3\pi}{32 G \rho}}. \tag{2.41}$$

The chemistry timesteps therefore become shorter as the maximum density increases.

The chemical model fails to converge where $\rho \gtrsim 10^{-10}\,{\rm g\,cm^{-3}}$. This value is exceeded midway through the FHSC phase only within 2-3 AU of the centre, or within 8 AU near midplane of the disc in the RHD model. To handle this, if the chemistry fails to converge for a particle, the chemistry timestep for that particle is halved. If the chemistry does converge with this smaller timestep KROME is called a second time for that particle with the same half–timestep such that the chemistry is evolved for the same net timestep. If the chemistry does not converge with the smaller timestep, the previous abundances

are retained and the number of times the particle has failed to converge is recorded. If a particle has failed to converge five times or if $\rho > 10^{-10}\ \mathrm{g\,cm^{-3}}$ the chemistry calculation is skipped and the current abundances are retained. All unconverged particles lie inside the FHSC and, for the RHD model, comprise only 1.7 per cent of the total mass during the FHSC stage and 2.8 per cent of the total mass after stellar core formation. These values are very similar for the MHD model. Since we are interested in modelling observational properties, the chemistry of the centre of the FHSC is inconsequential because the FHSC is extremely optically thick and submillimetre emission from this region would be reprocessed before reaching the observer.

Chapter 3

Modelling SEDs of candidate first hydrostatic cores

This chapter, except for Sections 3.4.5 and 3.4.6, form the basis of the paper 'What can the SEDs of first hydrostatic core candidates reveal about their nature?' (Young et al., 2018, MNRAS, 474, 800-823). The results described in Sections 3.4 and the related paragraphs of the Discussion (Section 3.5) differ slightly from the paper as we changed the criterion for selecting model SEDs.

3.1 Introduction

A commonly used method for classifying pre– and protostellar sources is to measure their SEDs and compare them to model SEDs generated from simple analytical models of the protostar, disc and envelope. Synthetic observations of the FHSC produced so far have not provided a clear picture of how to distinguish the FHSC from a starless core or a very young protostar using just its SED. SEDs can be produced from existing survey data therefore it would be useful to be able to use this to select targets for further observations.

In this chapter we explore the differences in the SED of FHSCs at various evolutionary stages and with different properties with the aim of determining whether the SED can shed light on the nature of FHSC candidates. As far as we are aware, there have been no

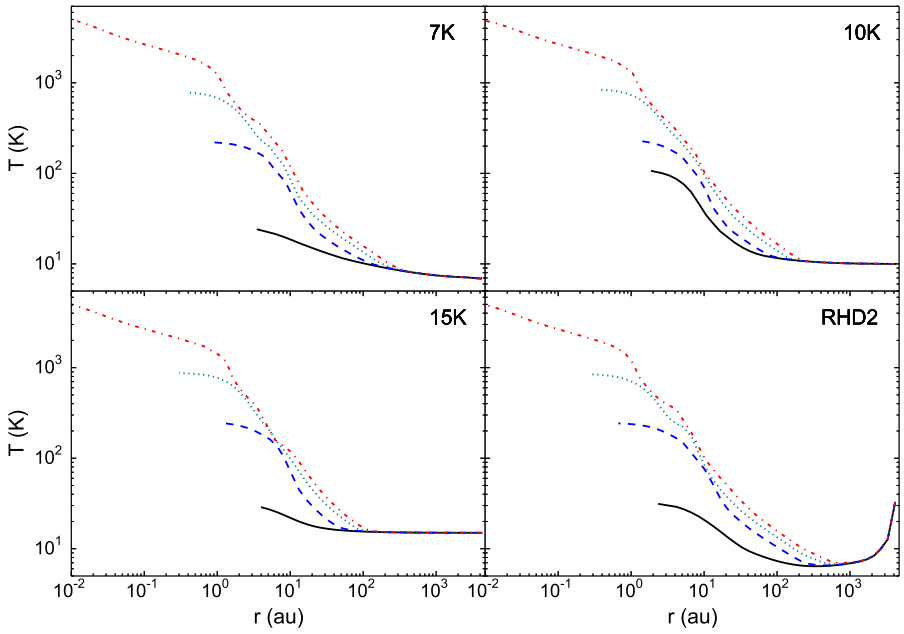

Figure 3.1: Temperature profiles during the collapse of initially static cores computed using the RHD1 model with initial temperatures 7 K, 10 K and 15 K, and for the RHD2 model. Snapshots are plotted when the central density is $1 \times 10^{-12}\,\mathrm{g\,cm^{-3}}$, $5 \times 10^{-11}\,\mathrm{g\,cm^{-3}}$, $1 \times 10^{-9}\,\mathrm{g\,cm^{-3}}$ and $1 \times 10^{-4}\,\mathrm{g\,cm^{-3}}$ in each panel. The temperature rises significantly only in the central $\sim 10\,\mathrm{AU}$ and at $r > 200\,\mathrm{AU}$ the temperature does not change significantly throughout the FHSC and the second collapse stages. For the RHD2 model, note the increase in temperature at radii $> 800\,\mathrm{AU}$ where there is less extinction of the ISRF.

other attempts to fit synthetic SEDs to particular observations of candidate FHSCs. Robitaille et al. (2007) produced a large set of synthetic protostar SEDs to create a fitting tool based on a χ^2 fitting method that observers can use to help interpret their observed SEDs. Here we adopt a similar systematic method to fit the SEDs of five candidates reported in the literature, five newly identified FHSC candidates in Serpens South and five candidates recently identified in Orion with model SEDs to test whether the SED can place constraints on their properties therefore help to better target sources designated as FHSC candidates for further observation.

3.2 Method

We performed 3-D radiation hydrodynamical (RHD) simulations of the collapse of molecular cloud cores to stellar core formation. These simulations are similar to those of Bate (2011) and Bate et al. (2014) and were performed for cores of different initial masses, rotation rates and radii. A few calculations were performed with magnetic fields, modelled with ideal magnetohydrodynamics (MHD). We also investigated the effect of an al-

ternative method of radiative transfer within the RHD model and of varying the external radiation field. Snapshots from these models were used as input for frequency–dependent radiative transfer modelling to produce synthetic SEDs. In the radiative transfer code we varied the dust grain properties and the viewing inclination.

3.2.1 Hydrodynamical models

Throughout this paper, we refer to the RHD method developed by Whitehouse et al. (2005) and Whitehouse and Bate (2006) as RHD1 (see Section 2.2.3). This model treats matter and radiation temperatures separately and performs radiative transfer using the flux–limited diffusion approximation. In these simulations the initial temperature is uniform and the boundary temperature is set equal to the initial temperature. As the core collapses and evolves, the central regions heat faster than the outer regions giving rise to the evolution in temperature profile shown in Fig. 3.1 for a non-rotating case. The majority of the infalling envelope remains cold throughout the FHSC phase.

We repeated calculations with the RHD model developed by Bate and Keto (2015) (hereafter RHD2, see Section 2.2.4) to compare the resulting SEDs from this more physical model with the simpler RHD1 model. In the RHD2 model, the initial gas and dust temperatures are the equilibrium temperatures calculated from the ISM heating and cooling processes. Initially, the temperature is lowest at the centre of the core due to extinction of the ISRF. Fig. 3.1 (lower right) shows the temperature profiles during the subsequent evolution of the core. As core collapse progresses, the centre heats up and warms the inner regions but a cold region remains between the internally heated central region and the outer regions of the core at $r \gtrsim 800\,\mathrm{AU}$ which are heated by the ISRF.

3.2.1.1 Initial conditions

The simulations start with a Bonnor-Ebert sphere for which the critical ratio of central density to density at the outer boundary is 14.1:1. A Bonnor-Ebert sphere has a density profile calculated for a self–gravitating fluid sphere in hydrostatic equilibrium and at pressure equilibrium with the outer boundary, which in this case is the ISM. We use an unstable density ratio of 15.1. Unless otherwise stated, the initial mass was $1\ \mathrm{M}_\odot$ and the initial

Table 3.1: A summary of the radiation hydrodynamical models performed. The parameters used in the hydrodynamical simulations to investigate the effect of changing the initial temperature, incident ISRF, mass, initial rotation, initial radius and magnetic field strength on the SED are listed in the respective rows. (a) The incident ISRF is changed by adding an additional boundary of molecular gas, expressed in terms of the column density of molecular hydrogen. (b) The MHD models employ the radiative transfer treatment of RHD2.

Parameter	Values tested	Values of fixed parameters
Temperature	7 K 10 K 15 K	RHD1 $1\ \mathrm{M}_\odot$ 4700 AU $\beta = 0$
ISRF[a]	none $1 \times 10^{20}\ \mathrm{cm}^{-2}$ $2 \times 10^{20}\ \mathrm{cm}^{-2}$ $5 \times 10^{20}\ \mathrm{cm}^{-2}$ $1 \times 10^{21}\ \mathrm{cm}^{-2}$ $5 \times 10^{21}\ \mathrm{cm}^{-2}$	RHD2 $1\ \mathrm{M}_\odot$ 4700 AU $\beta = 0$
Mass	$0.5\ \mathrm{M}_\odot$ 3700 AU $1\ \mathrm{M}_\odot$ 4700 AU $2\ \mathrm{M}_\odot$ 5900 AU $5\ \mathrm{M}_\odot$ 8000 AU	RHD2 $\beta = 0$
Rotation	$\beta = 0$ $\beta = 0.01$ $\beta = 0.05$ $\beta = 0.09$	RHD1 (10 K) & RHD2 $1\ \mathrm{M}_\odot$ 4700 AU
Radius	2000 AU 6000 AU 10 000 AU 11 400 AU	RHD2 $1\ \mathrm{M}_\odot$ $\beta = 0$
Magnetic Field[b]	$\mu = 5$ $\mu = 20$	RHD2 $1\ \mathrm{M}_\odot$ 4700 AU $\beta = 0.005$

radius was $7.0 \times 10^{16}\,\mathrm{cm}$ ($0.023\,\mathrm{pc}$, 4680 AU). These calculations were performed with a resolution ranging from 2.6×10^5 to 5×10^5 SPH particles.

We modelled the collapse of a molecular cloud core under different initial conditions to investigate differences in the SEDs. To explore the effects of initial temperature, we used RHD1 with uniform initial temperatures of $7\,\mathrm{K}$, $10\,\mathrm{K}$ and $15\,\mathrm{K}$ and RHD2 for a non–rotating $1\ \mathrm{M}_\odot$ core. We also varied the column density at the boundary in RHD2 to alter the intensity of the ISRF.

To investigate the effects of mass we modelled the collapse of non-rotating cores of masses $0.5\ \mathrm{M}_\odot$, $1\ \mathrm{M}_\odot$, $2\ \mathrm{M}_\odot$ and $5\ \mathrm{M}_\odot$, and radii of $5.56 \times 10^{16}\,\mathrm{cm}$ (3700 AU), $7.0 \times 10^{16}\,\mathrm{cm}$ (4700 AU), $8.82 \times 10^{16}\,\mathrm{cm}$ (5900 AU) and $12.0 \times 10^{16}\,\mathrm{cm}$ (8000 AU) respectively. The radii were chosen to maintain a constant initial central density of $\rho_{\max} = 1.38 \times 10^{-18}\,\mathrm{g\,cm^{-3}}$. This better reflects conditions in the interstellar medium than keeping a constant radius, since more massive molecular cloud cores have larger radii (e.g. Larson 1981). RHD2 was used for these calculations.

To investigate the effects of rotation we modelled the collapse of $1\ \mathrm{M}_\odot$ cores with RHD2 for different initial rotation rates. The initial angular velocity is set through the ratio of rotational energy to gravitational potential energy $\beta = E_{\mathrm{rot}}/E_{\mathrm{grav}}$. Here we used the values $\beta = 0$, 0.01, 0.05 and 0.09. These simulations were also repeated with RHD1 with a uniform initial temperature of $10\,\mathrm{K}$ for the comparison with observations and this is described in greater detail in Section 3.4.1.

We also performed collapse simulations of non-rotating $1\ \mathrm{M}_\odot$ cores with different initial radii, but with the same ratio of central density to density at the outer boundary of 15.1:1, as for the other simulations. Thus, these cores have different mean densities. The additional initial radii chosen were $3.0 \times 10^{16}\,\mathrm{cm}$ (2000 AU), $9.0 \times 10^{16}\,\mathrm{cm}$ (6000 AU), $11.0 \times 10^{16}\,\mathrm{cm}$ (7400 AU), $15.0 \times 10^{16}\,\mathrm{cm}$ (10 000 AU) and $17.0 \times 10^{16}\,\mathrm{cm}$ (11 400 AU). The central density of the cores then ranged from $1.1 \times 10^{-16}\,\mathrm{g\,cm^{-3}}$ for the smallest core to $5.9 \times 10^{-19}\,\mathrm{g\,cm^{-3}}$ for the $17.0 \times 10^{16}\,\mathrm{cm}$ core. RHD2 was used for these calculations.

Lastly, we performed radiation magnetohydrodynamical (RMHD) simulations. The simulations use a similar method to those of Bate et al. (2014), but here we use the radiative

transfer and ISRF treatment of Bate and Keto (2015). The RMHD simulations had an initial rotation corresponding to $\beta = 0.005$ because rotation is necessary for the formation of an outflow. The initial mass-to-flux ratios used were $\mu = 5$ and $\mu = 20$, with a total core mass of $1\ \mathrm{M}_{\odot}$ and initial radius of $7.0 \times 10^{16}\,\mathrm{cm}$. These simulations used a resolution of 10^6 SPH particles.

A summary of the hydrodynamical models is shown in Table 3.1.

3.2.1.2 Core collapse and FHSC evolution

The evolution of the collapsing core occurs in four stages: first collapse, FHSC phase, second collapse and stellar core formation. The evolution of the maximum density and temperature for cases computed using both RHD1 and RHD2 are shown in Fig.

At $\sim$2000 K (central density of $\sim 10^{-7}\,\mathrm{g\,cm^{-3}}$), molecular hydrogen begins to dissociate and the second collapse begins. The stellar core is formed after second collapse at a central density of $\sim 10^{-3}\,\mathrm{g\,cm^{-3}}$ but its temperature and density continue to rise rapidly.

We selected snapshots representing the major phases in FHSC formation and evolution from the RHD simulations for SED modelling. These are defined by the maximum density, as shown in Fig. 3.3, and give six snapshots (a to f): before FHSC formation; early-, mid- and late-FHSC phase; and two during second collapse. For some figures, we also show the snapshot just after the formation of the second (stellar) core at $\rho_{\mathrm{max}} = 10^{-2}\,\mathrm{g\,cm^{-3}}$ (snapshot g).

3.2.2 Modelling SEDs

Synthetic SEDs were created from the RHD models using TORUS for snapshots of the entire molecular core, including the FHSC and infalling envelope. We altered the dust grain size, dust grain type and inclination of the core relative to the observer to investigate the effects on the SEDs. The range of dust grain sizes used for calculating the grain size distribution with Equation 2.22 was $a_{\mathrm{min}} = 0.001\,\mu\mathrm{m}$ to $a_{\mathrm{max}} = 1.0\,\mu\mathrm{m}$. We then altered the maximum (a_{max}) in the range $0.5\,\mu\mathrm{m}$ to $1000\,\mu\mathrm{m}$ in separate simulations. SEDs were simulated for two different grain types: the silicate grain of Draine and Lee (1984) and the amorphous

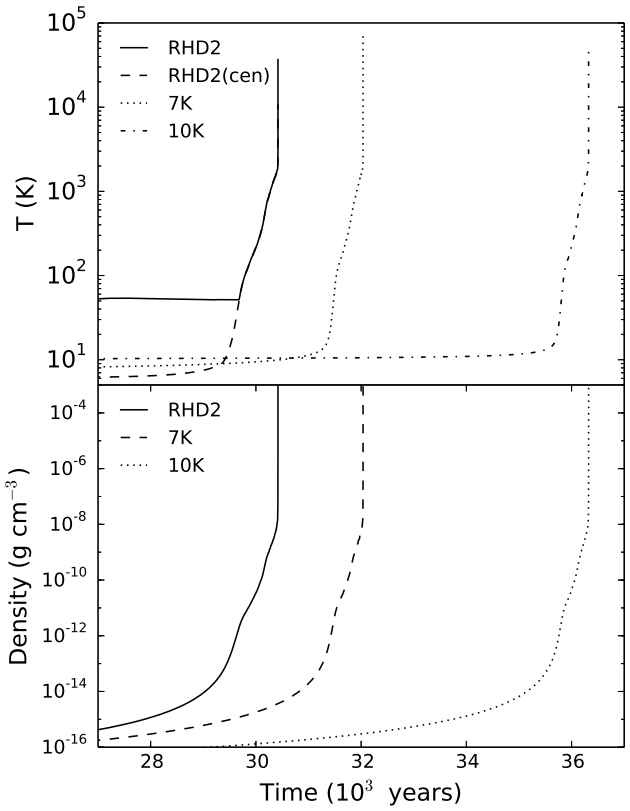

Figure 3.2: Evolution of the maximum temperature and density of the core for RHD1 models with uniform initial temperatures of 7 K and 10 K, and for the RHD2 model. For the RHD2 models, prior to the formation of the first core, the gas temperature is highest in the outer regions due to heating from the ISRF so we plot both the evolution of the maximum temperature, RHD2, and the temperature at the centre of the core, RHD2(cen). The core collapse proceeds fastest under the RHD2 model and an increase in initial temperature slows the collapse due to the additional thermal pressure. In each case, the FHSC forms and collapses at similar values of maximum density.

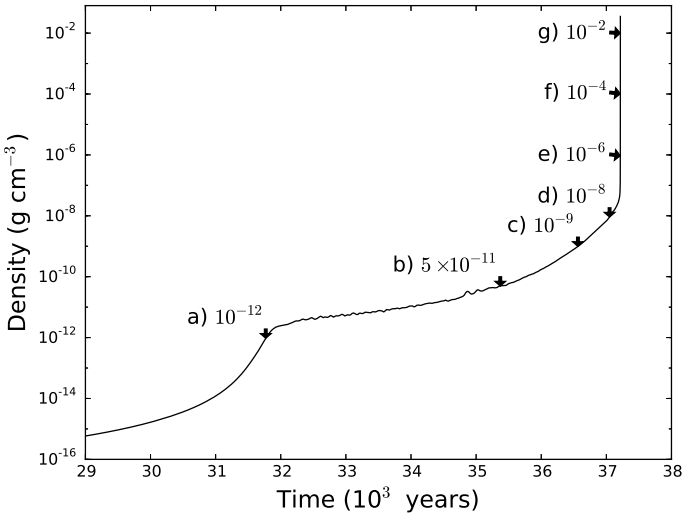

Figure 3.3: Evolution of the maximum density of a collapsing $1\ \mathrm{M}_\odot$ core with initial rotation $\beta = 0.09$ from the RHD2 model. The values of the maximum density used to select each snapshot for simulating SEDs are indicated in $\mathrm{g\,cm^{-3}}$. Snapshot (a) occurs just before FHSC formation and snapshot (d) is taken just before the onset of second collapse.

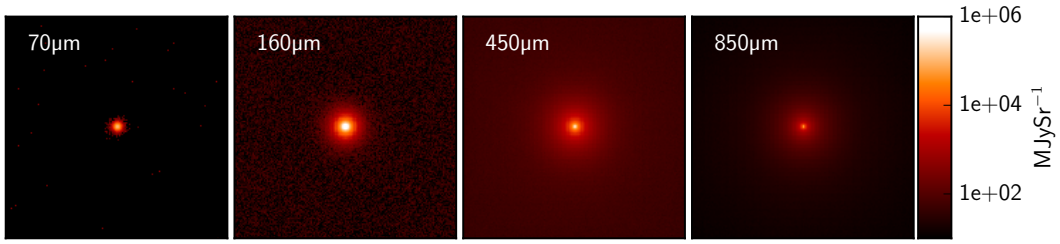

Figure 3.4: Synthetic images of the non-rotating FHSC from RHD2 at four commonly observed wavelengths. The images are each $1.1''$ across which corresponds to 286 AU at 260 pc. The $70\,\mu$m flux is emitted only in the warm central regions. The $450\,\mu$m and $850\,\mu$m images are dominated by emission from close to the FHSC, since the lower opacity allows radiation from deeper inside the core to escape, but there is also a significant contribution from emission from the cold envelope. The $70\,\mu$m and $160\,\mu$m images are affected by Monte Carlo noise because the emission from the envelope is very low.

carbon grain type of Zubko et al. (1996).

For all model SEDs, a distance of $260\,\mathrm{pc}$ was used because this was the best estimate of the distance to the Serpens South molecular cloud (Straizys et al. 2003), the region in which the new candidate FHSCs are located, at the time of simulating the SEDs. Rescaling for a different distance is straightforward and we exploit this when fitting to observations.

3.3 Results I: SED variation with core properties

In this section we describe the effects of various initial conditions and parameters on the evolution of the SED. These simulations were performed with no rotation, no magnetic field, a total core mass of $1\ \mathrm{M}_\odot$ and an initial radius of $7 \times 10^{16}\,\mathrm{cm}$ (4700 AU) using the RHD2 model unless otherwise stated. The SEDs were produced for a distance of $260\,\mathrm{pc}$ and an inclination of $0°$, with silicate type dust grains following the size distribution of $q = 3.5$ between $a_{\mathrm{min}} = 0.001\,\mu$m and $a_{\mathrm{max}} = 1.0\,\mu$m unless otherwise stated. SEDs are plotted with a flux scale cut off approximately an order of magnitude below the typical observational sensitivity of *Spitzer* at $24\,\mu$m.

3.3.1 Interpreting the SED

As is the case for many astrophysical objects, flux from a dense core is not emitted from a single "photosphere" at all wavelengths. It is useful to estimate where most of the flux at the observed wavelengths is emitted in order to understand the results in the following sections. The opacity depends upon the density and temperature of the dust, as well as

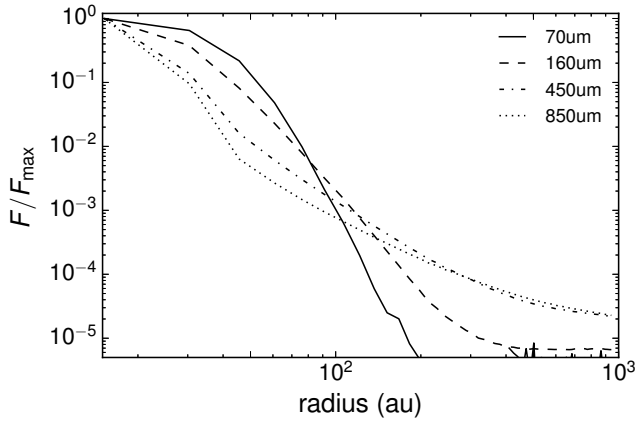

Figure 3.5: Radial average intensity profiles for the images of a non-rotating FHSC from RHD2 shown in Fig. 3.4 at four commonly observed wavelengths. The flux intensity profiles are normalised to the intensity in the centre of the FHSC image at each wavelength. The flux peaks more sharply at longer wavelengths because more of the observed flux was emitted from deeper within the core. There is also more emission from the cold envelope at the longer wavelengths.

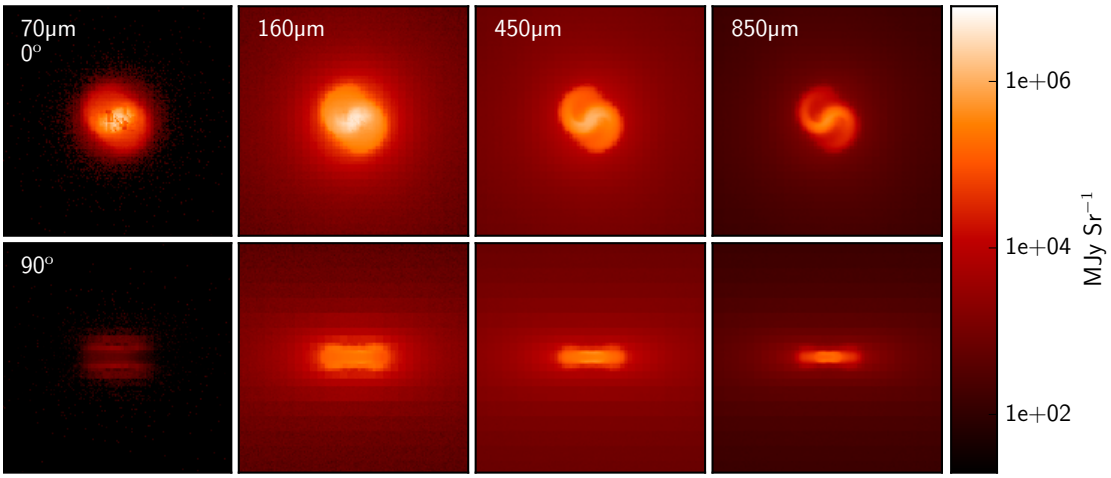

Figure 3.6: Synthetic images of the rotating FHSC from RHD1 with initial temperature of $10\,\mathrm{K}$ and initial rotation corresponding to $\beta = 0.05$ at four wavelengths with $i = 0°$ (face on) images above and $i = 90°$ images below. The images are each $1.1''$ across which corresponds to $286\,\mathrm{AU}$ at $260\,\mathrm{pc}$ and logarithmic scaling was used. Longer wavelengths allow us to see deeper into the core and distinguish smaller scale structures. At $i = 90°$ the observed $70\,\mu\mathrm{m}$ flux is emitted in the optically thin regions above and below the disc and the disc itself appears dark. The $70\,\mu\mathrm{m}$ and $160\,\mu\mathrm{m}$ images have a poorer resolution because most of the emission is coming from $> 20\,\mathrm{AU}$ from the centre where the AMR grid resolution is coarser.

the dust properties such as grain size and composition and the wavelength of the incident radiation. The density and temperature vary by several orders of magnitude and silicate dust grains sublimate at $\sim 1500\,\mathrm{K}$, causing the opacity to vary significantly as a function of radius and time.

The observed flux will be dominated by radiation from the smallest radii it can "escape" from, i.e. the photosphere. Masunaga et al. (1998) and Omukai (2007) discuss the locations of the photospheres in a pre-stellar core at different wavelengths in detail based on optical depth calculations. We produced synthetic images at the commonly observed wavelengths of $70\,\mu\mathrm{m}$, $160\,\mu\mathrm{m}$, $450\,\mu\mathrm{m}$ and $850\,\mu\mathrm{m}$ from a calculation of a non-rotating, and hence spherically-symmetric, early FHSC using RHD2. These objects are very faint at $24\,\mu\mathrm{m}$ so we did not produce images for that wavelength. The images shown in Fig. 3.4 show which structures are observed at each wavelength and, hence, which parts of the object contribute to the SED at each wavelength. We see in Figs. 3.4 and 3.5 that the $70\,\mu\mathrm{m}$ flux is emitted in the central regions of the core but the flux does not peak as sharply at the centre as for longer wavelengths. The opacity is higher at $70\,\mu\mathrm{m}$ and flux emitted from the very centre is obscured. Consequently, the FHSC is not directly visible at wavelengths shorter than $\sim 800\,\mu\mathrm{m}$ since it lies beneath the effective photospheres. The total flux at $850\,\mu\mathrm{m}$ is dominated by emission from the cold envelope but, since the opacity is low, the smaller structures in the warmer regions are distinguishable and the non-rotating source in Fig. 3.4 appears more compact. In reality, rotational structures are ubiquitous so we also present synthetic images of an FHSC from the model with initial rotation $\beta = 0.05$ using RHD1 and a uniform initial temperature of $10\,\mathrm{K}$ in Fig. 3.6. This calculation produces a rotationally unstable FHSC which goes bar-unstable and develops trailing spiral arms (c.f. Bate 1998). With rotation, the optical depth is reduced along the axial direction ($i = 0°$), which means that the observed flux is emitted from closer to the FHSC boundary than for the non-rotating core and we can see the central spiral morphology. At $i = 90°$ the hot central core is completely obscured at $70\,\mu\mathrm{m}$ and the observed flux at this wavelength is emitted in the lower density regions above and below the disc. At longer wavelengths the opacity decreases and a more compact structure is observed.

In summary, for all observed wavelengths the total flux is dominated by the regions

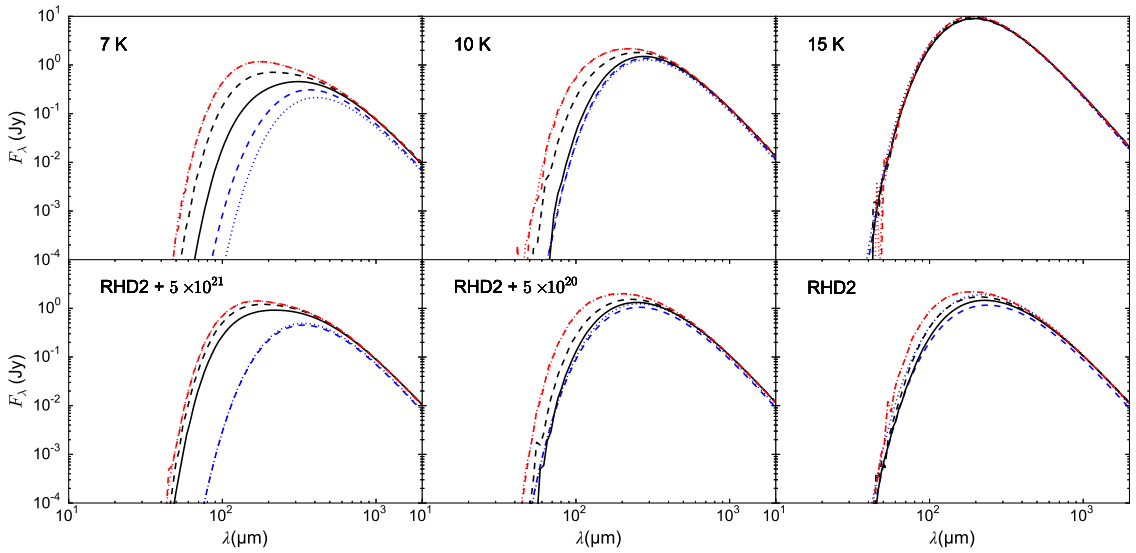

Figure 3.7: SED evolution for the collapse of cores of initial temperatures 7 K, 10 K and 15 K and for the RHD2 model (initial temperatures determined from exposure to the ISRF) with an additional boundary column density of $5 \times 10^{21}\,\mathrm{cm}^{-2}$, $5 \times 10^{20}\,\mathrm{cm}^{-2}$, and an unattenuated ISRF. SEDs are from snapshots where the central density is $1.4 \times 10^{-18}\,\mathrm{g\,cm}^{-3}$ (the initial conditions, blue dotted lines), $1 \times 10^{-12}\,\mathrm{g\,cm}^{-3}$ (blue dashed lines), $5 \times 10^{-11}\,\mathrm{g\,cm}^{-3}$ (solid black lines), $1 \times 10^{-9}\,\mathrm{g\,cm}^{-3}$ (dashed black lines), $1 \times 10^{-4}\,\mathrm{g\,cm}^{-3}$ (red dotted lines) and $1 \times 10^{-2}\,\mathrm{g\,cm}^{-3}$ (red dashed lines). The SEDs show less evolution for a warmer initial temperature because the initial SED is already brighter. Similarly, the RHD2 SEDs show less evolution with increased exposure to the ISRF.

surrounding the FHSC. It is therefore the temperature structure of this warm region outside the FHSC and the wider envelope that affects the shape of the SED which means that temperature differences within the FHSC are to a large extent irrelevant. This is what we consider in the following sections when comparing differences between SEDs of cores formed under different initial conditions.

3.3.2 Initial core temperature and external radiation

The temperature structure of the core changes as the object evolves and this directly affects the flux at each wavelength reaching an observer. We investigate the SED evolution first with cloud cores of uniform initial temperatures of 7 K, 10 K and 15 K using the RHD1 model and secondly, with a cloud core subjected to an interstellar radiation field (ISRF). We also compared the SED evolution of cores exposed to different ISRF intensities.

Fig. 3.7 shows the evolution of the SED as core collapse progresses from first collapse ($\rho_{\max} = 10^{-12}\,\mathrm{g\,cm}^{-3}$), through the FHSC stage, to second collapse ($\rho_{\max} = 10^{-4}\,\mathrm{g\,cm}^{-3}$) with the RHD1 model for the three values of initial temperature, as well as for the RHD2 model. For a higher initial temperature the SED is brighter and peaks at a shorter wave-

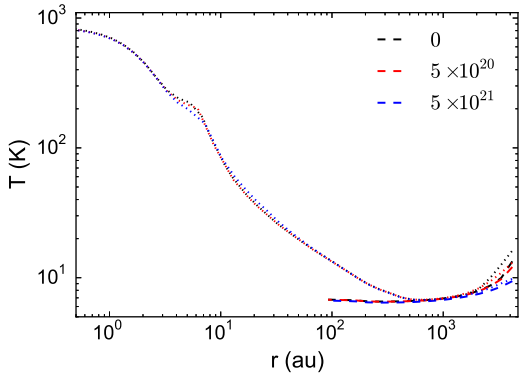

Figure 3.8: Radial dust temperature profiles for the initial conditions (dashed lines) and at $\rho_{\rm max} = 10^{-9}$ g cm^{-3} (dotted lines) for non-rotating pre-stellar cores with an additional boundary density, defined by the column number density of molecular hydrogen (shown in legend, cm^{-2}), to reduce the incident ISRF.

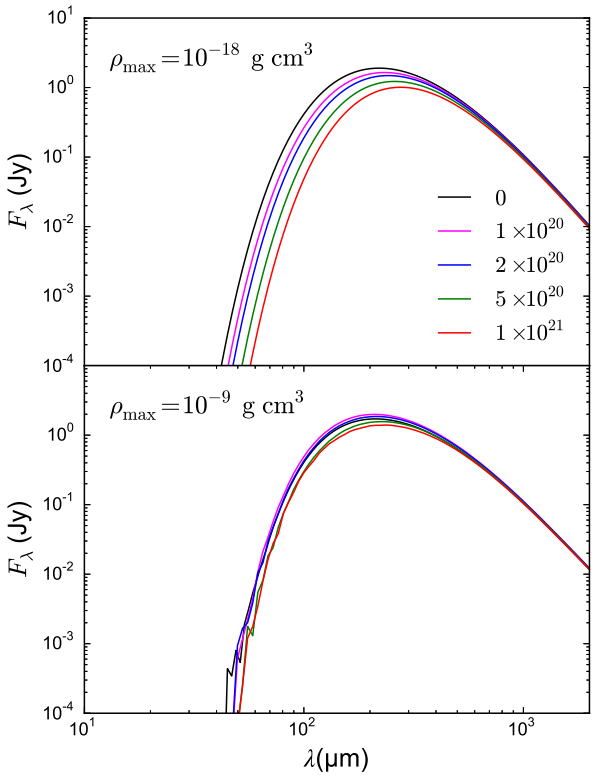

Figure 3.9: SEDs for the initial conditions (top) and at $\rho_{\rm max} = 10^{-9}$ g cm^{-3} for non-rotating protostellar cores with different column densities at the boundary to reduce the ISRF, defined by the column number density of molecular hydrogen (cm^{-2}) shown in the legend.

length early on in the collapse. As the core evolves and the FHSC forms the SED peak shifts to shorter wavelengths (Fig. 3.7, top row). For the cores with higher initial temperatures, there is less variation in the SED as the object evolves and we see that for an initial temperature of $15\,\mathrm{K}$ (Fig. 3.7, lower left panel) the SEDs are identical throughout, even to second collapse. This result indicates that, for warmer pre-stellar molecular cloud cores, no information can be gained from the SED as to its evolutionary state.

The differences in SED evolution between the cores with different initial temperatures suggests there must be differences in their radial temperature profiles. From the radial temperature profiles shown in Fig. 3.1 we can see that the FHSC has not heated gas beyond a radius of about $300\,\mathrm{AU}$ above its initial temperature in the $7\,\mathrm{K}$ case which means that the envelope remains colder than that of the $15\,\mathrm{K}$ core even to the second collapse phase when the central temperature quickly rises by several thousand Kelvin. The higher temperature of the envelope in the $15\,\mathrm{K}$ case leads to increased emission from larger radii and the photospheres will then be at a larger radii, where there is less heating from the FHSC. This effect is stronger at shorter wavelengths since the low density gas is still optically thin for $\lambda > 700\,\mu\mathrm{m}$. For a higher initial temperature, the regions probed by shorter wavelengths will therefore have a smaller temperature variation as the core evolves. Because of this and because much of the material is initially hotter, the SED displays less evolution.

There is also a difference in the shape of the FHSC SED for different initial temperatures. The SEDs of the warmer cores are closer to a single–temperature blackbody curve whereas the SEDs of the $7\,\mathrm{K}$ case become steeper at shorter wavelengths and flatter to longer wavelengths as the core evolves. Omukai (2007) also report SEDs of this shape and explain that it is due to the interplay of increasing optical depth with decreasing wavelength and decreasing temperature at larger radii. The photospheres of the cooler cores are nearer the FHSC where there is a steeper temperature gradient (see Fig. 3.1). The photospheres for different wavelengths will be at a spread of radii in all cases but when the envelope is cooler the set of observed wavelengths samples the region nearer the centre and so will sample a broader range of temperatures. The larger the differences in temperatures sampled by each wavelength, the less the SED will resemble that of a single

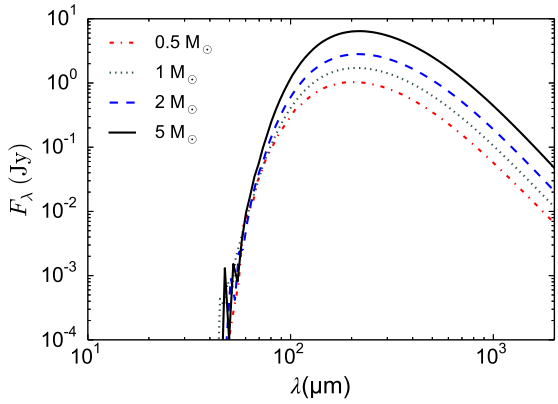

(a)

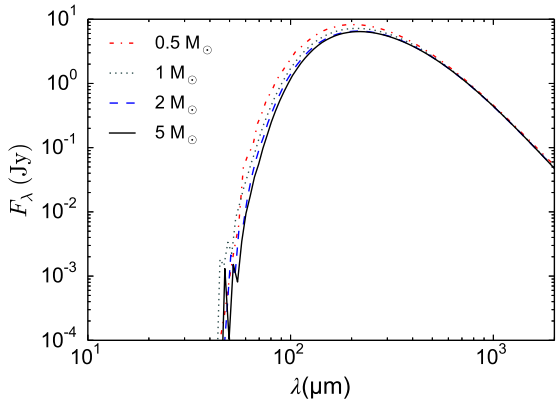

(b)

Figure 3.10: (a) SEDs for collapsing pre-stellar cores of different initial masses for snapshots when $\rho_{\rm max} = 10 \times 10^{-9}\,{\rm g\,cm^{-3}}$. (b) SEDs of different mass FHSCs scaled to fit the $5\ {\rm M}_\odot$ FHSC by minimising χ^2 for points $\lambda > 700\,\mu{\rm m}$. Higher mass cores are more luminous, as expected, but darker at $70\,\mu{\rm m}$ compared to $160\,\mu{\rm m}$.

temperature blackbody. We therefore expect the SEDs of colder cores to show the most evolution because the temperature contrast is greater and this contrast increases as the FHSC develops.

A uniform initial temperature is unrealistic (see e.g. Ward-Thompson et al. 2002; Nielbock et al. 2012; Roy et al. 2014); therefore we now consider a core exposed to the ISRF and use its equilibrium temperature profile as the initial temperature conditions.

The SED evolution with the RHD2 model is presented in Fig. 3.7 (bottom row). The RHD2 SEDs display a smaller increase in flux at shorter wavelengths as the core evolves than the RHD1 SEDs. The RHD2 SED of the early FHSC stage peaks at a shorter wavelength compared to those of the $7\,{\rm K}$ and $10\,{\rm K}$ RHD1 cores due to the heating of

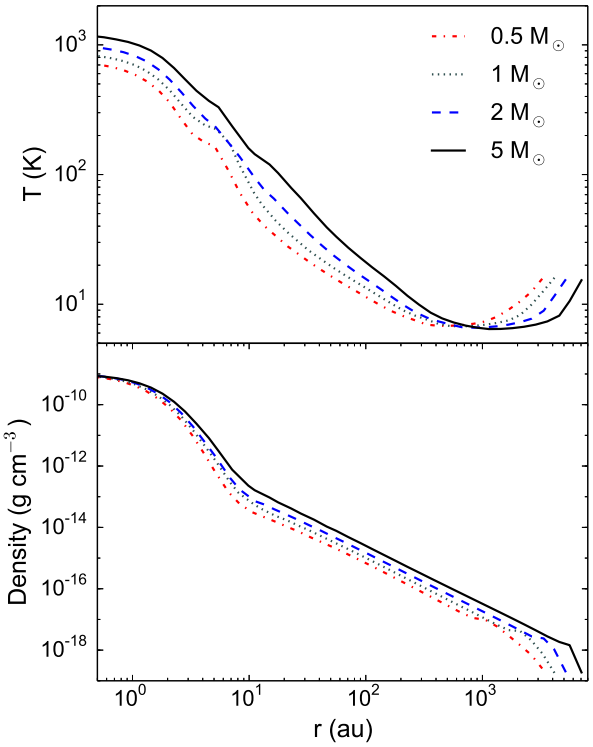

Figure 3.11: Radial profiles of the dust temperature and density for cores of different masses during the FHSC phase when $\rho_{\rm max} = 10 \times 10^{-9}\,{\rm g\,cm^{-3}}$. The FHSC extends to similar radii in all cases, as shown by the change in the slope of the density profile at $\sim 1 \times 10^{14}\,{\rm cm}$.

dust by the ISRF at $r > 2700\,{\rm AU}$ to more than $10\,{\rm K}$, as shown in Fig. 3.1 (lower right). This region contains around a third of the total mass, which means that the ISRF heats a greater proportion of the core than the FHSC does during its lifetime. The FHSC heating only makes a significant difference to the SED later on when the region surrounding the FHSC ($20 \lesssim r \lesssim 30$ AU) is heated to $> 20\,{\rm K}$. The SED is dominated by flux from the ISRF-heated region through to second collapse phase so we do not see the strong progression to shorter wavelengths as the core evolves that was the case for the cold RHD1 SEDs, as well as for the SEDs of Saigo and Tomisaka (2011), Commerçon et al. (2012a) and Young and Evans (2005). There is an increase in flux at $70\,\mu{\rm m}$ and $160\,\mu{\rm m}$, while the flux at longer wavelengths remains nearly constant and this could be useful for estimating the evolutionary stage of a source, even though the SEDs of the FHSC phase do not appear to be clearly distinct from those of the first and second collapse stages.

In the RHD1 models, gas and dust are assumed to have the same temperature, but using RHD2 the gas and dust temperatures may differ substantially. Dust emission is the main source of continuum emission and so the dust temperatures calculated in the

RHD2 model are used to produce the SEDs. The dust and gas temperatures only diverge significantly in the low density region at the edge of the core where they are not well coupled. We find there is, however, a significant difference in the SEDs if we use the gas temperature rather than the dust temperature because of this difference in the outer parts of the core. For detailed SED modelling it is therefore important to model the outer dust temperatures well. Given the differences in SED evolution between the RHD1 and RHD2 models, it appears beneficial to model the core collapse with the more physical radiative transfer method.

The ISRF incident on the protostellar core was varied by adding an additional column density of molecular material (gas and dust) at the boundary. This additional density is not included in the SED calculations so its only effect is to reduce the external radiation incident on the cloud core. In an observational study of dense cores, Kim et al. (2016) report that there is a temperature increase of 3-6 K between the central and outer regions of the core with the central temperature being 7-8 K. The temperature profiles in Fig. 3.8 show that the initial conditions of all of the RHD2 models fall within these ranges.

The SED evolution with RHD2 with boundary column density values of $5 \times 10^{20}\,\mathrm{cm}^{-2}$ and $5 \times 10^{21}\,\mathrm{cm}^{-2}$ of molecular hydrogen is shown in Fig. 3.7 (bottom row). For the initial conditions ($t = 0$), λ_{max} shifts to longer wavelengths for increased boundary density, as shown by Fig. 3.9, because heating from the ISRF is attenuated leading to lower dust temperatures in the outer regions of the core (see Fig. 3.8). However, once collapse begins, the increasingly dense central core becomes the dominant heat source and so there is much less of a difference between the SEDs of FHSCs from models with different values of the boundary column density after FHSC formation. We do also see greater evolution of the SED with a reduced ISRF because the infrared flux is less dominated by emission from the outer regions and is more sensitive to internal temperature changes.

In all cases except for the core with a uniform initial temperature of $15\,\mathrm{K}$, the SED peak shifts to shorter wavelengths and the total flux increases as the temperature increases in the central core. The SED begins to deviate from that of a blackbody because the envelope remains cold as the centre heats up. This change in the SED shape may allow more evolved cores to be distinguished from starless cores. However, protostellar cores with

initial temperatures of $\gtrsim 15\,\mathrm{K}$ or exposed to a strong ISRF are not expected to show much evolution so it is unlikely much information about the central object can be obtained from the SED. In this section we have studied only spherically–symmetric cases. These conclusions do not necessarily hold for rotating protostellar cores and we explore those cases further in Section 3.3.4.

3.3.3 Mass

The total luminosity of a dense core should be greater for a larger core mass but the fluxes at different wavelengths will not necessarily scale equally. We therefore simulated the collapse of $0.5\ \mathrm{M}_\odot$, $1\ \mathrm{M}_\odot$, $2\ \mathrm{M}_\odot$ and $5\ \mathrm{M}_\odot$ cores to investigate the variation in SED shape with mass and to determine how to scale model SEDs to observations. The initial radii were increased along with the mass so as to retain a constant initial central density of $\rho_{\mathrm{max}} = 1.38 \times 10^{-18}\,\mathrm{g\,cm^{-3}}$. The initial radii ranged from $3700\,\mathrm{AU}$ for $0.5\ \mathrm{M}_\odot$ to $8000\,\mathrm{AU}$ for $5\ \mathrm{M}_\odot$. These simulations were performed with the RHD2 model.

The SEDs of cores of different masses in Fig. 3.10 (a) show that increasing the total mass of the protostellar core results in an overall increase in flux, as expected, because there is more radiating material.

To compare the differences in SEDs further we scaled the SEDs of cores of different masses to the SED of the $5\ \mathrm{M}_\odot$ core (Fig. 3.10, b). Flux at wavelengths $\lambda > 700\,\mu\mathrm{m}$ depends upon the mass, temperature and dust emissivity of the source. Here, the dust properties are the same for each case and the temperatures are very similar, which means the effects of these factors on the flux at $\lambda > 700\,\mu\mathrm{m}$ are negligible and we can consider the flux here as being proportional only to the mass. To implement the scaling, we therefore multiplied each SED by a scale factor which was increased until the χ^2 value for wavelengths $\lambda > 700\,\mu\mathrm{m}$ was minimised.

When the SEDs are scaled in this way it is apparent that the lower mass cores are brighter at wavelengths $\lambda < 200\,\mu\mathrm{m}$ compared to longer wavelengths, an effect also found by Tomida et al. (2010a). We see from the density profile in Fig. 3.11 that in each case the FHSC has the same radius and that the density only deviates towards the boundary so

we would expect a similar flux at $\lambda < 100\,\mu\mathrm{m}$ from the hot FHSC. However, the radiation from the FHSC is absorbed by the cooler surrounding gas and most of the observed flux is emitted by the cooler gas further out. For cores of a greater total mass, the FHSC is surrounded by a more massive envelope which leads to disproportionately more longer wavelength emission and increased absorption of shorter wavelengths by the envelope. The same effect was later noted by Stamer and Inutsuka (2018), who argue that the observation of low mass FHSCs should be easier for this reason and because their lifetimes are longer.

The collapse occurs much more quickly for the more massive cores. For the $0.5\ \mathrm{M}_\odot$ core, the $\rho_{\max} = 10^{-9}\,\mathrm{g\,cm^{-3}}$ snapshot is taken at $35\,600\,\mathrm{yr}$ and for the $5\ \mathrm{M}_\odot$ core it is much sooner at $25\,700\,\mathrm{yr}$. Since the collapse of the $5\ \mathrm{M}_\odot$ core happens much more quickly, there is less time for the heat to disperse, leading to the hotter central temperature. Despite this, there is not much more infrared flux for the more massive cores because the SED is still dominated by emission from the cooler dust in the envelope.

When comparing to observations, it is useful to be able to scale synthetic SEDs since the sources will have various masses and distances, which may not be known precisely. We find the SED of an FHSC does vary with mass so there will be limits to scaling synthetic SEDs of a core of one mass to observations of a source of a different mass. This is considered further in Section 3.4.2.

3.3.4 Initial rotation

Differing initial rotation rates give rise to various structures. In the non-rotating case the FHSC is spherically symmetric but becomes increasingly oblate with faster rotation. For faster rotation rates, the FHSC may be dynamically rotationally unstable, developing spiral arms and perhaps fragmenting (e.g. Bate 1998, 2011; Saigo and Tomisaka 2006). If these structures lead to differences in the SED then this would provide a probe for the internal structures of pre-stellar cores without requiring high resolution imaging.

Dense cores are observed to have typical rotation rates corresponding to $\beta = 0.02$ (Goodman et al. 1993) and range between $\sim 10^{-4}$ and 0.07 (Caselli et al. 2002). We sim-

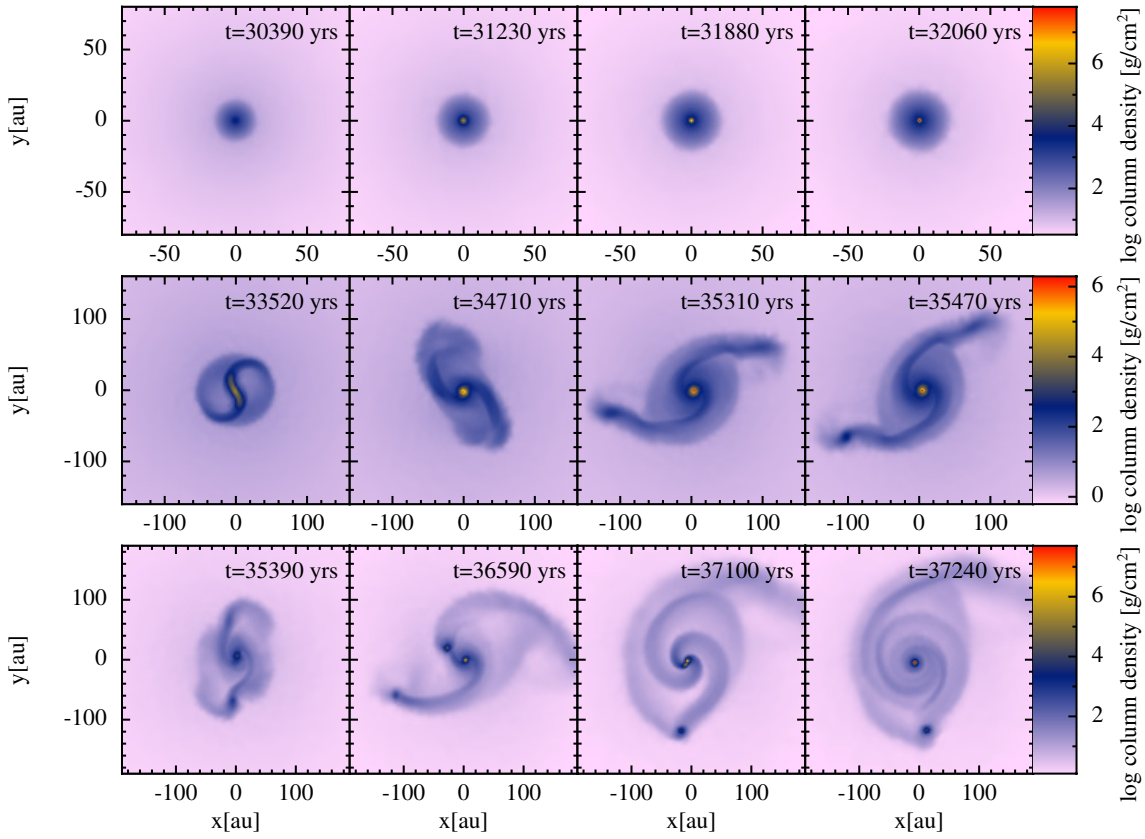

Figure 3.12: Snapshots of the column density for RHD2 simulations with initial rotation $\beta = 0.01$ (top row), $\beta = 0.05$ (middle row) and $\beta = 0.09$ (bottom row). These are some of the snapshots from which SEDs were simulated. The maximum density, $\rho_{\rm max}$ in each panel is $5 \times 10^{-11}\,{\rm g\,cm^{-3}}$, $10^{-9}\,{\rm g\,cm^{-3}}$, $10^{-8}\,{\rm g\,cm^{-3}}$ and $10^{-6}\,{\rm g\,cm^{-3}}$ from left to right. The FHSC is an oblate spheroid in the $\beta = 0.01$ simulation. The faster rotating cores form spiral arms and fragments. The two inner fragments formed in the $\beta = 0.09$ simulation fall back together before the onset of second collapse. At $t = 0$ the peak column density is $< 0.1\,{\rm g\,cm^{-2}}$.

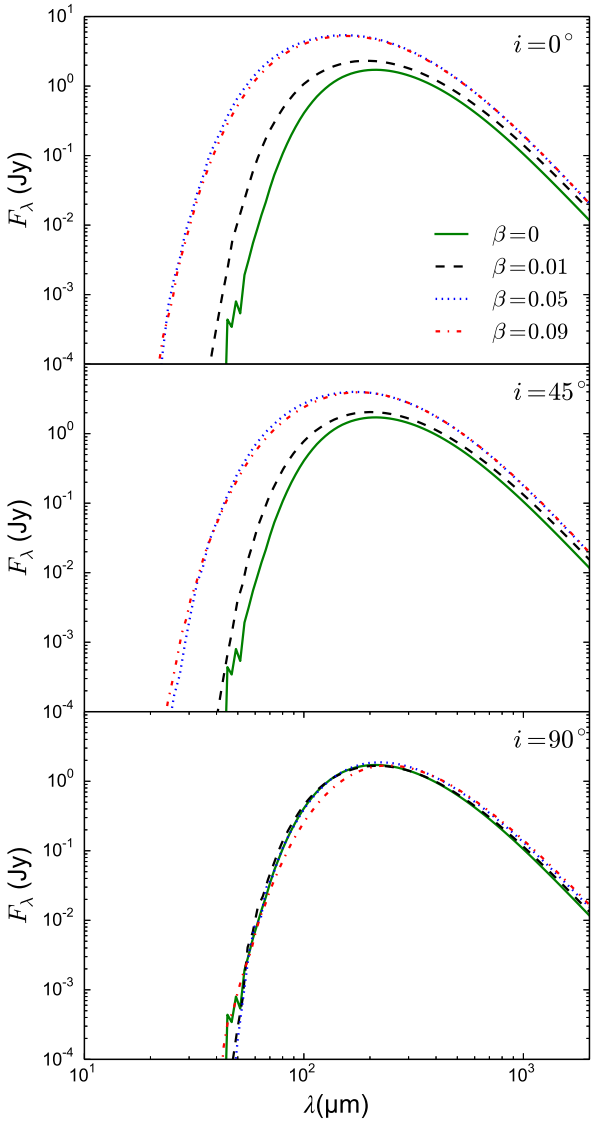

Figure 3.13: SEDs for collapsing pre-stellar cores with different initial rotation rates for snapshots from the RHD2 model when $\rho_{\rm max} = 10^{-9}\,{\rm g\,cm^{-3}}$. Rotation rate is defined via $\beta = E_{\rm rot}/E_{\rm grav}$. At faster rotation rates, the core is brighter in the far infrared when viewed face-on. At $90°$ the SEDs of cores with different rotation rates are very similar. The peak of the SED of the $\beta = 0.09$ FHSC is at a slightly longer wavelength because the fragmented FHSC lies within a disc so the opacity perpendicular to the rotation axis is greater than the opacity in the non-rotating case.

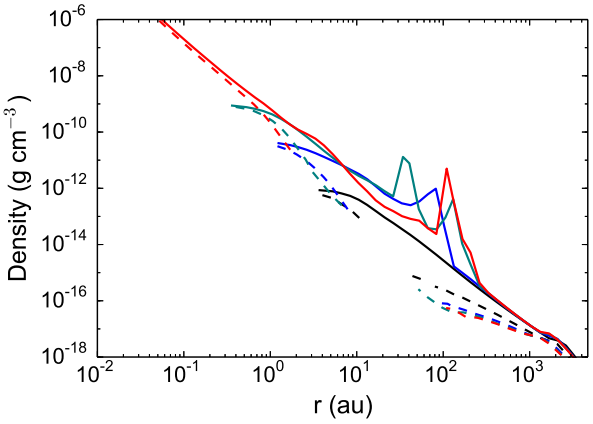

Figure 3.14: Radial density profiles of the core of initial rotation $\beta = 0.09$ at snapshots from the RHD2 model when the maximum density is $1 \times 10^{-12}\,\mathrm{g\,cm^{-3}}$ (black), $5 \times 10^{-11}\,\mathrm{g\,cm^{-3}}$ (blue),$1 \times 10^{-9}\,\mathrm{g\,cm^{-3}}$ (green) and $1 \times 10^{-6}\,\mathrm{g\,cm^{-3}}$ (red). Dashed lines show the vertical radial profile (i.e. along the rotation axis) and solid lines show the horizontal radial profile. There is a greater density in the horizontal direction, that is in the plane of the disc structure, and this difference increases as the object evolves. This difference in the density profiles in the horizontal and vertical directions is responsible for the difference between SEDs at different inclinations. The spike in the density is due the presence of a fragment and the gaps in the vertical profiles are where there are insufficient particles to calculate an average density.

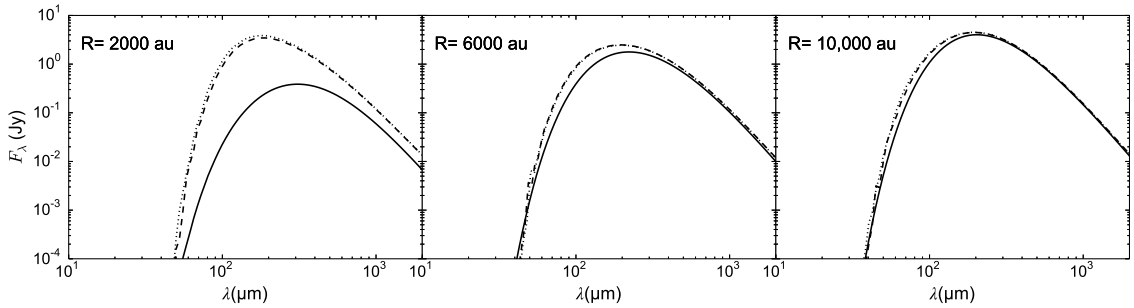

Figure 3.15: The evolution of SEDs for the collapse of $1\ \mathrm{M}_\odot$ non-rotating pre-stellar cores with initial radii of 2000 AU, 6000 AU and 10 000 AU from left to right. The SEDs are calculated from snapshots at values of maximum density of $1 \times 10^{-12}\,\mathrm{g\,cm^{-3}}$ (first collapse, solid lines), $1 \times 10^{-8}\,\mathrm{g\,cm^{-3}}$ (late FHSC stage, dashed lines) and $1 \times 10^{-4}\,\mathrm{g\,cm^{-3}}$ (second collapse, dotted lines). There is less variation of the SED as the core evolves for cores with larger initial radii. For an initial radius of 10 000 AU the second collapse SED is observationally indistinguishable from the SED of the early FHSC.

ulated SEDs for $\beta = 0$, 0.01, 0.05 and 0.09 to cover the range of observed values, noting that for $\beta < 0.01$ the structure is similar to that of a non-rotating ($\beta = 0$) core. The SEDs in this section were simulated using RHD2 but we also produced SEDs for rotating cores with RHD1 with an initial temperature of $T_{\rm initial} = 10\,{\rm K}$ for comparison with observations. The column density snapshots from the RHD2 simulations in Fig. 3.12 show the structure in each case. The $\beta = 0$ case is spherically-symmetric, the $\beta = 0.01$ case gives an oblate FHSC, $\beta = 0.05$ forms spiral arms and a small fragment before stellar core formation, and $\beta = 0.09$ forms spiral arms than fragments into three FHSCs, two of which merge before stellar core formation.

The initial rotation rate affects the shape of the SED as the object evolves. From Fig. 3.13 we see that the higher rotation rate leads to an SED with a peak at a shorter wavelength and a shallower slope to shorter wavelengths, at low inclinations (face on). With a faster rotating core there is less obscuring material between the core and observer at low inclinations. This is illustrated by plotting the radial density profiles along the rotation axis and perpendicular to the rotation axis, as shown in Fig. 3.14. At radii less than $1000\,{\rm AU}$ there is a clear difference in density at positions in the parallel and perpendicular directions due to the presence of a disc. This difference increases as the object evolves and more gas accretes onto the disc. As shown in Section 3.3.1, flux at $\lambda < 100\,\mu{\rm m}$ is emitted by the warm dust surrounding the FHSC. A lower density outside this region will reduce the opacity and therefore more flux will reach the observer. Hence at faster rotation rates, with a more oblate structure, the SED will peak at shorter wavelengths and there will be more flux at $\lambda < 100\,\mu{\rm m}$ and detectable flux even at $24\,\mu{\rm m}$ in many cases, when viewed at low inclinations (face-on), as we see in Fig. 3.13 (top).

The reverse is true for observations at high inclinations. The density increases perpendicular to the rotation axis as the disc structure forms, the opacity increases, and less radiation from the regions heated by the FHSC reaches the observer. This results in much less evolution of the SED. Beyond $\beta = 0.05$ the pattern is different because the FHSC fragments. The flux reaching an observer will therefore also depend on the location of the fragments because the structure is not axisymmetric.

The SEDs of cores with different rotation rates do have different properties, so it is

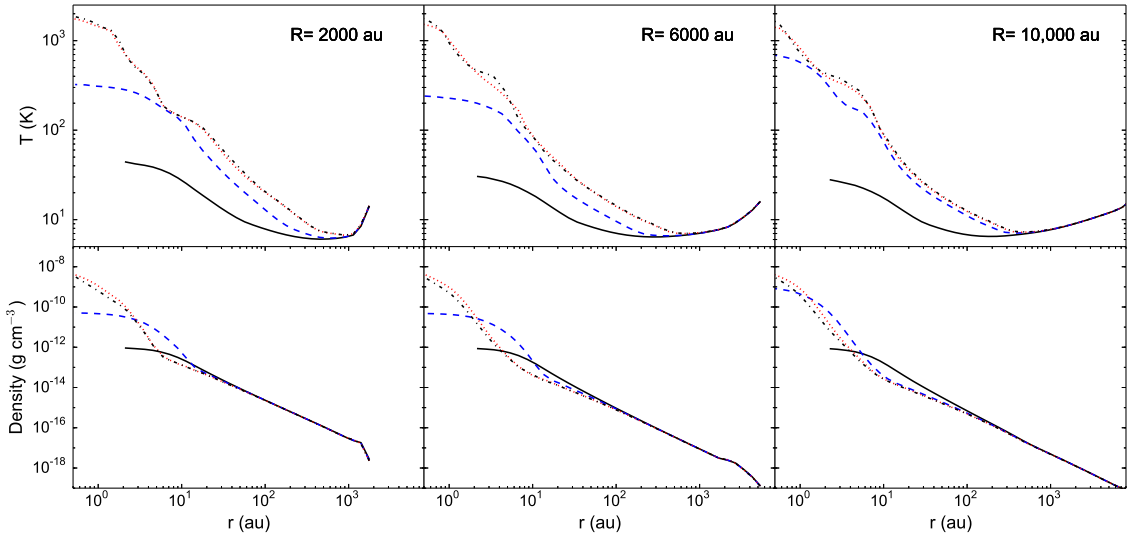

Figure 3.16: Radial density and temperature profiles during the collapse of $1\ \mathrm{M}_{\odot}$ non-rotating pre-stellar cores with initial radii of 2000 AU, 6000 AU and 10 000 AU for snapshots when the maximum density was $10^{-12}\,\mathrm{g\,cm^{-3}}$ (solid black lines), $5 \times 10^{-11}\,\mathrm{g\,cm^{-3}}$ (blue dashed lines), $1 \times 10^{-8}\,\mathrm{g\,cm^{-3}}$ (black dot-dashed line) and $10^{-4}\,\mathrm{g\,cm^{-3}}$ (red dotted lines). The differences in the temperature structures and the extent of the envelopes give rise to differences in their SEDs as seen in Fig. 3.15.

possible for an SED to provide some information as to the structure of the central regions of a collapsing pre-stellar core. At high inclinations the SEDs of cores with different rotation rates are very similar. In addition, the edge-on SEDs are very similar to those of less evolved cores in the first collapse or early FHSC phase. This means that any differences due to rotation may be difficult to interpret when the inclination is not known. SEDs would need to be combined with other forms of observation to infer the structure.

3.3.5 Initial radius

Cores of different initial radii but equal masses will necessarily have different density structures, which in turn will affect the temperature and opacity. The simulations for exploring the effects of varying the initial radius were performed using the RHD2 model for $1\ \mathrm{M}_{\odot}$ cores, with heating from the ISRF.

It is clear from the SEDs of evolving cores with different initial radii shown in Fig. 3.15 that there is much more variation as the object evolves for the core with the smallest initial radius. As for the case of an initial radius of $r_{\mathrm{ini}} = 4700\,\mathrm{AU}$ shown in Section 3.3.2, the SEDs of the core of $r_{\mathrm{ini}} = 6000\,\mathrm{au}$ do not show much evolution, with just a small increase in flux between $50\ \mu\mathrm{m}$ and $300\ \mu\mathrm{m}$ and no significant difference between the

SEDs of late FHSC and second collapse stages. When the initial radius is increased further there is even less variation of the SED with age of the core. As the initial radius of the core increases, it becomes less unstable to gravitational collapse so the collapse progresses mores slowly. The core of radius $r_{\rm ini} = 11\,400\,{\rm AU}$ did not collapse.

The radial density and temperature profiles of each core are shown in Fig. 3.16 and we find that the FHSC has the same radius in each case, as was reported by Vaytet and Haugbølle (2017). The first collapse SED is coldest for the smallest core. The smallest core is more dense so the ISRF is attenuated more strongly and does not heat the core as deeply as it does for the larger cores. The effect of this is apparent in Fig. 3.16 as the temperature falls more sharply near the boundary of the smaller core and the core has a lower minimum temperature. A greater fraction of the mass of the smaller core is cold, giving rise to a colder SED during the early FHSC stage for a smaller core.

The smallest core also has a brighter and more sharply peaked second collapse SED. In all cases, the FHSC heats the envelope out to $\sim 700\,{\rm AU}$ so for a smaller core, a larger fraction of the total mass is heated, leading to a warmer SED.

For larger cores we find that the evolution of the central object is almost completely obscured. Unless the core is rotating sufficiently to reduce the opacity significantly along the rotation axis, the application of SEDs to determine the evolutionary state of pre-stellar cores is limited to smaller cores.

3.3.6 Magnetic field

We performed MHD simulations of the collapse of a $1\ {\rm M}_\odot$ core with the radiative transfer treatment of RHD2 (see Section 3.2.1). These simulations use $\beta = 0.005$ and initial mass-to-flux ratios of $\mu = 5$ and $\mu = 20$, aligned with the rotation axis. Some observed FHSC candidates have substantial short wavelength emission ($\lambda < 100\,\mu{\rm m}$), and we wondered whether a magnetically-driven outflow from an FHSC core may be able to boost the observed short wavelength emission compared to that produced by an unmagnetised model. The magnetic field in the $\mu = 20$ case was too weak to produce an outflow and so we produced SEDs from snapshots from the $\mu = 5$ simulation in which an outflow

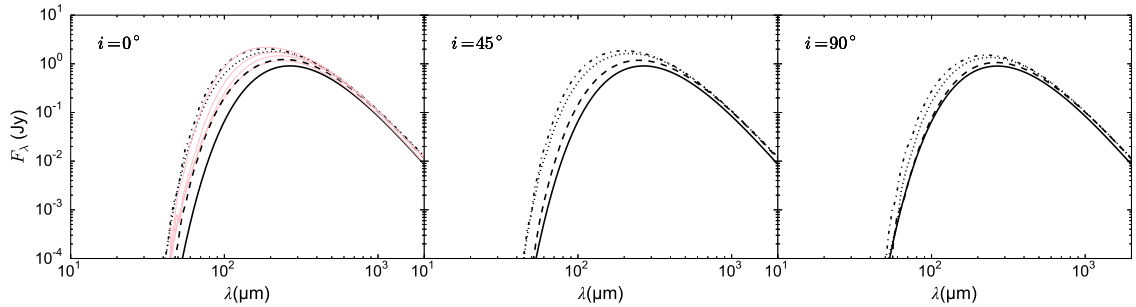

Figure 3.17: Evolution of the SED at three inclinations for a collapsing $1\ \mathrm{M}_\odot$ core with the MHD model with initial rotation $\beta = 0.005$ and $\mu = 5$. The SEDs were calculated from snapshots when the maximum density was $10^{-12}\,\mathrm{g\,cm^{-3}}$, $5 \times 10^{-11}\,\mathrm{g\,cm^{-3}}$, $1 \times 10^{-9}\,\mathrm{g\,cm^{-3}}$ and $10^{-4}\,\mathrm{g\,cm^{-3}}$ from right to left. The SED evolution from the non-rotating RHD2 model are shown in pink in the $i = 0°$ panel. The SED becomes bluer and brighter as the object evolves, however the presence of an outflow does not lead to any additional increase in infrared flux.

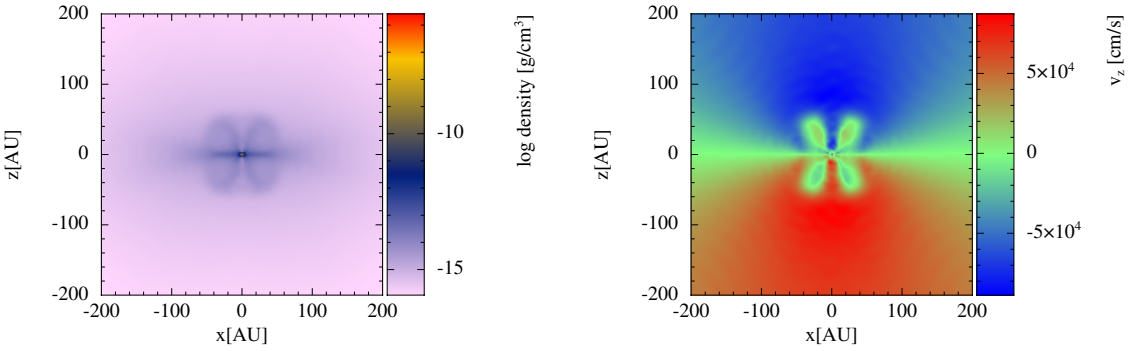

Figure 3.18: Density slice (left) and vertical velocity, v_z, slice (right) for the MHD snapshot used to produce an SED during the second collapse phase when the central density was $10^{-4}\,\mathrm{g\,cm^{-3}}$ (at 30 960 yr). The initial rotation was $\beta = 0.005$ and the initial mass-to-flux ratio was $\mu = 5$. At this stage, the outflow has not penetrated far into the cloud and we see that this does not reduce the density along the direction of the outflow and the infall motions are still much greater than outflow motions. Since the outflow affects only a small proportion of the core, the SED is similar to those of non-MHD simulations. The former FHSC extends to a radius of $\sim 7\,\mathrm{AU}$ in this snapshot.

develops late on in the FHSC phase (c.f. Bate et al. 2014).

The SED evolution with the MHD simulation is displayed in Fig. 3.17 and in the $i = 0°$ panel we also plot the SED evolution for RHD2 with $\beta = 0$. We see that the SED from the MHD model is initially colder, as was the case with the RHD2 model with the additional boundary column density, but subsequent SEDs are very similar. It is apparent that the presence of an outflow does not increase the flux at short wavelengths. Although the outflow contains a central region of reduced density, the outflow at this early stage is still sufficiently dense to absorb much of the flux from the core. Commerçon et al. (2012a) also report this effect: looking along the outflow of a magnetised FHSC there was no flux at $\lambda < 30\,\mu\mathrm{m}$. The vertical density slice through the core and the vertical velocities of the gas during the second collapse phase are shown in Fig. 3.18. These figures show that during the FHSC and second collapse phases, the outflow is still small so only a small proportion of the core is influenced by the outflow and the majority of the envelope structure is similar to the purely hydrodynamical case. It is, therefore, not surprising that the SEDs are similar for models with and without magnetic fields.

Lewis et al. (2015) and Lewis and Bate (2017) performed MHD simulations for a wide range of initial magnetic field magnitudes and orientations which all produced early protostellar outflows with velocities of $< 8\,\mathrm{km\,s^{-1}}$. Such slow outflows extended to less than $100\,\mathrm{AU}$ from the protostar before the stellar core forms (Fig. 3.18; Bate et al. 2014). Since both we and Commerçon et al. (2012a) find that MHD models of FHSCs do not produce SEDs that are significantly different to RHD models, we did not explore SED variation with magnetic field further.

3.3.7 Dust grain properties

There is currently significant uncertainty as to the nature of interstellar dust grains. These grains are usually assumed to be no larger than $1\,\mu\mathrm{m}$, however there have been several suggestions that there may be significant grain growth in dense regions of the ISM (e.g. Ormel et al. 2009; Butler and Tan 2009). Draine (2006) points out that there are regional differences in the wavelength dependence of interstellar extinction which suggests that the grain size distribution in the ISM does vary.

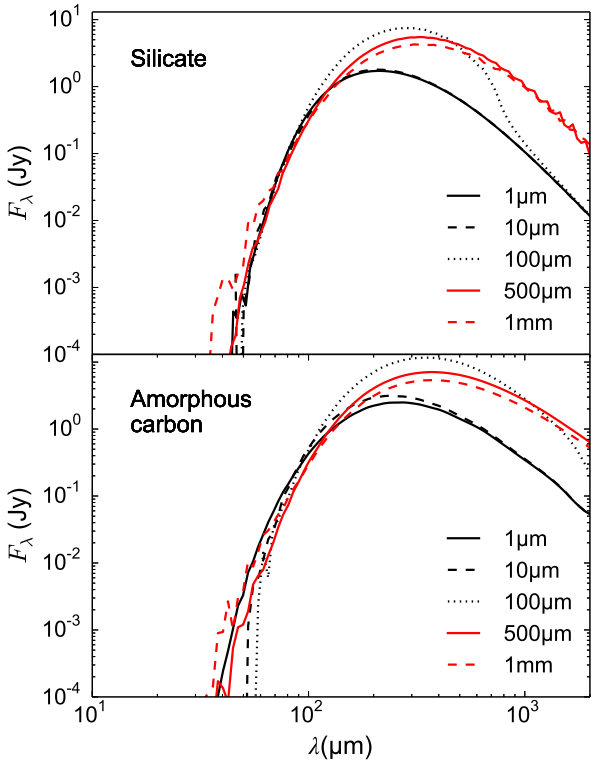

Figure 3.19: SEDs for a non-rotating FHSC with different maximum dust grain sizes ($a_{\rm max}$) using the RHD2 model. Top: silicate grain model. Bottom: amorphous carbon grain model.

Table 3.2: Parameters used to produce a range of model SEDs for both the RHD1, with initial temperature 10 K, and RHD2 models. The maximum density $\rho_{\rm max}$ is used to select specific evolutionary stages as shown in Fig. 3.3. β is the initial ratio of rotational energy to gravitational potential energy and $a_{\rm max}$ is the maximum dust grain size. The combinations of parameters give a total of 1440 synthetic SEDs, noting that $\beta = 0$ only has one possible inclination.

RHD Model	β	$\rho_{\rm max}$ (g cm^{-3})	Inclination	$a_{\rm max}$ (μm)	Grain Type
RHD1 (10K)	0	10^{-12}	0°	1	silicates
RHD2	0.01	5×10^{-11}	45°	10	graphite
	0.05	10^{-9}	90°	100	
	0.09	10^{-8}		200	
		10^{-6}		500	
		10^{-4}		1000	

Zubko et al. (2004) compared a variety of interstellar dust models to observational constraints and found that any linear combination of polycyclic aromatic hydrocarbon (PAH) molecules, silicate and amorphous carbon or graphite grains provide good fits to observational constraints. Here we simulate SEDs first with silicate grains and then with amorphous carbon grains. PAH molecules only provide a significant contribution to thermal emission for $\lambda < 40\,\mu\mathrm{m}$ (Zubko et al. 2004), which would only affect the $24\,\mu\mathrm{m}$ observational data points, for which there is little flux for these cool objects.

We assumed a maximum grain size $a_{\mathrm{max}} = 1\,\mu\mathrm{m}$ when simulating the SEDs in the previous sections but in this section we present results for when this maximum grain size is varied.

Decreasing a_{max} to below $1\,\mu\mathrm{m}$ has no effect on the SED, a result that is supported by the finding of Miyake and Nakagawa (1993) that opacities for $a_{\mathrm{max}} < 10\,\mu\mathrm{m}$ are the same as for a distribution of just submicrometre dust particles. The top panel of Fig. 3.19 shows the effect on the SED of increasing the maximum dust grain size. For particles with $10\,\mu\mathrm{m} \lesssim a_{\mathrm{max}} \lesssim 500\,\mu\mathrm{m}$ there is a very small decrease in flux at $50\,\mu\mathrm{m} \lesssim \lambda \lesssim 100\,\mu\mathrm{m}$ but the flux at $\lambda > 200\,\mu\mathrm{m}$ substantially increases for $a_{\mathrm{max}} \gtrsim 100\,\mu\mathrm{m}$. For $a_{\mathrm{max}} \gtrsim 500\,\mu\mathrm{m}$, there is a small increase in flux for $\lambda < 70\,\mu\mathrm{m}$ and, again, a substantial increase in flux at $\lambda > 200\,\mu\mathrm{m}$. Increasing a_{max} has the effect of increasing the millimetre dust opacity, as long as $a_{\mathrm{max}} \lesssim 1\,\mathrm{mm}$ (D'Alessio et al. 2001), which could explain the increased flux at the longer wavelengths with the larger grains. At the same time, for grain sizes over $10\,\mu\mathrm{m}$ the albedo, ω_ν, increases quickly from 0 to ~ 0.9 for $1\,\mathrm{cm}$ grains (D'Alessio et al. 2001) and so there is an additional contribution from scattered light when there are larger grains present. For larger a_{max}, the opacity is reduced for $\lambda \lesssim 100\,\mu\mathrm{m}$ (Miyake and Nakagawa 1993), which allows more flux from the core to reach the observer.

Varying the minimum dust grain size, a_{min}, between $0.001\,\mu\mathrm{m}$ and $0.05\,\mu\mathrm{m}$ with a_{max} fixed at $1\,\mu\mathrm{m}$ had no effect on the SED. Draine (2006) points out that for a grain size distribution of $p = 3.5$ most of the mass is contained in the large grains and so the numbers of large grains is affected little by a_{min}.

The results presented so far use silicate dust grains and next we compare these with

SEDs simulated with the amorphous carbon grain model of Zubko et al. (1996), shown in Fig. 3.19 (bottom). Compared to the SED produced using silicate grain properties with $a_{\rm max} = 1\,\mu{\rm m}$, the flux drops off less steeply either side of the peak with amorphous carbon with the result that there is more flux at both the shortest and longest detectable wavelengths. For $a_{\rm max} = 10\,\mu{\rm m}$, the flux at $\lambda < 100\,\mu{\rm m}$ decreases. Flux at $\lambda > 100\,\mu{\rm m}$ increases significantly for grains of $a_{\rm max} = 100\,\mu{\rm m}$ and larger, with the $\lambda < 100\,\mu{\rm m}$ flux returning to similar values as for $a_{\rm max} = 1\,\mu{\rm m}$ when $a_{\rm max} > 500\,\mu{\rm m}$.

The SED is very sensitive to grain size in the presence of large dust grains. The exact composition and size distribution of dust grains in pre-stellar cores is still largely unknown, therefore we consider a range of maximum sizes of both silicate and amorphous carbon grains when comparing to observed SEDs.

3.4 Results II: Comparison to observations

In this section we describe the set of model SEDs we have produced to compare to the observations of several FHSC candidates and the method used for estimating the mass in each case. We then discuss the FHSC candidates that we attempt to fit and the results of fitting models to those observed SEDs. We define the model SEDs with $\chi^2 < \chi^2_{\rm min} + 1$ as providing a "good" fit to give an indication of the variety of models providing a similar quality of fit to the best fitting model. We then look for consistencies among those best fitting models.

We divide the SED fitting results into three parts: in Section 3.4.3 are candidate FHSCs from the literature; in Section 3.4.4 are newly identified candidates in Serpens South; and in Section 3.4.5 are "PACS bright red sources" from the *Herschel* Orion Protostars Survey (HOPS). Note that the former two were published in Young et al. (2018) but the HOPS SED fits have not previously been published.

3.4.1 Selection of models

Simulations were performed for both RHD1 and RHD2 for four different initial rotation rates. Both RHD1 and RHD2 models were included to ascertain whether the more com-

plex treatment of radiative transfer would provide better fits to observations. For RHD1, a uniform initial temperature of $10\,\mathrm{K}$ was used. Fig. 3.3 shows the evolution of the maximum density from first to second collapse. The FHSC phase lasts from $\sim 4 \times 10^{-12}\,\mathrm{g\,cm^{-3}}$ to $\sim 5 \times 10^{-8}\,\mathrm{g\,cm^{-3}}$, but may commence at a higher maximum density for lower rotation rates. Six snapshots (a to f) were selected from each RHD model as indicated in Fig. 3.3 to allow comparison of the SED as the core evolves and also between SEDs of different cores at similar evolutionary stages.

Dust properties vary across different regions so we chose to simulate SEDs for a selection of different properties. Model SEDs which use amorphous carbon grains peak at longer wavelengths than the equivalent SED using silicate grains, which more closely matches the locations of some of the observed SED peaks. We chose the smallest value of $a_{\mathrm{max}} = 1\,\mu\mathrm{m}$ because reducing it below 1um had no effect and current observations indicate a maximum interstellar grain size of at least $1\,\mu\mathrm{m}$. We included SED models with dust grains $a_{\mathrm{max}} > 1\,\mu\mathrm{m}$ to try to reproduce the "wider" SED of SerpS-MM22 and the infrared–bright SEDs of Per-Bolo 58 and Chamaeleon-MMS1.

The range of parameters for which we simulated SEDs is outlined in Table 3.2 and this gives a total of 1440 synthetic SEDs which we compared with observations.

3.4.2 Scaling model SEDs

The difference between SEDs of varying mass cores described in 3.3.3 indicates that there are restrictions to using scaled SEDs to fit observations. To assess the validity of using scaled SEDs we applied the χ^2 fitting method to scale the SEDs of $0.5\ \mathrm{M}_\odot$, $1\ \mathrm{M}_\odot$ and $2\ \mathrm{M}_\odot$ cores during FHSC phase to the SED of a $5\ \mathrm{M}_\odot$ core also during FHSC phase. The monochromatic fluxes derived from the model SEDs of different mass cores at the wavelengths of the Serpens South observations (except $24\,\mu\mathrm{m}$) were multiplied by an increasing scale factor until the χ^2 value was minimised. The scaled monochromatic fluxes are plotted with the monochromatic fluxes of the $5\ \mathrm{M}_\odot$ SED in Fig. 3.20. The average errors of the observations of eight sources at these wavelengths are plotted with the synthetic $5\ \mathrm{M}_\odot$ fluxes.

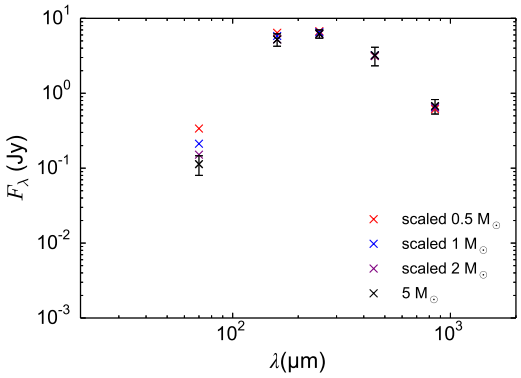

Figure 3.20: Monochromatic fluxes calculated from the SEDs of different mass FHSC models scaled to fit the SED of the $5\ \mathrm{M}_\odot$ FHSC via the χ^2 method described in Section 2.4.2. Error bars for the mean error of a selection of real, observed sources are plotted at the corresponding wavelengths. At $70\ \mu\mathrm{m}$ the scaled model fluxes lie outside the error bar which indicates that there is a limit to the scaling of a factor of ~ 2, beyond which the SEDs would be observationally distinguishable at $\lambda \lesssim 100\ \mu\mathrm{m}$.

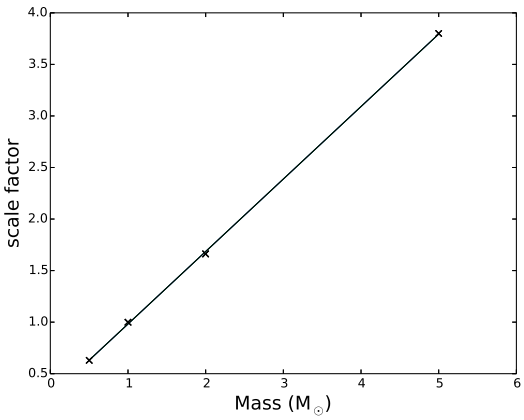

Figure 3.21: Scale factors necessary to scale the $1\ \mathrm{M}_\odot$ SED to the SEDs of three cores of different masses. Here we assume the same values of fractional uncertainty as for Fig. 3.20. A linear fit is calculated and plotted alongside.

The flux varies most between the different mass FHSCs at $70\ \mu\mathrm{m}$. At this point the scaled $2\ \mathrm{M}_\odot$ SED lies just outside the observational uncertainty, indicating that a mass difference of up to a factor of ~ 2 is indistinguishable observationally when scaled. From this we conclude that it is acceptable to scale $1\ \mathrm{M}_\odot$ SEDs to fit observations of different sources as long as the mass of the object lies in the range $0.5\ \mathrm{M}_\odot \lesssim M \lesssim 2\ \mathrm{M}_\odot$. Models fitted with scale factors outside this range must be treated with caution, particularly at $\lambda \lesssim 100\ \mu\mathrm{m}$.

There is also a distance contribution to the scaling factor which follows the inverse square relation for luminosity and distance. The distance contribution for the scaling of the SEDs simulated at a distance of $260\ \mathrm{pc}$ to observations can be estimated using

$$\text{scaling factor} = \left(\frac{260\ \mathrm{pc}}{D}\right)^2 \tag{3.1}$$

where D is the distance to the source. The scale factor will be > 1 for sources close than $260\ \mathrm{pc}$ and < 1 for sources further than $260\ \mathrm{pc}$.

The approximate distance to observed FHSC candidates is usually known. It is therefore possible to separate the mass and distance contributions to the scale factor. The

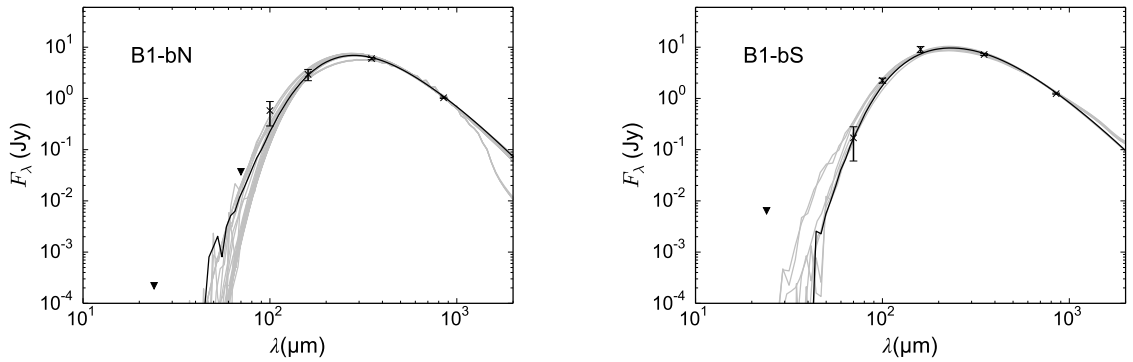

Figure 3.22: B1-bN (left) and B1-bS (right); arrows denote upper limits. Observational data from Hirano and Liu (2014) and Pezzuto et al. (2012). B1-bN: 27 model SEDs provided good fits. The best fitting model was from RHD1, $\beta = 0.09$, early FHSC, silicate grains, $a_{\rm max} = 10\,\mu{\rm m}$ and $i = 90°$. B1-bS: eight models provided good fits. The best fitting model was from RHD2, $\beta = 0.05$, early FHSC phase, silicate grains, $a_{\rm max} = 1\,\mu{\rm m}$ and $i = 90°$. Solid black line shows the best fitting model for each source and the other well fitting models are plotted in grey.

model SEDs used for fitting to observations are all from $1\ {\rm M}_\odot$ cores and Equation 3.1 will give the contribution of the distance to the scaling factor. Dividing the scale factor by this distance contribution will then provide the approximate contribution from the mass.

An estimate of the relation between mass and scale factor was obtained from scaling the $1\ {\rm M}_\odot$ SED to SEDs of three different values of core mass. The optimum scale factors for each value of mass are fitted by a linear relation of $\text{scale factor} = 0.7M + 0.3$ as shown in Fig. 3.21. It is the mass obtained from this relation that needs to lie in the range $0.5\ {\rm M}_\odot \lesssim M \lesssim 2\ {\rm M}_\odot$ for the fitting to be robust. There are often large uncertainties in the distance measurement so these mass values are only very approximate. We also note that it would be difficult to compare these values to observational estimates of core masses, which may include material contained within a smaller or larger radius.

3.4.3 Results of the SED fitting of literature FHSC candidates

We attempt to fit model SEDs to the observed SEDs of B1-bN and B1-bS (Pezzuto et al. 2012; Hirano and Liu 2014), Per-Bolo 58 (Hatchell et al. 2005; Enoch et al. 2006; Schnee et al. 2010; Enoch et al. 2010), Chamaeleon-MMS1 (Belloche et al. 2006; Tsitali et al. 2013; Väisälä et al. 2014) and CB17-MMS (Chen et al. 2012). These sources were described in Chapter 1, Section 1.6, where further details can be found. Per-Bolo 58 and Chamaeleon-MMS1 are brighter in the infrared than the other FHSC candidates while their SEDs peak at longer wavelengths. The B1-b sources and CB17-MMS are undetected at $24\,\mu{\rm m}$ and $70\,\mu{\rm m}$.

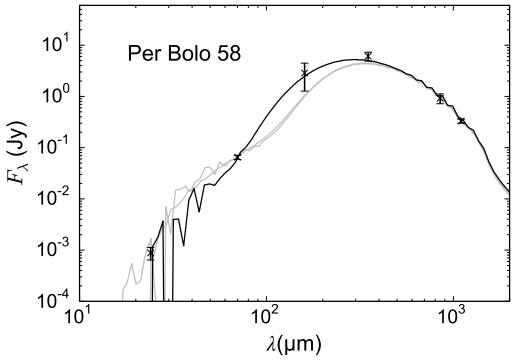

Figure 3.23: Per-Bolo 58; arrows denote upper limits. Observational data from Enoch et al. (2010). Just three model SEDs provided good fits. The best fitting model was from RHD2, $\beta = 0.09$, second collapse, silicate grains, $a_{\rm max} = 200\,\mu{\rm m}$ and $i = 90°$.

3.4.3.1 B1-bN and B1-bS

We attempted to fit the SEDs of FHSC B1-bN and B1-bS candidates using the photometry presented by Pezzuto et al. (2012) and Hirano and Liu (2014) [1]. These sources are thought to comprise a wide binary system and there is no evidence that either source contains multiple components (Tobin et al. 2016a). The SEDs and best fitting models are shown in Fig. 3.22.

The minimum χ^2 value obtained for fitting the SED of B1-bN was 0.21 and 27 models satisfied $\chi^2 < \chi^2_{\rm min}+1$. Nearly all of these were from RHD1 models and with silicate grains of $a_{\rm max} = 1\,\mu{\rm m}$. There was a preference for rotating, highly inclined models and SEDs of the first collapse or early FHSC stage. The optimum scale factor was 5.0 which gives a mass of $\sim 5.5\ {\rm M}_\odot$ at the distance of $235\,{\rm pc}$ (Pezzuto et al. 2012) and the effective dust opacity at $850\,\mu{\rm m}$ of the best fitting model was $4.0 \times 10^{-3}\,{\rm cm^2\,g^{-1}}$. B1-bN therefore looks to be a rotating young FHSC viewed at a high inclination, but is likely to be more massive than the $1\ {\rm M}_\odot$ cores used in our simulations.

B1-bS was well fitted by 8 model SEDs and the best fitting model has a χ^2 of 0.65. All of the best fitting models were from the RHD2 $\beta = 0.05$ or $\beta = 0.09$ simulations. They were snapshots mainly from the FHSC phase all with grains of a maximum size of $a_{\rm max} = 1\,\mu{\rm m}$ or $10\,\mu{\rm m}$. The optimum scale factor was $\sim$6 which gives a mass of $\sim 6.6\ {\rm M}_\odot$ at $235\,{\rm pc}$ and the $850\,\mu{\rm m}$ dust opacity was $3.9 \times 10^{-3}\,{\rm cm^2\,g^{-1}}$. Like B1-bN, B1-bS appears

1. We use the $70\,\mu{\rm m}$ colour corrected Herschel PACS fluxes from Hirano and Liu (2014) and discard the SPIRE fluxes because the beam sizes are larger than the separation between the sources.

to be a rotating FHSC located in a more massive core than those used in our simulations.

Slow molecular outflows have been detected for B1-bN and B1-bS (Hirano and Liu 2014; Gerin et al. 2015) and evidence of pseudo-disc rotation has been reported for B1-bS (Fuente et al. 2017) which are consistent with the sources being FHSCs. The B1-bS outflow is more extended, indicating that B1-bS could be more evolved. In Section 3.3.6 we find the SED does not change when there is an outflow from an FHSC so we would expect the results of the SED fitting to be similar had we included MHD models with outflows. I-Hsiu Li et al. (2017) find no evidence for grain growth in this core which would rule out the $10\,\mu\mathrm{m}$ model SEDs. They suggest that an alternative explanation for this SED shape (in the $800\,\mu\mathrm{m}$ to $8\,\mathrm{mm}$ range) is that the temperature or density increases towards the centre of the core. This is consistent with the structure of the FHSC and envelope that we model here and the corresponding SED appears to fit the fluxes well with a maximum grain size of $1\,\mu\mathrm{m}$.

3.4.3.2 Per-Bolo 58

Next, we attempted to fit the SED FHSC candidate Per-Bolo 58 in the Perseus molecular cloud (Hatchell et al. 2005; Enoch et al. 2006; Enoch et al. 2010; Schnee et al. 2010) and the results are shown in Fig. 3.23. The optimum scale factor was 0.75, giving a mass of $0.6\ \mathrm{M}_{\odot}$ at $260\,\mathrm{pc}$ (Enoch et al. 2010) and the $850\,\mu\mathrm{m}$ dust opacity was $4.0 \times 10^{-2}\,\mathrm{cm}^2\,\mathrm{g}^{-1}$. Per-Bolo 58 was fitted well by just three models, two from RHD1 and one from RHD2, and the minimum χ^2 value was 0.67. These were fast rotating cores at high inclination, in FHSC or second collapse phase. All three used silicate grains of $a_{\mathrm{max}} = 200\,\mu\mathrm{m}$, which was necessary to reproduce the combination of a peak between $200\,\mu\mathrm{m}$ and $300\,\mu\mathrm{m}$ and detectable flux at $24\,\mu\mathrm{m}$ and $700\,\mu\mathrm{m}$.

Enoch et al. (2010) used a distribution of dust grains with $a_{\mathrm{max}} = 0.5\,\mu\mathrm{m}$ and were able to produce an SED of this shape with either a wide outflow or a cavity in the envelope to allow the $24\,\mu\mathrm{m}$ to escape. As our models have shown, the outflow from an FHSC is unlikely to reduce the opacity to this extent. Similarly, we do not expect a cavity to be formed since in the lifetime of the FHSC the slow molecular outflow only reaches the innermost regions of the envelope. A slow bipolar outflow was discovered by Dunham et

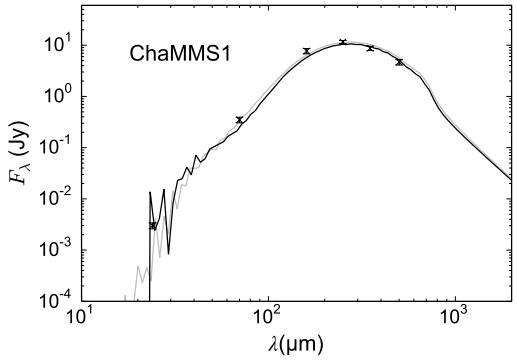

Figure 3.24: Chamaeleon-MMS1. Observational data from Väisälä et al. (2014). After SED fits which did not use all six data points were discarded, two models provided good fits. The best fitting model was from RHD2, $\beta = 0.09$, late FHSC, silicate grains, $a_{\rm max} = 100\,\mu{\rm m}$ and $i = 90°$.

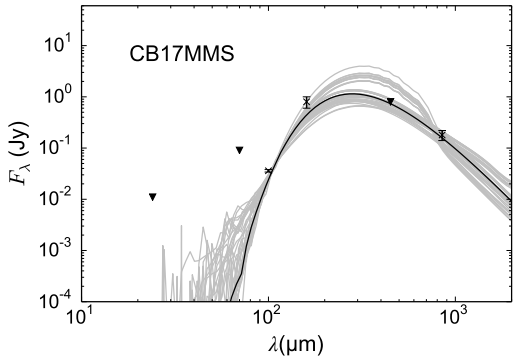

Figure 3.25: CB17-MMS; arrows denote upper limits. Observational data from Chen et al. (2012). 54 models provided good fits. The best fitting model was from RHD1, $\beta = 0$, first collapse stage with silicate grains of $a_{\rm max} = 10\,\mu{\rm m}$.

al. (2011) with properties that may be consistent with those of either FHSCs or protostars. Since we can only reproduce the SED shape with very large dust grains, this source is likely to be an FHSC only if such grains are present in collapsing pre-stellar cores. It is likely then that Per-Bolo 58 is more evolved than an FHSC. Another possibility is that the source is an unresolved multiple system, however this is ruled out by the multiplicity survey of Tobin et al. (2016a). Alternatively, Per-Bolo 58 could well be a very young protostar, perhaps not long after stellar core formation, with a disc and viewed edge-on such that much of the emission from the protostar is reprocessed.

3.4.3.3 Chamaeleon-MMS1

The results of the SED fitting for Chamaeleon-MMS1 using the monochromatic fluxes presented in Väisälä et al. (2014) and Tsitali et al. 2013 are presented in Fig. 3.24. The lowest χ^2 value is 3.4 and only two models fall within $\chi^2 < \chi^2_{\rm min} + 1$. The optimum scale

factor was 1.3, giving a mass of $0.3\ \mathrm{M}_{\odot}$ at $160\,\mathrm{pc}$ (Väisälä et al. 2014) and the dust opacity at $850\,\mu\mathrm{m}$ was $7.0 \times 10^{-3}\,\mathrm{cm}^2\,\mathrm{g}^{-1}$. These models were both from RHD2 and with $\beta = 0.09$. Both used silicate grains of $a_{\mathrm{max}} = 100\,\mu\mathrm{m}$. Cha-MMS1 was not well fitted by the FHSC models here, which means that it is likely to be more evolved.

Väisälä et al. (2014) attempted to fit the SED of Cha-MMS1 using the protostar SED fitting tool of Robitaille et al. (2006) and Robitaille et al. (2007). The failure to produce a good fit led them to conclude that Cha-MMS1 is more likely to be a second (stellar) core, that is newly formed and accreting, and this is consistent with the results of our fitting which point to an object at least as evolved as a late FHSC. Väisälä et al. (2014) also derive the ratio of rotational to gravitation energy to be $\beta = 0.07$, which is consistent with the fast rotation rates we find. The only models that produce an acceptable fit include large ($a_{\mathrm{max}} = 100\,\mu\mathrm{m}$) dust grains to fit the near straight slope between $24\,\mu\mathrm{m}$ and $160\,\mu\mathrm{m}$. It may be that a more evolved object with a disc has an SED of a similar shape while assuming only smaller grains as was suggested for Per-Bolo 58.

3.4.3.4 CB17-MMS

From its SED, shown in Fig. 3.25, CB17-MMS (Chen et al. 2012) looks cooler and younger than the previous two sources, with a peak between $\sim 150\,\mu\mathrm{m}$ and $\sim 250\,\mu\mathrm{m}$. The minimum χ^2 value was 0.44 and 54 models provided similar quality fits. All of these best fitting models were from RHD1 and more than half of them used silicate dust grains. Faster rotation rates are favoured at $i = 90°$, although non-rotating and slower rotating cores at lower inclinations are also among the best fitting models. There is a preference for snapshots from first collapse and early FHSC stages. The optimum scale factor was ~ 0.8 for the models using silicate grains and ~ 0.3 for those using carbon grains. This gives a mass of $< 0.6\ \mathrm{M}_{\odot}$ at $250\,\mathrm{pc}$. The smaller scale factor leads to a mass contribution below the range studied here. The dust opacity at $850\,\mu\mathrm{m}$ of the best fitting model was $3.9 \times 10^{-3}\,\mathrm{cm}^2\,\mathrm{g}^{-1}$.

The SED fitting appears strongly constrained by the $450\,\mu\mathrm{m}$ upper limit, which leads to a poorer fit of the $100\,\mu\mathrm{m}$ and $160\,\mu\mathrm{m}$ detections. The fitting results indicate that CB17-MMS is indeed likely to be an FHSC but could be an even younger collapsing pre-stellar

core without a central object although the $100\,\mu\mathrm{m}$ detection would most likely indicate the former. The model SED scaling indicates a low mass object and, as we show in Section 3.4.2, the SEDs of lower mass cores are relatively brighter at wavelengths $< 200\,\mu\mathrm{m}$ and this could explain why the source is detected at $100\,\mu\mathrm{m}$ but not at $450\,\mu\mathrm{m}$. Kinematic data with a high spatial resolution would determine whether there is a disc and thus whether this is a more evolved, rotating object viewed edge-on or a symmetrical collapsing pre-stellar core. Chen et al. (2012) present CO observations which may show evidence of a slow outflow. If this is correct, the collapsing core models can be ruled out and CB17-MMS remains a likely FHSC.

3.4.4 Results of the SED fitting of Serpens South FHSC candidates

We also attempt to fit the SEDs of five newly identified FHSC candidates. These are compact submillimetre, infrared–faint sources in Serpens South, a region discovered in the observations of Gutermuth et al. (2008) with the *Spitzer* Space Telescope. Further observations (e.g. Maury et al. 2011; Könyves et al. 2015; Nakamura et al. 2011; Kirk et al. 2013) have revealed Serpens South to be a dense filamentary cloud, with a large number of protostars and a high star formation rate (SFR) of $23\ \mathrm{M}_{\odot}\ /\mathrm{Myr}$, which makes Serpens South a promising place to look for FHSC candidates. Four of the sources, Aqu-MM2, SerpS-MM22, SerpS-MM19 and Aqu-MM1 are listed in Maury et al. (2011). The fifth source, HGBS J182941.1-021339, we refer to as K242, after its identification in the catalogue of Könyves et al. (2015).

The SEDs of the Serpens South FHSC candidates are constructed from $24\,\mu\mathrm{m}$ *Spitzer* MIPS 1, $70\,\mu\mathrm{m}$ and $160\,\mu\mathrm{m}$ (*Herschel* PACS), $250\,\mu\mathrm{m}$ (*Herschel* SPIRE) and $450\,\mu\mathrm{m}$ and $850\,\mu\mathrm{m}$ (SCUBA-2) fluxes. The observations, data reduction and monochromatic fluxes are detailed in Appendix A of Young et al. (2018). The objects are all faint at $24\,\mu\mathrm{m}$, with only SerpS-MM22 detected. B1-bN, CB17-MMS, SerpS-MM19 and K242 are also undetected at $70\,\mu\mathrm{m}$. While the four other candidates have SEDs similar to those of cold gas clumps, SerpS-MM22 is unusual in that it is brighter than the others in the infrared while the SED peak is still around $200\,\mu\mathrm{m}$.

At the time the SED fitting was performed, there was some uncertainty as to the

distance of Serpens South, ranging from 225 $\pm$ 55 pc derived by Straizys et al. (2003) to the commonly adopted value of $260\,\mathrm{pc}$ (Gutermuth et al. 2008; Bontemps et al. 2010; Maury et al. 2011; Könyves et al. 2015) and the more recent suggestion that it is physically associated with Serpens Main at 415 $\pm$ 5 pc (Dzib et al. 2010). The most up-to-date measurement is now 436.0 $\pm$ 9.2 pc (Ortiz-León et al. 2017). While fitting the observations, we scale the model SEDs and discuss the results considering both distances of $260\,\mathrm{pc}$ and $430\,\mathrm{pc}$. The results of the SED fitting of these sources is in Fig. 3.26.

3.4.4.1 Aqu-MM2

For Aqu-MM2, the minimum χ^2 was 4.29 and three models fitted well from FHSC stage and second collapse. These were from the RHD2 model, were rotating quickly and had silicate grains of $a_{\mathrm{max}} = 10\,\mu\mathrm{m}$.

The optimum scale factor of the best fitting model was 4.1 from which we estimate the mass contribution to be $5\ \mathrm{M}_{\odot}$ at $260\,\mathrm{pc}$ or $15\ \mathrm{M}_{\odot}$ at $430\,\mathrm{pc}$. The $850\,\mu\mathrm{m}$ dust opacity was $3.9 \times 10^{-3}\,\mathrm{cm}^2\,\mathrm{g}^{-1}$. The best fitting model SEDs have been scaled beyond a factor of two which means the models are likely to be brighter at $70\,\mu\mathrm{m}$ than a similar source of a higher mass. Given that the scaled low-mass model SEDs were not quite able to fit the $70\,\mu\mathrm{m}$ point along with the other photometric observations, we are unable to place strong constraints on this source. However, it seems likely that Aqu-MM2 is at least as evolved as an FHSC and is rotating, therefore a resolved observation would be likely to show rotational structures.

An outflow has been observed at this source (Dunham et al. 2014) with a maximum velocity of $9\,\mathrm{km\,s}^{-1}$, which is faster than expected from an FHSC. It looks likely that Aqu-MM2 is more evolved than an FHSC and, if so, this demonstrates an overlap in the SED properties of some FHSCs and protostars.

3.4.4.2 SerpS-MM22

SerpS-MM22 is detected at all of the observed wavelengths and is brighter at $24\,\mu\mathrm{m}$ and $70\,\mu\mathrm{m}$ than the other sources even though the peak still appears to lie between $200\,\mu\mathrm{m}$ and $300\,\mu\mathrm{m}$, which suggests that it is unlikely to be an FHSC. The smallest χ^2 value was 4.02

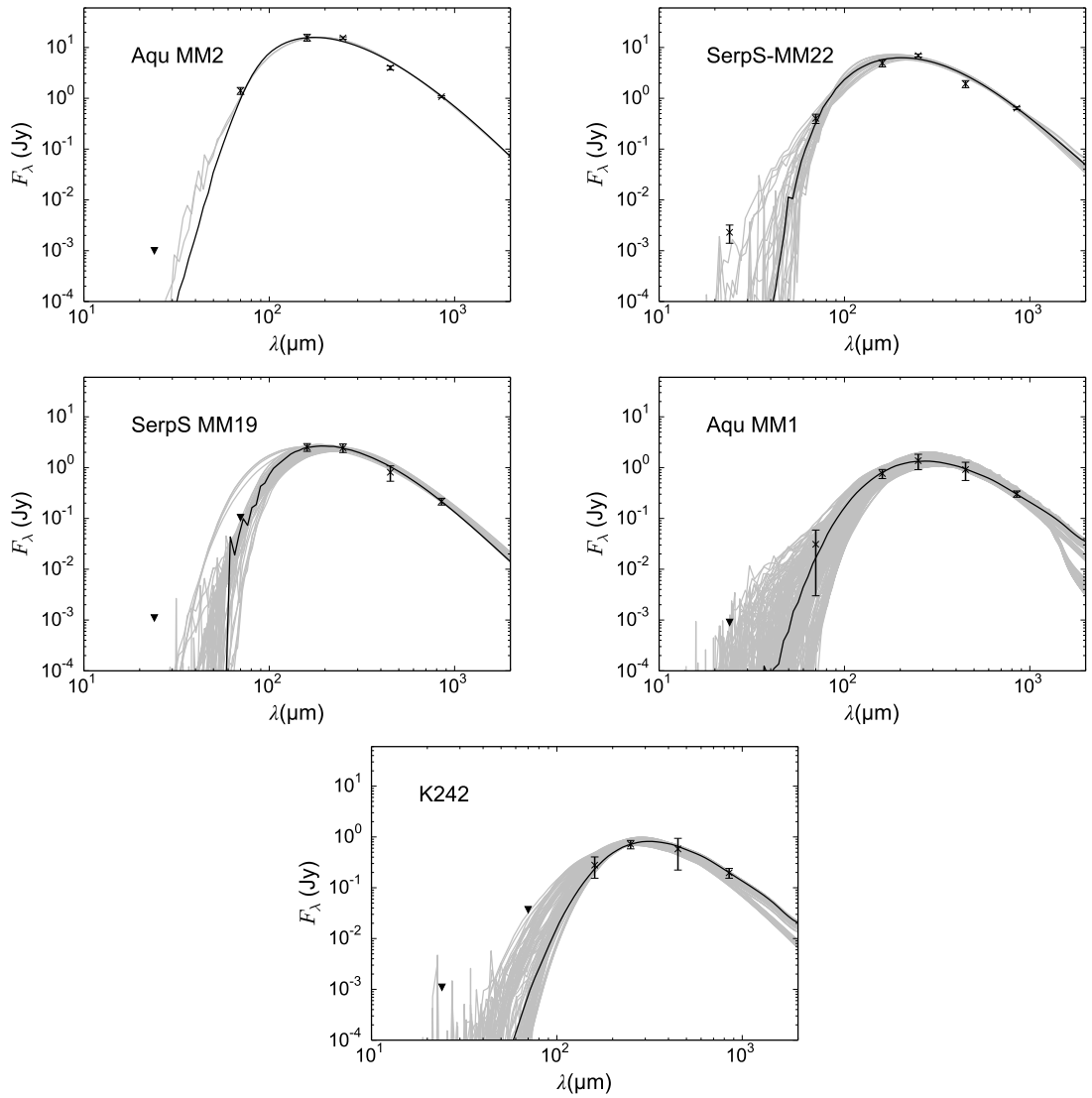

Figure 3.26: FHSC candidates from observations of the Serpens South region (see Appendix A of Young et al. (2018)); arrows denote upper limits. The best fitting model SEDs are plotted in black and the other model SEDs with $\chi^2 < \chi^2_{\rm min} + 1$ are plotted in grey. The best fitting model SEDs are: (Aqu-MM2) RHD2, $\beta = 0.05$, silicate grains, $a_{\rm max} = 10\,\mu$m, i =0°, early FHSC. (SerpS-MM22) RHD2, $\beta = 0.09$, carbon grains, $a_{\rm max} = 10\,\mu$m, i =0° FHSC. (SerpS-MM19) RHD2, $\beta = 0.0$, silicate grains, $a_{\rm max} = 10\,\mu$m, i =0° and late FHSC. (Aqu-MM1) RHD2, $\beta = 0.05$, carbon grains, $a_{\rm max} = 1\,\mu$m, i =90°, early FHSC. (K242) RHD1, $\beta = 0.01$, carbon grains, $a_{\rm max} = 1\,\mu$m, i =90°, early FHSC.

and 32 models fell within $\chi^2 < \chi^2_{\rm min} + 1$.

Since none of the models could replicate the broad shape of the SED of SerpS-MM22 and none came close to fitting the $24\,\mu{\rm m}$ flux it would not be meaningful to draw conclusions regarding the properties of the source. As expected, there was little consistency among the "best fitting" models, except that most were from RHD2 and all but one used grains of $a_{\rm max} < 100\,\mu{\rm m}$. Given the variation of properties among the best fitting models and the poor quality of the fits, we are not able to constrain the nature of this source, but it is likely to be at least as evolved as an FHSC, and may have a stellar core.

3.4.4.3 SerpS-MM19

SerpS-MM19 is undetected at $24\,\mu{\rm m}$ and $70\,\mu{\rm m}$ but the peak is between $150\,\mu{\rm m}$ and $200\,\mu{\rm m}$. This source is fitted reasonably well by our models with a minimum χ^2 of 0.19 and 66 model SED are defined as providing good fits. The optimum scale factor of the best fitting model is 1.2, which gives a mass of $1.3\ {\rm M}_\odot$ at $260\,{\rm pc}$ or $4.2\ {\rm M}_\odot$ at $430\,{\rm pc}$. The $850\,\mu{\rm m}$ dust opacity of this model was $4.0 \times 10^{-3}\,{\rm cm^2\,g^{-1}}$. All of the best fitting models are from the RHD2 model and used silicate dust grains with $a_{\rm max} = 1\,\mu{\rm m}$ or $a_{\rm max} = 10\,\mu{\rm m}$. The best fitting models favour a more slowly rotating core but there is no consistency for evolutionary stage or inclination.

3.4.4.4 Aqu-MM1

For Aqu-MM1 the minimum χ^2 value was 0.07 and 230 models fell within $\chi^2 < \chi^2_{\rm min} + 1$. This large number of models is probably due to the large uncertainty of the $70\,\mu{\rm m}$ point. With such a large number of models with similarly good fits, there is little consistency among the properties of the selected models and we are unable to place constraints on the nature of this source.

3.4.4.5 K242

For K242, the smallest χ^2 value was 0.01 and 119 models fitted well. There was a strong preference for the RHD1 model and for amorphous carbon grains. For all 119 models, $a_{\rm max} = 1\,\mu{\rm m}$ or $a_{\rm max} = 10\,\mu{\rm m}$. The optimum scale factor was 0.35 which gives a mass of

$<0.3\ \mathrm{M}_\odot$ at $260\,\mathrm{pc}$ or $0.9\ \mathrm{M}_\odot$ at $430\,\mathrm{pc}$. The $850\,\mu\mathrm{m}$ dust opacity was $1.3\,\mathrm{cm}^2\,\mathrm{g}^{-1}$. There was also a clear preference for models from the first collapse and FHSC stages, which indicates that this source is likely to be a FHSC in a low mass core.

3.4.5 Results of the SED fitting of PACS Bright Red sources

Five sources have been identified as extremely young Class 0 protostars from the set of PACS Bright Red sources found in the *Herschel* Orion Protostar Survey (HOPs, Stutz et al. 2013) and may be FHSCs. These sources lie at ~ 450 pc (Menten et al. 2007; Hirota et al. 2007; Sandstrom et al. 2007) in the Orion molecular clouds and for more detail see Section 1.6.7. The SEDs were taken from the HOPS data set from the Infrared Science Archive [2] (Furlan et al. 2016). We use the HOPs identifiers below and the corresponding identifiers from Stutz et al. (2013) are also given in brackets. The observed SEDs and the best fitting model SEDs are shown in Fig. 3.27.

3.4.5.1 HOPS 398 (082005)

The minimum χ^2 value was 0.1 and 13 models are considered good fits. These had a scale factor of 5.0 which suggests a core mass of 18 $\mathrm{M}_\odot$ at a distance of 420 pc. This is outside the range for which the fitting is reliable so these results are only tentative. All selected model SEDs were taken from the FHSC phase or later and most used silicate dust grains of $a_{\mathrm{max}} = 10\,\mu\mathrm{m}$.

3.4.5.2 HOPS 399 (082012)

The minimum χ^2 was 3.9 and the next lowest χ^2 was 31.6. It is apparent that this best fitting model SEDs is unable to fit all of the observed fluxes. The scale factor of the best fitting model was 6.0, corresponding to a mass of 22 $\mathrm{M}_\odot$ which is also outside of the range studied. The best fitting model is fast rotating FHSC at low inclination. This source is much brighter than a core containing an FHSC is expected to be. In addition, none of the model FHSC SEDs fitted well which indicates that HOPS 399 is likely to be more evolved.

A fast outflow of $> 10\ \mathrm{km\,s}^{-1}$ has been discovered at HOPS 399 (Tobin et al. 2016b) and is thought to have an inclination of $50°$, which is less than the value of $76°$ obtained

2. http://irsa.ipac.caltech.edu/data/Herschel/HOPS/overview.html

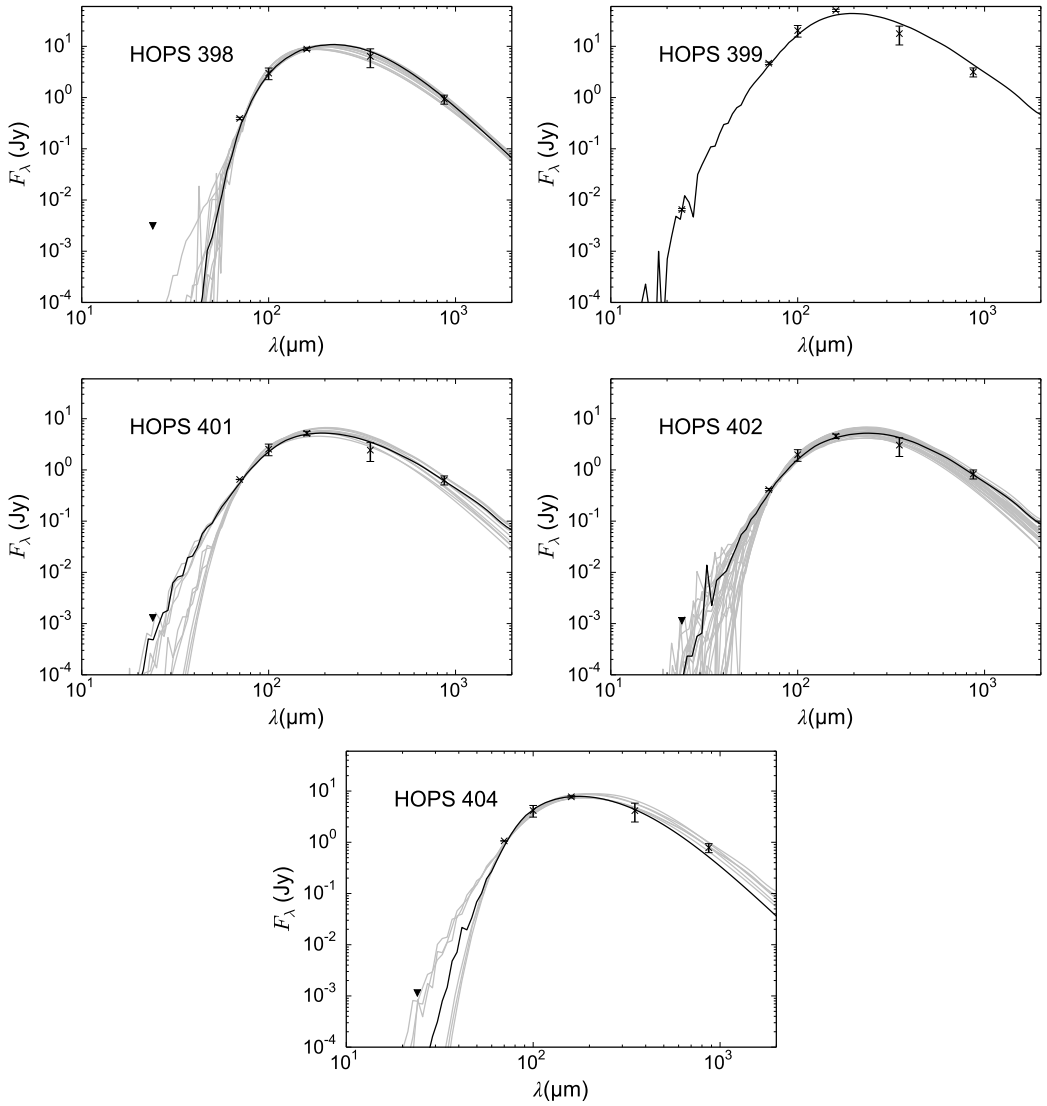

Figure 3.27: Best fitting model SEDs for the five "extreme class 0" HOPS sources (Stutz et al. 2013). These SEDs were constructed using photometry from Furlan et al. (2016). Arrows denote upper limits and the best–fitting models were plotted in black.

from the SED fitting of Furlan et al. (2016). With this inclination, the extinction caused by the disc will be less than previously thought suggesting the source could be fainter and younger. We can rule out the possibility that it is younger because of the presence of a fast outflow so perhaps HOPS 399 is particularly deeply embedded. The detection of this extended outflow confirms the results of our SED fitting which suggested that HOPS 399 is more evolved than an FHSC. Tobin et al. (2015a) found the visibility profile of HOPS 399 to be consistent with that of a more evolved protostar with a disc which further supports the decision to rule it out as a FHSC candidate.

3.4.5.3 HOPS 401 (091015)

HOPS 401 was fitted well by 11 model SEDs from late FHSC and second collapse phases with moderate rotation ($\beta = 0.01$–0.05) and inclination $\leq 45°$. All models used dust grains with $a_{\rm max} = 1\,\mu{\rm m}$ or $a_{\rm max} = 10\,\mu{\rm m}$. The minimum χ^2 was 0.22 and the scale factor was 0.8 which gives an approximate core mass of 1.3 $M_\odot$, which is well within the range for producing robust results. HOPS 401 is therefore a fair FHSC candidate.

3.4.5.4 HOPS 402 (091016)

HOPS 402 was fitted well by 31 model SEDs and the minimum χ^2 was 0.21. There is a clear preference for a moderate rotation rate with nearly half of these selected models taken from the $\beta = 0.05$ model. All the selected models used grains with $a_{\rm max} = 1\,\mu{\rm m}$ or $a_{\rm max} = 10\,\mu{\rm m}$ and most were from late FHSC or second collapse stages. The scale factor of 1.0 corresponds to a core mass of 3.3 $M_\odot$. This mass is $> 2\ M_\odot$ and is therefore beyond the upper limit for which the fitting is robust so we only tentatively suggest that HOPS 402 may be a FHSC with moderate rotation but could also be slightly more evolved.

3.4.5.5 HOPS 404 (097002)

HOPS 404 was also fitted well by 7 model SEDs and had a minimum χ^2 value of 0.37. These all have moderate rotation rates with $\beta = 0.01$ or $\beta = 0.05$ and an inclination of $0°$ or $45°$. The selected models have silicate or amorphous carbon dust grains with maximum size $10\,\mu{\rm m}$ or $1\,\mu{\rm m}$. Most models are from late FHSC stage but two were from the second collapse stage. The scale factors of the best fitting models vary from 1.04 to 3.85 which

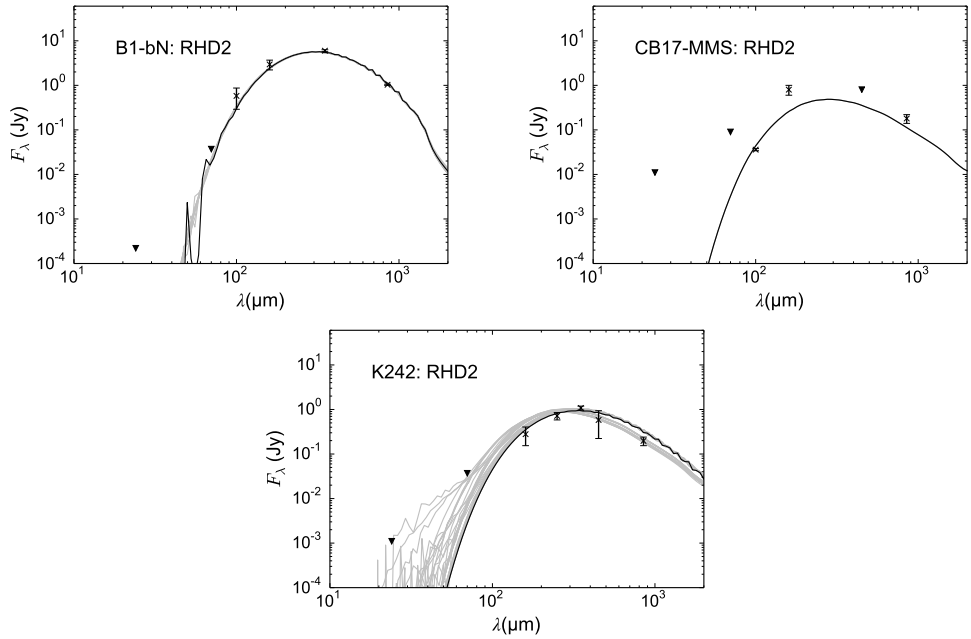

Figure 3.28: SEDs of selected FHSC candidates fitted exclusively with RHD2 model SEDs. Arrows denote upper limits and the best–fitting models are plotted in black.

correspond to a core mass of 3.4 to 14 $M_\odot$. The fitting indicates that HOPS 404 may be a FHSC but the estimated mass is above the range for which the fitting is robust so this result should be treated with caution.

3.4.6 Fitting with RHD2 SEDs only

The sources B1-bN, CB17-MMS and K242, were fitted best by RHD1 SEDs so we tried performing the fitting again using only the RHD2 SEDs to see if it was possible to obtain a good fit from the more physical model. These results are presented in Fig. 3.28.

We were not able to obtain a good fit for CB17-MMS with only RHD2 model SEDs because the SEDs were too "warm": a lower envelope temperature is required to reproduce the position of the SED peak and submillimetre brightness. B1-bN was only fitted well by RHD2 SEDs with a maximum grain size of $200\,\mu\mathrm{m}$, which is probably unrealistic. For K242 we obtained reasonable fits with RHD2 SEDs. The properties derived from this fitting are very similar to those from the RHD1 fits except that the RHD2 fits require the source to be younger. For such young objects, the heating of the envelope by the ISRF has a significant effect on the submillimetre flux and is likely to cause variation between the SEDs of similar sources in different environments.

3.5 Discussion

We have performed 3-D RHD simulations of the collapse of pre-stellar cores with a range of properties and then modelled the SEDs of these FHSCs and their envelopes using a radiative transfer code. The properties of the FHSCs themselves are very similar, the only real variation being in the increase in radius and oblateness with rotation. These simulations have shown that differences in the core properties lead to variations in the SED and that these variations are due to differences in the temperature structure and morphology of the collapsing envelope rather than the FHSC itself.

Many properties have similar effects on the SED, for example a higher mass, lower ISRF exposure, slower rotation and higher inclination all lead to a steeper drop in flux in the far-infrared. Differences in the initial rotation rate and core radius (with a constant mass and Bonnor-Ebert density profile) gave rise to the greatest SED variation. Many factors have a significant effect on the SED but only models with faster rotation can produce detectable flux at $24\,\mu\mathrm{m}$. This may be a property that can be constrained with the SED and can also be verified through molecular line observations. We find a shift of the SED peak to shorter wavelengths and an increase in far infrared flux as the FHSC evolves, which is consistent with the findings of others, including Omukai (2007) and Tomida et al. 2010a. We also find, however, this effect is considerably reduced by a higher initial temperature or a larger initial radius, to the extent that for $T_{\mathrm{init}} = 15\,\mathrm{K}$ or $r_{\mathrm{init}} = 1.5 \times 10^{17}\,\mathrm{cm}$ (10 000 AU) there is no SED evolution.

Boss and Yorke (1995) simulated SEDs based on the hydrodynamical calculations of Boss (1993). These are 3-D models of the collapse of dense core with a maximum radius of $50\,\mathrm{AU}$ with a resolution of $1\,\mathrm{AU}$. The maximum temperature at the time for which the SED is calculated is $\sim$190 K. A two–component grain model was used, comprising refractory species (silicates and graphites) and ices and the distance was assumed to be $100\,\mathrm{pc}$. The SED features a "warm shoulder" shortwards of $100\,\mu\mathrm{m}$ in the face-on direction, due to the warm FHSC. We do not find this warm shoulder in the SEDs in this paper and the SEDs of Boss and Yorke (1995) are also more sharply peaked. Their simulations only extend to $50\,\mathrm{AU}$ therefore there will be significant flux missing at all wavelengths (see the radial intensity profiles in Fig. 3.5). The SED is more sharply peaked because there

is less emission from the cold envelope. This also results in a relatively brighter SED at $\lambda < 100\,\mu\mathrm{m}$. With a much smaller envelope, there is far less extinction of the warm core. This results, again, in a brighter SED at short wavelengths.

The protostellar SEDs of Young and Evans (2005) were calculated from analytical models of a protostar, disc and envelope. The FHSC initially has a radius of 5 AU and its radius is decreased over a 100 year period until it has a radius of 3 $\mathrm{R}_{\odot}$ representing the protostar. The disc is only present after the protostar (effectively, the second core) has formed. This model cannot take into account the subtleties of the small–scale structures as well as our SPH model does. In particular, the disc structure forms early on and obscures the FHSC. Only the first panel in Fig. 8 of Young and Evans (2005) corresponds to the FHSC phase and this SED peaks at $\sim 250\,\mu\mathrm{m}$. After this, there is predicted to be detectable emission from the protostar at 1–10 $\mu\mathrm{m}$. The assumed distance here was $140\,\mathrm{pc}$ as opposed to our distance of $260\,\mathrm{pc}$, which will cause the SEDs to be brighter. During the second collapse, the stellar core forms in the centre of the former FHSC so it is not realistic to simply model the formation of the stellar core as a shrinking FHSC because much of the former FHSC will be left behind. It is therefore likely that these models underestimate the extinction of the flux emitted by the FHSC and the newly formed stellar core, which is still deeply embedded in the remnants of the FHSC before the disc forms.

In Section 3.3.7 we described how changing the maximum dust grain size shifted the SED peak by up to $200\,\mu\mathrm{m}$ and can cause the object to appear nearly an order of magnitude brighter at submillimetre wavelengths. The choice of dust grain model can therefore have a significant impact on SED modelling. We chose to include models with very large grains in our selection for fitting to observations because it appears to be the only way to reproduce both the $70\,\mu\mathrm{m}$ flux and a peak at $\lambda > 200\,\mu\mathrm{m}$ that we see in several observations of FHSC candidates. There is evidence for dust grains in dense molecular cores with $a_{\mathrm{max}} > 1.5\,\mu\mathrm{m}$ from coreshine observations (Steinacker et al. 2015), of micron sized grains in the ISM from detectors on solar system spacecraft (e.g. Gruen et al. 1994; Sterken et al. 2014) and of $\sim 40\,\mu\mathrm{m}$ sized Earth–impacting meteoroids (e.g. Baggaley 2000). Ormel et al. (2009) suggests that if molecular cloud lifetimes are lengthened by long–term support mechanisms, dust aggregates of $\sim 100\,\mu\mathrm{m}$ may be produced. From measurements of the

spectral index of the millimetre dust opacity, Ricci et al. (2010) also argue that millimetre–sized grains may already exist in class 0 YSOs so it is perhaps not unreasonable to expect grain sizes of over $10\,\mu\mathrm{m}$ in pre-stellar cores although we note that there are also proto-stellar cores for which there is no evidence of grain growth (e.g. I-Hsiu Li et al. 2017). The sources that were fitted best by our model SEDs, except Per-Bolo 58, were fitted well exclusively by models with $a_{\max} = 1\,\mu\mathrm{m}$ or $a_{\max} = 10\,\mu\mathrm{m}$, possibly indicating that the remainder would be better fitted by models with a different combination of other parameters rather than with very large grains. The alternative is that sources best fit by models with large grains are more evolved but embedded objects. Indeed, the SEDs of Per-Bolo 58 and Cha-MMS1 appear similar to the SEDs of more evolved objects, most likely accreting stellar cores, as shown by Young and Evans (2005) and Dunham et al. (2010).

We set out to ascertain whether an SED is useful for constraining the nature of these sources by fitting the model SEDs to observations. We note that the set of models covers a limited range of parameters: for example, we show in 3.4.2 that these models are less likely to be valid for sources outside a mass range of $0.5 \lesssim M \lesssim 2\ \mathrm{M}_{\odot}$ and we only use an initial radius of $7 \times 10^{16}\,\mathrm{cm}$. We note that some of the χ^2 values are very small because there are a large number of free parameters compared to the number of data points and many of the data points have large error bars or are only upper limits. This does not, however, present a problem because we use the χ^2 values to compare the relative quality of fits of different model SEDs to the data rather than performing formal χ^2 fitting. Despite similarities in the SEDs of some models, such as between inclined, rotating FHSCs and young cores in first collapse phase, we find it is possible to constrain the nature of the sources in some cases. Some sources are better constrained than others. None of our model SEDs fitted Aqu-MM2 and SerpS-MM22 well. These sources are more luminous than the other Serpens South candidates and, even at the close distance, the models required scaling beyond the range of masses for which the SEDs are valid. It is possible that these sources could be fitted by using a combination of parameters we have not considered here, such as a different radius, greater mass and a fast rotation rate. It is more likely, however, that Aqu-MM2 and SerpS-MM22 are more evolved young protostars, especially given the bolometric luminosities of 0.95 $\mathrm{L}_{\odot}$ and 0.2 $\mathrm{L}_{\odot}$ (Maury et al. 2011). The estimated masses of the PBRs were nearly all $> 2\ \mathrm{M}_{\odot}$, higher than the range of masses considered here,

and only HOPS 401 remains a strong FHSC candidate based on this SED fitting since its best–fitting models are exclusively from the FHSC phase and its mass is estimated to be $\approx 1.3\ \mathrm{M}_{\odot}$.

The results of fitting models for K242 and HOPS 401 provided some insight into their nature because there was a high level of consistency among the properties of the best fitting models. Interestingly, where there was a strong preference for models from the early FHSC phase, no models were selected for the earlier first collapse stage, suggesting that these two stages are observationally distinguishable. After first collapse the $160\ \mu\mathrm{m}$ flux rises quickly relative to the longer wavelengths and the peak shifts. The cold, dim first collapse SEDs could not be reproduced by a more evolved object, even at high inclination, meaning that it does seem possible to differentiate between empty "starless" cores and cores containing an FHSC. Similarly, Commerçon et al. (2012a) suggest that a starless cores and an FHSC are distinguishable at far-infrared wavelengths. CB17-MMS was fitted by both first collapse SEDs and SEDs from more evolved cores at high inclination, so there is some level of degeneracy between those parameters. However, we can see from Fig. 3.25 that none of the models is able to fit the $160\ \mu\mathrm{m}$ flux and the other data points concurrently and the location of the SED peak is not well constrained. This is likely to explain the spread of best fitting models, since the location of the peak is different for very young pre-stellar cores and more evolved cores at high inclination.

On the other hand, it is more difficult to distinguish between an FHSC and more evolved object observationally. Where the SED fitting shows a strong preference for the late FHSC stage, for example HOPS 401, second collapse SEDs also provide good fits. Differences in the SED are caused by changes in the temperature structure and opacity of the envelope and infalling material. These changes are more significant between first collapse and FHSC formation as the object transitions from the isothermal to adiabatic phase. Second collapse takes place far quicker than the first and, although the temperature rises quickly, it does so primarily within the radius of the FHSC. The SED only allows observers to probe down to the region surrounding the FHSC. This region is slow to heat and so there are unlikely to be significant differences between the SEDs of the FHSC, second collapse and early stellar core phases.

Aqu-MM1 and K242 were well fitted by model FHSC SEDs and had correspondingly low χ^2 values. More than 200 models provided good fits for Aqu-MM1 and, consequently, there was no consistency among them. Even though it is not possible to further constrain the properties of this source it remains a good FHSC candidates. In such cases, this SED fitting is useful for indicating which sources are promising FHSC candidates and which can be rejected. The dust grain size distribution strongly affects the shape of the SED. Because of this, maximum grain size was perhaps the most consistently fitted property. Models with $a_{\rm max} > 10\,\mu{\rm m}$ were only among the best fitting models for Per-Bolo 58 and Cha-MMS 1. This supports the idea that large dust grains are unlikely to be present in the envelopes of pre–stellar cores. It is possible that grain growth is occurring in Per-Bolo 58 and Cha-MMS 1 or both sources could be more evolved objects.

Omukai (2007) suggests that the optical depth is reduced enough in the vertical direction of a rotating core that FHSC radiation may be visible at low inclinations. However, like Saigo and Tomisaka (2011), we find that the FHSC heats the region immediately surrounding it and that it is from this region that most of the observed radiation is emitted. Even for a core with a higher rotation rate viewed face-on the FHSC is unlikely to be directly visible at wavelengths $< 850\,\mu{\rm m}$.

Currently, a detection at $70\,\mu{\rm m}$ is used to distinguish protostellar (class 0) sources from starless cores after radiative transfer modelling showed that the $70\,\mu{\rm m}$ flux is proportional to the internal luminosity (Dunham et al. 2008) and from previous attempts to model FHSC SEDs. With a realistic density structure, we find that the FHSC is obscured which significantly reduces the $70\,\mu{\rm m}$ flux (see also Saigo and Tomisaka 2011; Commerçon et al. 2012a). The $70\,\mu{\rm m}$ flux is highly dependent upon the structure of the centre of the core and the extent of the envelope. With a photometric sensitivity of a few ${\rm mJy}$ at $70\,\mu{\rm m}$, *Herschel* may be able to detect some FHSCs, depending on the geometry of the FHSC and its envelope but others will be too faint.

RHD2 includes a more physical treatment of radiation than RHD1 and we do see a strong preference for SEDs produced from the RHD2 model in the SED fitting, which indicates that the more realistic temperature structure provides a better fit to observations. Only three of the FHSC candidates here, B1-bN, CB17-MMS and K242, were fitted best

by RHD1 SEDs and these are the only sources to have SED peaks at $\lambda > 250\,\mu\mathrm{m}$. The SEDs produced from RHD2 models all peaked at shorter wavelengths than this, except when large dust grains were used, due to heating from the ISRF. We attempted to fit these three sources with only RHD2 SEDs but were only able to obtain a good fit for K242. It is interesting to note that K242 appears to lie outside the main filament (see Fig. A1 of Young et al. (2018)), which means the ISRF and extinction could be different for this source. When the incident ISRF was reduced, the SED peaked at a longer wavelength. This suggests that the preference for RHD1 SEDs could simply be due to local differences in the ISRF and we have not included model SEDs of cores with different levels of exposure to the ISRF in the fitting procedure. It should be possible to distinguish a more evolved core with an initially low temperature from a less evolved core with an initially higher temperature because the temperature structure will be different, as shown in Section 3.3.2. When the FHSC forms, the temperature in much of the envelope remains unchanged. The emission from the inner envelope, which makes a significant contribution to the SED, from the more evolved core will still be less bright than from the same region of the less evolved but initially warmer core for most of the lifetime of the FHSC, leading to a difference in the shape of the SED.

Finally, the selection of the best fitting SEDs is sensitive to small differences in the observed fluxes. Consequently, any errors in the observation could lead to a different interpretation of the properties of the core, although these are not expected to affect the possibility of distinguishing starless cores and FHSCs.

3.6 Conclusion

We have produced RHD simulations of the collapse of pre-stellar cores with different initial properties. Snapshots from these models at the key stages of FHSC formation and evolution were then used to simulate SEDs using a 3D radiative transfer code. We compared the SEDs of cores at different stages in their evolution and of cores with different properties. Secondly, we fitted the observed SEDs of several FHSC candidates with model SEDs from a set of 1440.

Differences in the temperature structure of the core affect the shape of the SED even

though the FHSC itself is not observable directly at wavelengths $< 850\,\mu\mathrm{m}$. Most notably, fast rotation leads to significant flux at $24\,\mu\mathrm{m}$ during FHSC phase and so FHSC candidates with observed flux at this wavelength should not necessarily be ruled out. If the core is initially warmer (e.g. $15\,\mathrm{K}$) or initially less compact (e.g. $r_{\mathrm{ini}} = 1.5 \times 10^{17}\,\mathrm{cm}$) we find no evolution of the SED as the core evolves, which means a younger core could appear more evolved.

Some of the FHSC candidates were fitted well by just a small number of model SEDs with consistent properties, which allowed us to make suggestions as to their nature. We found that the SED may be used to distinguish between cores undergoing first collapse and cores containing an FHSC but not between the FHSC and second collapse stages. Although FHSC SEDs may appear featureless, they can nonetheless be useful in characterising sources and ruling out candidates that are probably more evolved.

Of the FHSC candidates that we have fitted with model SEDs, B1-bN, CB17-MMS, Aqu-MM1, K242 and HOPS 401 are most likely to be FHSCs. Aqu-MM2 is likely to be rotating and at a low inclination. SerpS-MM19 may be more evolved than an FHSC but is probably rotating moderately quickly and oriented at a high inclination. Aqu-MM1 is also likely to have a high rotation rate and to have an edge-on inclination and CB17-MMS could be an FHSC embedded in an edge-on disc. From our results, we consider Chamaeleon-MMS1 and Per-Bolo 58 to be more evolved and they have probably undergone stellar core formation.

Chapter 4

Synthetic molecular line observations of the first hydrostatic core from chemical calculations

This chapter, except for Sections 4.3.2 and 4.5.5, form the basis of the paper 'Synthetic molecular line observations of the first hydrostatic core from chemical calculations' (Young et al., 2019, MNRAS, 487, 2853–2873).

4.1 Introduction

In Chapter 3 we showed that SED fitting can shed light on the likely nature of FHSC candidates and is useful for indicating which sources warrant further observation in the search for the FHSC. Nevertheless, we still require spatially resolved observations and kinematic data for further insight into the evolutionary stage of these objects. In this chapter we simulate molecular line observations of the FHSC from hydrodynamical models with the aim of predicting distinguishing characteristics of the FHSC stage that may be inferred from high resolution observations, in particular with ALMA.

Modelling molecular line emission requires some assumption of the chemical abundance of the species in question. It is inaccurate to assume a constant abundance because

many species are significantly depleted in pre–stellar cores due to high rates of freeze–out at the high densities and low temperatures. One better alternative would be to use a "drop model", for which the abundance is assumed to be constant except in regions where the temperature and density are within a specified range, in which case a lower "depleted" abundance is used. This approach works well for simple structures like analytical disc models but the temperature and density structures that develop as the FHSC forms and evolves are more complex. The depletion is also time–dependent, which is not accounted for with a drop model. Furthermore, abundances of species like HCO^+ depend upon chemical reactions and the availability of reactants rather than upon the temperature and density directly. For these reasons, we opt to model the chemical evolution and use the calculated chemical abundances to model spectral lines.

Here we first outline the choice of hydrodynamical models, the implementation of the chemical model and the radiative transfer calculations used to produce synthetic molecular line observations. We then present the results of the chemical modelling and the synthetic observations, which we compare with observations and with previous theoretical work.

4.2 Hydrodynamical models

There are several steps involved with simulating molecular line observations. First, we run R(M)HD models of the FHSC formation and evolution. Second, we post–process these hydrodynamical models to calculate the chemical abundances for each position throughout the simulation to obtain pseudo–time–dependent chemistry. Third, we select snapshots from the hydrodynamical + chemical models and use the physical conditions and chemical abundances for the frequency–dependent radiative transfer calculations, which produce the spectral cubes. We then process the data cubes to produce spectra and moment maps. CASA was used to simulate ALMA observations.

Two key types of structure associated with the FHSC are nonaxisymmetric disc structures (e.g. spiral arms) and outflows. Magnetic fields are required to drive outflows (e.g. Bate et al. 2014; Lewis et al. 2015) but the magnetic braking effect of ideal MHD sup-

presses the formation of rotational structures (e.g. Bate et al. 2014). For this reason we performed two simulations: firstly a radiation hydrodynamical model, which we will refer to as the RHD model, to examine rotational structures and secondly a radiation magnetohydrodynamical model, which we will refer to as the MHD model, to simulate observations of the outflow.

Both simulations start with a dense core that is modelled as a 1 $M_\odot$ Bonnor-Ebert sphere of radius $7 \times 10^{16}\,\mathrm{cm}$ ($\sim 4700\,\mathrm{AU}$), central density $8.34 \times 10^{-18}\,\mathrm{g\,cm^{-3}}$ using 3.5×10^6 SPH particles. The density contrast between the central and outer regions of the core was 15.1.

For the RHD model an initial uniform rotation of $\Omega = 2.02 \times 10^{-13}$ rad s^{-1} was used, which gives a rotational to gravitational energy ratio $\beta = 0.02$, to produce an FHSC with non-axisymmetric features.

For the MHD model, we place the Bonnor-Ebert sphere in a warm, low density, cubic ambient medium of side length $2.8 \times 10^{17}\,\mathrm{cm}$. The ratio of the density of the outer regions of the core and the ambient medium (the box) was 30:1, similar to the models of Bate et al. (2014). The initial mass–to–flux ratio is $\mu = 5$, $\Omega = 3.44 \times 10^{-13}$ rad s^{-1} and $\beta = 0.05$. An outflow is launched from the FHSC and this extends to $\sim 150\,\mathrm{AU}$ by the time the stellar core forms.

4.3 Chemical modelling

4.3.1 Method and initial conditions

Chemistry calculations were performed using KROME (Grassi et al. 2014), as described in Section 2.5. We include gas–phase and gas–grain reaction. Adsorption and desorption reactions are included by considering the frozen–out species as separate species with their own abundances.

We calculate the chemical abundances by post–processing the SPH simulations. The total mass density, gas temperature, dust temperature and extinction for each particle are provided by the SPH calculation for each timestep. KROME is called for each SPH particle

Table 4.1: Elemental abundances used for the calculation of initial ISM abundances. These were mostly taken from Reboussin et al. (2014) and references therein and are very similar to the initial abundances of Hincelin et al. (2016) except for S^+. We use the higher S^+ abundance from the latter work. a) Wakelam and Herbst (2008), b) Jenkins (2009), c) Hincelin et al. (2011) d) Graedel et al. (1982).

Element	Abundance (n_j/n_H)
H_2	0.5
He	9×10^{-2} a
N	6.2×10^{-5} b
O	1.4×10^{-4} c
C^+	1.7×10^{-4} b
S^+	8×10^{-8} d
Si^+	8×10^{-9} d
Fe^+	3×10^{-9} d
Na^+	2×10^{-9} d
Mg^+	7×10^{-9} d
P^+	2×10^{-10} d
Cl^+	1×10^{-9} d

and the chemistry is evolved for a time equal to the difference between the current and previous hydrodynamical outputs.

First we calculate the chemical evolution for dense, cold ISM conditions: $T = 10\,\mathrm{K}$, $\rho = 4 \times 10^{-18}\,\mathrm{g\,cm^{-3}}$ ($n_{H2} = 10^6$ cm^{-3}), $A_v = 20$ and cosmic ray ionisation rate $\zeta = 1.3 \times 10^{-17}\,\mathrm{s^{-1}}$. The elemental abundances given in Table 4.1 which were taken from Reboussin et al. (2014) and Hincelin et al. (2016). The dust grain abundance is calculated assuming a dust-to-gas ratio of 0.01 and that all dust grains have a negative charge initially. The initial electron abundance is found from the difference between the number density of cations and that of negatively charged grains such that the gas and dust have no net charge.

The chemical abundances were evolved under the above conditions and most closely matched those observed in the dense cores TMC-1 and L134N (Agúndez and Wakelam 2013) at $t = 1.2 \times 10^5$ years. These abundances are therefore taken as the initial values and assigned to every SPH particle in the simulated dense core. Next, the chemistry was evolved for each particle in the initial Bonnor-Ebert sphere under their individual density, temperature and extinction values for $60\,000$ years, which is approximately the free–fall time of the core, to calculate the initial chemical abundances throughout the simulated dense core.

From this point, the new values of ρ, $T_{\rm gas}$, $T_{\rm dust}$ and A_v are provided by the SPH model for the next timestep and the chemical abundances calculated for the time between the current and previous timesteps. For the first $\sim 30\,000$ years, during the first collapse, the physical conditions change slowly so it is unnecessary to calculate chemical abundances after every hydrodynamical timestep. After each chemistry timestep, the next minimum chemistry timestep is set relative to the local free-fall time: $\delta t = \frac{1}{3} t_{\rm ff}$, where $t_{\rm ff} = \sqrt{3\pi/32G\rho}$. The chemistry timesteps therefore decrease as the maximum density increases. During the first collapse stage the chemistry timestep decreases from $\delta t \approx 8000$ years to a few hundred years. During FHSC phase, the chemistry timestep is $\sim$20–80 years.

We note that the very centre of the core is $\sim 7\,{\rm K}$ initially which means that the network was extrapolated below its minimum temperature of $10\,{\rm K}$. In the central regions of the core the visual extinction of the ISRF becomes very large so a cap of $A_v = 86$ is implemented. This leads to effectively zero rates for reactions driven by UV photons for these regions.

4.3.2 Timestepping

The initial dense core is modelled as a Bonnor–Ebert sphere heated by the ISRF. The density, temperature and visual extinction throughout the core differ from the values used to calculate the initial chemical abundances so the chemistry should be allowed to evolve for the initial dense core conditions for some time before the collapse commences. This is in addition to the time of 120 kyr for which the chemistry in was evolved in 0-D under fixed dense ISM conditions for producing initial abundances to assign to particles in the initial dense core.

The formation mechanism and lifetime of dense cores is uncertain so it is not clear how long the chemistry should be evolved for in the dense core before it collapses. Previous similar work has assumed various values for this initial chemistry timestep. For example, the initial dense core used by Hincelin et al. (2016) has a uniform density ($3.97 \times 10^{-18}\,{\rm g\,cm^{-3}}$) and temperature (11 K) and the chemistry is initially evolved for 600 kyr; Dzyurkevich et al. (2016) evolved the chemistry for a total time of 600 kyr; Furuya

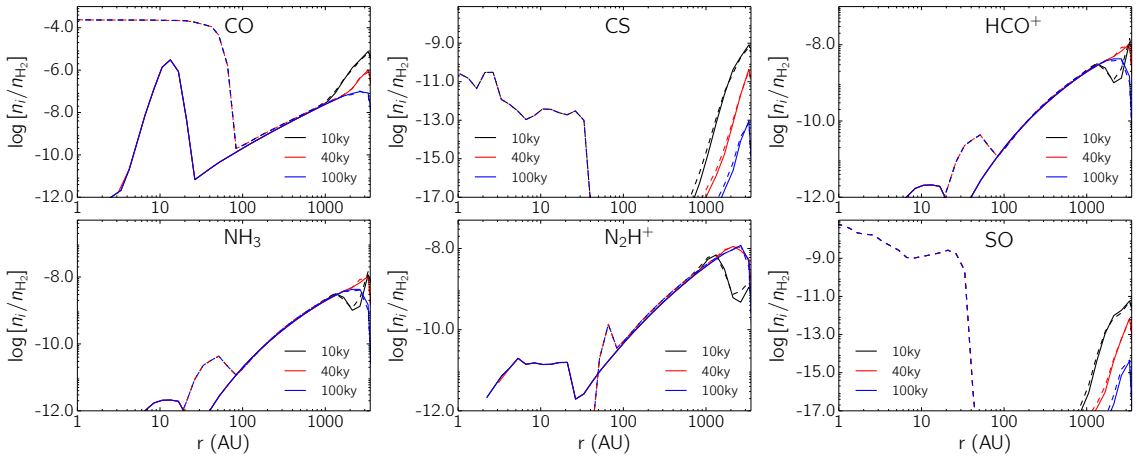

Figure 4.1: Abundance profiles of selected species for 30 550 years (solid lines) and 33 540 years (dashed lines) after the onset of the cloud collapse (central density $10^{-12}\,\mathrm{g\,cm^{-3}}$ and $5 \times 10^{-11}\,\mathrm{g\,cm^{-3}}$) after the chemistry has been allowed to evolve under the initial conditions for 10 kyr (black lines), 40 kyr (red lines) and 100 kyr (blue lines).

et al. (2012) evolve the chemistry in 0-D for 100 kyr then for a further 160 kyr in the core (which is the sound crossing time of the core); van Weeren et al. (2009) also evolve the chemistry in 0-D for 100 kyr but then for 300 kyr in core; and Aikawa et al. (2008) evolved the chemistry for 10^6 years in the core.

As explained earlier in Section 4.3.1, we first evolve the chemistry in 0-D for 1.2×10^5 years, at which time it best matched abundances measured observationally for two dense cores. To assess the most representative length of this initial chemical timestep we modelled the evolution of the chemical abundances from low resolution SPH models with initial chemical timesteps of 10, 40 and 100 kyr. These were $1\,\mathrm{M}_\odot$ Bonnor-Ebert clouds with an initial rotation rate corresponding to $\beta = 0.05$.

Fig. 4.1 shows the abundance profiles for six selected species for 30 550 years after the onset of collapse ($\rho_{\mathrm{cen}} = 10^{-12}\,\mathrm{g\,cm^{-3}}$, just before FHSC formation) and for 33 540 years after the onset of collapse ($\rho_{\mathrm{cen}} = 5 \times 10^{-11}\,\mathrm{g\,cm^{-3}}$, during the FHSC stage) for the three different initial chemistry timesteps. We can see that the abundances of the low density gas tracers HCO^+, NH_3 and N_2H^+ are identical at $r < 1000$ AU , which indicates that the initial chemistry timestep, or age of the core, is less important for these on the scale of the FHSC structures. However, the difference in abundances of HCO^+, NH_3 and N_2H^+ due to the age of the core will become significant for observations that are sensitive to emission on larger scales. The abundance of CO is identical out to a radius of 1000 AU,

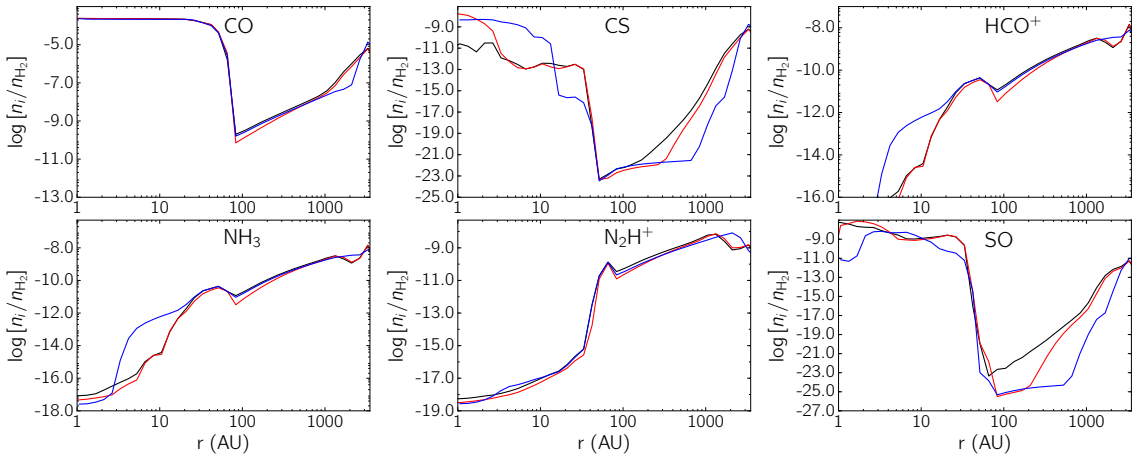

Figure 4.2: Abundance profiles of selected species after 33 540 years after the onset of cloud collapse (central density $5 \times 10^{-11}\,\mathrm{g\,cm^{-3}}$) after evolving the chemistry for every hydrodynamical timestep (black), evolving the chemistry for a maximum timestep of $\delta t = \frac{1}{3} t_{\mathrm{ff}}$ (red) and evolving the chemistry for this timestep only (blue). See text for further explanation.

beyond which we see that there is more CO in the gas phase for cores with shorter initial chemistry timesteps since there has been less time for the CO to freeze out. For CS and SO, the dense gas tracers, there is some difference in abundances for $r \gtrsim 100$ AU with abundances in the infalling envelope being higher for shorter initial chemistry timesteps, even after FHSC formation.

Within the FHSC itself the temperature quickly exceeds 100 K and the desorption timescales become extremely short so the extent to which species are initially frozen out becomes insignificant and the abundances do not depend on the initial timestep. The regions of the envelope where there is some difference in abundances are 10-100 times less dense that the outer regions of the FHSC and the CS abundances are more than four orders of magnitude lower than in the FHSC and more than six for SO. The differences in abundance due to the initial chemistry timestep are therefore insignificant compared to the abundances in the much denser regions near the FHSC, which is where most of the observable emission from the these species originates. The choice of initial chemistry timestep appears, therefore, to matter little when calculating chemical abundances from which to simulate observations. We finally choose to evolve the chemistry for 60 000 years in the initial core because this is approximately its free–fall time.

In Chapter 2.5.3 we discussed how it is not always necessary to evolve the chemistry for every hydrodynamical timestep. In Fig. 4.2 we show the difference in abundance

profiles during the FHSC stage after evolving the chemistry with different timesteps for a total of $33\,540$ years after the onset of collapse. First, we evolve the chemistry for every hydrodynamical output file which gives a maximum timestep of 5660 years early in collapse and a minimum of 22 years after FHSC formation. Secondly we set the minimum chemistry timestep relative to the local free–fall time, which gives chemistry timesteps of 8500 years during the first collapse and 22 years after FHSC formation when every hydrodynamical output is used. Finally we evolve the chemistry for an equivalent length of time for just the snapshot taken at $33\,540$ years, i.e. for $33\,540$ years plus the initial $60\,000$ years.

For all species shown, the abundance profiles are very similar after the chemistry was evolved for every hydrodynamical file (Fig. 4.2, black lines) and when the timestep was set via the free–fall time (red lines). The exception to this is the peak abundance of CS which is ~ 1000 times higher in the latter case, although the abundance in the two cases only diverges within $r < 4$ AU. Differences in chemical abundances deep within the FHSC will not affect the spectrum because it is optically thick. The abundance profile for when the chemistry was evolved for just the $33\,540$ year snapshot (blue lines) is very similar for CO and N_2H^+ but differs for the other species considered. CS and SO are frozen out to a greater degree in the envelope because the chemistry has been evolved for longer at the higher density. During the first collapse the density in this region was lower so the adsorption rates were lower at this time. The abundances of HCO^+ and NH_3 between 3 and 10 AU are much higher too, which shows that it is important to consider the physical history for these species too.

In summary, the choice of initial chemistry timestep is only significant if CS or SO emission from large (100-1000s AU) scales is to be considered. For CO and N_2H^+ after FHSC formation it is unnecessary to calculate the evolution of chemical abundances as the cloud collapses and is sufficient to calculate abundances only for the snapshot of interest. Otherwise, the chemical history is important and the chemically evolution should be modelled fully. Taking a maximum chemistry timestep of $\delta t = \frac{1}{3} t_{\rm ff}$ is sufficient for obtaining chemical abundances.

4.4 Radiative transfer

We took snapshots from the chemical post–processing of the hydrodynamical models to synthesize the line emission of selected molecular species with TORUS, as described in Section 2.3. First the adaptive mesh refinement (AMR) grid is populated from the SPH particles following the method described by Rundle et al. (2010). The SPH particles were mapped onto the cubical AMR grid of side length $6 \times 10^{15}\,\mathrm{cm}$ (400 AU) and mass resolution of $10^{27}\,\mathrm{g}$ per grid cell for the radiative transfer modelling, with the exception of the HCO^+ models. The density and temperature are low enough outside this region that the contribution to the spectrum is negligible relative to the contribution from the inner few 10s of AU. There is, however, a significant contribution from the envelope to the $HCO^+(1-0)$ spectrum, therefore a larger grid of $8 \times 10^{16}\,\mathrm{cm}$ (5350 AU) with a coarser mass resolution ($10^{28}\,\mathrm{g}$ per cell) was used for this transition.

The level populations were calculated assuming local thermodynamic equilibrium (LTE) and are calculated iteratively from the radiation incident on each cell. This is a valid assumption here because the density in the simulated collapsing cloud is higher than the critical density for the species and transitions considered. A Monte Carlo method is used to follow the emission and absorption of continuum and line photon packets through the model to an observer. A turbulent line broadening of $0.1\,\mathrm{km\,s^{-1}}$ is applied. A position-position-velocity (PPV) FITS image cube is produced for an observer at 150 pc. The PPV cubes have a side length of 370 AU and 81 channels from $-4\,\mathrm{km\,s^{-1}}$ to $4\,\mathrm{km\,s^{-1}}$, giving a channel width of $0.1\,\mathrm{km\,s^{-1}}$.

The silicate dust grain type of Draine and Lee (1984) with a power law distribution of grain sizes between $0.1\,\mu\mathrm{m}$ and $1\,\mu\mathrm{m}$ of $n(a) \propto a^{-q}$ with $q = 3.5$ (Mathis et al. 1977) was used to calculate the dust extinction, continuum emission for the continuum images, and the continuum contribution to the spectra.

4.4.1 Processing image files

The PPV cubes generated straight from TORUS are noise–free so it is sufficient to perform the continuum subtraction with just one line–free channel. Integrated intensity maps were

constructed from the continuum–subtracted PPV cubes by summing the channels as follows, where Δv is the channel width:

$$I = \sum_{v=1}^{n} I_v \Delta v. \tag{4.1}$$

Spectra were calculated by averaging pixels within a 0.35 arcsec diameter aperture for CS and SO, and within a 0.67 arcsec aperture for CO and HCO^+ for which the emission is more extended.

ALMA observations were simulated from the PPV cubes using the `simalma` routine in CASA (McMullin et al. 2007). Channels corresponding to $-4.0\,\mathrm{km\,s^{-1}}$ to $-3.5\,\mathrm{km\,s^{-1}}$ and $3.5\,\mathrm{km\,s^{-1}}$ to $4.0\,\mathrm{km\,s^{-1}}$ for which there was no line emission were averaged and subtracted from all channels to remove the continuum emission.

Position–velocity diagrams were constructed for CO PPV cubes to examine rotation. The PV cuts were taken perpendicular to the rotation axis, through the midplane of the disc or pseudo–disc. The brightness of each velocity channel at each position was calculated by adding the intensity of pixels within $\pm$ 0.15 arcsec above and below this centre line.

4.5 Results

4.5.1 Morphology and velocity structure of the hydrodynamical models.

The evolution of the maximum density and central temperature are presented in Fig. 4.3. Initially the temperature is lowest at the centre of the core and the temperature remains $\approx$ 15 K at the edge throughout the simulation due to heating by the ISRF. It is therefore more useful to compare the central temperature rather than maximum temperature. The FHSC forms after $29\,500$ years in the RHD model and after $30\,700$ years in the MHD model. The FHSC is deemed to have formed when the rapid increase in central density and temperature that occurs during first collapse ceases and the density and temperature continue increasing at a slower rate (just after point (a) in Fig. 4.3). The FHSC lasts for 3500 years in the RHD model and for 1300 years in the MHD model. The lifetime is shorter in the MHD model because magnetic braking slows the rotation such that the rotational support

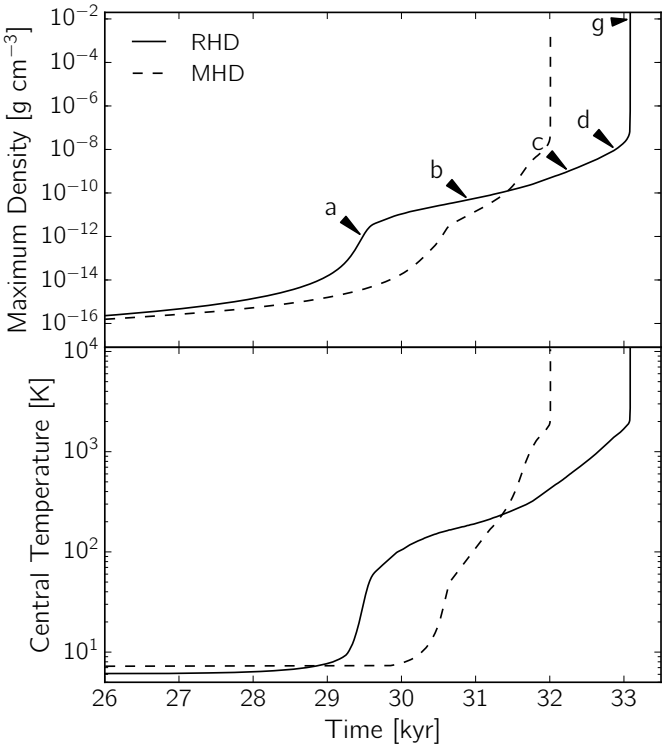

Figure 4.3: The time evolution of the maximum density (top) and central temperature (bottom) for the RHD model (solid lines) and MHD model (dashed lines). Snapshots were taken from these models at certain values of maximum density for comparing evolutionary stages and simulating observations. These are indicated for the RHD model. Snapshot (a) is taken just before the FHSC forms. The density and temperature increase more slowly after this point before rapidly increasing again during the second collapse.

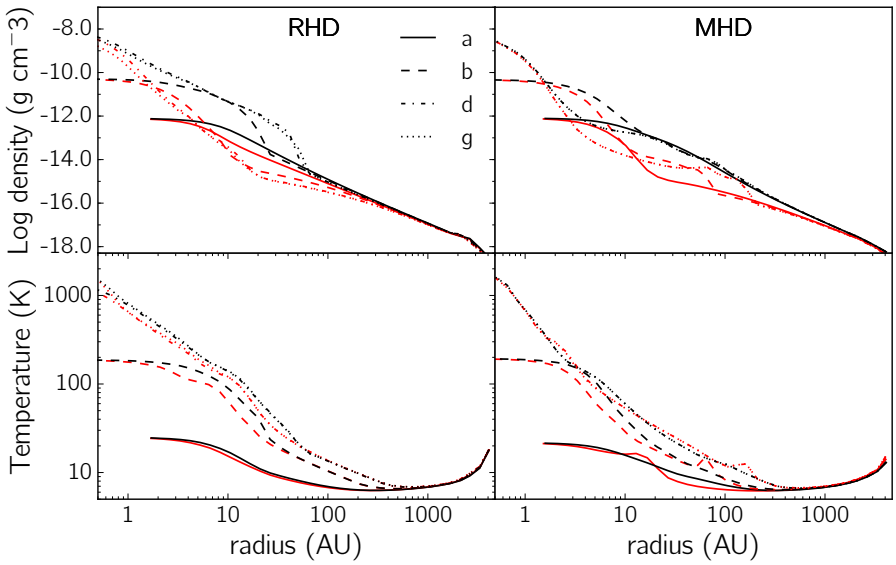

Figure 4.4: Density and temperature radial profiles for the RHD and MHD models at snapshots before FHSC formation (a), during the FHSC stage (b, d) and after the formation of the stellar core (g). Profiles are shown parallel to the rotation axis (black) and perpendicular to the rotation axis (red).

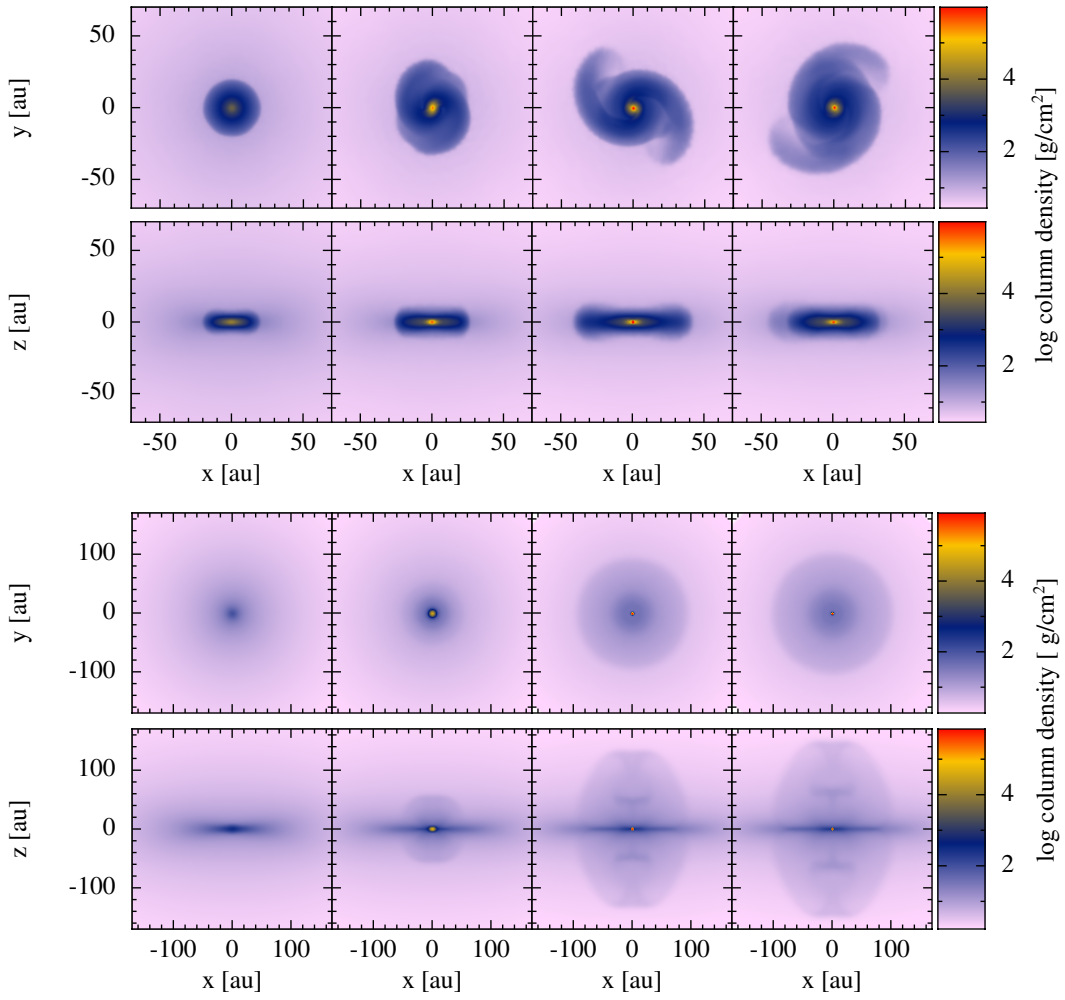

Figure 4.5: Evolution of the column density of the RHD model viewed at $i = 0°$ and $i = 90°$ (upper two rows) and of the MHD model also viewed at the same inclination angles (lower two rows). From left to right, panels show FHSC snapshots (b), (c) and (d) and the stellar (second) core snapshot (g). The development of spiral structure is apparent in the RHD model and the outflow is seen in the MHD model at $i = 90°$.

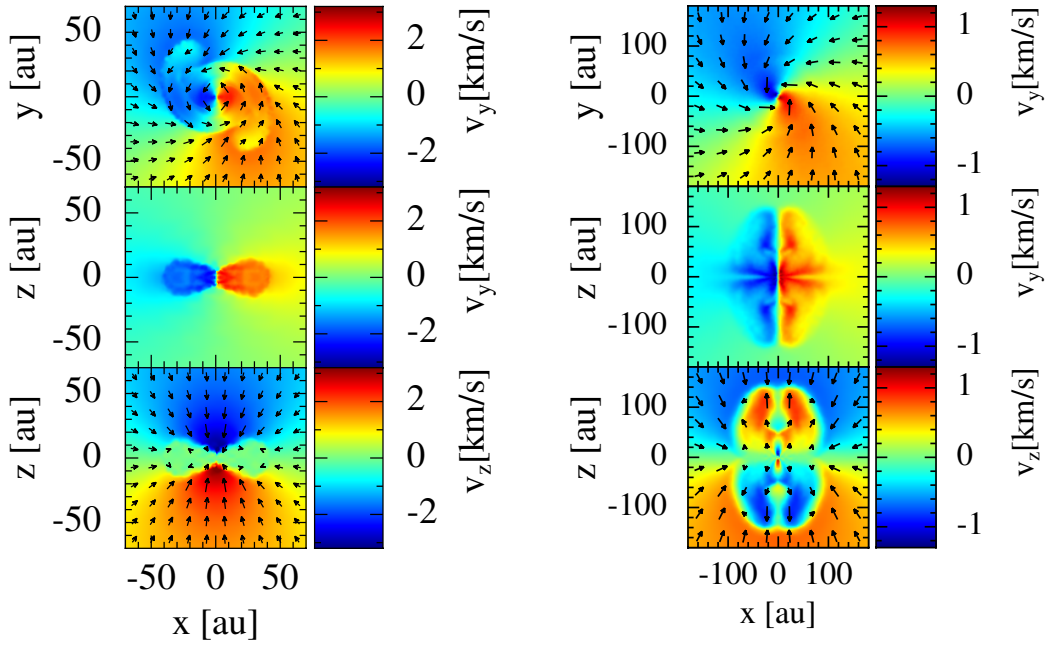

Figure 4.6: Velocity structure at snapshot (d) (late FHSC). Left panels: RHD model. Cross-section of the velocity component approaching an observer viewing the system edge–on, v_y, in the midplane (top) showing a rotationally supported disc; v_y, as viewed edge–on (centre); the vertical component of the velocity, v_z, (bottom). Arrows show the direction of the net velocity. Right panels: As above but for the MHD model. The key features are the rotating pseudo-disc and outflow. The highest velocities are due to infall within $\pm$20 AU.

is reduced.

We take snapshots from the hydrodynamical models at selected times to allow comparison of the synthetic observations for different evolutionary stages. These are taken at the following values of the central density: (a)$10^{-12}\,\mathrm{g\,cm^{-3}}$, (b) $5 \times 10^{-11}\,\mathrm{g\,cm^{-3}}$, (c) $10^{-9}\,\mathrm{g\,cm^{-3}}$, (d) $10^{-8}\,\mathrm{g\,cm^{-3}}$, (g) $10^{-2}\,\mathrm{g\,cm^{-3}}$ (these are the same values as used in Chapter 3). Snapshot (a) is taken just before FHSC formation, (b), (c) and (d) are during the FHSC stage and (g) is taken just after the formation of the stellar core. Density and temperature profiles for four key evolutionary stages are presented in Fig. 4.4. It is important to note that the temperature remains < 100 K at $r > 10$ AU even at snapshot (g), i.e. shortly after stellar core formation, and $T < 300$ K at $r > 4$ AU (see Fig. 4.4) which means the chemical network is valid for observable size scales.

The morphology of the RHD and MHD models is shown in Fig. 4.5. In the RHD model (upper two panels), the FHSC has the form of a rotationally supported disc which

increases in radius from ~ 20 AU to ~ 35 AU (c.f. Bate 1998, 2011). Late in the FHSC stage, after $32\,000$ years, a spiral instability develops. The disc is also apparent in the diagrams of the velocity structure shown in Fig. 4.6, upper panels, as well as the infall perpendicular to the plane of the disc. After second collapse and the formation of the second (stellar) core, the disc and spiral structures persist.

In the MHD model, the FHSC forms after $30\,700$ years. The cloud core is initially rotating quickly in this model but the rotation is significantly reduced by magnetic braking and the FHSC is not rotationally supported. A pseudo-disc forms around the FHSC, comprised of gas with infalling, rotating motions (see Fig. 4.6). An outflow is launched around 400 years after FHSC formation, the structure of which is shown in Fig. 4.5, lower panels, and the lower panels of Fig. 4.6. Outflow velocities reach $0.5\,\mathrm{km\,s^{-1}}$ to $1.0\,\mathrm{km\,s^{-1}}$ at distances of 20 to 150 AU from the midplane. Infall continues through the pseudo–disc at $|v| \leq 0.5\,\mathrm{km\,s^{-1}}$ and also vertically within $r < 10$ AU with velocities exceeding $1\,\mathrm{km\,s^{-1}}$. The line–of–sight rotational velocities in the outflow and pseudo–disc are similar to the outflow and infall velocities which means that all of these regions must be considered to understand the nature of the spectra.

Infall velocities reach $\sim 3\,\mathrm{km\,s^{-1}}$ in the RHD model but are lower in the MHD model due to additional magnetic pressure and remain $< 1.5\,\mathrm{km\,s^{-1}}$ after stellar core formation.

4.5.2 Chemical evolution

Chemical abundances as a function of radius for the RHD case are shown in Figs. 4.7 and 4.8. From here on we refer to chemical abundances relative to the abundance of molecular hydrogen. Other species with high abundances not shown here include CCH, HCN, HNC and H_2O. Some interesting species such as methanol and formaldehyde form primarily through grain surface reactions and so we cannot calculate realistic abundances for these. The abundances beyond $100\,\mathrm{AU}$ remain mostly unchanged throughout FHSC phase and stellar core formation because the temperature and density change very little. However, for nearly all the species shown, there is a dramatic change at $r \lesssim 30\,\mathrm{AU}$ when the FHSC forms and the gas–phase abundances increase quickly. We note that the abundances of the species discussed here are also high at large radii in the envelope and surrounding

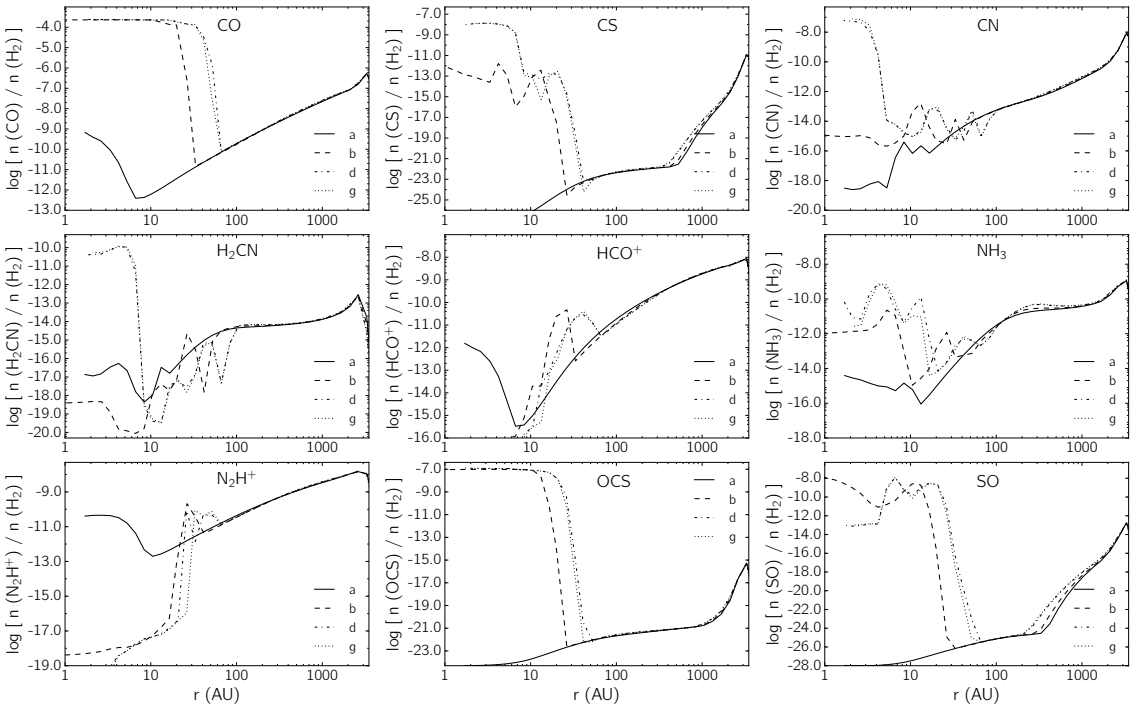

Figure 4.7: Average abundances of selected species calculated for the RHD model perpendicular to the rotation axis for snapshots a–g taken as the FHSC forms and evolves (see Fig. 4.3).

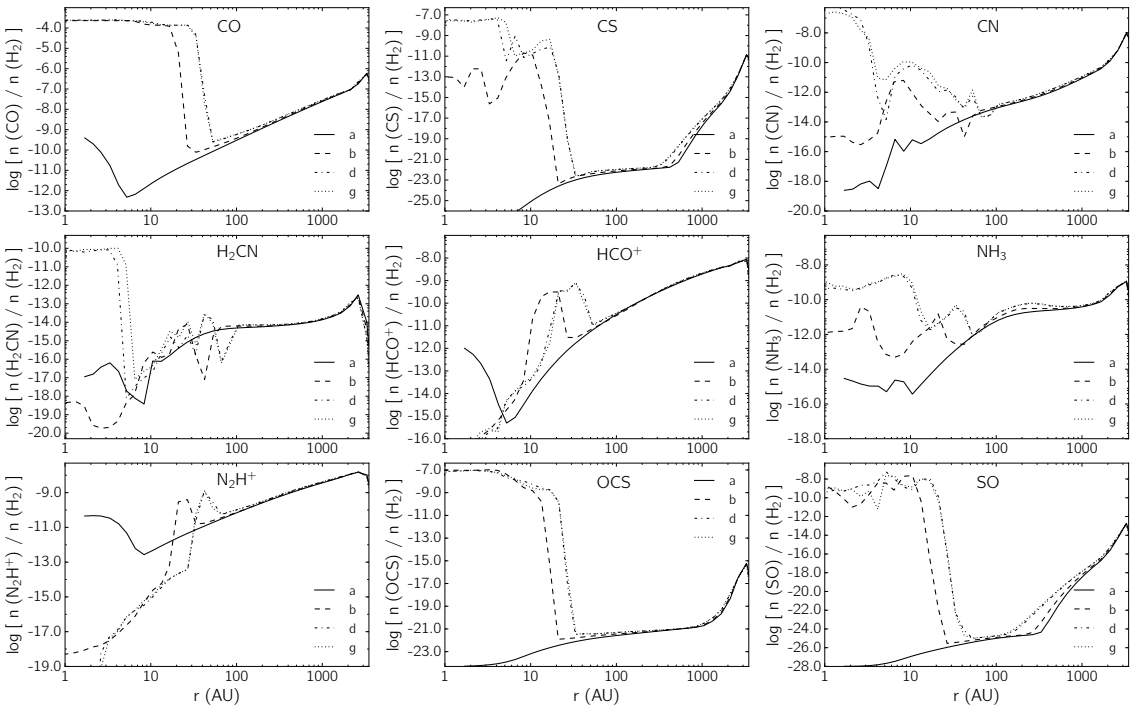

Figure 4.8: Same as for Fig. 4.7 but in the vertical direction (parallel to the rotation axis).

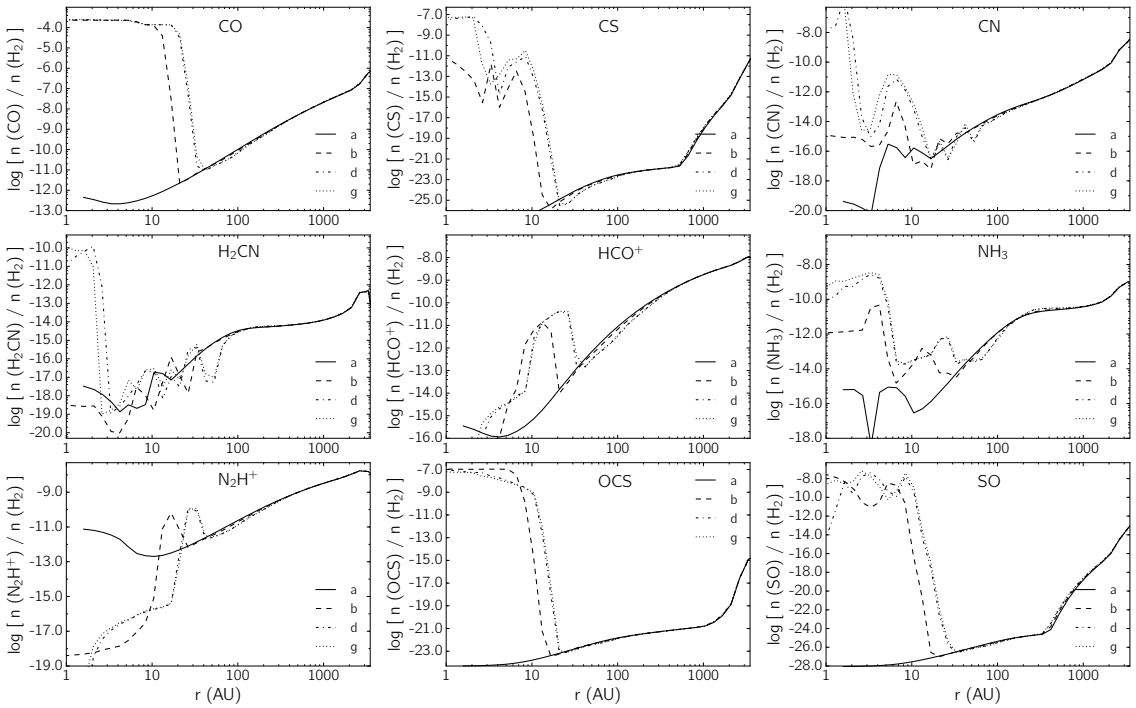

Figure 4.9: Average abundances of selected species from the MHD model perpendicular to the rotation axis.

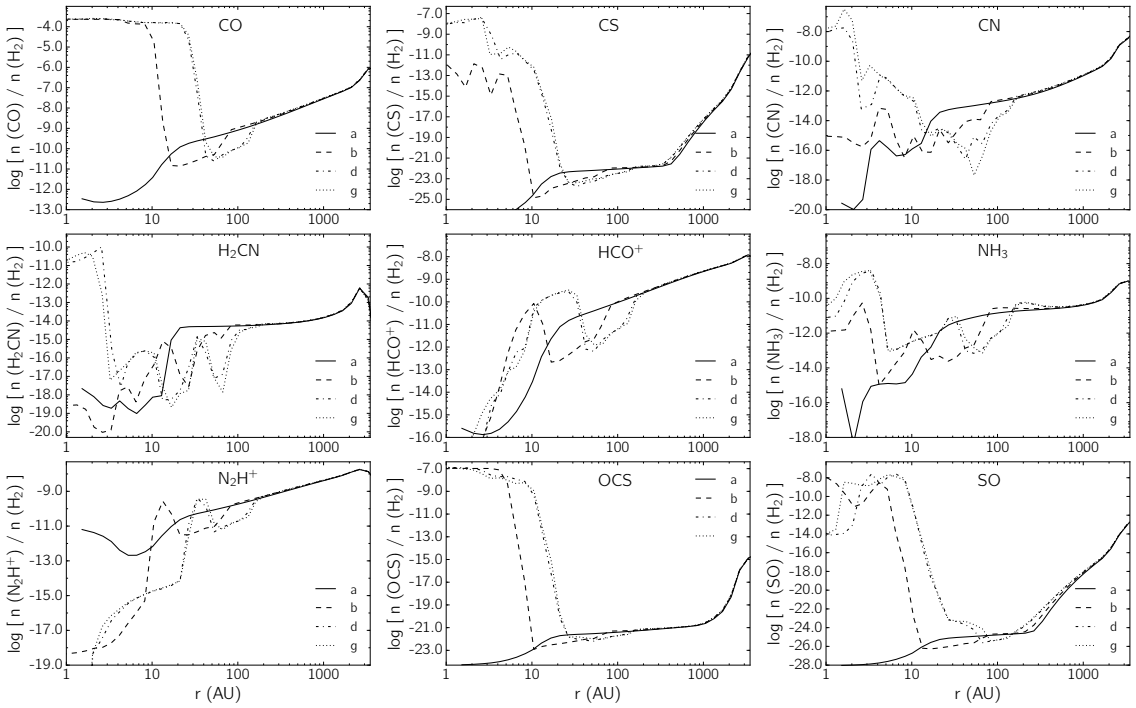

Figure 4.10: Same as for Fig. 4.9 in the vertical direction.

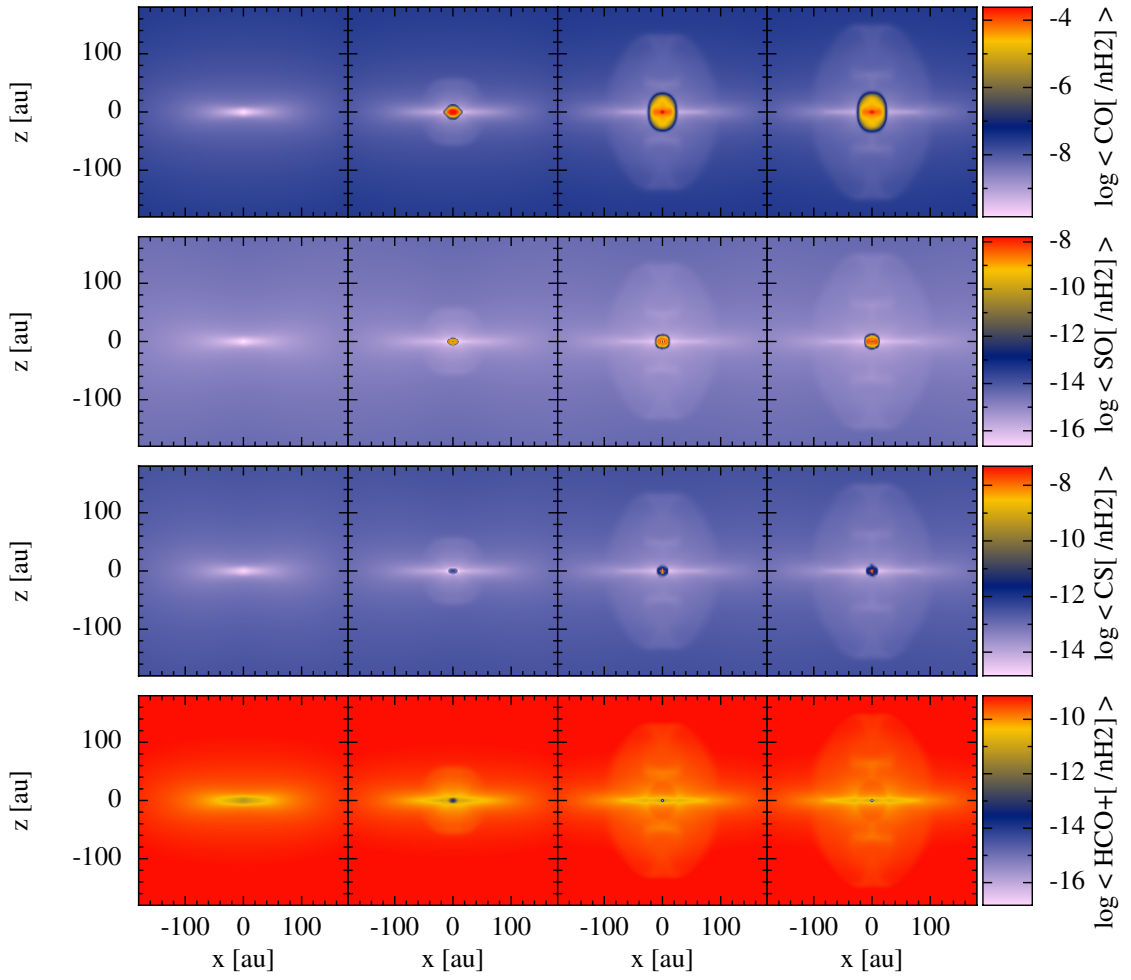

Figure 4.11: Mass weighted average abundances (relative to n_{H_2}) of selected species from the MHD model, viewed at $i = 90°$. From left to right, the snapshots are of the first collapse (a), early FHSC (b), late FHSC (d), and just after stellar core formation (g).

molecular cloud. However, if we select transitions that are excited at the higher temperatures of the warm core then it is only the abundances towards the centre of the cloud core that matter for observations.

The abundance of CS peaks sharply within a radius of a few AU, indicating that it traces the warmest region at the centre of the FHSC. The peak abundance increases significantly during the FHSC stage so we may expect to see CS lines brighten as the core evolves. CN traces a similar region but its central abundance increases later than CS. The abundance of H_2CN increases rapidly within the FHSC and becomes 4–5 orders of magnitude higher than in the surrounding envelope, which may provide an indication of the FHSC.

OCS, SO and CO trace the FHSC but to different radii. In the RHD model, these species trace regions within $\sim$ 15, 20 and 30 AU respectively in the disc plane. For these species, the peak abundance does not change after the FHSC forms but the radius within which the abundance is high increases as the disc warms up. For example, CO desorbs from dust grains as soon as the FHSC forms and the size of the disc traced by CO increases from $\sim 15\,\mathrm{AU}$ to $\sim 30\,\mathrm{AU}$ in the first half of the FHSC phase. OCS follows the same pattern but traces the disc to a smaller ($< 15\,\mathrm{AU}$) radius.

Abundances in the MHD model (Figures 4.9, 4.10 and 4.11) are similar except in the vertical direction after the outflow is launched. HCO^+ and CO are abundant out to larger radii in the vertical direction than the horizontal due to the outflow. SO still appears to trace the central core well since the abundance decreases by several orders of magnitude at $10\,\mathrm{AU}$ even in the direction of the outflow. In the MHD model, the peak abundance of SO increases by a factor of 10 during FHSC stage.

The abundance of HCO^+ is lowest in the centre of the core after FHSC formation and increases with radius. There is a region of enhanced HCO^+ abundance within a shell at $\sim$10 - 50 AU. The abundance of HCO^+ is lower in the outflow than surrounding envelope and lower still in the pseudo–disc. HCO^+ is therefore likely to trace the inner envelope structure, but not the disc or pseudo–disc.

The abundance of NH_3 peaks within the FHSC in the MHD model and to a lesser

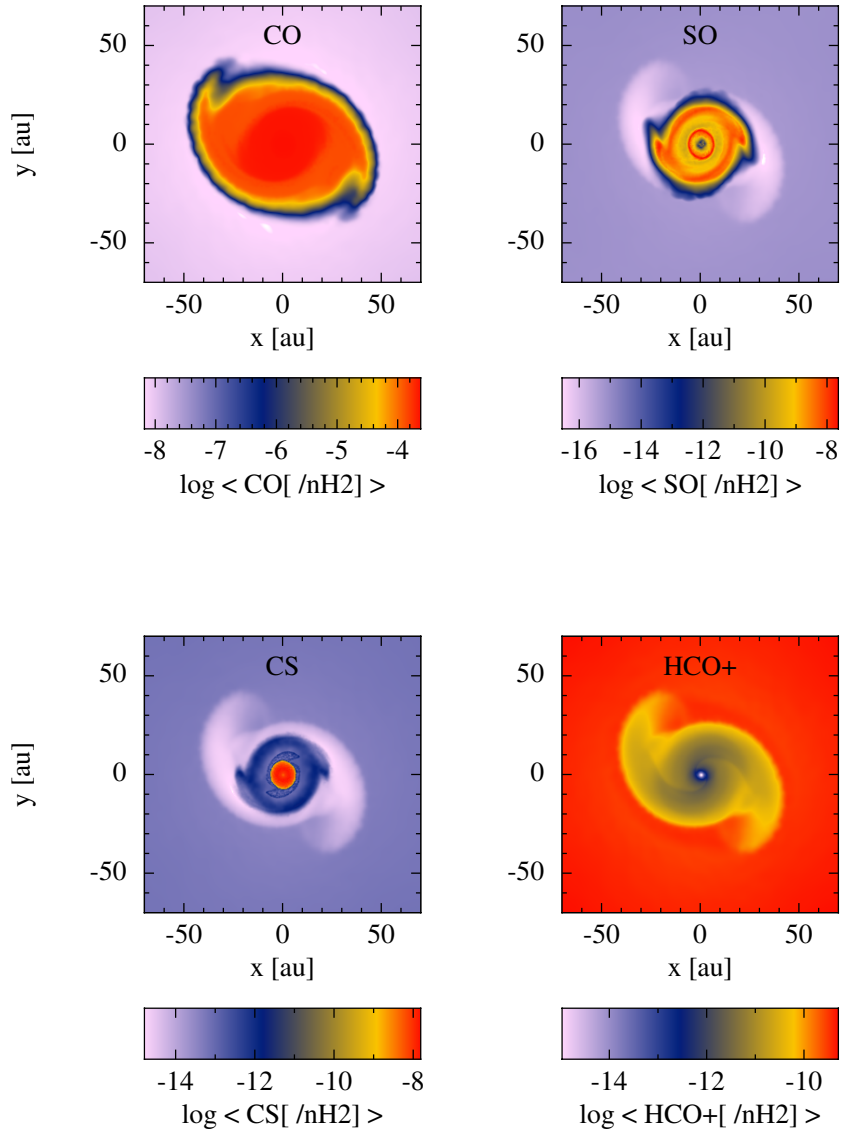

Figure 4.12: Mass weighted average abundance relative to n_{H_2} for snapshot (d), late FHSC for CO, SO, CS and HCO^+ respectively. CO and CS trace the spiral structure of the FHSC and CS traces just the central few AU. The HCO^+ abundance is lower in the spiral arms than in the envelope.

extent also in the RHD model. NH_3 is depleted to a radius of ∼100 AU within the pseudo–disc and within the outflow. In the RHD model, NH_3 is depleted within the spiral arms but the abundance is high within a radius of $r \lesssim 30$ AU and is high in the envelope.

Abundances of the other species here peak sharply in the centre, except for SO which traces out to 8 AU above the midplane and CO which traces out to 20 AU. At this distance, CO should trace the base of the outflow but SO is more likely to trace the infall close to the centre of the core.

The chemical abundances within and close to the FHSC are very different to the abundances in the centre of the pre-stellar core before FHSC formation because many species desorp from the dust grains with the rapid increase in temperature. For both models, the species that show significant evolution in abundance during the FHSC stage are CS, NH_3 and SO. The abundance of OCS in the centre of the core decreases during FHSC stage in the MHD model.

For all species considered here, clues to the evolutionary stage of the core are likely to be given by changes in envelope structures revealed by certain species rather than by changes in chemical abundances alone. Murillo et al. (2018) conclude from observations of two Class 0 protostars that temperature is a key factor in driving the chemical composition of a protostellar envelope. Since the temperature structures are similar, it is likely that the kinematics rather than the chemical abundances will prove a better diagnostic of the FHSC.

4.5.3 Synthetic observations

In this section we present synthetic observations of CO $(4-3)$ (461.041 GHz), SO (8_7-7_6) (340.714 GHz), CS $(8-7)$ (391.847 GHz) and HCO^+ $(1-0)$ (89.198 GHz). These species were chosen because they are expected to have high enough abundances to be detectable and to trace different structures. CS also shows a significant change in abundance as the FHSC grows. CN, NH_3 and N_2H^+ are also likely to trace FHSC structures. However, at the moment we are unable to compute the hyperfine structure lines necessary to model the emission from these molecules.

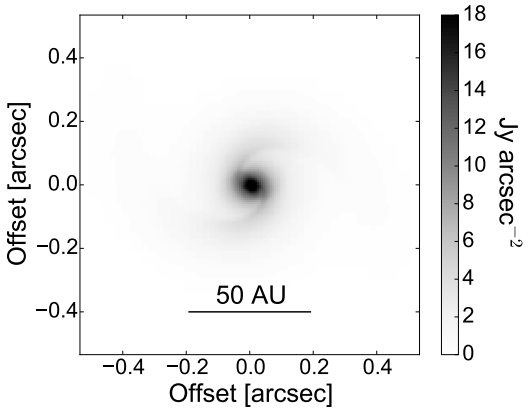

Figure 4.13: 230 GHz (1.3mm) continuum image for snapshot (d) from the RHD model. At millimetre wavelengths the continuum emission is brightest in the centre of the FHSC only and the spiral features are faint. The brightness scale has been capped at 18.0 Jy arcsec^{-2} but the maximum intensity is 20.2 Jy arcsec^{-2}.

4.5.3.1 Continuum

The $230\,\mathrm{GHz}$ continuum image of the late FHSC from the RHD model is presented in Fig. 4.13 to allow comparison with line observations. The continuum emission here is tracing the denser regions such that the centre of the FHSC appears bright and the spiral structures are only visible within 20 AU.

4.5.3.2 CO

From Fig. 4.12 it is clear that CO traces the region containing the spiral structures in the RHD model. The integrated intensity maps for a snapshot late in the FHSC stage for both the RHD and MHD models are shown in Fig. 4.14. The CO $(4-3)$ line appears to trace the rotational structures present in the RHD model in the face–on direction. The CO $(4-3)$ emission reveals two spiral arms but the emission traces the lower density region rather than the spiral features seen in the column density and dust continuum emission (Fig. 4.13).

There are significant absorption features in the integrated intensity maps where the FHSC continuum emission is absorbed by cooler gas in front of it. This effect is occasionally seen in observations of Class 0 protostars (e.g. Ohashi et al. 2014). The FHSC is smaller in the MHD model so a smaller region is seen in absorption. The FHSC remains axisymmetric in the MHD model and the integrated intensity map shows a 50 AU diameter disc–like structure.

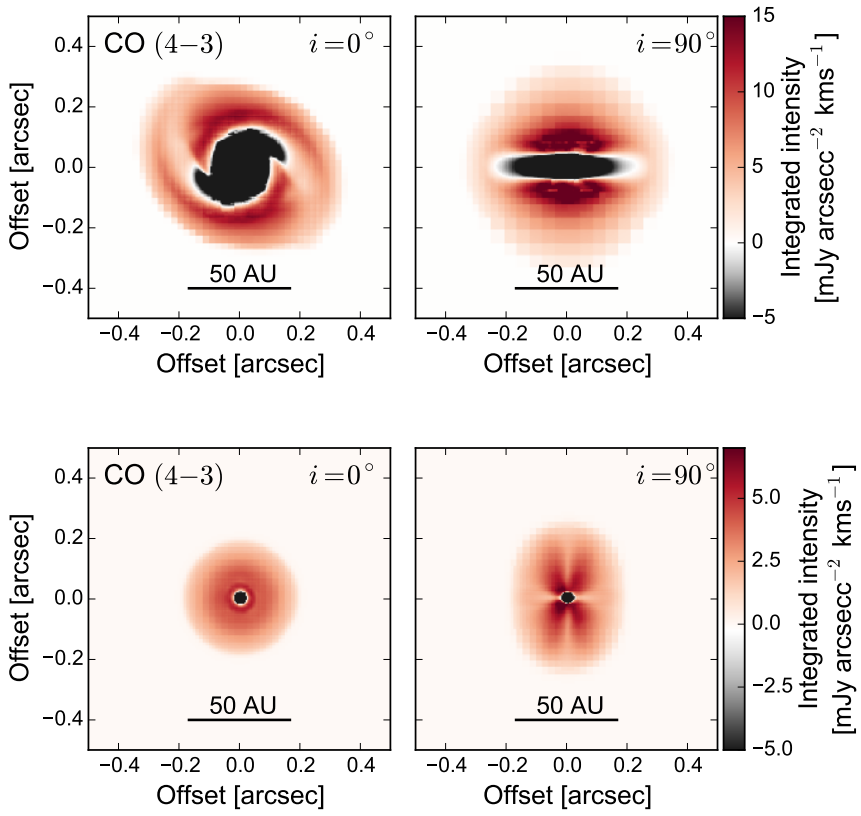

Figure 4.14: Top: CO $(4-3)$ integrated intensity map for late FHSC in the RHD model, after subtracting continuum emission. Bottom: As above but for the MHD model.

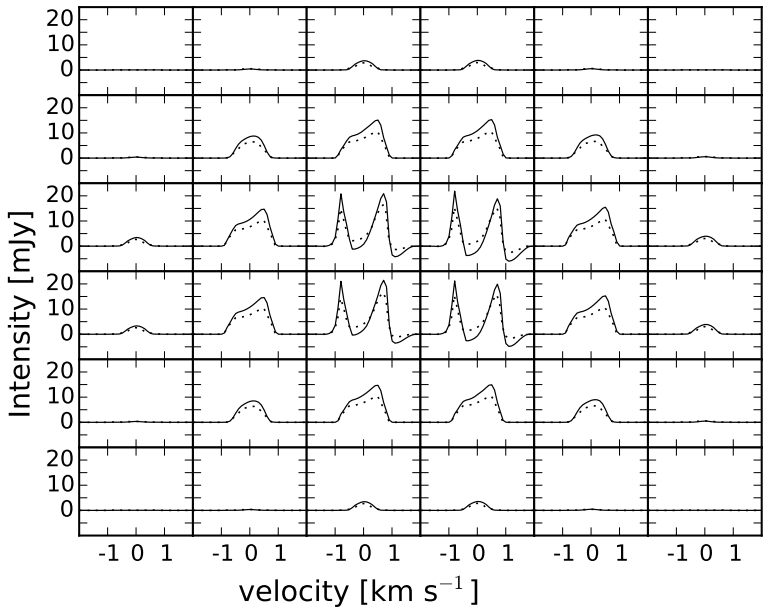

Figure 4.15: Spectra for CO $(4-3)$ (solid lines) and CO $(3-2)$ (dotted lines) at $i = 0°$ (face-on) during late FHSC stage (d) of the MHD model. Each panel covers an area of 0.08×0.08 arcsec^2. The outflow has recently been launched and is apparent from the double peak.

When viewed side–on (inclination $i = 90°$) the dense inner envelope is bright in emission for the RHD model. The outflow structure of the MHD model is apparent in the CO $(4-3)$ emission. The CO abundance varies by less than an order of magnitude across the inner region which it traces, indicating that the outflow structure in Fig. 4.14, bottom right, is not caused by an increased CO abundance in the outflow. The brighter structures are where the velocities are higher because emission at the higher velocities ($> 1\,\mathrm{km\,s^{-1}}$) suffers much less from self–absorption.

The spectra of the late FHSC snapshot from the MHD model in Fig. 4.15 reveal the kinematics that could be detected at $i = 0°$. The spectrum for each panel was calculated simply by summing the intensities for each pixel in the area of the image covered by the panel. The CO $(4-3)$ spectra are brighter, more sharply peaked and have deeper absorption features than the CO $(3-2)$ spectra. The line profiles for the snapshot just after stellar core formation are very similar, only slightly brighter.

At $i = 0°$ we are looking down the direction of the outflow. The double–peaked spectra in the four central panels are indicative of the blue– and redshifted components with velocities of $\sim 1\,\mathrm{km\,s^{-1}}$. Self–absorption at low velocities also contributes to the central dip. There is a second absorption feature at $\sim 1\,\mathrm{km\,s^{-1}}$ which is caused by infalling gas directly in front of the FHSC (see Fig. 4.14, lower right). Outside of the central four panels, the spectra peak at $\sim 0.7\,\mathrm{km\,s^{-1}}$. The redshifted emission from the far side outflow is brighter than the emission from the approaching part of the outflow, which causes this asymmetry in the spectra. The nearside emission is self–absorbed because the gas in the outflow, through which the emission propagates, is moving at similar velocities to the emitting gas and this is not the case for the far side emission. The effect of the near side infalling gas on the redshifted outflow CO emission is negligible because the CO abundance is very low in the envelope.

To examine the observable kinematics further we plot the position–velocity cuts for three snapshots during FHSC stages (b,c,d) and shortly after stellar core formation (g) in Fig. 4.16 for both the RHD and MHD models. These were constructed from the $i = 90°$ velocity cubes as described in Section 4.4.1.

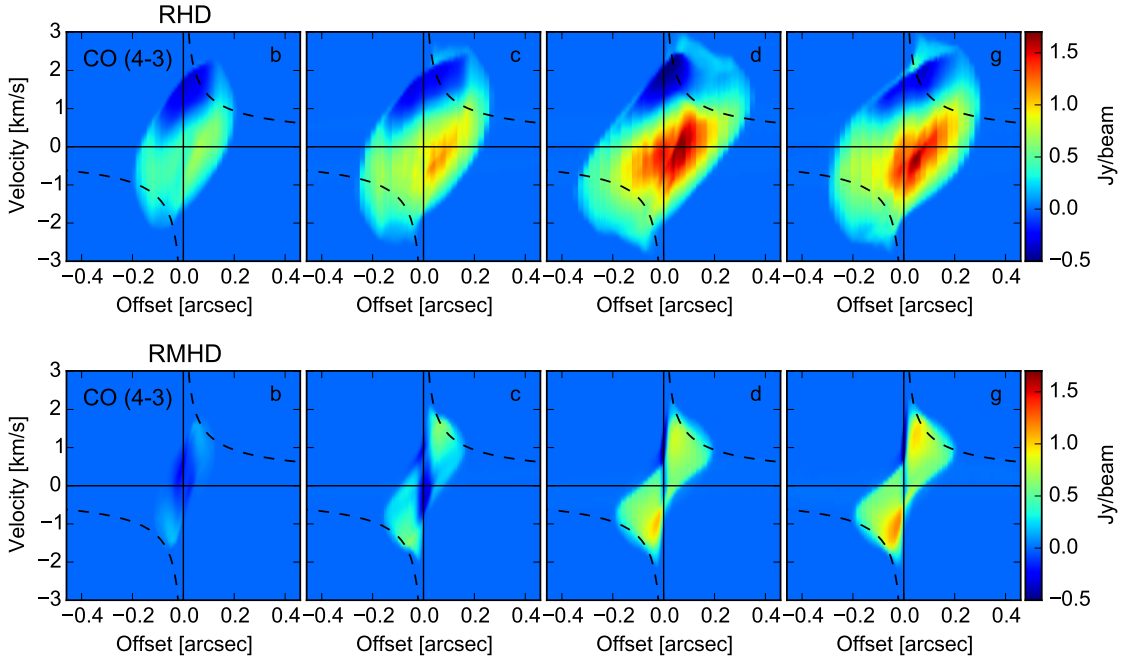

Figure 4.16: Position–velocity diagrams for CO $(4-3)$ for a series of snapshots of the FHSC (b, c, d) and newly formed stellar core (g) viewed at $i = 90°$ inclination. The intensity was summed over an 0.3 arcsec slice centered on the plane of the disc. Dashed lines show the Keplerian rotation profile for a $0.03\ \mathrm{M}_{\odot}$ central protostar.

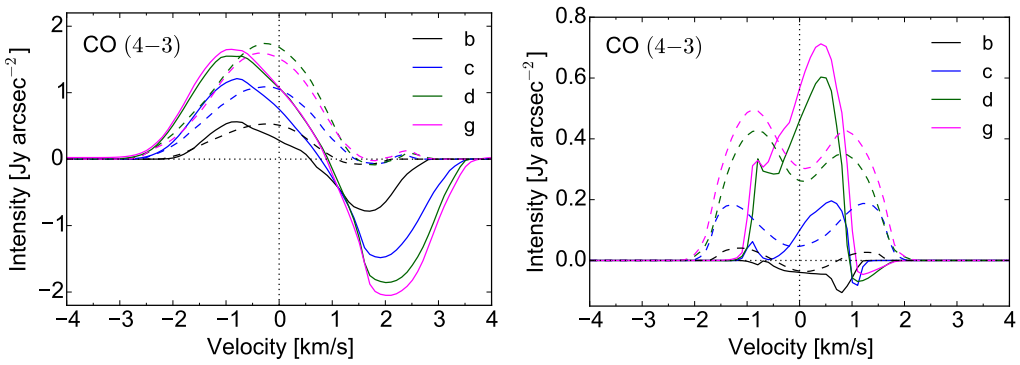

Figure 4.17: Spectra averaged over a central 0.67 arcsec diameter aperture for RHD model (top) and MHD model (bottom). Solid lines: $i = 0°$, dashed lines: $i = 90°$. Letters refer to evolutionary stage as defined in Section 4.5.1.

The RHD PV diagrams show the characteristics of a rotating infalling structure. The broad absorption feature at $\sim 1-2\ \mathrm{km\,s^{-1}}$ indicates infalling gas and the velocity increases towards positive offsets because of the contribution of rotation. CO is frozen out just outwards of the spiral shocks at $r \gtrsim 40$ AU. The extent of the emission increases as the temperature increases and CO desorbs at increasing radii. There is blueshifted emission to the right hand, receding, side of the object because the gas on the far side has a component in the direction of the observer as it spirals towards the disc. This emission is not self–absorbed due to the velocity difference between the emitting gas and the gas in the disc and near–side envelope through which it passes.

The PV diagram for the MHD model appears to be closer to a Keplerian rotation profile, although this is misleading because there is no rotationally supported disc and gas is spiralling inward through the pseudo–disc. CO is frozen out at $r \gtrsim 20$ AU so there is no emission beyond ± 0.2 arcsec.

Earlier in the FHSC stage (snapshots b and c) absorption occurs at negative velocities. For snapshot (c), this is likely to be due to absorption in the young outflow. By snapshot (d) absorption occurs only at $v \gtrsim 0.4\,\mathrm{km\,s^{-1}}$ and is restricted to a very narrow region of < 0.04 arcsec. The nature of the CO $(4-3)$ absorption feature could provide an indication of the evolutionary stage.

From the evolution of the spectra averaged within a 0.35 arcsec circle shown in Fig. 4.17, the difference between the RHD and MHD models is even more apparent. The disc in the RHD model is seen almost entirely in absorption against the continuum. Early in the FHSC stage (b) the absorption and emission features are similar in magnitude in the RHD model. The brightness of the emission changes little through to when the stellar core forms but the depth of absorption increases by up to a factor of 3. There is no disc in the MHD model and much of the emission is from the outflow. At (b) the line is entirely in absorption at $i = 0°$. The development of the outflow leads to the emission brightening as gas–phase CO is present in high abundance in a more extended region.

At $i = 90°$ a double–peaked rotation signature is not seen in the RHD model due to the strong absorption at positive velocities by infalling material. The rotating outflow

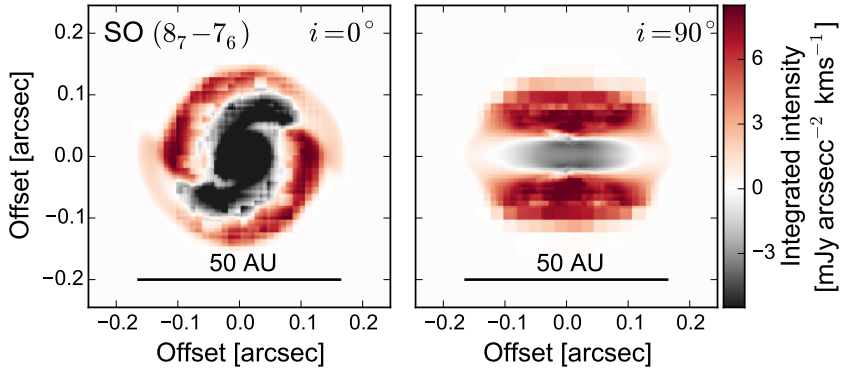

Figure 4.18: SO $(8_7 - 7_6)$ integrated intensity maps for the RHD model. We do not show the MHD model because the scale of the emission would be too small to resolve.

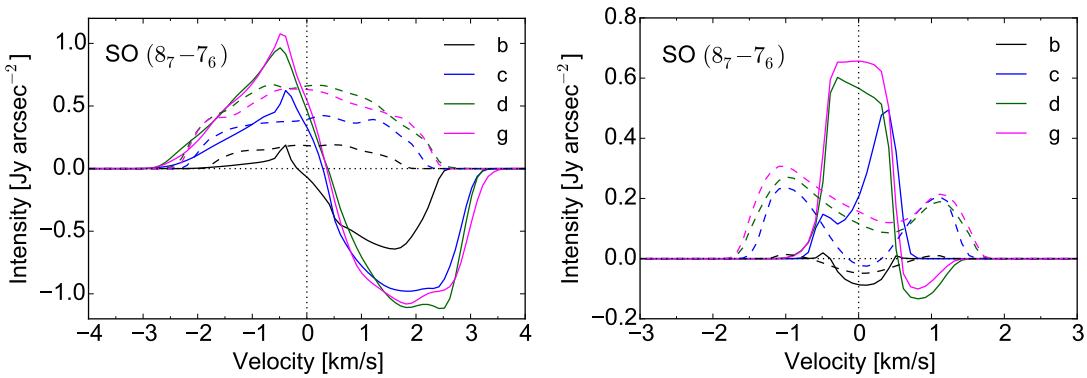

Figure 4.19: Evolution of the SO $(8_7 - 7_6)$ line profile in the MHD model for RHD model (top) and MHD model (bottom). Each spectrum is averaged over pixels within a central 0.35 arcsec (53 AU) diameter circular beam. Solid lines: $i = 0°$, dashed lines: $i = 90°$.

produces a double–peaked spectrum in the MHD model, however, which may be mistaken for a rotating disc (Fig. 4.17, bottom panel, dashed lines).

Our models assume a turbulent velocity of $0.1\,\mathrm{km\,s^{-1}}$ and we note that a higher value will result in less self–absorption at the systematic velocity of the FHSC as well as slightly broader line widths.

4.5.3.3 SO

The abundance of SO is $\sim 1 \times 10^{-9}$ within $r < 20$ AU in the RHD model and within $r < 10$ AU in the MHD model and drops off rapidly outside this region, meaning it is a tracer of the FHSC only in the RHD model (Fig. 4.12) and of the FHSC and very inner envelope in the MHD model (Fig. 4.11). At a distance of 150 pc, the region traced in the MHD model is only 0.13 arcsec across so the object will not be well resolved. The

abundance of SO is lower in the outer parts of the spiral arms of the RHD model, although SO traces the inner spiral well (Fig. 4.12). In Fig. 4.18, the integrated intensity plots reveal significant absorption as seen in CO, which actually traces out the central spiral structure. Emission is limited to a pair of spiral arms at $r \sim 20$ AU. At $i = 90°$, we see a "hamburger" structure with emission from above and below the midplane.

SO ($8_7 - 7_6$) spectra for the MHD model are shown in Fig. 4.19. The line brightens considerably during the early FHSC stage as the temperature increases quickly in the central few AU and SO traces an increasing radius. The region traced by SO incorporates only a small section of the outflow where the outflow velocities are $< 0.5\,\mathrm{km\,s^{-1}}$. In the same region, the infall and rotation velocities are $\sim 1\,\mathrm{km\,s^{-1}}$.

The spectra show a clear evolution during FHSC stage. At snapshot (b) the emission is undetectable and the line is symmetrical in absorption. By snapshot (c) the outflow has launched and the line is asymmetrical since it is affected by self–absorption by outflowing gas, giving rise to a redshifted peak. From snapshot (d) there is an absorption feature against the continuum. This becomes less pronounced after the stellar core formation because the density distribution becomes more sharply peaked. The peak becomes more symmetrical as emission from the outflow brightens.

At $i = 90°$, the emission peaks at $\pm\ 1.2\,\mathrm{km\,s^{-1}}$ and the blueshifted peak is brighter, as expected for an infalling, rotating structure. The central absorption dip is skewed to positive velocities due to absorption by infalling material (with a positive recession velocity). The infall velocity is lower here than in the vertical direction due to the added effect of rotation.

Without an outflow, the spectra for the RHD model are quite different. There is a very strong absorption feature from 1.5 to 2.5 $\mathrm{km\,s^{-1}}$. After stage (c) this does not deepen although the emission peak brightens between snapshots (c) and (d). The $i = 90°$ spectra do not display the characteristic double peak. Looking at the integrated intensity images in Fig. 4.18 we can see that the disc is seen nearly entirely in absorption. Rotation speeds are low above and below the disc where the emission originates and emission at higher velocities is less bright than the low velocity emission from nearer the centre.

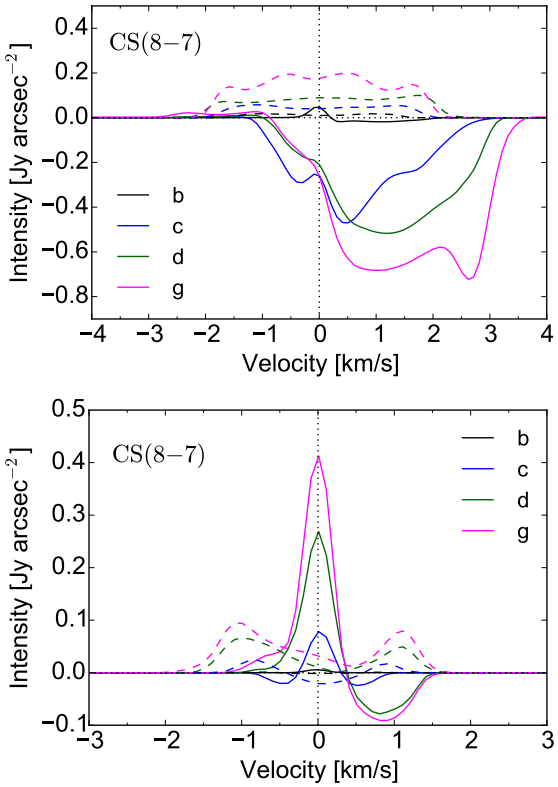

Figure 4.20: Spectra for CS $(8-7)$ obtained from a 0.35 arcsec aperture from the RHD model (top) and MHD model (bottom). Solid lines $i = 0°$; dashed lines $i = 90°$.

4.5.3.4 CS

The average CS abundance for the late FHSC of the RHD model is presented in the final panel of Fig. 4.12. The abundance peaks at a few 10^{-8} within $r < 10$ AU in a symmetrical distribution and is several orders of magnitude lower elsewhere. We therefore do not expect CS to be useful for tracing rotational structures. The emission will not be well resolved so we consider only the spectra obtained from the total emission within a 0.35 arcsec aperture centred on the FHSC.

Fig. 4.20 shows the spectra for CS $(8-7)$. CS is extremely depleted towards the centre of the cloud core prior to FHSC formation and the abundance soon after formation is still too low to be detectable.

In the MHD model, at $i = 0°$ from snapshot (c) onwards, a sharp peak develops around the CS $(8-7)$ line centre and this brightens considerably between the FHSC and stellar core stages. There is an absorption feature at $\sim 1\,\mathrm{km\,s^{-1}}$. At the frequency of the CS $(8-7)$ transition $(391.8\,\mathrm{GHz})$, the envelope is optically thin and most of the continuum

emission originates within the FHSC or from the very inner envelope near to the FHSC. The optically thin gas directly in front of the FHSC is infalling with a velocity of $\sim 1\,\mathrm{km\,s^{-1}}$ and absorbs the continuum emission. The peaks of the spectra are symmetrical and show no evidence of the outflow. The CS $(8-7)$ line brightens between during and beyond the FHSC stage.

At stage (c), mid–FHSC stage, we see symmetrical absorption features around the central peak. The outflow has launched by then with a velocity $< 1\,\mathrm{km\,s^{-1}}$. The gas is still relatively dense and therefore absorbs radiation from the FHSC, but does so predominantly at blueshifted frequencies since this gas is approaching the observer. Within $\lesssim 5\,\mathrm{AU}$ from the centre, the gas is infalling at a similar speed to the outflow, which creates the redshifted absorption feature.

At $i = 90°$, the CS $(8-7)$ line is double–peaked because of the rotation of the FHSC. The emission is fainter due to the increased optical depth caused by the disc structure such that the emission comes from a slightly larger radius where the temperatures are a little lower. The central dip is deepened by absorption and is skewed to positive velocities due to infall as discussed above.

Spectra from the RHD model show only absorption at $i = 0°$ and little asymmetry at $i = 90°$. Absorption at increasing velocities as the FHSC evolves indicates the increasing infall velocities. In the ideal MHD model, the additional support from the magnetic field reduces infall speeds so the spectra reveal a narrower velocity range.

4.5.3.5 HCO^+

The abundance of HCO^+ is highest in the regions of the lowest density and it is depleted in the FHSC and disc (Fig. 4.12). The integrated intensity map for the RHD model (Fig. 4.21, top left) shows an asymmetrical ring with a central hole. This feature is commonly observed in HCO^+ near protostellar sources, albeit on scales of 100s AU rather than 10s AU (e.g. Jørgensen et al. 2013). Only the inner envelope at $r \sim 30$–50 AU is warm enough to produce significant HCO^+ $(1-0)$ emission and within the disc the HCO^+ emission is much fainter, primarily due to depletion at $r \lesssim 15$ AU (see Figs. 4.7 - 4.11). At $i = 90°$, the approaching (left) side is visibly brighter in both models. This is a well known phe-

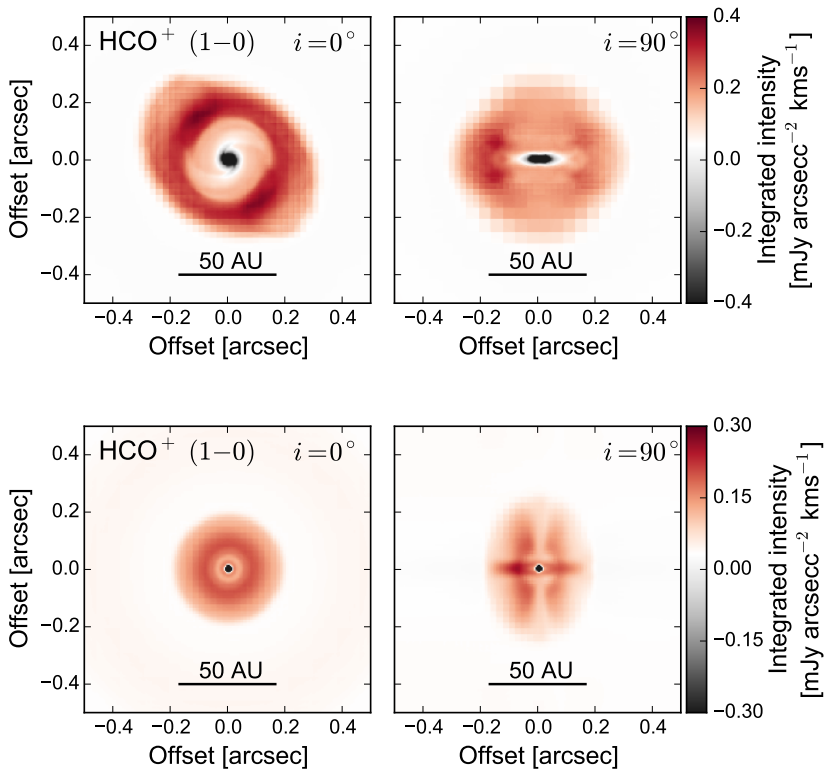

Figure 4.21: HCO^+ $(1-0)$ Integrated intensity for snapshot (d). Middle: RHD model; Bottom: MHD model

nomenon for rotating, infalling envelopes observed in an optically thin line.

The emission in the MHD model also has the appearance of a disc and a smaller region is traced. What we see is not just the pseudo–disc but also the conical outflow from above. At $i = 90°$, the emission is also less extended than in the RHD model, despite the presence of an outflow. Here the HCO^+ line traces the pseudo–disc and outflow and there are brighter structures in the outflow like those seen in the CO emission. The spectra for both models are double–peaked at $i = 0°$. For the RHD model this is due to the combination of infall motions and the self–absorption dip at low velocities. The spectra for the MHD model have similar features but the infall speeds are lower. The emission from the outflow at $i = 0°$ in the MHD model at $\sim -0.5\,\mathrm{km\,s^{-1}}$ reduces the depth of the dip between the central and blue shifted peaks from snapshot (c) onwards.

Before FHSC formation there is no central emission peak at the line centre. This central peak brightens as the core evolves and, from late in the FHSC stage, it is brighter than the blueshifted peak. This is true for both RHD and MHD models and provides a

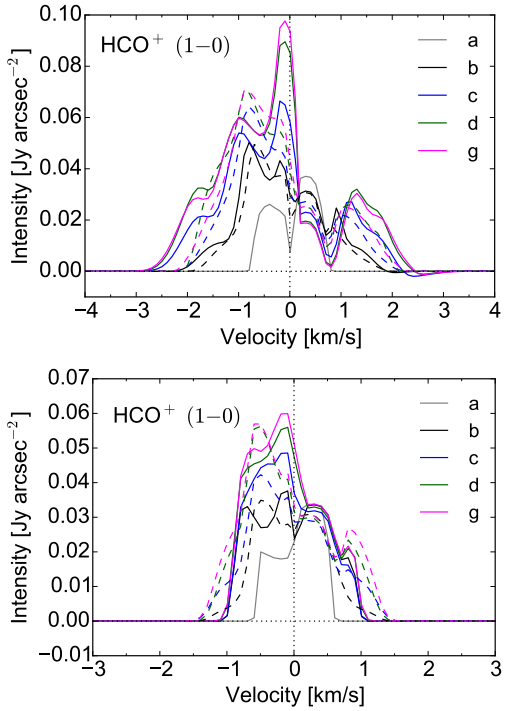

Figure 4.22: HCO^+ $(1-0)$ spectra for RHD model (top) and MHD model (bottom) within a 0.67 arcsec aperture. N.B. These use a grid of 5350 AU rather than the 400 AU grid used for the other species.

possible indication of the presence of an FHSC. The relative strengths of the line centre and red– and blueshifted peaks do depend on the aperture over which the spectra are averaged. The HCO^+ abundance is extremely low in the centre so this emission at the line centre is not simply coming from the FHSC. In the RHD model, the HCO^+ abundance increases within a shell between $\sim$ 20-30 AU (c.f. Figs. 4.7 and 4.8). This coincides with the outer regions of the disc–shaped FHSC, which strongly suggests that we are seeing the build up of material in the midplane. This feature is weaker in the MHD model (c.f. Figs. 4.9 and 4.10), which makes sense because gas is infalling along the midplane, i.e. the radial velocity = 0 for $i = 0$, but no disc forms so the density is lower.

4.5.4 Detectability with ALMA

In this section we examine the observability of features identified in the previous section by simulating ALMA observations. For all synthetic ALMA observations we assume a realistic precipitable water vapour (pwv) = 0.8 mm, unless otherwise stated, and use Briggs weighting. Simulated ALMA integrated intensity maps are presented in Fig. 4.23 and spectra in Figs. 4.24 and 4.25.

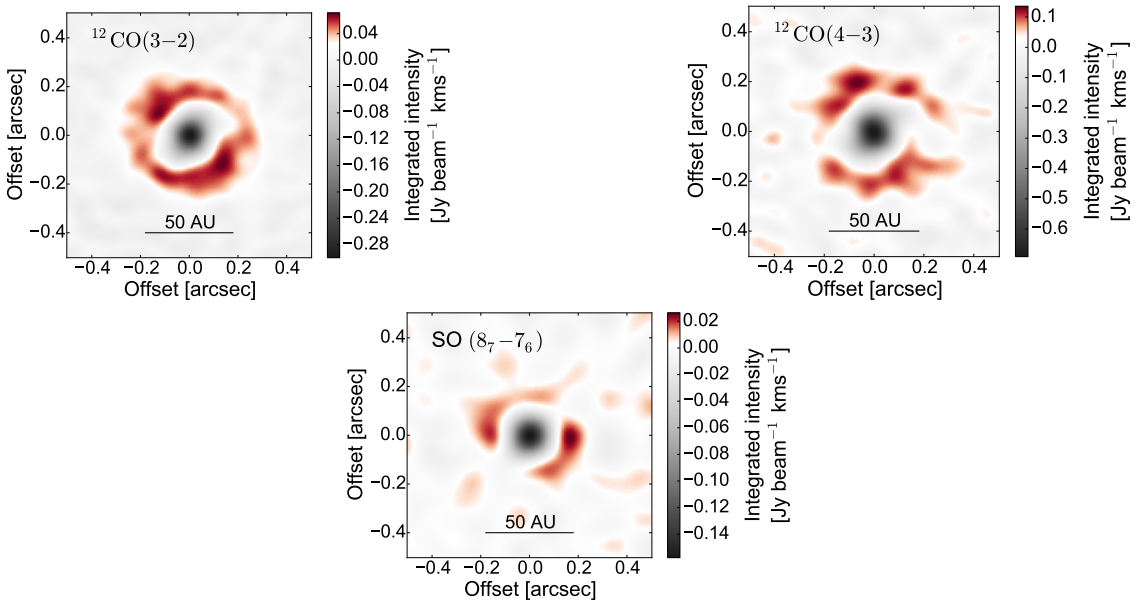

Figure 4.23: Synthetic ALMA observations of snapshot (d) of the RHD model in the face–on direction all with pwv = 0.8: CO $(3-2)$ 4h total time, ALMA out16 configuration giving 0.08×0.1 arcsec beam; CO $(4-3)$, ALMA out14 configuration giving 0.11×0.09 arcsec beam, 8h total integration; SO $(8_7 - 7_6)$, ALMA out14 configuration giving 0.15×0.12 arcsec beam, 8h total time.

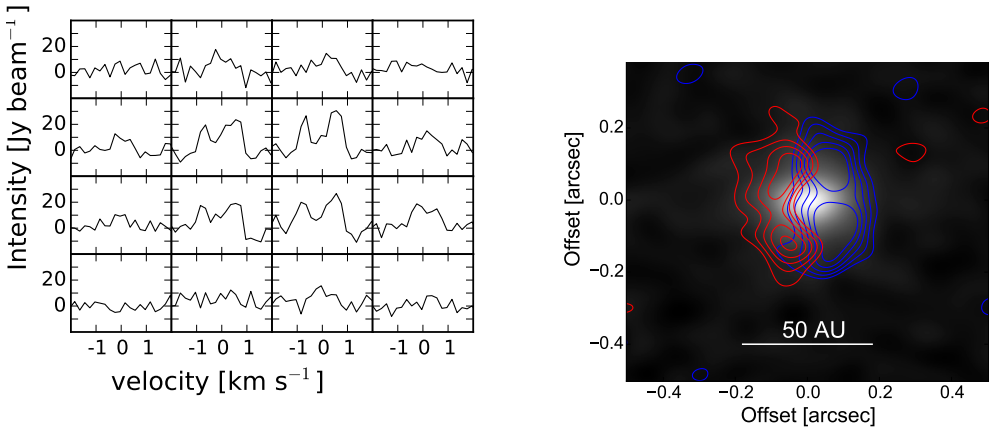

Figure 4.24: Synthetic ALMA observations of the MHD model snapshot (d) in CO $(4-3)$. Left: face–on direction, total integration time of 8 hours, pwv = 0.8 mm and 0.1×0.09 arcsec beam. Each panel is 0.12 arcsec across. Right: Red and blue contours show integrated intensity in the edge–on direction from $0\,\mathrm{km\,s^{-1}}$ to $4\,\mathrm{km\,s^{-1}}$ and $-4\,\mathrm{km\,s^{-1}}$ to $0\,\mathrm{km\,s^{-1}}$ respectively. Continuum is shown in greyscale. A total integration of 6 hours, beam size 0.1×0.09 arcsec and pwv = 0.5.

The asymmetric CO $(4-3)$ emission is discernible after a total on source time of 8 hours with the `out14` configuration (beam size 0.11×0.09 arcsec) (Fig. 4.23, centre panel). The absorption at the centre is very prominent and certainly detectable with a shorter integration. No additional detail is gained by using a smaller beam due to the increased noise. The CO $(3-2)$ line (Fig. 4.23, left panel) is brighter and it is possible to obtain a similar level of detail with the `out16` configuration (0.1×0.08 arcsec beam) with a far shorter 4 hour integration. Emission from the spiral arms clearly traces the asymmetric central region where the CO is seen in absorption. The CO $(3-2)$ line is more likely to be contaminated by the foreground cloud so it is encouraging that the detection of nonaxisymmetric structure is achievable in the higher $(4-3)$ transition. SO $(8_7 - 7_6)$ is also detectable (Fig. 4.23, right panel) and traces the spiral arms clearly with a total integration of 8 hours and the `out14` configuration (0.09×0.1 arcsec beam).

The CO $(4-3)$ spectrum in Fig. 4.15 showed a double–peaked feature, characteristic of the outflow, and we find that it should be possible to detect this with ALMA. In Fig. 4.24, top, the panels each cover a larger area due to the lower resolution of the convolved image but the feature is present in the central panels after a total on source time of 8 hours. A high resolution of ~ 0.1 arcsec is needed to detect the double–peak, otherwise it is hidden by low velocity emission from the pseudo–disc.

Many of the observed candidate FHSCs have accompanying detections of slow outflows. In Section 4.5.3.2 we showed that CO emission should trace the inner regions of the outflow. However, in the simulated ALMA observation in Fig. 4.24, bottom panel, there is no clear outflow structure either in the continuum or CO $(4-3)$ line emission. The line emission reveals red– and blueshifted lobes, indicative of the rotation of the outflow. The rotation velocities are comparable to, or higher than, the outflow velocities. Even at low inclinations, the outflow motions were not detectable but rotation should be observable with ALMA with a 6 hour integration.

The SO $(8_7 - 7_6)$ transition revealed a shift in the line centre and the development of an absorption feature between snapshots (c) and (d). This difference is still clear in the simulated ALMA observation (Fig. 4.25, upper panel) and may provide a method for distinguishing a source midway through FHSC stage from a more evolved object. In

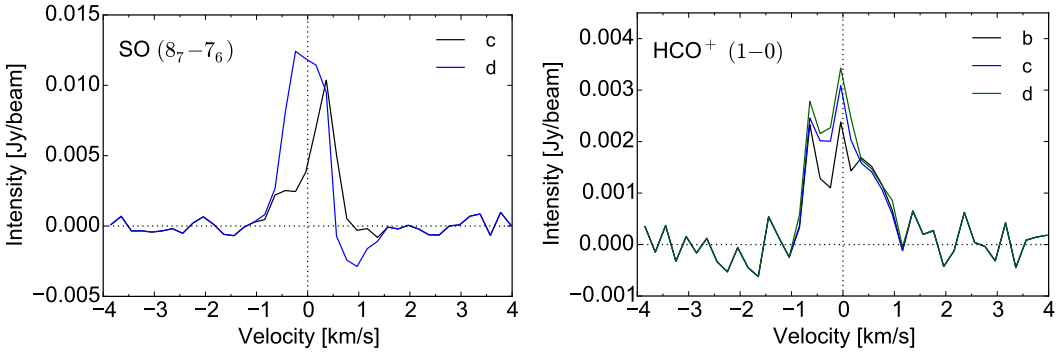

Figure 4.25: Synthetic ALMA spectra of the MHD model in the face–on direction. Top: SO $(8_7 - 7_6)$, 8 hours total integration, out14 configuration. It is possible to distinguish spectra early and late in FHSC stage at $i = 0°$ as the outflow develops. Bottom: MHD model HCO$^+$ (1-0), 8 hours total integration, 0.21×0.25 arcsec beam. As the FHSC grows emission increases at the line centre and becomes brighter than the blue peak and this is still discernible in the synthetic interferometric spectra.

HCO$^+$ too (Fig. 4.25, lower panel), the difference between the spectra of snapshots (b) and (c) is clear although somewhat more subtle.

CS emission was found to be indistinguishable from noise even with an 8 hour integration with pwv $= 0.5$ mm for both the $(8 - 7)$ and $(2 - 1)$ transitions from the MHD model. The CS $(8 - 7)$ line only became detectable for the last snapshot (g) with excellent observing conditions of pwv$= 0.2$ mm and an 8 hour integration with the `out20` configuration.

4.5.5 Disc accretion feedback

So far we have calculated the chemical abundances until only shortly after the formation of the stellar core and have found that there is little change in the chemical abundances in the envelope because the temperature structure at $r \gtrsim 200$ AU remains largely unchanged. After the stellar core forms, thermal feedback will alter the temperature of the envelope. Although the intrinsic luminosity of the protostar will be low for some time, accretion luminosity is expected to be significant.

We now extend the RHD simulation for a few hundred years beyond stellar core formation to allow the temperatures in the envelope to rise so we can explore whether there is a difference in the chemistry of the envelope and over what timescales this might occur. To extend the calculations significantly beyond stellar core formation, we need to use sink particles because the particle timesteps become very small at high densities (Bate

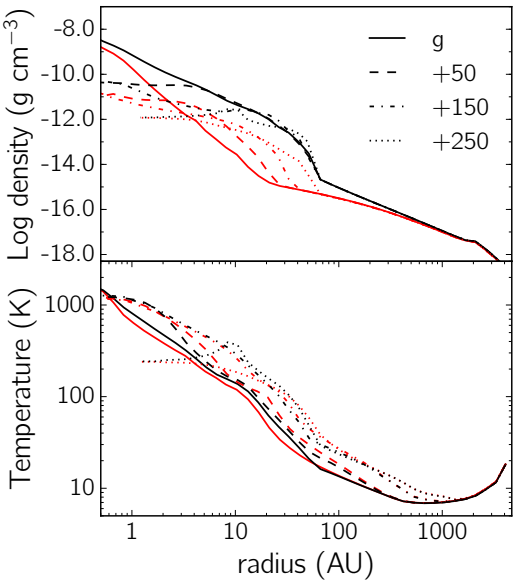

Figure 4.26: Evolution of the density and temperature profiles after stellar core formation from the disc accretion feedback model. Snapshots are taken shortly after the formation of the stellar core (g) and at 50, 150 and 250 years later. Black lines: horizontally averaged profiles. Red lines: vertically averaged profiles.

1995). A sink particles is inserted after the stellar core has formed, when the maximum density exceeds $0.1\,\mathrm{g\,cm^{-3}}$, and gas within 0.1 AU of the sink particle is accreted. The accretion luminosity is the dominant source of heating at this early stage and to model this we use the disc accretion feedback model of Jones and Bate (2018). For this, a sub—grid model is implemented in which the sink particle represents a protostar and a disc with gas accreting through the disc onto the star. The disc has an outer accretion radius of 0.1 AU and an inner radius of 0.02 AU . For the first ten years after sink formation the accretion rate is very high as the remnants of the FHSC fall onto the stellar core. After this, the accretion rate becomes more steady and the accretion luminosity is calculated assuming an initial accretion rate of 10^{-6} $\mathrm{M_\odot}$ year^{-1} and is added as a source term into the flux–limited diffusion equations for gas particles surrounding the protostellar sink particle.

Fig. 4.26 shows the evolution of the density and temperature profiles after the formation of the stellar core with this disc accretion feedback model. The central density decreases quickly after stellar core formation as the gas is accreted onto the protostar. At $r > 10$ AU the density profile in the disc plane changes little but in the vertical direction the density increases as material in the envelope falls inwards. The temperature increases substantially over the 250 years out to $r = 1000$ AU and the radius at which $T > 25$ K, the

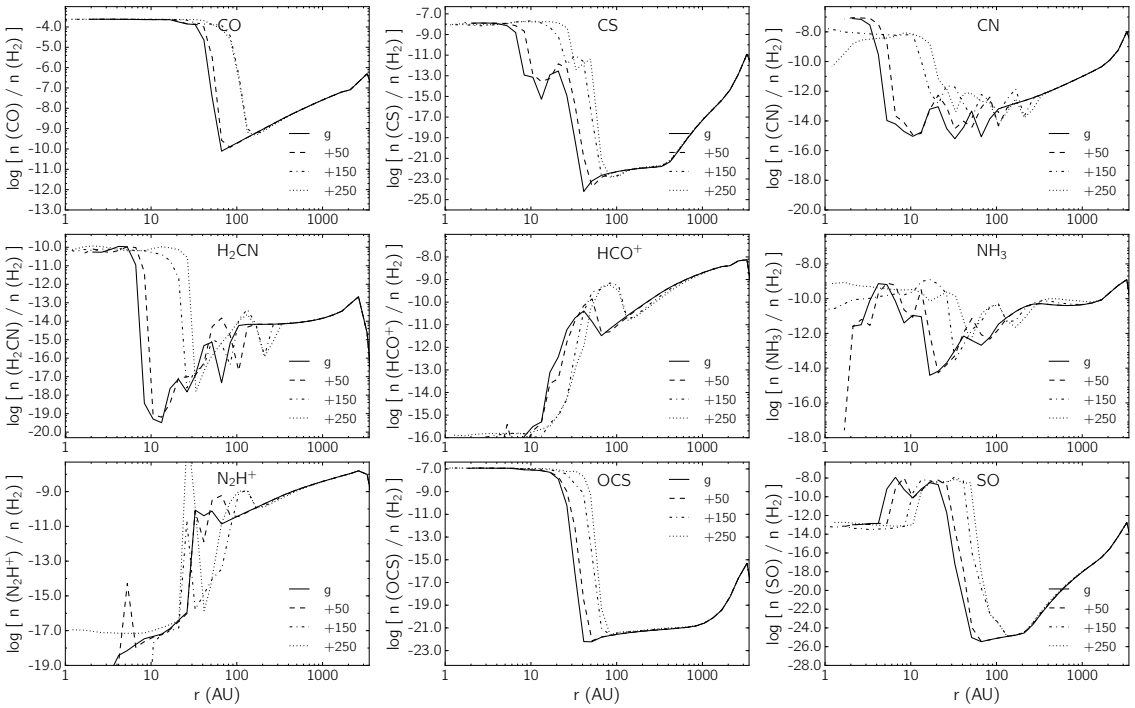

Figure 4.27: Abundance profiles perpendicular to the rotation axis with the stellar feedback model for snapshots taken at stellar core formation (snapshot g) and 50, 150 and 250 years later.

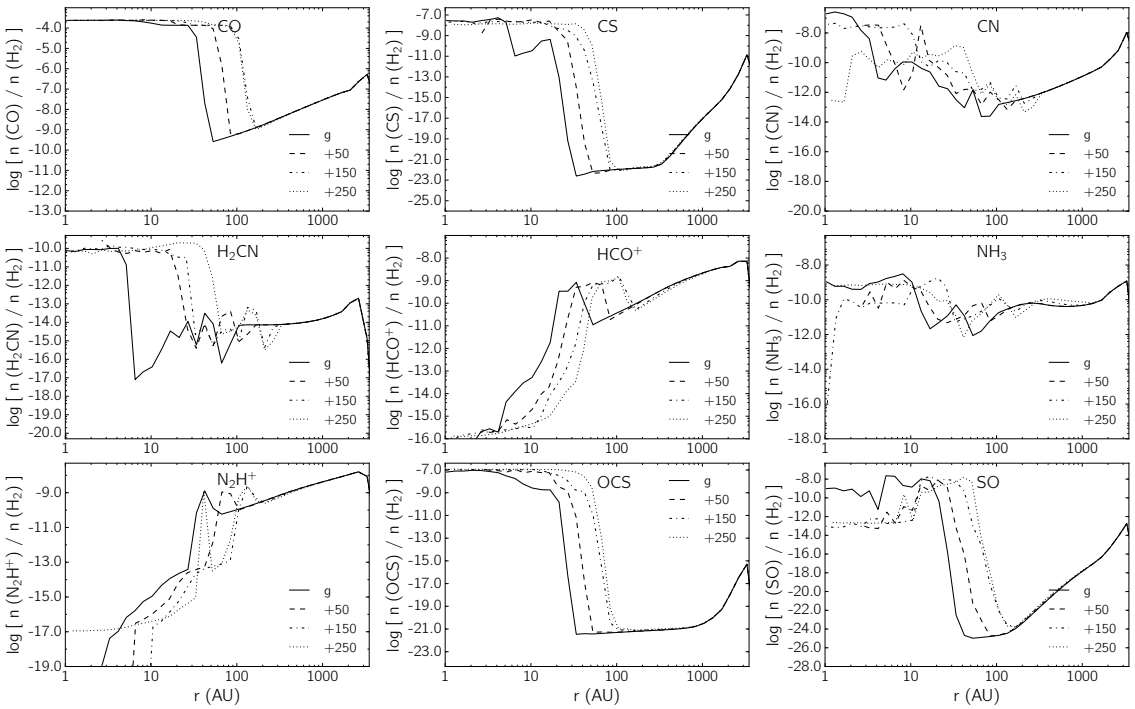

Figure 4.28: Abundance profiles parallel to the rotation axis with the stellar feedback model for snapshots taken at stellar core formation (snapshot g) and 50, 150 and 250 years later.

approximate sublimation temperature of CO, increases from ~ 60 AU to ~ 150 AU .

The abundance profiles for snapshot 'g' (stellar core formation), and 50, 150 and 250 years later are presented in Figs. 4.27 and 4.28. The rapid increase of temperature results in the sublimation radius of many species increasing quickly too in the space of just 250 years. In this time, the extent of the disc traced by CO, SO and OCS doubles. CS, CN and H_2CN were previously only present in significant abundances in the centre of the FHSC but are present within a region of tens of AU after 250 years. The change in the abundance profile of CS is particularly interesting because during the FHSC stage we found that CS traced too small a region to be spatially resolvable. In this short time, CS now traces the inner disc and envelope to $r \lesssim 30$ AU .

These rapid changes in the abundance profiles are likely to cause the spectra of extremely young protostars to be distinct from the spectra of FHSCs, which offers some hope for distinguishing between the two stages observationally. We note that the accretion rate soon after stellar core formation is uncertain and the value we use for the initial accretion rate may be rather conservative. A higher accretion rate will produce a higher accretion luminosity and the gas temperatures will increase even faster.

4.6 Discussion

4.6.1 Chemical abundances

Abundances of chemical species that form primarily on the surface of dust grains are highly underestimated and so we do not simulate observations for them. We now compare the abundances of several species presented in this paper with observed values, bearing in mind that the observed values were measured for dense starless cores. We will later compare our chemical abundances to the results of other simulations in 4.6.5.

The calculated initial abundance of CO is 1×10^{-4} which is similar to the measured CO abundances in TMC-1 (1.7×10^{-4}) and L134N (8.7×10^{-5}) (Agúndez and Wakelam 2013; Dickens et al. 2000). As the core collapses and the density increases, the CO freezes out and the abundance is lower than in TMC-1 and L134N, which is to be expected as the density exceeds that of L134N ($n_{H2} \approx 2 \times 10^4\,\mathrm{cm}^{-3}$ which corresponds to

$8 \times 10^{-20}\,\mathrm{g\,cm^{-3}}$, Dickens et al. 2000) and TMC-1 ($n_{H2} \approx 8 \times 10^{4}\,\mathrm{cm^{-3}}$ which corresponds to $3 \times 10^{-20}\,\mathrm{g\,cm^{-3}}$, Pratap et al. 1997).

The initial abundance of HCO^+ is 7×10^{-9} which is similar to the measured abundance of 7.9×10^{-9} in L134N (Dickens et al. 2000) and a little lower than the value of 9.3×10^{-9} found for TMC-1 (Pratap et al. 1997). The calculated HCO^+ abundance is close to the observational values than that of CO.

The initial abundance of CS (2×10^{-8}) is an order of magnitude greater than that observed in TMC-1 (Pratap et al. 1997) and the KIDA network overestimates the CS abundance for t $<10^6$ years. CS freezes out in the collapsing dense core and only exceeds 10^{-10} in the central few AU. Observations of the FHSC candidate Cha-MMS1 (Tsitali et al. 2013) find a CS abundance of 2.5×10^{-9} at a radius of 8000 AU, which is consistent with our calculations if extrapolated to this radius.

The SO abundance is significantly lower by ~ 4 orders of magnitude initially than observed in TMC-1 and L134N. The initial abundance of NH_3 is initially ten times lower than observed in TMC-1 and L134N and reaches a few 10^{-9} in the core.

4.6.2 Spatially resolved structures

The spiral structure that develops in the RHD model should easily be spatially resolved in dust continuum observations. Indeed, there are now several examples of such structures observed in discs (e.g. Grady et al. 2013; Pérez et al. 2016; Stolker et al. 2016). We can examine whether the rotational or outflow structures are more prominent in line observations than the continuum after modelling the chemical evolution and the line emission.

The spiral structure remains more easily observed in continuum emission on scales of $\sim$ 20 AU. This is, in part, because the lines of species that trace the FHSC are seen in absorption against the continuum across most of the FHSC. SO $(8_7 - 7_6)$, CO $(3-2)$ and CO $(4-3)$ do however trace the spiral structure on scales of 50-60 AU where the continuum emission is much fainter.

While HCO^+ and CO emission traces the outflow, the extent is very small at a rep-

resentative distance of 150 pc. HCO^+ emission is also very faint. Any structure will be difficult to distinguish from noise even with an on source time of 8 hours.

Observations of CO $(4-3)$ and SO (8_7-7_6) lines could be used to supplement continuum observations of rotating candidate FHSCs at low inclinations to provide evidence of rotational structures. For the MHD model here, it looks unlikely that the outflow will be detectable in HCO^+ line emission maps. The outflow is not well defined in the simulated ALMA integrated intensity map, but red and blue lobes are just detectable within 8 hours in CO $(4-3)$ (see Fig. 4.24, right panel).

4.6.3 Kinematics

Currently, the outflow velocity is one of the factors considered when classifying a faint, young source as a candidate FHSC. FHSC outflows are expected to be wide and to have velocities of a few $\mathrm{km\,s^{-1}}$ (e.g. Tomisaka 2002; Machida et al. 2008; Bate et al. 2014; Lewis and Bate 2017; Wurster et al. 2018). Some sources identified as candidate FHSCs have later been reclassified when further observations revealed a collimated outflow, faster than $\sim 10\,\mathrm{km\,s^{-1}}$ once inclination effects were considered (e.g. Per-Bolo 58, Dunham et al. 2006, and B1-bS, Gerin et al. 2015). During the relatively short lifetime of the FHSC, the extent of the outflow is only a few 100 AU and infall velocities are comparable to outflow velocities so it is questionable whether the FHSC outflow would be detectable.

Of the species considered here, only CO spectra clearly show the signature of the outflow. This is because the CO abundance is much higher in the outflow out to ~ 30 AU above the midplane than in the envelope. However, the outflow velocities are so slow that once we consider a moderate inclination the outflow velocity component becomes negligible in comparison to the rotational and, in reality, turbulent motions. The contribution of the outflow to the $HCO^+(1-0)$ spectrum is less clear. This line is optically thin and still dominated by infall due to the higher relative abundance in the envelope than the denser central regions.

The different chemical species trace infall on different scales. Infall is apparent in the optically thick lines as redshifted absorption against the continuum. Species such as

CS and SO trace regions within the FHSC and a few AU above the midplane and reveal infall onto the FHSC. As expected, HCO^+ traces larger scale infall onto the disc.

Most of these species display the double–peaked rotation signature in the spectra viewed from edge–on. This is not true of SO, CS or CO from the RHD model, however. In both CO and SO the disc is seen in absorption. SO traces a smaller radius than CO but most of the central part of the disc is optically thick. The SO emission comes from essentially a narrow ring offset from the midplane. The resulting spectrum is then missing the double peak. The same is true for CS but on a smaller scale. We emphasize that the rotation signatures appear to be stronger for the MHD model which does not have a rotationally supported disc but has a rotating outflow.

4.6.4 Observing with ALMA

Many species that may in theory distinguish features associated with the FHSC, including CS, are likely to be too faint to detect, even with ALMA. Temperatures are still very low in much of the object so abundances of ISM species are depleted with respect to the surrounding envelope. In addition, outflow and disc structures are still relatively compact (100s and 10s of AU respectively). Efforts to identify an FHSC should therefore concentrate on just the most abundant species.

Although these structures are still compact, the resolution is a less important consideration than minimising the noise. We find the optimum resolution is 0.08 to 0.1 arcsec for detecting rotational structures at 150 pc. With a synthesized beam of 0.1 arcsec, the largest recoverable scale is ~ 1.5 arcsec which means that emission from the inner envelope should be acceptably recovered. Observations were synthesized here with a realistic value for pwv = 0.8. For worse observing conditions, the FHSC structures are very likely to be indistinguishable from noise. In order to detect the outflow spatially in CO, pwv ≤ 0.5 is necessary. An on source time of 8 hours is required for the lines modelled here. Only CO $(3-2)$ is feasible with a shorter, 4 hour, integration.

4.6.5 Comparison to other work

There have been only a few prior attempts to model chemistry of collapsing dense cores that we know of, some from analytical density and temperature structures and some from hydrodynamical models. We compare to the following work, where possible, since not every paper includes every chemical species. Aikawa et al. (2008) calculated chemical abundances for a 1-D frequency–dependent radiation hydrodynamical model of a collapsing core. The chemical calculations included gas–phase and grain surface reactions and assumed low metal elemental abundances. van Weeren et al. (2009) performed similar calculations but from 2-D hydrodynamical models, allowing the effects of a disc structure to be explored. The chemical evolution was followed for 700 tracer particles by calculating gas–phase, gas–grain and grain surface reactions. Furuya et al. (2012) used a 3-D RMHD model of a collapsing 1 $M_{\odot}$ cloud, calculating chemistry for 10^5 tracer particles. Gas–phase and grain surface reactions were included. Hincelin et al. (2016) specifically set out to look for chemical differences between different components of the core in 3-D. They performed several RMHD simulations of a collapsing 1 $M_{\odot}$ cloud and calculated the chemical evolution of 10^6 tracer particles with gas–phase and grain surface reactions. Dzyurkevich et al. (2016) used a reduced network of mainly gas–grain H-C-O chemistry to calculate abundances at the same time as calculating the dynamical evolution of the collapse of a dense core. Maret et al. (2013) attempted to model the chemistry and two line profiles to compare to two observed pre–stellar cores. They took an analytical density profile which did not vary in time since they did not seek to model a collapsing core but these results are useful to compare with the abundances in the envelope here. The chemical model included gas–phase and gas–grain reactions. We note that the above papers quote abundances relative to the total density of hydrogen nuclei and we account for this in the comparison.

The highest abundances of CO that we obtained during the collapse of the pre–stellar core are approximately a factor of 2 higher than those reported by Furuya et al. (2012), which used a ≈ 50 per cent lower elemental C^+ abundance. The envelope abundance of CO was a few $\times 10^{-7}$ which is similar to the values of Hincelin et al. (2016), Furuya et al. (2012) and to the abundance from the fiducial single sized dust grain model (S1) of

Dzyurkevich et al. (2016) at ~ 2000 AU.

In the envelope, we find an HCO^+ abundance of a few $\times 10^{-9}$, which is similar to that of van Weeren et al. (2009) and Dzyurkevich et al. (2016) at ~ 6000 AU in their models. This abundance is a little higher than that found for similar radii by Maret et al. (2013) and Aikawa et al. (2008).

Abundances of CS in the FHSC and envelope have previously been calculated to be a few $\times 10^{-11}$ (Hincelin et al. 2016; van Weeren et al. 2009) or as high as 10^{-8} (Aikawa et al. 2008). Between these regions CS is very highly depleted. We find the abundance in the centre to be a few $\times 10^{-9}$ and a few $\times 10^{-12}$ in the outer envelope.

The abundance of NH_3 is lower than the central values of a few 10^{-6} to a few 10^{-5} reported by others (Aikawa et al. 2008; van Weeren et al. 2009; Hincelin et al. 2016). The initial abundance of N_2H^+ agrees well with the envelope abundances of van Weeren et al. (2009) and Hincelin et al. (2016). The abundance in the centre is a few 10^{-20} as was found by Hincelin et al. (2016) but we find the abundance in the disc and pseudo–disc to be far lower than the abundances they report for those regions.

Synthetic CS spectra were presented by Tomisaka and Tomida (2011) and these are qualitatively very different to those here, but their models assumed a constant CS abundance of 4×10^{-9} throughout whereas we expect CS to be depleted as the pre–stellar core collapses. It is not returned to the gas phase in the envelope until some time after the protostar has formed (see also Aikawa et al. 2008 for a study of the chemical changes that occur as the protostellar core warms up). We find that the CS sublimation radius extends to $\sim$ 10–15 AU in the MHD model (Figs. 4.7 and 4.8) so does not trace the gas kinematics. In the RHD model, the CS sublimation radius extends to 20–30 AU (Figs. 4.9 and 4.10) because the FHSC is larger due to the greater rotational support. In addition, because of the freeze–out, the CS $(8-7)$ emission is faint, and likely to be undetectable during much of the FHSC phase.

Hincelin et al. (2016) find that species such as CS and HCO^+ may be useful for distinguishing the envelope from the outflow and pseudo–disc. We also find a difference in abundance between the envelope and these components but for CS the spectrum is still

dominated by the central few AU where the abundance of CS and temperature are much higher. For HCO^+, the decrease in abundance in the disc and outflow is offset by the enhanced density and temperature such that the outflow and pseudo–disc are brighter than the envelope in emission maps. We agree with their conclusion that the chemistry of the envelope alone cannot distinguish between FHSC formation models. The temperature profile of the envelope changes very little and changes in the composition of the envelope are likely to occur only on longer timescales. Nevertheless, the spectra are very sensitive to the distribution of chemical species so chemical evolution should certainly be taken into account when simulating molecular line observations.

4.6.6 Determining evolutionary stage

The main objective of modelling the chemistry and synthetic observations of the FHSC is to determine how to distinguish it from "empty" pre–stellar cores and from very young protostars. The abundances of CS and SO are extremely low before FHSC formation and the SO $(8_7 - 7_6)$ line becomes detectable midway through the FHSC stage. CS $(8 - 7)$ remains undetectable with 8 hours integration with ALMA throughout FHSC stage and will still be close to the detection limit after soon after stellar core formation, even in the best observing conditions. A detection of CS at subarcsecond scales would preclude a source from being an FHSC.

We saw in Section 4.5.5 that after the stellar cores forms thermal feedback from accretion warms the inner envelope and disc such that CO, CS and SO trace regions up to 100 AU , 250 years after stellar core formation. CS emission from the infalling envelope is therefore very likely to be detectable and perhaps even spatially resolved at this stage in contrast to the faint CS emission from the small region close to the FHSC. This strengthens the case for CS as an indicator of an object more evolved than the FHSC, although we note that there was some variation in peak abundance of CS as calculated with the KIDA 2011 and KIDA 2014 networks (see Sections 2.5.2 and Appendix A).

Changes in the shape of the SO $(8_7 - 7_6)$ spectrum at low inclinations when the outflow is launched should be detectable with ALMA. The central peak of HCO^+ $(1 - 0)$ becomes brighter than the blueshifted peak late in the FHSC stage, offering another

possible indicator of evolutionary stage.

Factors other than age cause considerable variation in the properties of the spectra. For this reason, it is probably not possible to provide generic criteria to distinguish an FHSC from a stellar core. The positive identification of the FHSC is going to require specific modelling of individual sources based on observationally derived morphology, magnetic field and dust properties to determine the spectra expected from those specific conditions.

4.6.7 Comparison to observations of candidate FHSCs

There are a few published observations of candidate FHSCs with better than 1000 AU resolution. We now consider whether these sources are genuinely in the FHSC stage in light of this work and also from the SED fitting of Chapter 3.

CS $(2-1)$ and CS $(5-4)$ transitions have been detected at the FHSC candidate Chamaeleon-MMS1 (Tsitali et al. 2013). We do not expect there to be detectable CS emission from the FHSC and what is detected here is mostly emission from the surrounding envelope since the beam size (24.9 arcsec) is much larger than our models. It would be informative to obtain interferometric observations of CS emission with a smaller beam to determine its source. The abundance of CS increases quickly within $r < 50$ AU after stellar core formation, during which time the extent of the outflow would not have increased significantly. The stellar core outflow is expected to launch very quickly after stellar core formation unless the magnetic field is weak or misaligned. While it is unlikely that Cha-MMS1 is an FHSC, it is also unlikely to have evolved far beyond stellar core formation. Further observations suggest rotational motions and an absence of shocks, which also points to it being a very young object. The results of previous SED fitting indicated too that Cha-MMS1 is more likely to be a very young protostar than an FHSC (see Chapter 3).

Another candidate is L1451-mm where a slow, poorly collimated outflow was detected in CO $(2-1)$ (Pineda et al. 2011; Tobin et al. 2015a). We find that CO should indeed trace the outflow although in the synthetic observations the velocity channels trace the ro-

tational motions of the outflow. The observed CO extends for several hundred AU which is a far larger region than we would expect, unless the lifetime of the FHSC is longer than expected.

Two candidate FHSCs in Ophiuchus presented by Friesen et al. (2018) are also consistent with the results here. Blue– and redshifted CO $(2-1)$ emission was detected at SM1N without a clear outflow morphology. This is what we find from simulated ALMA observations: the FHSC outflow has a small extent and once the image was convolved with the ALMA beam and noise was added we did not see a clear outflow structure. N6-mm also appears to have a compact and broad outflow. No absorption against the continuum was observed at either source but this is not expected in CO from the MHD model.

The SED of CB17-MMS1 is consistent with a young FHSC. There is also a rather confusing structure seen in CO $(2-1)$ emission thought to be associated with the source (Chen et al. 2012). If this is tracing an outflow then the extent is probably too great for an FHSC since we expect only the central part of the outflow to be detectable where temperatures are high enough for CO to desorb from dust grains.

B1-bN is another FHSC candidate that has been observed several times now. Previous SED modelling indicated that the source is consistent with an FHSC but only if it has a substantial disc and is viewed at a near side–on inclination (see Chapter 3, Young et al. 2018). An outflow has been detected in CO $(2-1)$ (Hirano and Liu 2014), H_2CO $(2_{02}-1_{01})$ and several CH_3OH $(3-2)$ lines (Gerin et al. 2015). This outflow is thought to extend to ≈ 1000 AU (see Table 3 of Gerin et al. 2015). We find that CO only traces the inner few 10s of AU of the outflow and H_2CO and CH_3OH are unlikely to trace a much more extended region than CO. Therefore it is difficult to explain this observation as an FHSC outflow with such a large extent. Gerin et al. (2015) also point out that the outflow is not aligned with the magnetic field which means it is possible that the source is a slightly more evolved object but with a shorter and less well collimated outflow than might be expected for its age.

In Chapter 3 we concluded that the candidate FHSC Per-Bolo 58 is unlikely to be a true FHSC based on the results of the SED fitting. It remains a puzzling source, however,

and has been observed several times. As mentioned previously, a slow bipolar outflow with a charactersitic velocity of $2.9\,\mathrm{km\,s^{-1}}$ was discovered by Dunham et al. (2011) and this has a clear jet–like morphology. The detection of these clear jet–like lobes in ^{12}CO $(2-1)$ indicates that the outflow must have a reasonably high inclination and therefore the outflow velocity will be higher once deprojected, and probably faster than that expected for a FHSC. Furthermore, in our model CO traced only the base of the outflow and the observed Per-Bolo 58 outflow extends > 1000 AU .

4.6.8 Limitations

The chemical network used here omitted grain–surface reactions and we therefore excluded species known to be governed by surface reactions. Species such as formaldehyde and methanol are very likely to be good tracers of the outflow so it is worth modelling observations of these in future. The chemical network we have used is valid between 10-800 K and is extrapolated in the inner 1 AU after late FHSC stage. While this is unlikely to affect the results here which concern larger scales, the calculated abundances in the centre of the FHSC may be different when additional reactions and correct rates are considered.

In this chapter we used two extreme models: one which forms a disc and another which forms an outflow and pseudo–disc. Other initial conditions will result in a combination of these structures, which may alter the spectral features. Specific modelling is therefore required to compare with particular sources in detail.

4.7 Conclusions

We have presented synthetic CO, CS, SO and HCO^+ observations produced from hydrodynamical and chemical modelling of the formation and evolution of the first hydrostatic core. We showed that rotational structures should be detectable by ALMA in CO $(4-3)$ and SO (8_7-7_6) transitions in realistic observing conditions. CO emission did not reveal the outflow morphology in simulated ALMA maps but red and blue lobes caused by rotation, rather than outflowing motions, were detectable.

Regarding determining the evolutionary stage, we find changes in SO and HCO^+

spectra as the FHSC develops when viewed at a low inclination. We find that CS is undetectable during the FHSC stage with a reasonable integration time and observing conditions with ALMA. This means that candidate FHSCs with CS detections on subarcsecond scales (i.e. without significant contribution from the envelope) are unlikely to be FHSCs; they are likely to be more evolved.

FHSC structures are still very compact and most chemical species are frozen out in much of the inner envelope. Although chemical evolution alone is unlikely to provide a diagnostic of the FHSC, synthetic molecular line observations should account for chemical evolution. Using constant spatial abundances is likely to lead to incorrect synthetic observations.

Finally, we compare these results with selected candidate FHSCs. We rule out B1-bN due to the detection of an outflow which extends $\sim$1000 AU. Cha-MMS1 is more likely to be a very young protostar but we cannot rule it out completely because there is no reported detection of an outflow and existing observations resolve regions no smaller than 1000 AU. L1451-mm is unlikely to be in FHSC stage because the extent of the observed outflow is greater than we would expect. Similarly, if the observed CO emission near CB17-MMS1 is tracing an outflow driven by the source then it is too extended to be driven by an FHSC. This leaves Oph A SM1N and N6-mm as the most promising sources to follow up.

Identifying the FHSC in nature will require interferometric observations of lines such as CO $(4-3)$ and SO (8_7-7_6) with a spatial resolution ~ 0.05 arcsec and a velocity resolution of $0.2\,\mathrm{km\,s^{-1}}$ to detect structures on the scale of a few 10s AU. Detection of these lines should be achievable within an 8 hour integration with ALMA.

Chapter 5

Chemical modelling of star cluster formation

5.1 Introduction

In this chapter we apply the chemical calculations developed in Chapter 4 to a larger scale model of the formation of a stellar cluster. Previously, the chemical calculations were limited to single collapsing cores but we are now able to investigate the chemical abundances in the wider context of the surrounding molecular cloud. We also compare the chemical abundances calculated with KROME to those found from the simple chemical model employed in the RHD code of Bate and Keto (2015), which was used for the 1 $\mathrm{M}_{\odot}$ core models and for the 500 $\mathrm{M}_{\odot}$ cluster formation discussed in this chapter.

5.2 Method

We follow a similar approach to post–processing the hydrodynamical simulation as presented in Chapter 4. The hydrodynamical model we use here was the calculation presented in Bate (2019), using the solar metallicity opacities. This calculation follows the collapse of a molecular cloud under self–gravity and includes radiative transfer and the diffuse ISM model of Bate and Keto (2015). Included in the latter is a simple chemical model which computes abundances of C, C^+ and gas–phase CO, including CO depletion

(Keto and Caselli 2008) to allow accurate calculation of cooling rates. A model for the formation and dissociation of molecular hydrogen (Glover et al. 2010) is also included for calculating heating rates.

The abundances of atomic carbon, CO and C^+ are calculated using the following two equations (Keto and Caselli 2008; Glover and Clark 2012a; Bate and Keto 2015):

$$\frac{\mathrm{CO}}{\mathrm{C}^+} = \frac{6 \times 10^{-16} n_{\mathrm{H2}}}{1.4 \times 10^{-11} G_0 \exp(-3.2 A_v)}, \tag{5.1}$$

$$\frac{\mathrm{C}}{\mathrm{C}^+} = \frac{6 \times 10^{-16} n_{\mathrm{H2}}}{2.1 \times 10^{-10} G_0 \exp(-2.6 A_v)}. \tag{5.2}$$

Here G_0 is the ISRF in units of the Habing flux (Habing 1968) and we use $G_0 = 1$. The visual extinction is calculated with Equation 2.17.

The initial spherical cloud is formed of 500 $\mathrm{M}_\odot$ of molecular gas and has a radius of 0.404 pc (83 300 AU) giving a uniform initial density of 1.2×10^{-19} $\mathrm{g\,cm^{-3}}$ ($\mathrm{n_H} \sim 6 \times 10^4\,\mathrm{cm^{-3}}$). An initial turbulent velocity field was applied and the initial temperature is set so that the cloud is in equilibrium with the ISRF, as for the RHD2 model of Chapter 3 and the RHD model of Chapter 4. The calculations are described in detail in Bate (2019).

This cluster calculation used 3.5×10^7 SPH particles. The memory of regular compute nodes is exceeded if we require an array storing abundances of 679 chemical species for each particle. To avoid this issue we divide the cluster into eight parts. Since the chemical calculation for each particle is independent of the other particles, the post–processing of each part of the model can be undertaken separately. This process follows the same method as used in Chapter 4: the chemical solver KROME is called for each particle and the abundances are updated accordingly. The separate parts of the model are then later merged together.

This model makes use of sink particles, which were inserted when the density exceeded $10^{-5}\,\mathrm{g\,cm^{-3}}$. This occurs during the second collapse, before the stellar core forms. Any gas particle within $r_{acc} = 0.5$ au of a sink particle is accreted if it is bound and it has insufficient specific angular momentum to form a circular orbit at r_{acc} from the sink

particle. Sink particles within 0.03 au of each other are merged and there is no radiative feedback from the sink particles.

The main difference here is that we start with a whole molecular cloud rather than an isolated dense core, which means that a different initial timestep should be used. The initial abundances used to set each SPH particle initially are identical to those used for the dense cores in Chapter 4, calculated for dense ISM conditions with $T = 10$ K, $\rho = 4 \times 10^{-18}\,\mathrm{g\,cm^{-3}}$ and $A_v = 20$. The chemistry was evolved for 1000 yrs for the initial uniform sphere. After this, the minimum chemistry timestep was 700 yrs. As for the $1\ \mathrm{M}_\odot$ core calculations, this means that not every SPH dump file is used because the temperature and density tend to change slowly between consecutive files.

5.3 Results and discussion

As the cloud collapses, dense filaments begin to form due the turbulent velocity field that was applied initially. Dense cores form primarily in the centre of the cloud and also along the dense filaments. The development of these structures can be seen in the column density figures in the top row of Fig. 5.1. The dense cores which continue collapsing form protostars which are represented by sink particles, shown as white circles in the figure. The protostars interact gravitationally which causes some of them to be flung away from their birthplaces into less dense regions of the cloud.

We first discuss the distribution of chemical abundances in the collapsing cloud and then compare the abundances calculated by post–processing the hydrodynamical calculation with KROME to the abundances calculated in the hydrodynamical model for determining cooling rates.

5.3.1 Chemical abundances in the molecular cloud

In Fig. 5.1 we present the column density, gas temperature, dust temperature and abundances of CO, SO, HCO^+ and CS for a 0.6 pc $\times 0.4$ pc region at the centre of the molecular cloud for snapshots taken at $148\,400$, $190\,300$ and $227\,900$ yrs after the start of the simulation. The temperatures are lower in the higher density regions due to efficient cooling

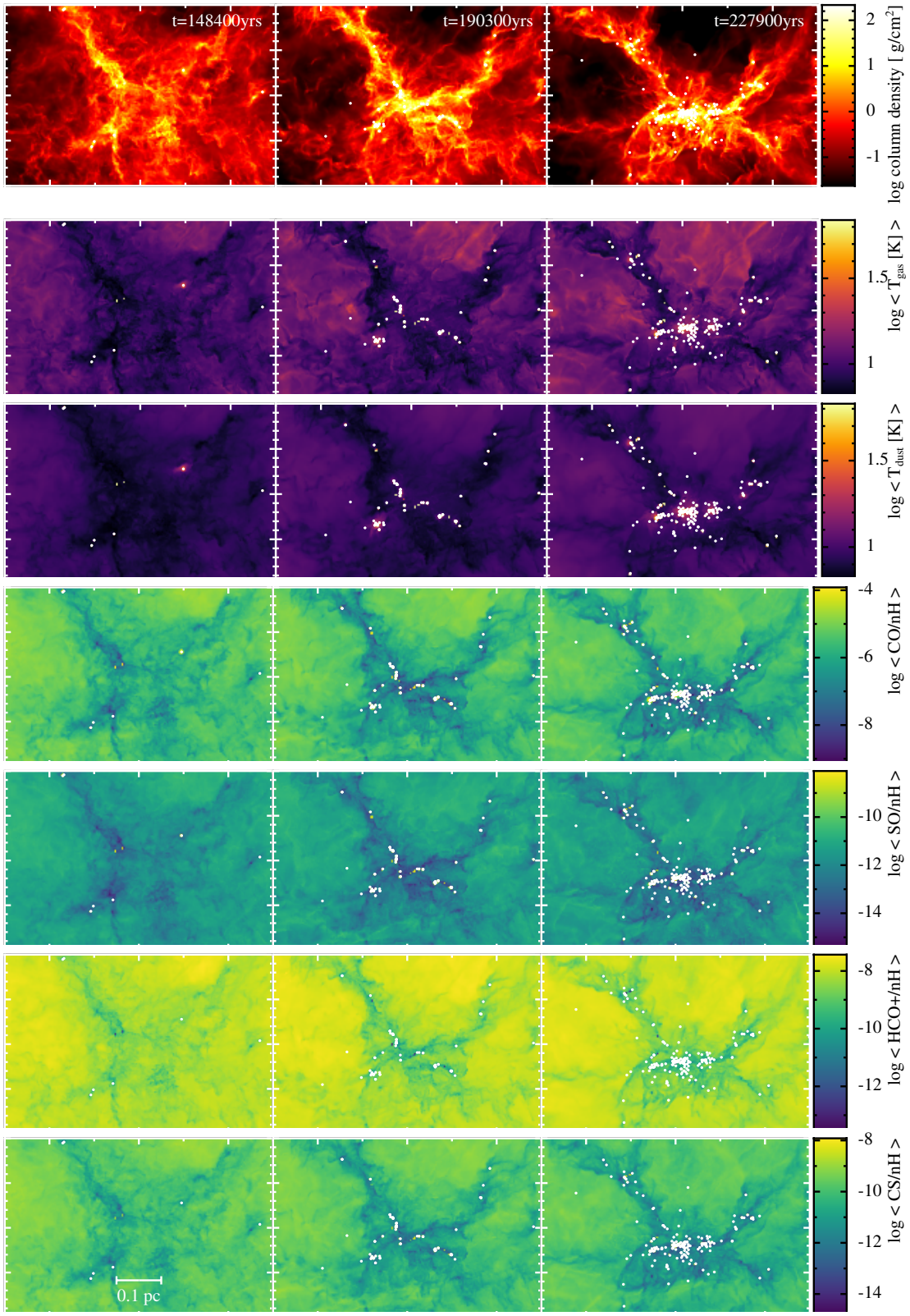

Figure 5.1: Rows 1–3: Column density and mass–weighted average gas temperature and dust temperature from the RHD calculation. Rows 3–6: mass–weighted average abundances of CO, SO, HCO^+ and CS for three snapshots calculated with KROME . Protostars (sink particles) are plotted as white circles and each panel spans 0.6×0.4 pc.

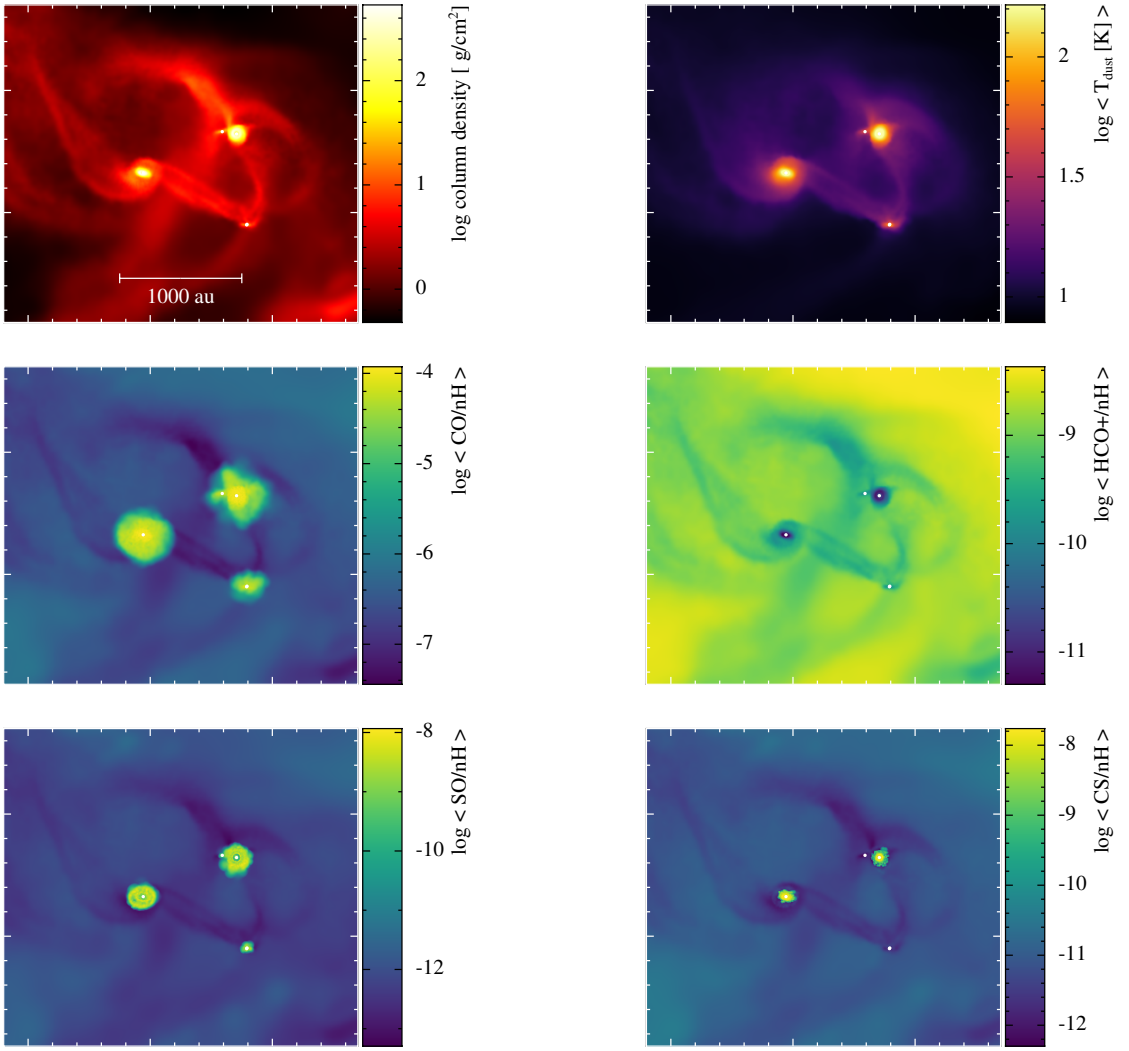

Figure 5.2: Column density and mass–weighted dust temperature and selected chemical abundances of a zoomed–in region of the cluster showing the increased abundances on small scales close to the protostars due to desorption. 1000 AU $\simeq$ 0.005 pc, sink particles are plotted as white circles.

by dust grains. The exception to this is on small scales of $\sim$ 100 au near to the protostars where gravitational contraction heats the gas. In the regions of lower density we can see that the dust temperatures tend to be lower than the gas temperatures because dust cools more efficiently than gas and the two components are less well coupled at lower densities.

The abundance of CO in the gas phase decreases as the density increases throughout the simulation since the adsorption rate increases with increasing density. In the regions where stars form, the CO abundance is at least 1000 times lower than in the wider molecular cloud. As we saw in Chapter 4, CO desorbs rapidly when the dust temper-

ature $T_{\rm dust} \gtrsim 25$ K which is reached shortly before FHSC formation. In each snapshot of CO there are some dense cores where CO is being desorbed but have yet to reach the density required for a sink particle and towards the centre of the cluster larger regions of gas–phase CO are forming where the density of protostars is higher. However, it is still noticeable that the CO abundance is highest only in very small scale regions at this early stage and abundances remain low for most of the centre of the cluster.

We see depletion of HCO^+, SO and CS in the dense filaments as well. The abundance of HCO^+ is highest in the cloud outside of these filaments. CS, however, is depleted relative to its initial calculated ISM abundance of $n_{\rm CS}/n_{\rm H} = 8.5 \times 10^{-9}$ in most of the region shown and the abundance decreases throughout the calculation, except near to protostars.

We present a zoomed–in region of the cluster in Fig. 5.2 to show the chemical changes on the smaller scales where protostars have formed. This region spans approximately 3000 AU $\times$ 3000 AU and contains four sink particles within filaments of dense gas. Two of the protostars have large discs of diameters 100–200 AU . As we also saw in Chapter 4, once the FHSC forms, the temperature is high enough for all species to be rapidly desorbed but only within $r < 100$ au of the centre of the FHSC. The gas–phase abundance of CO is high out to $r \approx 300$ AU of the sink particles with discs and the SO abundance is high out to $r \approx 100$ AU . CS desorbs later at higher temperatures and we only see high CS abundances near to the protostars with large discs. We found previously that after the formation of the stellar core, gas–phase CS was present in significant quantities only within a few AU of the centre of core. HCO^+ is destroyed at high densities and so its abundance near the protostars is even lower than in the nearby dense filaments.

HCO^+ is commonly used to trace dense gas because, as we see here in Fig. 5.2, it does not suffer from significant depletion, except within the dense filaments. CO, SO and CS are still significantly depleted in this dense part of the cloud and their abundances will not increase without radiative feedback from the protostars.

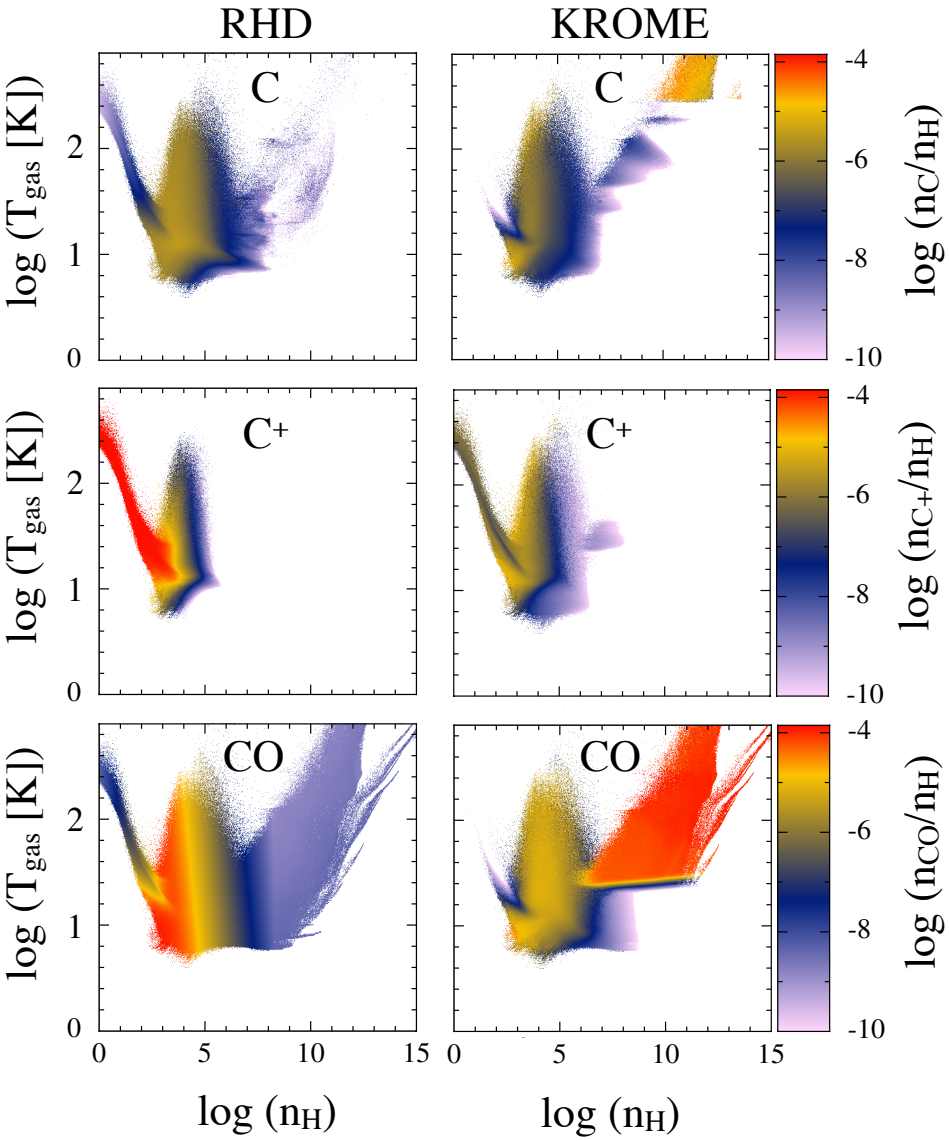

Figure 5.3: Phase diagrams of gas temperature versus density at 227 900 yrs (the end of the hydrodynamical calculation). Left column: abundances from the simple chemical model implemented in the RHD calculation of Bate (2019) (solar metallicity) for each value of temperature and density. Right column: abundances calculated with KROME . The phase diagram for frozen–out CO is included in Fig. 5.4.

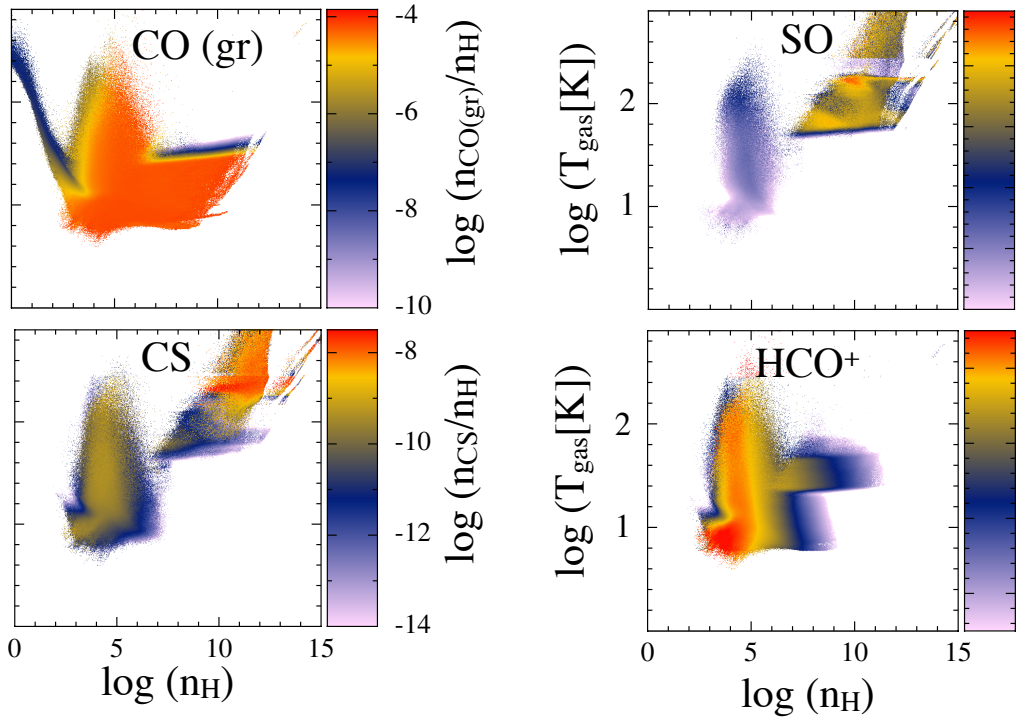

Figure 5.4: Phase diagrams of gas temperature versus density at 227 900 yrs (the end of the hydrodynamical calculation) as for Fig. 5.3 but for species from the KROME model only. CO (gr) refers to CO frozen out onto dust grains.

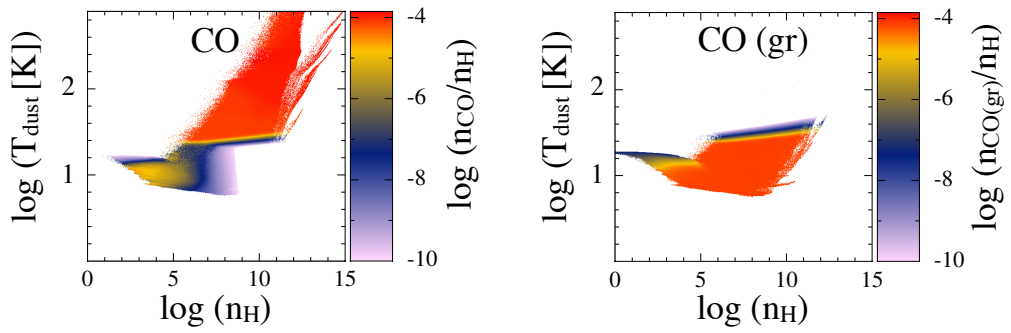

Figure 5.5: Phase diagrams of dust temperature versus density at 227 900 yrs (the end of the hydrodynamical calculation) as for gas–phase CO and CO frozen out onto dust grains, CO (gr).

5.3.2 Comparison with the abundances from the RHD model

Simple carbon chemistry was implemented in the RHD model for more accurate calculation of cooling rates since CO is a major coolant in the ISM and the gas cooling rate therefore depends on the abundance of CO. This model does not treat the desorption of CO after it has frozen out. We compare the abundances of atomic carbon, C^+ and CO obtained from this simple model with the abundances obtained from post–processing the hydrodynamical simulation with KROME. Fig 5.3 shows phase diagrams of density versus gas temperature and abundances relative to total hydrogen for the RHD calculation on the left and from the KROME chemistry calculation on the right for atomic carbon, C^+ and gas–phase CO.

The desorption of CO results in much higher abundances at $n_H \gtrsim 10^6\ cm^{-3}$ in the KROME model. In the KROME model, there is a clear change at ≈ 25 K above which CO is completely in gas phase at densities $n_H \gtrsim 10^6\ cm^{-3}$. Below this temperature, the rate of adsorption is higher and we see in Fig. 5.4 that CO is frozen out here. At $n_H \gtrsim 10^{10}\ cm^{-3}$ and $T > 300$ K there is an increased abundance of atomic carbon which we do not see in the simple chemical model.

In the regions of intermediate density $n_H = 10^3$–$10^6\ cm^{-3}$ the abundance of atomic carbon is similar for both models. The abundance of C^+ decreases slightly less quickly with density in the KROME chemistry calculation. The abundance of CO relative to hydrogen is $\sim 10^{-5}$ over most of this density range in the KROME chemistry model but in the simple model, the abundance reaches $\sim 10^{-4}$ where $n_H = 10^3$–$10^4\ cm^{-3}$. Where the temperatures are high enough for CO to sublimate, the CO reacts to form other molecules such as HCO^+.

HCO^+ is formed primarily by the reaction of CO with H_3^+ (Lee et al. 2004) and this explains the distribution seen in Fig. 5.4. HCO^+ is found in the regions where $n_H \approx 10^4$–$10^9\ cm^{-3}$ and CO is abundant in the gas–phase. In the denser regions, charged species are depleted so there is negligible H_3^+ available and so HCO^+ is also depleted.

SO and CS, being heavier molecules, desorb at higher temperatures than CO and we see that the gas–phase abundances of these species are only significant in the warm,

high density regions. At number densities of $n_H \approx 10^4$–10^9 cm^{-3} gas–phase CS is present in low abundance but the abundance of SO is much lower. Sulfur preferentially forms SO over CS (Lee et al. 2004) but at temperatures $\lesssim 100$ K H_2O, which is a main source of oxygen, is frozen out. Without oxygen available, the CS remains.

Towards the edge of the cloud where $n_H \lesssim 10^3$ cm^{-3}, the carbon is almost entirely ionised in the simple chemical model. This is expected because there is less extinction of the ISRF so photoionisation and photodissociation reaction rates are high. The abundances of C^+ and atomic carbon are lower in the KROME chemical model. This may be partly because additional chemical reactions are possible and the carbon is contained in free radicals and other molecules as well as being in the form of C^+. However, the low abundance of C^+ is more likely to be a result of the initial conditions as we consider below.

In this very low density region we also find a much lower abundance of CO in the KROME model. Fig. 5.4, top left panel, shows that CO in the low density regions is frozen out. In these regions the gas temperature is over 100 K but the dust temperature stays below 20 K. The thermal desorption rate is set from the dust temperature whereas the adsorption rate is related to the gas temperature (c.f. Equations 2.31 and 2.29). The CO freezes out early in the simulation when the chemistry is evolved for the initial conditions, i.e. the uniform density cloud. As the hydrodynamical model evolves, the molecular cloud expands outwards and density of the outer regions decreases and the gas temperature there rises due to heating by the ISRF. The gas and dust temperatures are poorly coupled at these very low densities so, while the gas heats up, the dust stays cold and the CO does not sublimate even with the high gas temperatures. Cosmic rays can heat dust grains which causes CO to desorb but the timescale for this process is much longer than the length of the simulation so the total CO desorption by both mechanisms remains negligible. In Fig. 5.5, we plot phase diagrams for gas–phase CO and frozen out CO, "CO (gr)", with respect to the dust temperature rather than the gas temperature. These confirm that the CO evaporates as expected for grain temperatures $\gtrsim 25$ K. In addition, there is a slope between $n_H \sim 10^6$ cm^{-3} and $\sim 10^{11}$ cm^{-3} because the rate of adsorption increases with both density and gas temperature. The chemical model assumes that all CO is desorbed at 25 K so the abundance of CO may be overestimated because some CO remains trapped

in the ice mantle at higher temperatures.

The chemical abundances calculated for the low density region near the edge of the cloud are probably not realistic because in nature these regions would not have been dense enough in the past for CO (and other species) to freeze out. In this region, the molecular cloud meets the diffuse ISM and we would therefore expect the chemical abundances here to be similar to those of the ISM.

5.4 Conclusion

In this chapter we have presented the results of post–processing a hydrodynamical model of star cluster formation with the chemical model that was used in Chapter 4. This has provided an insight into how the chemical abundances evolve on scales larger than the 1 $M_{\odot}$ dense cores modelled previously. The outcome of modelling a whole cluster emphasises the results from Chapter 4 that within a star–forming cloud most species are highly depleted with respect to ISM abundances except within the inner envelope near the FHSC.

Comparing the simple chemical model with the results of the chemical post–processing with KROME, we find that the abundances of atomic carbon are similar but, at first inspection, the abundance of C^+ may be overestimated by the simple model. In the KROME model, however, gas–phase species freeze out in the molecular cloud and do not sublimate when the edge of the cloud expands and warms up because the dust temperature remains low. This will reduce the amount of carbon in the gas phase which is almost certainly the cause of the low C^+ abundance.

Time–dependent chemistry can capture effects that are missed by equilibrium approximations but the dependence on the physical history can substantially affect the calculated abundances in unexpected ways. For this kind of chemical modelling, the physical initial conditions need to be considered carefully to understand and mitigate any unrealistic results.

Chapter 6

Conclusion

6.1 Summary

The earliest stages of star formation are difficult to observe. The evolutionary sequence of very young sources is often not clear and the parent cloud, the structure of the envelope and orientation of the disc are among factors which have a significant effect on the appearance of a protostellar source. Theoretical work can explain the mechanisms of low mass star formation reasonably well but the problem of how to verify the predicted stages observationally still requires more attention. Synthetic observations can be produced from theoretical models to help us understand how the predicted properties of an object translate into specific observables. The development of the FHSC is an important stage first predicted fifty years ago but the FHSC has never been firmly identified in nature. For this to be possible, more specific criteria are needed to show how to distinguish the FHSC from more evolved objects.

In this thesis we have predicted a variety of observational characteristics of the FHSC. In particular we have considered how to distinguish the FHSC from other faint, young objects to help determine the best way to target candidate FHSCs and to provide synthetic observations to compare these sources with. These synthetic observations were all produced from hydrodynamical models of the collapse of a 1 $\mathrm{M}_{\odot}$ dense core which provide a realistic density and temperature structure that does not depend on any assumed

analytical density distribution.

In Chapter 3 we studied how the SED varies with the properties of the FHSC and as the FHSC evolves. We expect more shorter wavelength emission ($\lambda < 100$ μm) to be detected for sources that are at lower inclinations, rotating more quickly or in lower mass cores. We did find that several properties had similar effects on the SED, for example rotating sources viewed edge–on may look younger because more of the shorter wavelength radiation is reprocessed in the disc and envelope. We then fitted the SEDs of 15 candidate FHSCs from a set of 1440 synthetic SEDs produced from hydrodynamical and radiative transfer models with various properties. This showed that SEDs can provide an insight into the properties of these sources, even accounting for the degeneracy of the SEDs of some models with different properties. The SED fitting is helpful for choosing which sources to target in future observations because it can indicate whether a source is likely to have evolved beyond the FHSC stage. Some sources such as B1-bN were fitted well by FHSC SEDs but have extended outflows which means they are actually more evolved. SED fitting is a useful first step in identifying FHSCs in nature but it is limited and needs to be used alongside kinematic data.

The next step was to produce synthetic molecular line observations. In Chapter 4 we post–processed an RHD and an RMHD simulation to calculate chemical abundances as the FHSC forms and evolves. The abundances of most species are strongly depleted throughout the collapse of the pre–stellar core except close to the centre, near to the FHSC. Only the central few 10s of AU are traced by CO and SO and these will show up the disc and inner envelope. HCO^+ emission is expected to trace the infalling, rotating inner envelope. However, this emission may be too faint to be detectable in a reasonable integration time with even the superior sensitivity of ALMA. CS is depleted in all but the central few AU and is unlikely to be detectable at dense core scales until late in the FHSC stage.

The presence of a slow outflow is often used to argue that a protostellar source may be a FHSC rather than a more evolved object. Since CO only traces the inner few AU of the outflow and is frozen out elsewhere we do not expect CO emission to trace the FHSC outflow motions. The outflow gas motions are too slow to be distinguishable from the turbulent motion of foreground gas at all but the lowest inclinations and will

be challenging to detect even at a face–on orientation. Rotational motions of the outflow may however be detectable and we showed that red and blue lobes of CO $(4-3)$ emission could be detected with ALMA.

With these results, we rule out candidate FHSCs that have detected outflows extending a few hundred AU or more and recommend that ALMA observations with a spatial resolution of ~ 0.05 arcsec, a velocity resolution of $0.2\ \mathrm{km\,s^{-1}}$ and an 8 hour integration are required to detect FHSC structures in CO or SO line emission.

In Chapter 5, we applied the chemistry calculations to a model of the formation of a star cluster from a high density ($\sim 6 \times 10^4\,\mathrm{cm^{-3}}$)500 $\mathrm{M_\odot}$ cloud. We found that most species are depleted compared to ISM abundances throughout much of the cloud and are only released back into the gas–phase in small regions near to where protostars are forming or have formed. The chemical abundances calculated for the outer parts of the cloud are not likely to be realistic because many species remain frozen out due to the uniform initial density of the cloud.

6.2 Future directions

As we mentioned in Chapter 4, the physical properties of pre–stellar objects such as the rotation, mass and magnetic field strength vary and it is not possible to give generic observational criteria for the positive identification of a FHSC. Now we are able to determine which are the strongest candidates, we can start to construct tailored models for individual candidate FHSCs based on their observationally–derived properties. ALMA observations of Cha-MMS1 with subarcsecond resolution are currently scheduled and these will provide suitable observational data to compare with bespoke models.

Most of the FHSC candidates that we fitted with model SEDs in this thesis are unfortunately too distant for high resolution observations since they will be considerably fainter than the synthetic observations, which were calculated for a distance of 260 pc and 150 pc for the SEDs and molecular lines respectively, and the angular sizes will be very small. We need to continue searching for nearby FHSC candidates at distances $\lesssim 250$ pc, such as in the Taurus and Ophiuchus molecular clouds, and preferably in the Southern

sky so they are observable with ALMA. This is where the SED fitting will continue to prove useful to pick out sources that are more likely to contain a FHSC. This may involve finding existing photometry from catalogues of protostars which usually include several unclassified sources or sources loosely classified as Class 0 that could be less evolved.

In this thesis, we only model line emission for four chemical species. Many molecules have now been detected in star–forming regions and several of these are commonly used to trace gas structures and dynamics. It would be interesting to see whether N_2H^+ traces the envelope where other species are frozen out, since this may reveal outflow as well as infall motions. Formaldehyde and methanol are often found to trace outflows. Both species form primarily through chemical reactions on the surface of dust grains and we would need to repeat the chemical calculations with a full gas–grain network to predict their abundances. If grain surface reactions enable these species to form in the outflow then line emission from the outflow may be detectable to a greater extent than we, somewhat pessimistically, predicted. N_2H^+ and methanol produce spectra with hyperfine structure lines, which we were not able to model. A next step would be to implement the calculation of hyperfine lines in TORUS using a method of Keto and Rybicki (2010), for example.

We have shown that our chemical calculations with KROME can be used to study chemical evolution on molecular cloud scales. However, more thought needs to be given to the initial conditions, particularly at the surface of the cloud. A better way should be found to initialise the chemical abundances to avoid unrealistic depletion towards the edge of the cloud. An improved strategy could be to wait for the cloud to evolve slightly to a more physical density and temperature profile before evolving the chemistry. Alternatively, the abundances could be initialised from a 1-D rather than a 0-D model so that the initial abundances depend on the radius.

As observations are becoming more sensitive, it is becoming clear that there are a number of pre– or proto–stellar sources that do not fit in the current protostellar classification schemes. PACS Bright Red sources like those fitted in Chapter 3 have high enough luminosities that they must contain protostars but are faint or undetected at $24\,\mu\mathrm{m}$. On the other hand, sources such as Per-Bolo 58 have a very low luminosity but have extended

outflows, with velocities higher than would be expected for an FHSC. It is currently difficult to explain what these sources are: perhaps they are deeply embedded protostars or they could be very low mass objects. Future work could explore the likely nature of these sources.

The appearance of protostellar objects is largely affected by the extinction of foreground gas and dust and the contribution of radiation from the surrounding parent cloud. We could sample protostars formed in the cluster simulation and model the radiative transfer to help understand how the SEDs and spectra are affected by the position of the protostar within the cloud and by turbulent foreground gas. It is possible to choose the temperature and luminosity of the star represented by sink particles with TORUS which would allow many combinations of protostar luminosities and locations in the cloud to be tested. We could also compare the spectra of these "embedded" protostars with the spectra calculated for the individual dense cores to show how contamination from foreground cloud motions may affect observations.

Another possibility is that these protostars may have disrupted outflows or very weak outflows due to misalignment of the rotation axis and magnetic field. Such sources would differ from the canonical protostar, disc and outflow structure for which the vast majority of synthetic observations are produced. A disrupted outflow may increase the density above the protostar, causing an increase in extinction. This scenario could be tested by performing frequency–dependent radiative transfer modelling with TORUS on MHD models which exhibit these features (e.g. Lewis et al. 2015).

6.3 Outlook

Since the full operation of ALMA began in 2014, protostars and protoplanetary discs have been observed with high resolutions which has revealed structures and kinematics on unprecedented size scales. The detection of the faint, compact structures associated with the FHSC will be challenging but, for relatively close sources, should now be within reach, thanks to ALMA. Fifty years after the FHSC was first predicted, and following decades of theoretical modelling and technological progress, we have reached the point where it

should be possible to detect and characterise it in nature.

The Appendices

Appendix A

Comparison of chemical abundances to the KIDA 2014 network

We performed the chemical calculations again for the MHD model of Chapter 4 with the gas phase reactions from KIDA 2014 network (Wakelam et al. 2015) to examine how the results might differ. The gas–grain reactions which were added to the KIDA network separately remain unchanged. Figs. A.1 and A.2 show the resulting abundance profiles averaged in the plane of the disc and the rotation axis respectively.

The abundance profiles are mostly very similar with the 2011 and 2014 KIDA networks because it is the gas–grain reactions which drive the abundances outside of the FHSC. The snapshot taken during the first collapse (a) shows higher central abundances for CO and HCO^+. This is simply because the desorption of these species happens very quickly at this stage so the abundances increase rapidly and the exact abundance is sensitive to the exact moment it is measured. For CO, the peak abundance in the FHSC is slightly lower early in the FHSC stage but reaches $\sim 1 \times 10^{-4}$ by late in the FHSC stage, as it did with the KIDA 2011 network. The sublimation radius extends to 20 AU in the plane of the disc, as before. The SO abundance is slightly higher deep within the FHSC but the profiles are very similar. The abundances profiles of HCO^+ are very similar for both networks. With the 2014 network, the CS abundance may be nearly an order of magnitude higher deep within the FHSC ($r \lesssim 3$ AU). Comparing all of the molecular profiles shown

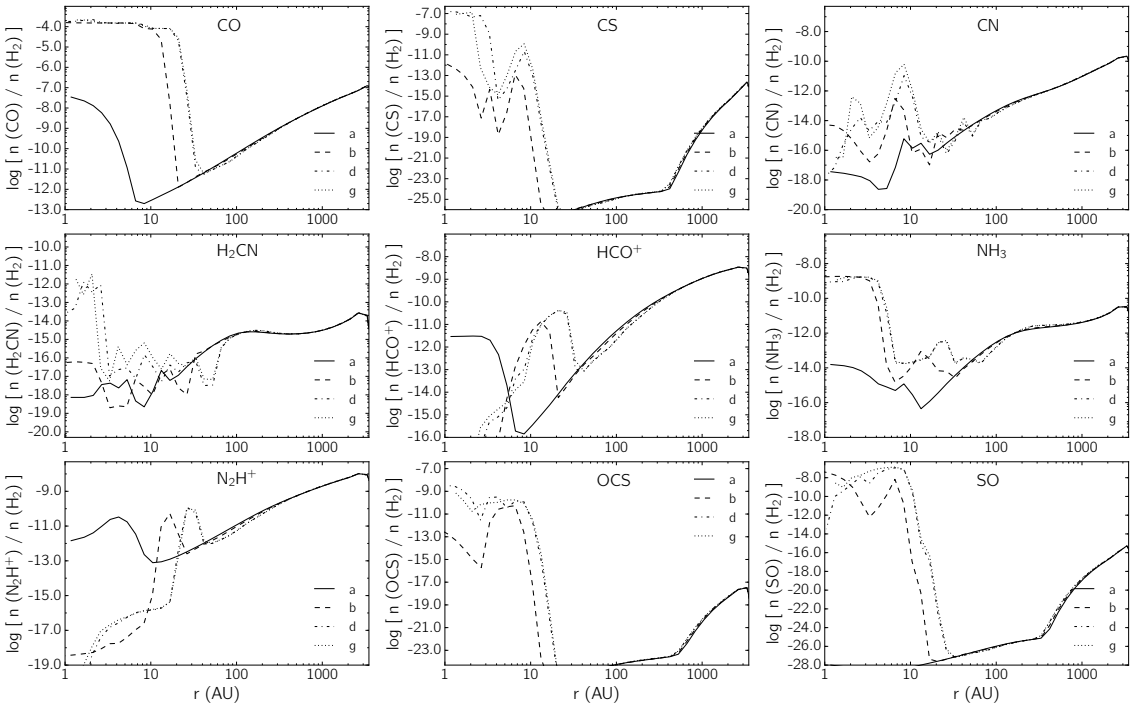

Figure A.1: Average abundances of selected species from the MHD model perpendicular to the rotation axis, calculated using the KIDA 2014 chemical network.

in Figs. 4.9 and 4.10 with those in Figs. A.1 and A.2, only OCS has substantially different abundances over a wide range of radii.

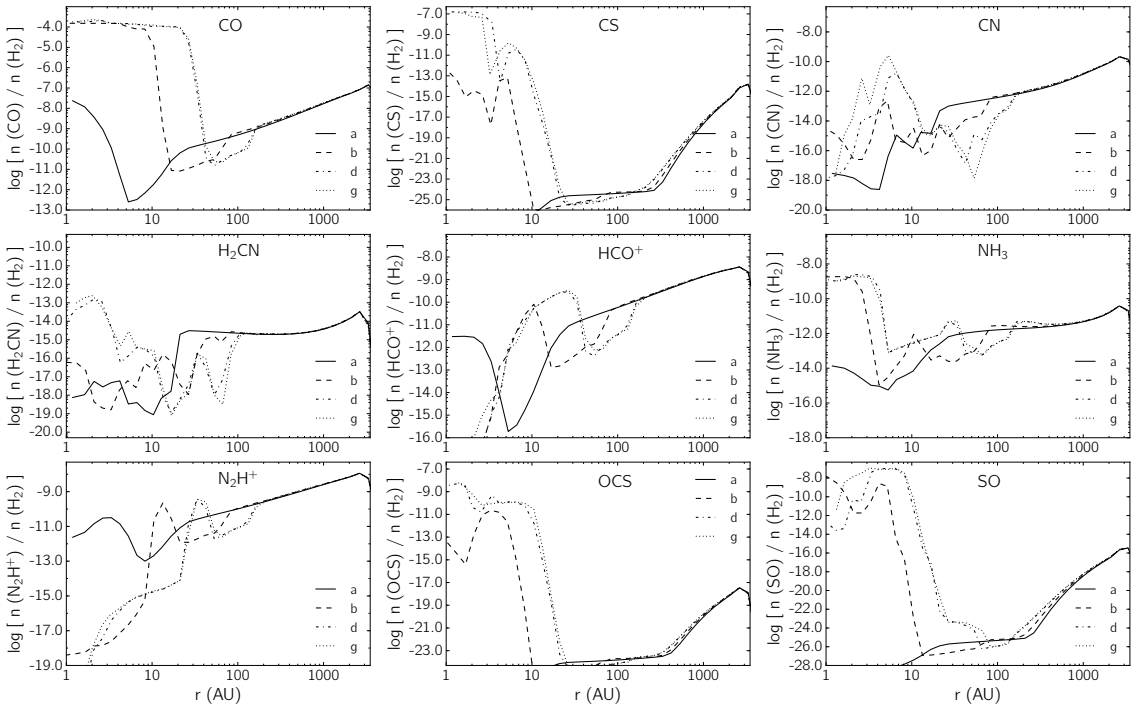

Figure A.2: Average abundances of selected species from the MHD model parallel to the rotation axis, calculated using the KIDA 2014 chemical network.

Bibliography

Acreman, David M., Kevin A. Douglas, Clare L. Dobbs, and Christopher M. Brunt. 2010a. 'Synthetic HI observations of a simulated spiral galaxy.' MNRAS 406 (August): 1460–1470.

Acreman, David M., Tim J. Harries, and David A. Rundle. 2010b. 'Modelling circumstellar discs with three-dimensional radiation hydrodynamics.' MNRAS 403 (April): 1143–1155.

Adelson, Lawrence M., and Chun Ming Leung. 1988. 'On the effects of rotation on interstellart molecular line profiles.' MNRAS 235 (November): 349–364.

Agúndez, M., and V. Wakelam. 2013. 'Chemistry of Dark Clouds: Databases, Networks, and Models.' *Chemical Reviews* 113 (December): 8710–8737.

Aikawa, Y., V. Wakelam, R. T. Garrod, and E. Herbst. 2008. 'Molecular Evolution and Star Formation: From Prestellar Cores to Protostellar Cores.' ApJ 674 (February): 984–996.

Allen, Anthony, Zhi-Yun Li, and Frank H. Shu. 2003. 'Collapse of Magnetized Singular Isothermal Toroids. II. Rotation and Magnetic Braking.' ApJ 599 (December): 363–379.

Andre, P., D. Ward-Thompson, and M. Barsony. 1993. 'Submillimeter continuum observations of Rho Ophiuchi A - The candidate protostar VLA 1623 and prestellar clumps.' ApJ 406 (March): 122–141.

Baggaley, W. J. 2000. 'Advanced Meteor Orbit Radar observations of interstellar meteoroids.' J. Geophys. Res. 105 (May): 10353–10362.

Banerjee, Robi, and Ralph E. Pudritz. 2006. 'Outflows and Jets from Collapsing Magnetized Cloud Cores.' ApJ 641 (April): 949–960.

Bate, M. 1995. PhD diss., -.

Bate, M. R. 1998. 'Collapse of a molecular cloud core to stellar densities: the first three-dimensional calculations.' ApJ 508:L95–L98.

———. 2011. 'Collapse of a molecular cloud core to stellar densities: the formation and evolution of pre-stellar discs.' *MNRAS* 417:2036–2056.

Bate, M. R., and E. R. Keto. 2015. 'Combining radiative transfer and diffuse interstellar medium physics to model star formation.' *MNRAS* 449 (May): 2643–2667.

Bate, M. R., T. S. Tricco, and D. J. Price. 2014. 'Collapse of a molecular cloud core to stellar densities: stellar-core and outflow formation in radiation magnetohydrodynamic simulations.' *MNRAS* 437:77–95.

Bate, Matthew R. 2010. 'Collapse of a molecular cloud core to stellar densities: the radiative impact of stellar core formation on the circumstellar disc.' MNRAS 404 (May): L79–L83.

———. 2019. 'The statistical properties of stars and their dependence on metallicity.' MNRAS 484, no. 2 (April): 2341–2361.

Bate, Matthew R., Ian A. Bonnell, and Nigel M. Price. 1995. 'Modelling accretion in protobinary systems.' MNRAS 277 (November): 362–376.

Belloche, A., B. Parise, F. F. S. van der Tak, et al. 2006. 'The evolutionary state of the southern dense core Chamaeleon-MMS1.' A&A 454 (August): L51–L54.

Benson, P. J., and P. C. Myers. 1989. 'A Survey for Dense Cores in Dark Clouds.' *The Astrophysical Journal Supplement Series* 71 (September): 89.

Bhandare, A., R. Kuiper, T. Henning, et al. 2018. 'First Core Properties: From Low- to High-mass Star Formation.' A&A 618 (October): A95.

Black, D. C., and P. Bodenheimer. 1975. 'Evolution of rotating interstellar clouds. I. Numerical techniques.' ApJ 199 (August): 619–632.

Bok, Bart J., and Edith F. Reilly. 1947. 'Small Dark Nebulae.' ApJ 105 (March): 255.

Bontemps, S., P. André, V. Könyves, et al. 2010. 'The Herschel first look at protostars in the Aquila rift.' A&A 518 (July): L85.

Boss, A. P. 1993. 'Evolution of the Solar Nebula. II. Thermal Structure during Nebula Formation.' ApJ 417 (November): 351.

Boss, A. P., and H. W. Yorke. 1995. 'Spectral energy of first protostellar cores: Detecting 'class -I' protostars with ISO and SIRTF.' ApJL 439 (February): L55–L58.

Burke, J. R., and D. J. Hollenbach. 1983. 'The gas-grain interaction in the interstellar medium - Thermal accommodation and trapping.' ApJ 265 (February): 223–234.

Butler, M. J., and J. C. Tan. 2009. 'Mid-Infrared Extinction Mapping of Infrared Dark Clouds: Probing the Initial Conditions for Massive Stars and Star Clusters.' ApJ 696 (May): 484–497.

Caselli, P., P. J. Benson, P. C. Myers, and M. Tafalla. 2002. 'Dense Cores in Dark Clouds. XIV. N_2H^+ (1-0) Maps of Dense Cloud Cores.' ApJ 572 (June): 238–263.

Chen, X., H. G. Arce, M. M. Dunham, et al. 2012. 'Submillimeter Array and Spitzer Observations of Bok Globule CB 17: A Candidate First Hydrostatic Core?' ApJ 751 (June): 89.

Collings, M. P., and M. R. S. McCoustra. 2012. 'Laboratory studies of desorption from model interstellar ices using surface science methodologies.' In *EAS Publications Series*, edited by C. Stehlé, C. Joblin, and L. d'Hendecourt, 58:315–326. February.

Collings, Mark P., Mark A. Anderson, Rui Chen, et al. 2004. 'A laboratory survey of the thermal desorption of astrophysically relevant molecules.' MNRAS 354, no. 4 (November): 1133–1140.

Commerçon, B., P. Hennebelle, E. Audit, G. Chabrier, and R. Teyssier. 2010. 'Protostellar collapse: radiative and magnetic feedbacks on small-scale fragmentation.' A&A 510 (February): L3.

Commerçon, B., R. Launhardt, C. Dullemond, and Th. Henning. 2012a. 'Synthetic observations of first hydrostatic cores in collapsing low-mass dense cores I. Spectral energy distributions and evolutionary sequence.' A&A 545.

Commerçon, B., F. Levrier, A. J. Maury, T. Henning, and R. Launhardt. 2012b. 'Synthetic observations of first hydrostatic cores in collapsing low-mass dense cores. II. Simulated ALMA dust emission maps.' A&A 548 (December): A39.

Crapsi, A., P. Caselli, C. M. Walmsley, et al. 2005. 'Probing the Evolutionary Status of Starless Cores through N_2H^+ and N_2D^+ Observations.' ApJ 619, no. 1 (January): 379–406.

D'Alessio, P., N. Calvet, and L. Hartmann. 2001. 'Accretion Disks around Young Objects. III. Grain Growth.' ApJ 553 (May): 321.

di Francesco, J., II Evans N. J., P. Caselli, et al. 2007. 'An Observational Perspective of Low-Mass Dense Cores I: Internal Physical and Chemical Properties.' In *Protostars and Planets V*, edited by Bo Reipurth, David Jewitt, and Klaus Keil, 17. January.

Dickens, J. E., W. M. Irvine, R. L. Snell, et al. 2000. 'A Study of the Physics and Chemistry of L134N.' ApJ 542 (October): 870–889.

Dipierro, G., L. Ricci, L. Pérez, et al. 2018. 'Rings and gaps in the disc around Elias 24 revealed by ALMA.' MNRAS 475, no. 4 (April): 5296–5312.

Draine, B. T. 1978. 'Photoelectric heating of interstellar gas.' ApJS 36 (April): 595–619.

———. 2006. 'On the Submillimeter Opacity of Protoplanetary Disks.' ApJ 636 (January): 1114.

Draine, B. T., and H. M. Lee. 1984. 'Optical properties of interstellar graphite and silicate grains.' ApJ 285 (October): 89–108.

Dunham, M. M., H. G. Arce, D. Mardones, et al. 2014. 'Molecular Outflows Driven by Low-mass Protostars. I. Correcting for Underestimates When Measuring Outflow Masses and Dynamical Properties.' ApJ 783 (March): 29.

Dunham, M. M., X. Chen, H. G. Arce, et al. 2011. 'Detection of a Bipolar Molecular Outflow Driven by a Candidate First Hydrostatic Core.' ApJ 742 (November): 1.

Dunham, M. M., A. Crapsi, N. J. Evans II, et al. 2008. 'Identifying the Low-Luminosity Population of Embedded Protostars in the c2d Observations of Clouds and Cores.' ApJS 179 (November): 249–282.

Dunham, M. M., N. J. Evans II, T. L. Bourke, et al. 2006. 'The Spitzer c2d Survey of Nearby Dense Cores. I. First Direct Detection of the Embedded Source in IRAM 04191+1522.' ApJ 651 (November): 945–959.

Dunham, M. M., N. J. Evans II, S. Terebey, C. P. Dullemond, and C. H. Young. 2010. 'Evolutionary Signatures in the Formation of Low-Mass Protostars. II. Toward Reconciling Models and Observations.' ApJ 710 (February): 470–502.

Dunham, M. M., S. S. R. Offner, J. E. Pineda, et al. 2016. 'An ALMA Search for Substructure, Fragmentation, and Hidden Protostars in Starless Cores in Chamaeleon I.' ApJ 823 (June): 160.

Dzib, S., L. Loinard, A. J. Mioduszewski, et al. 2010. 'VLBA Determination of the Distance to Nearby Star-forming Regions. IV. A Preliminary Distance to the Proto-Herbig AeBe Star EC 95 in the Serpens Core.' ApJ 718 (August): 610–619.

Dzyurkevich, Natalia, Benoıt Commerçon, Pierre Lesaffre, and Dimitry Semenov. 2016. '3D radiative hydrodynamic simulations of protostellar collapse with H-C-O dynamical chemistry.' *ArXiv e-prints* (May): arXiv:1605.08032.

Enoch, M. L., J.-E. Lee, P. Harvey, M. M. Dunham, and S. Schnee. 2010. 'A Candidate Detection of the First Hydrostatic Core.' ApJL 722 (October): L33–L38.

Enoch, M. L., K. E. Young, J. Glenn, et al. 2006. 'Bolocam Survey for 1.1 mm Dust Continuum Emission in the c2d Legacy Clouds. I. Perseus.' ApJ 638 (February): 293–313.

Estalella, R., G. Anglada, A. K. Dı az-Rodrı guez, and J. M. Mayen-Gijon. 2019. 'Analysis and test of the central-blue-spot infall hallmark.' *arXiv e-prints* (April): arXiv:1904.10737.

Fehlberg, E. 1969. *Low-order classical Runge-Kutta formulas with stepsize control and their application to some heat transfer problems.* Technical report 315. NASA.

Friesen, R. K., A. Pon, T. L. Bourke, et al. 2018. 'ALMA detections of the youngest protostars in Ophiuchus.' ApJ 869 (December): 158.

Fuente, A., M. Gerin, J. Pety, et al. 2017. 'Chemical segregation in the young protostars Barnard 1b-N and S: evidence of pseudo-disk rotation in Barnard 1b-S.' A&A 606 (August): L3.

Furlan, E., W. J. Fischer, B. Ali, et al. 2016. 'The Herschel Orion Protostar Survey: Spectral Energy Distributions and Fits Using a Grid of Protostellar Models.' ApJS 224 (May): 5.

Furuya, K., Y. Aikawa, K. Tomida, et al. 2012. 'Chemistry in the First Hydrostatic Core Stage by Adopting Three-dimensional Radiation Hydrodynamic Simulations.' ApJ 758 (October): 86.

Garrod, R. T., V. Wakelam, and E. Herbst. 2007. 'Non-thermal desorption from interstellar dust grains via exothermic surface reactions.' A&A 467 (June): 1103–1115.

Gerin, M., J. Pety, A. Fuente, et al. 2015. 'Nascent bipolar outflows associated with the first hydrostatic core candidates Barnard 1b-N and 1b-S.' A&A 577 (May): L2.

Glover, S. C. O., C. Federrath, M. -M. Mac Low, and R. S. Klessen. 2010. 'Modelling CO formation in the turbulent interstellar medium.' MNRAS 404, no. 1 (May): 2–29.

Glover, Simon C. O., and Paul C. Clark. 2012a. 'Approximations for modelling CO chemistry in giant molecular clouds: a comparison of approaches.' MNRAS 421, no. 1 (March): 116–131.

———. 2012b. 'Is molecular gas necessary for star formation?' MNRAS 421 (March): 9–19.

Goldsmith, Paul F. 2001. 'Molecular Depletion and Thermal Balance in Dark Cloud Cores.' ApJ 557 (August): 736–746.

Goodman, A. A., P. J. Benson, G. A. Fuller, and P. C. Myers. 1993. 'Dense Cores in Dark Clouds. VIII. Velocity Gradients.' ApJ 406 (April): 528.

Grady, C. A., T. Muto, J. Hashimoto, et al. 2013. 'Spiral Arms in the Asymmetrically Illuminated Disk of MWC 758 and Constraints on Giant Planets.' ApJ 762 (January): 48.

Graedel, T. E., W. D. Langer, and M. A. Frerking. 1982. 'The kinetic chemistry of dense interstellar clouds.' *The Astrophysical Journal Supplement Series* 48 (March): 321–368.

Grassi, T., S. Bovino, D. R. G. Schleicher, et al. 2014. 'KROME - a package to embed chemistry in astrophysical simulations.' MNRAS 439 (April): 2386–2419.

Gruen, E., B. Gustafson, I. Mann, et al. 1994. 'Interstellar dust in the heliosphere.' A&A 286 (June): 915–924.

Gutermuth, R. A., T. L. Bourke, L. E. Allen, et al. 2008. 'The Spitzer Gould Belt Survey of Large Nearby Interstellar Clouds: Discovery of a Dense Embedded Cluster in the Serpens-Aquila Rift.' ApJL 673 (February): L151.

Habing, H. J. 1968. 'The interstellar radiation density between 912 A and 2400 A.' *Bulletin of the Astronomical Institutes of the Netherlands* 19 (January): 421.

Haikala, L. K., J. Harju, K. Mattila, and M. Toriseva. 2005. 'Clumpy filaments of the Chamaeleon I cloud: $C^{18}O$ mapping with the SEST.' A&A 431 (February): 149–163.

Harries, T. J. 2000. 'Synthetic line profiles of rotationally distorted hot-star winds.' MNRAS 315:722–734.

Harries, Tim, Tom Haworth, David Acreman, Ahmad Ali, and Tom Douglas. 2019. 'The TORUS radiation transfer code.' *arXiv e-prints* (March): arXiv:1903.06672.

Harsono, D., E. F. van Dishoeck, S. Bruderer, Z.-Y. Li, and J. K. Jørgensen. 2015. 'Testing protostellar disk formation models with ALMA observations.' *Astron. and Astrophys* 577:A22.

Hasegawa, T. I., and E. Herbst. 1993. 'New gas-grain chemical models of quiescent dense interstellar clouds - The effects of H2 tunnelling reactions and cosmic ray induced desorption.' MNRAS 261 (March): 83–102.

Hasegawa, T. I., E. Herbst, and C. M. Leung. 1992. 'Models of gas-grain chemistry in dense interstellar clouds with complex organic molecules.' ApJS 82 (September): 167–195.

Hatchell, J., J. S. Richer, G. A. Fuller, et al. 2005. 'Star formation in Perseus. Clusters, filaments and the conditions for star formation.' A&A 440 (September): 151–161.

Hennebelle, P., and A. Ciardi. 2009. 'Disk formation during collapse of magnetized protostellar cores.' A&A 506 (November): L29–L32.

Hennebelle, P., and S. Fromang. 2008. 'Magnetic processes in a collapsing dense core. I. Accretion and ejection.' A&A 477 (January): 9–24.

Hincelin, U., B. Commerçon, V. Wakelam, et al. 2016. 'Chemical and Physical Characterization of Collapsing Low-mass Prestellar Dense Cores.' *ApJ* 822 (May): 12.

Hincelin, U., V. Wakelam, F. Hersant, et al. 2011. 'Oxygen depletion in dense molecular clouds: a clue to a low O_2 abundance?' A&A 530 (June): A61.

Hindmarsh, A. C. 1983. *IMACS Trans. Sci. Comput.* 1:55.

Hirano, N., and F.-c. Liu. 2014. 'Two Extreme Young Objects in Barnard 1-b.' ApJ 789 (July): 50.

Hirota, Tomoya, Takeshi Bushimata, Yoon Kyung Choi, et al. 2007. 'Distance to Orion KL Measured with VERA.' PASJ 59 (October): 897.

I-Hsiu Li, J., H. B. Liu, Y. Hasegawa, and N. Hirano. 2017. 'Systematic Analysis of Spectral Energy Distributions and the Dust Opacity Indices for Class 0 Young Stellar Objects.' ApJ 840 (May): 72.

Jeans, J. 1928. *Astronomy and cosmogony.* Cambridge University Press.

Jenkins, Edward B. 2009. 'A Unified Representation of Gas-Phase Element Depletions in the Interstellar Medium.' ApJ 700, no. 2 (August): 1299–1348.

Jones, Michael O., and Matthew R. Bate. 2018. 'Sink particle radiative feedback in smoothed particle hydrodynamics models of star formation.' MNRAS 480, no. 2 (October): 2562–2577.

Jørgensen, J. K., R. Visser, N. Sakai, et al. 2013. 'A Recent Accretion Burst in the Low-mass Protostar IRAS 15398-3359: ALMA Imaging of Its Related Chemistry.' ApJL 779 (December): L22.

Kauffmann, J., F. Bertoldi, II Evans N. J., and C2D Collaboration. 2005. 'Spitzer discovery of very low luminosity objects.' *Astronomische Nachrichten* 326, no. 10 (December): 878–881.

Keto, Eric, and Paola Caselli. 2008. 'The Different Structures of the Two Classes of Starless Cores.' ApJ 683, no. 1 (August): 238–247.

Keto, Eric, and George Rybicki. 2010. 'Modeling Molecular Hyperfine Line Emission.' ApJ 716 (June): 1315–1322.

Kim, G., C. W. Lee, M. Gopinathan, W.-S. Jeong, and M.-R. Kim. 2016. 'Dense Molecular Cores Being Externally Heated.' ApJ 824 (June): 85.

Kirk, H., P. C. Myers, T. L. Bourke, et al. 2013. 'Filamentary Accretion Flows in the Embedded Serpens South Protocluster.' ApJ 766 (April): 115.

Könyves, V., P. André, A. Men'shchikov, et al. 2015. 'A census of dense cores in the Aquila cloud complex: SPIRE/PACS observations from the Herschel Gould Belt survey.' A&A 584 (December): A91.

Lada, C. J., and B. A. Wilking. 1984. 'The nature of the embedded population in the rho Ophiuchi dark cloud : mid-infrared observations.' ApJ 287 (December): 610–621.

Lada, Charles J. 1987. 'Star formation: from OB associations to protostars.' In *Star Forming Regions*, edited by Manuel Peimbert and Jun Jugaku, 115:1. IAU Symposium. January.

Larson, R. B. 1969. 'Numerical calculations of the dynamics of a collapsing proto-star.' *MNRAS* 145:271–295.

———. 1981. 'Turbulence and star formation in molecular clouds.' MNRAS 194 (March): 809–826.

Lee, Chin-Fei, Zhi-Yun Li, Naomi Hirano, et al. 2018. 'ALMA Observations of the Very Young Class 0 Protostellar System HH211-mms: A 30 au Dusty Disk with a Disk Wind Traced by SO?' ApJ 863 (August): 94.

Lee, Jeong-Eun, Edwin A. Bergin, and II Evans Neal J. 2004. 'Evolution of Chemistry and Molecular Line Profiles during Protostellar Collapse.' ApJ 617, no. 1 (December): 360–383.

Leger, A., M. Jura, and A. Omont. 1985. 'Desorption from interstellar grains.' A&A 144, no. 1 (March): 147–160.

Levermore, C. D., and G. C. Pomraning. 1981. 'A flux-limited diffusion theory.' ApJ 248 (August): 321–334.

Lewis, B. T., and M. R. Bate. 2017. 'The dependence of protostar formation on the geometry and strength of the initial magnetic field.' MNRAS 467 (May): 3324–3337.

Lewis, B. T., M. R. Bate, and D. J. Price. 2015. 'Smoothed particle magnetohydrodynamic simulations of protostellar outflows with misaligned magnetic field and rotation axes.' MNRAS 451 (July): 288–299.

Machida, Masahiro N., Shu-ichiro Inutsuka, and Tomoaki Matsumoto. 2008. 'High- and Low-Velocity Magnetized Outflows in the Star Formation Process in a Gravitationally Collapsing Cloud.' ApJ 676 (April): 1088–1108.

Maret, S., E. A. Bergin, and M. Tafalla. 2013. 'Chemical modeling of the L1498 and L1517B prestellar cores: CO and HCO^+ depletion.' A&A 559 (November): A53.

Masunaga, H., S. M. Miyama, and S.-i. Inutsuka. 1998. 'A Radiation Hydrodynamic Model for Protostellar Collapse. I. The First Collapse.' ApJ 495 (March): 346–369.

Mathis, J. S., W. Rumpl, and K. H. Nordsieck. 1977. 'The size distribution of interstellar dust grains.' ApJ 217 (October): 425.

Maureira, M. J., H. G. Arce, M. M. Dunham, et al. 2017a. 'Kinematics of a Young Low-mass Star-forming Core: Understanding the Evolutionary State of the First-core Candidate L1451-mm.' ApJ 838 (March): 60.

Maureira, M. J., H. G. Arce, S. S. R. Offner, et al. 2017b. 'A Turbulent Origin for the Complex Envelope Kinematics in the Young Low-mass Core Per-bolo 58.' ApJ 849 (November): 89.

Maury, A. J., P. André, A. Men'shchikov, V. Könyves, and S. Bontemps. 2011. 'The formation of active protoclusters in the Aquila rift: a millimeter continuum view.' A&A 535 (November): A77.

Mayen-Gijon, J. M., G. Anglada, M. Osorio, et al. 2014. 'Signatures of infall motions in the images of the molecular emission of G31.41+0.31 hot molecular core.' MNRAS 437 (February): 3766–3775.

Mayne, N. J., T. J. Harries, J. Rowe, and D. M. Acreman. 2012. 'Bayesian fitting of Taurus brown dwarf spectral energy distributions.' MNRAS 423 (June): 1775–1804.

McMullin, J. P., B. Waters, D. Schiebel, W. Young, and K. Golap. 2007. In *Astronomical Data Analysis Software and Systems XVI (ASP Conf. Ser. 376)*, edited by R. A. Shaw, F. Hill, and D. J. Bell, 127. San Francisco, CA: ASP.

Mellon, Richard R., and Zhi-Yun Li. 2008. 'Magnetic Braking and Protostellar Disk Formation: The Ideal MHD Limit.' ApJ 681 (July): 1356–1376.

Menten, K. M., M. J. Reid, J. Forbrich, and A. Brunthaler. 2007. 'The distance to the Orion Nebula.' A&A 474, no. 2 (November): 515–520.

Miyake, K., and Y. Nakagawa. 1993. 'Effects of particle size distribution on opacity curves of protoplanetary disks around T Tauri stars.' *Icarus* 106 (November): 20.

Monaghan, J. J. 1992. 'Smoothed particle hydrodynamics.' *Ann.Rev.Astron.Astrophys* 30:543–547.

Morris, J. P., and J. J. Monaghan. 1997. 'A Switch to Reduce SPH Viscosity.' *Journal of Computational Physics* 136 (September): 41–50.

Muñoz Caro, G, A Jiménez-Escobar, Jose Martin Gago, et al. 2010. 'New results on thermal and photodesorption of CO ice using the novel InterStellar Astrochemistry Chamber (ISAC).' *Astronomy and Astrophysics* 522 (November): 108–.

Murillo, Nadia M., Ewine F. van Dishoeck, Matthijs H. D. van der Wiel, et al. 2018. 'Tracing the cold and warm physico-chemical structure of deeply embedded protostars: IRAS 16293-2422 versus VLA 1623-2417.' *ArXiv e-prints* (May): arXiv:1805.05205.

Nakamura, F., K. Sugitani, Y. Shimajiri, et al. 2011. 'Molecular Outflows from the Protocluster Serpens South.' ApJ 737 (August): 56.

Narayanan, Gopal, and Christopher K. Walker. 1998. 'A Parameterized Study of the Detection of Infall in Protostellar Systems.' ApJ 508, no. 2 (December): 780–790.

Narayanan, Gopal, Christopher K. Walker, and Henry D. Buckley. 1998. 'The "Blue-Bulge" Infall Signature toward IRAS 16293-2422.' ApJ 496, no. 1 (March): 292–310.

Nielbock, M., R. Launhardt, J. Steinacker, et al. 2012. 'The Earliest Phases of Star formation (EPoS) observed with Herschel: the dust temperature and density distributions of B68.' A&A 547 (November): A11.

Ohashi, Nagayoshi, Kazuya Saigo, Yusuke Aso, et al. 2014. 'Formation of a Keplerian Disk in the Infalling Envelope around L1527 IRS: Transformation from Infalling Motions to Kepler Motions.' ApJ 796 (December): 131.

Omukai, K. 2007. 'Observational Characteristics of the First Protostellar Cores.' PASJ 59 (June): 589–606.

Ormel, C. W., D. Paszun, C. Dominik, and A. G. G. M. Tielens. 2009. 'Dust coagulation and fragmentation in molecular clouds. I. How collisions between dust aggregates alter the dust size distribution.' A&A 502 (August): 845–869.

Ortiz-León, G. N., S. A. Dzib, M. A. Kounkel, et al. 2017. 'The Gould Belt Distances Survey (GOBELINS). III. The Distance to the Serpens/Aquila Molecular Complex.' ApJ 834 (January): 143.

Oya, Y., K. Moriwaki, S. Onishi, et al. 2018. 'Chemical and Physical Picture of IRAS 16293-2422 Source B at a Sub-arcsecond Scale Studied with ALMA.' ApJ 854, no. 2 (February): 96.

Pérez, Laura M., John M. Carpenter, Sean M. Andrews, et al. 2016. 'Spiral density waves in a young protoplanetary disk.' *Science* 353 (September): 1519–1521.

Persson, Magnus Vilhelm. 2014. *SEDs of the different protostellar evolutionary stages,* August.

Pezzuto, S., D. Elia, E. Schisano, et al. 2012. 'Herschel observations of B1-bS and B1-bN: two first hydrostatic core candidates in the Perseus star-forming cloud.' A&A 547 (November): A54.

Pineda, J. E., H. G. Arce, S. Schnee, et al. 2011. 'The Enigmatic Core L1451-mm: A First Hydrostatic Core? Or a Hidden VeLLO?' ApJ 743 (December): 201.

Pratap, P., J. E. Dickens, R. L. Snell, et al. 1997. 'A Study of the Physics and Chemistry of TMC-1.' ApJ 486 (September): 862–885.

Price, D. J., and J. J. Monaghan. 2005. 'Smoothed Particle Magnetohydrodynamics - III. Multidimensional tests and the ∇.B= 0 constraint.' MNRAS 364 (December): 384–406.

Price, Daniel J. 2012. 'Smoothed particle hydrodynamics and magnetohydrodynamics.' *Journal of Computational Physics* 231 (February): 759–794.

Price, Daniel J., Terrence S. Tricco, and Matthew R. Bate. 2012. 'Collimated jets from the first core.' MNRAS 423 (June): L45–L49.

Priestley, F. D., S. Viti, and D. A. Williams. 2018. 'An Efficient Method for Determining the Chemical Evolution of Gravitationally Collapsing Prestellar Cores.' AJ 156 (August): 51.

Rawlings, J. M. C., and J. A. Yates. 2001. 'Modelling line profiles in infalling cores.' MNRAS 326, no. 4 (October): 1423–1430.

Reboussin, L., V. Wakelam, S. Guilloteau, and F. Hersant. 2014. 'Grain-surface reactions in molecular clouds: the effect of cosmic rays and quantum tunnelling.' MNRAS 440 (June): 3557–3567.

Reipurth, B., L. -A. Nyman, and R. Chini. 1996. 'Protostellar candidates in southern molecular clouds.' A&A 314 (October): 258–264.

Ricci, L., L. Testi, A. Natta, and K. J. Brooks. 2010. 'Dust grain growth in ρ-Ophiuchi protoplanetary disks.' A&A 521 (October): A66.

Robitaille, T. P. 2017. 'A modular set of synthetic spectral energy distributions for young stellar objects.' A&A 600 (April): A11.

Robitaille, T. P., B. A. Whitney, R. Indebetouw, and K. Wood. 2007. 'Interpreting Spectral Energy Distributions from Young Stellar Objects. II. Fitting Observed SEDs Using a Large Grid of Precomputed Models.' ApJS 169 (April): 328–352.

Robitaille, T. P., B. A. Whitney, R. Indebetouw, K. Wood, and P. Denzmore. 2006. 'Interpreting Spectral Energy Distributions from Young Stellar Objects. I. A Grid of 200,000 YSO Model SEDs.' ApJS 167 (December): 256–285.

Roy, A., P. André, P. Palmeirim, et al. 2014. 'Reconstructing the density and temperature structure of prestellar cores from Herschel data: A case study for B68 and L1689B.' A&A 562 (February): A138.

Rundle, D., T. J. Harries, D. M. Acreman, and M. R. Bate. 2010. 'Three-dimensional molecular line transfer: a simulated star-forming region.' *MNRAS* 407 (September): 986.

Saigo, K., and K. Tomisaka. 2011. 'Spectrum Energy Distribution and Submillimeter Image of a Rotating First Core.' ApJ 728, no. 2 (February): 78.

Saigo, Kazuya, and Kohji Tomisaka. 2006. 'Evolution of First Cores in Rotating Molecular Cores.' ApJ 645 (1): 381.

Saigo, Kazuya, Kohji Tomisaka, and Tomoaki Matsumoto. 2008. 'Evolution of First Cores and Formation of Stellar Cores in Rotating Molecular Cloud Cores.' ApJ 674 (February): 997–1014.

Sandstrom, Karin M., J. E. G. Peek, Geoffrey C. Bower, Alberto D. Bolatto, and Richard L. Plambeck. 2007. 'A Parallactic Distance of $389^{+24}{}_{-21}$ Parsecs to the Orion Nebula Cluster from Very Long Baseline Array Observations.' ApJ 667, no. 2 (October): 1161–1169.

Schnee, S., M. Enoch, D. Johnstone, et al. 2010. 'An Observed Lack of Substructure in Starless Cores.' ApJ 718 (July): 306–313.

Schöier, F. L., F. F. S. van der Tak, E. F. van Dishoeck, and J. H. Black. 2005. 'An atomic and molecular database for analysis of submillimetre line observations.' *Astron. and Astrophys* 432:369–379.

Smith, R. Scott, C. Huang, E. K. L. Wong, and Bruce D. Kay. 1997. 'The Molecular Volcano: Abrupt CCl_4 Desorption Driven by the Crystallization of Amorphous Solid Water.' Phys. Rev. Lett. 79, no. 5 (August): 909–912.

Stamer, T., and S.-i. Inutsuka. 2018. 'Radiation Hydrodynamics Simulations of Spherical Protostellar Collapse for Very Low Mass Objects.' ApJ 869, no. 2 (November): 179.

Steinacker, J., M. Andersen, W.-F. Thi, et al. 2015. 'Grain size limits derived from 3.6 μm and 4.5 μm coreshine.' A&A 582 (October): A70.

Sterken, Veerle J., Andrew J. Westphal, Nicolas Altobelli, et al. 2014. 'Stardust Interstellar Preliminary Examination X: Impact speeds and directions of interstellar grains on the Stardust dust collector.' *Meteoritics & Planetary Science* 49 (9): 1680–1697.

Stolker, T., C. Dominik, H. Avenhaus, et al. 2016. 'Shadows cast on the transition disk of HD 135344B. Multiwavelength VLT/SPHERE polarimetric differential imaging.' A&A 595 (November): A113.

Straizys, V., K. Cernis, and S. Bartasiūtė. 2003. 'Interstellar extinction in the direction of the Aquila Rift.' A&A 405 (July): 585–590.

Stutz, A. M., J. J. Tobin, T. Stanke, et al. 2013. 'A Herschel and APEX Census of the Reddest Sources in Orion: Searching for the Youngest Protostars.' ApJ 767 (April): 36.

Tobin, J. J., L. W. Looney, Z.-Y. Li, et al. 2016a. 'The VLA Nascent Disk and Multiplicity Survey of Perseus Protostars (VANDAM). II. Multiplicity of Protostars in the Perseus Molecular Cloud.' ApJ 818 (February): 73.

Tobin, J. J., A. M. Stutz, P. Manoj, et al. 2016b. 'Characterizing the Youngest Herschel-detected Protostars. II. Molecular Outflows from the Millimeter and the Far-infrared.' ApJ 831 (November): 36.

Tobin, J. J., A. M. Stutz, S. T. Megeath, et al. 2015a. 'Characterizing the Youngest Herschel-detected Protostars. I. Envelope Structure Revealed by CARMA Dust Continuum Observations.' ApJ 798 (January): 128.

Tobin, John J., Leslie W. Looney, David J. Wilner, et al. 2015b. 'A Sub-arcsecond Survey Toward Class 0 Protostars in Perseus: Searching for Signatures of Protostellar Disks.' ApJ 805 (June): 125.

Tomida, K., M. N. Machida, K. Saigo, K. Tomisaka, and T. Matsumoto. 2010a. 'Exposed Long-lifetime First Core: A New Model of First Cores Based on Radiation Hydrodynamics.' *The Astrophysical Journal* 725 (December): L239–L244.

Tomida, K., S. Okuzumi, and M. N. Machida. 2015. 'Radiation Magnetohydrodynamic Simulations of Protostellar Collapse: Nonideal Magnetohydrodynamic Effects and Early Formation of Circumstellar Disks.' ApJ 801:117.

Tomida, K., K. Tomisaka, T. Matsumoto, et al. 2010b. 'Radiation Magnetohydrodynamics Simulation of Proto-stellar Collapse: Two-component Molecular Outflow.' *The Astrophysical Journal* 714 (May): L58–L63.

Tomida, Kengo, Kohji Tomisaka, Tomoaki Matsumoto, et al. 2013. 'Radiation Magnetohydrodynamic Simulations of Protostellar Collapse: Protostellar Core Formation.' ApJ 763 (January): 6.

Tomisaka, K., and K. Tomida. 2011. 'Observational Identification of First Cores: Non-LTE Radiative Transfer Simulation.' PASJ 63 (October): 1151–1164.

Tomisaka, Kohji. 2002. 'Collapse of Rotating Magnetized Molecular Cloud Cores and Mass Outflows.' ApJ 575 (August): 306–326.

Tricco, Terrence S., and Daniel J. Price. 2012. 'Constrained hyperbolic divergence cleaning for smoothed particle magnetohydrodynamics.' *Journal of Computational Physics* 231 (August): 7214–7236.

———. 2013. 'A switch to reduce resistivity in smoothed particle magnetohydrodynamics.' MNRAS 436 (December): 2810–2817.

Tsitali, A. E., A. Belloche, B. Commerçon, and K. M. Menten. 2013. 'The dynamical state of the first hydrostatic core candidate Chamaeleon-MMS1.' A&A 557 (September): A98.

Tsukamoto, Y., K. Iwasaki, S. Okuzumi, M. N. Machida, and S. Inutsuka. 2015. 'Effects of Ohmic and ambipolar diffusion on formation and evolution of first cores, protostars, and circumstellar discs.' MNRAS 452, no. 1 (September): 278–288.

Väisälä, M. S., J. Harju, M. J. Mantere, et al. 2014. 'High-resolution ammonia mapping of the very young protostellar core Chamaeleon-MMS1.' A&A 564 (April): A99.

van Weeren, R. J., C. Brinch, and M. R. Hogerheijde. 2009. 'Modeling the chemical evolution of a collapsing prestellar core in two spatial dimensions.' A&A 497 (April): 773–787.

Vaytet, N., E. Audit, G. Chabrier, B. Commerçon, and J. Masson. 2012. 'Simulations of protostellar collapse using multigroup radiation hydrodynamics. I. The first collapse.' A&A 543 (July): A60.

Vaytet, N., G. Chabrier, E. Audit, et al. 2013. 'Simulations of protostellar collapse using multigroup radiation hydrodynamics. II. The second collapse.' A&A 557 (September): A90.

Vaytet, N., and T. Haugbølle. 2017. 'A grid of one-dimensional low-mass star formation collapse models.' A&A 598 (February): A116.

Wakelam, V., E. Herbst, J.-C. Loison, et al. 2012. 'A KInetic Database for Astrochemistry (KIDA).' ApJS 199 (March): 21.

Wakelam, V., J.-C. Loison, E. Herbst, et al. 2015. 'The 2014 KIDA Network for Interstellar Chemistry.' ApJS 217 (April): 20.

Wakelam, Valentine, and Eric Herbst. 2008. 'Polycyclic Aromatic Hydrocarbons in Dense Cloud Chemistry.' ApJ 680 (June): 371.

Walker, Christopher K., Gopal Narayanan, and Alan P. Boss. 1994. 'Spectroscopic Signatures of Infall in Young Protostellar Systems.' ApJ 431 (August): 767.

Ward-Thompson, D., P. André, and J. M. Kirk. 2002. 'The initial conditions of isolated star formation - V. ISOPHOT imaging and the temperature and energy balance of pre-stellar cores.' MNRAS 329 (January): 257–276.

Ward-Thompson, D., and A. P. Whitworth. 2011. *An introduction to star formation.* Cambridge University Press.

Wardle, Mark, and Arieh Koenigl. 1993. 'The Structure of Protostellar Accretion Disks and the Origin of Bipolar Flows.' ApJ 410 (June): 218.

White, R. J., T. P. Greene, G. W. Doppmann, K. R. Covey, and L. A. Hillenbrand. 2007. 'Stellar Properties of Embedded Protostars.' In *Protostars and Planets V*, edited by Bo Reipurth, David Jewitt, and Klaus Keil, 117. January.

Whitehouse, S. C., and M. R. Bate. 2006. 'The thermodynamics of collapsing molecular cloud cores using smoothed particle hydrodynamics with radiative transfer.' MNRAS 367 (March): 32–38.

Whitehouse, S. C., M. R. Bate, and J. J. Monaghan. 2005. 'A faster algorithm for smoothed particle hydrodynamics with radiative transfer in the flux-limited diffusion approximation.' *MNRAS* 364 (December): 1367.

Whittet, D. C. B., P. A. Gerakines, A. L. Carkner, et al. 1994. 'A Study of the Chamaeleon-I Dark Cloud and T-Association - Part Six - Interstellar Polarization Grain Alignment and Magnetic Field.' MNRAS 268 (May): 1.

Wurster, James, Matthew R. Bate, and Daniel J. Price. 2018. 'The collapse of a molecular cloud core to stellar densities using radiation non-ideal magnetohydrodynamics.' MNRAS 475 (April): 1859–1880.

Wurster, James, Daniel J. Price, and Matthew R. Bate. 2016. 'Can non-ideal magnetohydrodynamics solve the magnetic braking catastrophe?' MNRAS 457, no. 1 (March): 1037–1061.

Young, A. K., M. R. Bate, C. F. Mowat, J. Hatchell, and T. J. Harries. 2018. 'What can the SEDs of first hydrostatic core candidates reveal about their nature?' MNRAS 474 (February): 800–823.

Young, Alison K., Matthew R. Bate, Tim J. Harries, and David M. Acreman. 2019. 'Synthetic molecular line observations of the first hydrostatic core from chemical calculations.' MNRAS 487, no. 2 (August): 2853–2873.

Young, C. H., and N. J. Evans II. 2005. 'Evolutionary Signatures in the Formation of Low-Mass Protostars.' ApJ 627 (July): 293–309.

Young, C. H., J. K. Jørgensen, Y. L. Shirley, et al. 2004. 'A "Starless" Core that Isn't: Detection of a Source in the L1014 Dense Core with the Spitzer Space Telescope.' *ApJS* 154:396.

Yun, Joao Lin, and Dan P. Clemens. 1990. 'Star Formation in Small Globules: Bart BOK Was Correct!' ApJ 365 (December): L73.

Zitzwitz, P., and R. Neff. 1995. *Physics*. Glencoe.

Zubko, V. G., V. Mennella, L. Colangeli, and E. Bussoletti. 1996. 'Optical constants of cosmic carbon analogue grains - I. Simulation of clustering by a modified continuous distribution of ellipsoids.' MNRAS 282 (October): 1321–1329.

Zubko, V., E. Dwek, and R. G. Arendt. 2004. 'Interstellar Dust Models Consistent with Extinction, Emission, and Abundance Constraints.' ApJS 152 (June): 211–249.